

D Meson Hadronic Decays at CLEO-c

by
Fan Yang

Submitted in Partial Fulfillment
of the
Requirements for the Degree of
Doctor of Philosophy

Supervised by
Professor Edward H. Thorndike

Department of Physics and Astronomy
Arts, Sciences and Engineering
School of Arts and Sciences

University of Rochester
Rochester, New York

April 2008

To My Family

Curriculum Vitae

The author was born on June 5, 1978 in Xingcheng, Liaoning, China. He attended Nankai University from 1997 to 2004 and received a Bachelor of Science degree in 2001 and a Master of Science degree in 2004. From 2001 to 2004 he worked as a research assistant in the BES Collaboration. In September, 2004, he began graduate study in the Department of Physics and Astronomy at the University of Rochester and received a Master of Arts degree in 2006. Since 2005 he has been a member of the CLEO Collaboration. His thesis adviser has been Professor Edward H. Thorndike.

Acknowledgments

It would not have been possible to have written this thesis without the help of many people. I would like to thank the wonderful crew of CESR and CLEO personnel that have built and maintained the wonderful facilities at Cornell's Laboratory for Elementary-Particle Physics, allowing me to do such exciting analyses.

Foremost, I would like to express my sincere gratitude to my supervisor, Prof. Edward Thorndike, for his guidance and discussions on physics. Ed's ability to grasp the theoretical issues pertaining to experimental analyses is something that I admire greatly. I feel I have become an experimentalist from learning so much from Ed. During my graduate school career, I was deeply impressed and influenced by his diligence, his positive attitude, his forward thinking and attention to detail. I am truly honored to have the opportunity to work with him.

Performing an analysis can sometimes be quite an adventure. I feel I was extremely lucky to have been in a wonderful research team. I am very grateful to the members of the Rochester group; this includes both present members: Chul Su Park, Hajime Muramatsu and Jonathan Insler, and the past member, Qing He. Without their help, I wonder if I could have finished my research in four years. Chul Su's expertise in both experimental physics and computing techniques is something I hope I can emulate when I am a post-doc myself. Hajime's ability to understand any experimental concept has made physics discussion quite deep and rewarding. I thank Jonathan Insler and Qing He for their helpful discussions. I would like to thank Jie Chen, one of my best friends, he helped to make a good starting for me at CLEO.

I wish to express my sincere thanks to the paper committees. I would like to thank Prof. Jon Rosner, from University of Chicago and Prof. Roy Briere, from Carnegie Mellon University, for their assistance in understanding the theory in these analyses. I would like to thank Peter Onyisi, from University of Chicago for many good suggestions on the detailed analysis techniques. I also would like to thank the members of my previous paper committees: Prof. Steve Blusk, from Syracuse University, Anders Ryd and Steve Stroiney, from Cornell University, Daniel Cronin Hennessy, from University of Minnesota for their outstanding contributions to the publications.

I would like to thank my friends who I met at University of Rochester, Renjie Li, Ceng Gao, Zhi Lu, Bo Fu, and who I met at CLEO, Xin Shi, Bo Xin, Junyan Ge, Ji Li, Kaiyan Gao. I am continually grateful for the friendships, the support and encouragement during my years at Rochester and Cornell.

There are many members of the collaboration I interacted with during my stay at Wilson Lab. I wish to extend my thanks to all those who have helped me with my research work in CLEO Collaboration, in the Department of Physics, University of Rochester, and in the Department of Physics, Cornell University.

Finally, my deepest gratitude goes to my parents and my sisters for their love and support throughout my life. I would like to thank my wife for her love, patience, understanding, and support. To them I dedicate this thesis.

Abstract

The CLEO-c experiment is the best arena in which to study most D meson decay phenomena. Precise measurements of hadronic decays of D mesons allow us to better constrain parameters of the Standard Model.

We study the inclusive decays of D_s^+ mesons, using data collected near the $D_s^{*+}D_s^-$ peak production energy $E_{\text{cm}} = 4170$ MeV by the CLEO-c detector. We report the inclusive yields of D_s^+ decays to K^+X , K^-X , K_S^0X , π^+X , π^-X , π^0X , ηX , $\eta'X$, ϕX , ωX and $f_0(980)X$, and also decays into pairs of kaons, $D_s^+ \rightarrow K\bar{K}X$. Using these measurements, we obtain an overview of D_s^+ decays.

The measurements of inclusive decays of D_s^+ mesons indicate that the inclusive ω yield, $D_s \rightarrow \omega X$, is substantial. Using the same $D_s^{*+}D_s^-$ data sample, we search for D_s^+ exclusive hadronic decays involving ω . We report the first observation of $D_s^+ \rightarrow \pi^+\pi^0\omega$ decay and first upper limits on $D_s^+ \rightarrow \pi^+\eta\omega$, $D_s^+ \rightarrow K^+\pi^0\omega$, $D_s^+ \rightarrow K^+\omega$, and $D_s^+ \rightarrow K^+\eta\omega$ decays. Our measurement of $D_s^+ \rightarrow \pi^+\omega$ decay is consistent with other experiments.

Using the data collected on $\psi(3770)$ resonance and near the $D_s^{*+}D_s^-$ peak production energy by the CLEO-c detector, we study the decays of charmed mesons D^0 , D^+ , and D_s to pairs of light pseudoscalar mesons P . We report branching fractions of Cabibbo-favored, singly-Cabibbo-suppressed, and doubly-Cabibbo-suppressed decays. We normalize against the Cabibbo-favored D modes, $D^0 \rightarrow K^-\pi^+$, $D^+ \rightarrow K^-\pi^+\pi^+$, and $D_s^+ \rightarrow K^+K_S^0$. These measurements of $D \rightarrow PP$ decays allow the testing of flavor symmetry and the extraction of key amplitudes.

Contents

1	Introduction	1
1.1	The Standard Model	1
1.2	Elementary Particles	2
1.2.1	Leptons	3
1.2.2	Quarks	4
1.2.3	Bosons	5
1.3	Fundamental interactions	5
1.3.1	Gravitation	7
1.3.2	Electromagnetism	7
1.3.3	Weak Interaction	8
1.3.4	Strong Interaction	8
1.4	Inclusive Decays of D_s^+ Meson	10
1.4.1	D_s^+ Meson Decays Through Weak Annihilation	10
1.4.2	Statistical Isospin Model	12
1.4.3	Predicted Inclusive Yields for D_s^+ Decays	14
1.5	D_s^+ Exclusive Hadronic Decays Involving ω	21
1.6	Decays of Charmed Mesons to Pairs of Pseudoscalars	21
2	CESR and CLEO detector	23
2.1	CESR	24
2.2	CLEO-c detector	27
2.2.1	ZD	28
2.2.2	Drift chamber	30
2.2.3	RICH detector	33
2.2.4	Crystal Calorimeter	38

2.2.5	Magnets	39
2.2.6	Muon detector	40
2.3	Trigger and Data acquisition	40
2.3.1	Tracking trigger	41
2.3.2	Calorimeter trigger	41
2.3.3	Global Level-1 Trigger	42
2.3.4	The CLEO Data Acquisition System	44
2.4	Event reconstruction	45
2.5	Monte Carlo simulation	45
3	Inclusive Yields for D_s^+ Decays	48
3.1	Data sample	48
3.2	D_s Tag Technique	50
3.2.1	Tag Selection	50
3.2.2	Recoil Mass Against D_s Tag	51
3.2.3	Second Recoil Mass Against D_s Tag	52
3.2.4	Slow Track Veto and K_S^0 Flight Significance Cut	52
3.2.5	D_s Tag Yields	53
3.3	Signal Selection	55
3.3.1	Track Selection	55
3.3.2	Particle Identification	55
3.3.3	K_S^0 and π^0 Selection	56
3.3.4	η , η' , ϕ , ω , and $f_0(980)$ Selection	57
3.4	$D_s^+ \rightarrow K^+/K^-/\pi^+/\pi^- X$ Branching Fractions	58
3.4.1	Analysis Technique	58
3.4.2	Background and Fake Rate Study	59
3.4.3	The Cross-Fake Rates among e^\pm , K^\pm and π^\pm	64
3.4.4	μ^\pm Fake to K^\pm and π^\pm	65
3.4.5	π^\pm from K_S^0 Decay	65
3.4.6	Other Background Sources	65
3.4.7	K^\pm and π^\pm PID Efficiencies	76
3.4.8	Tracking Efficiency	76
3.4.9	$D_s^+ \rightarrow K^+/K^-/\pi^+/\pi^- X$ Branching Fractions	81

3.5	$D_s^+ \rightarrow K_S^0/\pi^0/\eta/\eta'/\phi/\omega/f_0(980) X$ Branching Fractions	88
3.5.1	$D_s^+ \rightarrow K_S^0 X$ Branching Fraction	88
3.5.2	$D_s^+ \rightarrow \pi^0 X$ Branching Fraction	88
3.5.3	$D_s^+ \rightarrow \eta X$ Branching Fraction	89
3.5.4	$D_s^+ \rightarrow \eta' X$ Branching Fraction	95
3.5.5	$D_s^+ \rightarrow \phi X$ Branching Fraction	95
3.5.6	$D_s^+ \rightarrow \omega X$ Branching Fraction	98
3.5.7	$D_s^+ \rightarrow f_0(980) X$ Branching Fraction	98
3.6	Inclusive Yields of D_s^+ into Two Kaons	98
3.7	D_s^+ Inclusive K_L^0 Decays	105
3.8	D_s^+ Inclusive $\eta\eta X$, $\eta\eta' X$, $\eta\phi X$ and $\eta\omega X$ Decays	105
3.9	Systematics	115
3.9.1	D_s Tag Systematics	115
3.9.2	MC Efficiency Statistical Error	115
3.9.3	Tracking and PID	115
3.9.4	e, K, π Production Rate	115
3.9.5	e, K, π PID Effect on Cross-Fake Rate	116
3.9.6	Uncertainty for $D_s^+ \rightarrow f_0(980) X$	116
3.9.7	Branching Fraction Truncation	117
3.9.8	The Effect from $D_s^{*+} \rightarrow D_s^+ \pi^0$ Decay	117
3.9.9	$D_s^+ \rightarrow K^+ K^+ X$ Monte Carlo Efficiency	119
3.9.10	D_s Single Tag Efficiency	119
3.9.11	Correction Factor and Systematic Summary	119
3.10	Results	119
4	General Discussions on D_s Decays	126
4.1	Measurements Summary	126
4.2	Variable Definitions and Notations	126
4.2.1	Classify “Quark-Level Final States”	126
4.2.2	Cabibbo-Favored Decays with $s\bar{s}$ in Final States	129
4.2.3	Singly-Cabibbo-Suppressed Decays with \bar{s} in Final States	129
4.2.4	Singly-Cabibbo-Suppressed Decays with $s\bar{s}\bar{s}$ in Final States	129
4.2.5	Doubly-Cabibbo-Suppressed Decays with $\bar{s}\bar{s}$ in Final States	130

4.2.6	Annihilation Decays without s or \bar{s} in Final States	130
4.2.7	Extra η Decays	130
4.2.8	η and η' from $D_s \rightarrow \bar{s}$ Decay	131
4.3	Build χ^2 for Our Global Fit	131
4.4	Results from Global Fit	132
4.5	Singly-Cabibbo-Suppressed Decay Rate	133
4.6	Minimum Yields of π^+ , π^- , and π^0	134
4.7	D_s Inclusive ω Decay	136
5	Search for D_s^+ Exclusive Hadronic Decays Involving ω	137
5.1	Data and Monte Carlo Samples	138
5.2	Event Selection	138
5.2.1	Double-Tagging Technique	138
5.2.2	Good Track Selection and PID	138
5.2.3	π^0 and η Selection	139
5.3	Yields in Data	139
5.3.1	Absolute Branching Fractions	139
5.3.2	$D_s^+ \rightarrow \pi^+ \pi^0 \omega$	140
5.3.3	$D_s^+ \rightarrow \pi^+ \omega$	140
5.3.4	$D_s^+ \rightarrow \pi^+ \eta \omega$	144
5.3.5	$D_s^+ \rightarrow K^+ \pi^0 \omega$	147
5.3.6	$D_s^+ \rightarrow K^+ \omega$	147
5.3.7	$D_s^+ \rightarrow K^+ \eta \omega$	147
5.4	Double Check for D_s^+ Inclusive Decays	151
5.5	Data and Monte Carlo Comparison	152
5.6	Systematics	155
5.6.1	D_s Tag and MC Efficiency Statistical Errors	155
5.6.2	Tracking and PID	155
5.6.3	Background Contributions from D_s Tag Sideband	159
5.6.4	Resonant Structure	159
5.6.5	Region Definition	159
5.6.6	Correction Factor	159
5.6.7	Systematic Summary	159

5.7	Results	160
6	Decays of Charmed Mesons to Pairs of Pseudoscalars	161
6.1	$D(D_s^+, D^+, D^0) \rightarrow PP$ Decays Review	161
6.2	Data Samples	165
6.2.1	$D^0\bar{D}^0$ and D^+D^- Data Sample	165
6.2.2	$D_s^{*+}D_s^-$ Data Sample	165
6.2.3	Monte Carlo Sample	165
6.3	Single Tag Method at $\psi(3770)$	166
6.3.1	ΔE Distributions	172
6.3.2	Fit Function for M_{bc} Distribution	172
6.3.3	Monte Carlo Efficiencies	173
6.4	Single Tag Method at $E_{cm} = 4170$ MeV	173
6.4.1	First Recoil Mass Variable $M_{recoil}(D_s)$	175
6.4.2	Second Recoil Mass Variable $M_{recoil}(D_s + \gamma)$	175
6.4.3	Slow Track Veto and K_S^0 Flight Significance Requirement	178
6.4.4	Fit Function for $M(D_s)$ Distribution	178
6.4.5	Monte Carlo Efficiencies	178
6.5	Tag Selection Requirements	179
6.6	Non-Resonant D Decay Background	180
6.7	Yields in Data	180
6.7.1	Absolute and Relative Branching Fractions	180
6.7.2	Data Yields	181
6.8	Systematics	212
6.8.1	Recoil Mass Requirements for D_s^+ Modes	212
6.8.2	MC Efficiencies, Tracking, and PID	213
6.8.3	π^0 , η , and K_S^0 Systematics	213
6.8.4	ΔE Requirement for D^0 and D^+ Modes	213
6.8.5	Background Shape	214
6.8.6	Crystal Ball Signal Shape for D^0 and D^+ Modes	214
6.8.7	Double Gaussian Signal Shape for D_s^+ Modes	214
6.8.8	Input Branching Fraction	214
6.8.9	Systematic Summary	215

6.9 Results Summary	215
Bibliography	222

List of Tables

1.1	Fundamental interactions [3]. Both magnitude (“relative strength”) and “range”, given in the table, are meaningful only within a rather complex theoretical framework. The force carriers of fundamental interactions are listed in the third column.	9
1.2	Statistical model predictions for charge states in $(K\bar{K}n\pi)_{I=I_3=1}$ [5]. . .	14
1.3	Statistical model predictions for charge states in $(n\pi)_{I=I_3=1}$ [5]. . .	14
1.4	Statistical model predictions for charge states in $K + (n\pi)$ arising from singly-Cabibbo-suppressed D_s^+ decays. A statistical average of contributions from $I = 1/2$ and $I = 3/2$ final states has been taken as in Table I of Ref. [15] [5].	15
1.5	Predictions of the $q\bar{q}$ pair production model for charge states in $(n\pi)_{I=I_3=1}$ [5].	
	15	
1.6	Predictions of the $q\bar{q}$ pair production model for charge states in $(K\bar{K}n\pi)_{I=I_3=1}$, for color-favored (T) and color-suppressed (C) amplitudes [5]. . . .	15
1.7	Predictions of the $q\bar{q}$ pair production model for charge states in $K + (n\pi)$, for color-favored (T) and color-suppressed (C) amplitudes [5]. .	16
1.8	D_s^+ branching fractions to leptonic, semileptonic, and hadronic modes [11]. Values for bracketed modes are inferred from statistical model. Second errors are systematic uncertainties obtained by differences between predictions of the statistical isospin model and the model based on $q\bar{q}$ production. Modes with $\mathcal{B} < 10^{-3}$ are omitted [5].	17
1.9	Inclusive yields of pions from various final states in D_s^+ decays [5]. .	18
1.10	Inclusive yields of kaons from various final states in D_s^+ decays [5]. .	19

1.11	Inclusive yields of η , η' , ϕ , and ω from various final states in D_s^+ decays [5].	20
3.1	Summary of data sets used in this analysis.	50
3.2	Three cleanest tag modes. They are reproduced from the existing v2 D_s tag [29] modes by applying additional cuts on the sub-resonance states; ΔM_ϕ (± 10 MeV), ΔM_{K^*} (± 75 MeV). Mode numbers in the first column are re-defined mode number used in this analysis.	51
3.3	D_s tag yields. Here N_R is the yield in $M(D_s)$ signal (resonance) region, N_B is the yield in $M(D_s)$ sideband region, and s is the sideband scaling factor obtained from the fit to $\Delta M(D_s)$. N_{Tag} is the sideband-subtracted tag yield.	54
3.4	Estimated Backgrounds from all kinds of particles faking a K^+ .	83
3.5	Estimated Backgrounds from all kinds of particles faking a K^- .	84
3.6	Estimated Backgrounds from all kinds of particles faking a π^+ .	85
3.7	Estimated Backgrounds from all kinds of particles faking a π^- .	86
3.8	The observed numbers, estimated background numbers, and signal yields for all inclusive two kaon modes.	105
3.9	Systematic uncertainties from fake rates.	117
3.10	Single tag efficiencies and correction factors.	120
3.11	Systematic summary.	123
3.12	D_s inclusive yield results. Uncertainties are statistical and systematic, respectively. The inclusive K_L^0 results are only used as a check for K_S^0 . PDG [11] averages are shown in the last column, when available.	125
4.1	Measurements summary.	127
4.2	Results from the global fit. The central values of parameters are listed in the second column. The errors: δ_1 is statistical uncertainty, δ_2 is from phase space factor $C_1 = 1.25 \pm 0.25$, δ_3 is from phase space factor $C_2 = 0.75 \pm 0.25$, δ_4 is from $f_1 + f_2 = 0.5 \pm 0.5$, and δ_5 is from the $\mathcal{B}(\text{extra } \eta) = (6.0 \pm 3.9)\%$.	132

4.3	The minimum yields of π^+ , π^- , and π^0 for each category. We compute the yields of π^+ , π^- , and π^0 that come from signal particles. In addition to that, we add charged pions to conserve charge. Semileptonic decays have charge conserved via e^+ or μ^+ , consequently we perform a subtraction to allow for that.	135
5.1	The detailed yields. Here N_{Sg} is the observed event number from ω mass signal region, N_{Sd} is the scaled event number from ω mass sideband regions, N_{Ss} is the sideband-subtracted double-tag yield, and N_{Up} is the number that is used to set upper limit at 90% confidence level for low statistics modes.	151
5.2	Main systematic uncertainties and correction factors.	160
5.3	Results of search for D_s^+ exclusive hadronic decays involving ω . Uncertainties are statistical and systematic, respectively.	160
6.1	CLEO-c previous published results of $D^0 \rightarrow PP$ decays, and $D^0 \rightarrow PP$ modes not measured.	162
6.2	CLEO-c previous published results of $D^+ \rightarrow PP$ decays, and $D^+ \rightarrow PP$ modes not measured.	163
6.3	CLEO-c previous published results of $D_s^+ \rightarrow PP$ decays, and $D_s^+ \rightarrow PP$ modes not measured.	164
6.4	The definitions of ΔE signal region and the low and high side ΔE sideband regions for D^0 modes.	166
6.5	The definitions of ΔE signal region and the low and high side ΔE sideband regions for D^+ modes.	172
6.6	D^0 modes Monte Carlo efficiencies.	174
6.7	D^+ modes Monte Carlo efficiencies.	174
6.8	D_s^+ modes Monte Carlo efficiencies.	179
6.9	D^0 mode Monte Carlo efficiency and data yield.	181
6.10	D^+ mode Monte Carlo efficiency and data yield.	181
6.11	D_s^+ mode Monte Carlo efficiency and data yield.	182
6.12	Uncertainties and Correction Factors	213
6.13	D^0 mode systematics summary.	216
6.14	D^+ mode systematics summary.	217

6.15 D_s^+ mode systematics summary.	218
6.16 Relative and absolute branching fractions of $D^0 \rightarrow PP$ modes.	219
6.17 Relative and absolute branching fractions of $D^+ \rightarrow PP$ modes.	220
6.18 Relative and absolute branching fractions of $D_s^+ \rightarrow PP$ modes.	221

List of Figures

1.1	Elementary particles in the Standard Model [3]. Detailed information of each particle including mass, charge, spin and name are shown. The 12 fundamental fermionic flavours are divided into three generations of four particles each. The three generations of leptons and quarks are shown in first three columns. The last column shows force carrier bosons.	6
1.2	Flavor topologies for describing charm decays [18]. T : color-favored tree; C : color-suppressed tree; E exchange; A : annihilation.	22
2.1	Cornell Electron Storage Ring (CESR). Figure from Ref. [21].	24
2.2	Exaggerated schematic of CESR beam orbits, showing the “pretzel” structure designed to keep beams separate [23].	26
2.3	3-D view of the CLEO-c detector [23].	27
2.4	The CLEO-c detector [23].	28
2.5	Schematic for ZD wire vertex chamber. Figure from Ref. [21].	29
2.6	Charge collection and multiplication in the drift chamber. Figure from Ref. [21].	30
2.7	dE/dx vs. momentum scatter plots for different particles. Figure from Ref. [21].	32
2.8	$r - \phi$ cross-section view of the CLEO RICH detector. Figure from Ref. [21].	34

2.9	Cherenkov images produced by track crossing sawtooth (top) and flat (bottom) radiators [23]. The small squares indicate charge detected in pads of RICH wire chamber. Large rectangles outline 24×40 pad arrays. Hits in the middle of the images are due to the charged track crossing the wire chamber. The other hits are due to Cherenkov photons. The flat radiator image consists of half of the Cherenkov ring, with the other half trapped in the radiator by total internal reflection. The sawtooth radiator image consists of two Cherenkov images distorted by refraction on two sides of the tooth.	36
2.10	Kaon efficiency (filled circles) and pion fake rate (open circles) measured for various cuts on the χ^2 difference between kaon and pion mass hypotheses for tracks with momentum between 0.7 and 2.7 GeV/c [23].	37
2.11	$M(\gamma\gamma)$ resolution for π^0 candidates [23].	39
2.12	Flowchart for data within the calorimeter trigger [23].	43
2.13	Architecture of the CLEO Data Acquisition System [23].	46
3.1	The typical Feynman diagrams of D_s^+ Cabibbo-favored decay (a), singly Cabibbo-suppressed decay (b) and (c), doubly Cabibbo-suppressed decay (d), and annihilation decays (e) and (f).	49
3.2	Typical M_{recoil} vs. $M(D_s)$ distribution obtained from signal Monte Carlo sample: $D_s^- \rightarrow \phi\pi^-, \phi \rightarrow K^+K^-$	51
3.3	The left plot shows the clear bump structure in the high side tail of $M(D_s)$ distribution. After we apply the slow track veto and K_S^0 flight significance requirement, the bump disappears.	53
3.4	The mass difference $\Delta M(D_s) \equiv M(D_s) - m_{D_s}$ distributions in each tag mode after first recoil mass and second recoil mass cuts are applied. We fit the $\Delta M(D_s)$ distribution (open circle) to the sum (solid curve) of signal (double Gaussian) plus background (second degree polynomial, dashed curve) functions. Signal shape parameters ($A_1/A_2, \mu_1, \sigma_1, \mu_2$ and σ_2) are obtained from fits in mcDD-mix and fixed during the fit. Primary purpose of the fit is to obtain the sideband scaling factor.	54

3.5	Observed momentum spectra of charged kaons, pions, and electrons. Red rectangles are obtained from data and blue solid histograms are Monte Carlo.	60
3.6	Monte Carlo truth information on e^+ momentum spectrum.	61
3.7	Monte Carlo truth information on e^- momentum spectrum.	61
3.8	Monte Carlo truth information on K^+ momentum spectrum.	62
3.9	Monte Carlo truth information on K^- momentum spectrum.	62
3.10	Monte Carlo truth information on π^+ momentum spectrum.	62
3.11	Monte Carlo truth information on π^- momentum spectrum.	63
3.12	Momentum bin definitions for fake rates and background study. The separate boxes indicate the different momentum regions. We merge the bins with the same color into a big bin to make sure there is enough statistics in each bin for fake rates and background study.	63
3.13	e^+ fake to K^+ rate.	67
3.14	π^+ fake to K^+ rate.	67
3.15	μ^+ fake to K^+ rate.	68
3.16	Other background fake to K^+	68
3.17	e^- fake to K^- rate.	69
3.18	π^- fake to K^- rate.	69
3.19	μ^- fake to K^-	70
3.20	Other background fake to K^-	70
3.21	e^+ fake to π^+ rate.	71
3.22	K^+ fake to π^+ rate.	71
3.23	μ^+ fake to π^+ rate.	72
3.24	Real π^+ background from K_S^0 decay.	72
3.25	Other background fake to π^+	73
3.26	e^- fake to π^- rate.	73
3.27	K^- fake to π^- rate.	74
3.28	μ^- fake to π^-	74
3.29	Real π^- background from K_S^0 decay.	75
3.30	Other background fake to π^-	75
3.31	K^+ PID efficiency.	77
3.32	K^- PID efficiency.	77

3.33 π^+ PID efficiency.	78
3.34 π^- PID efficiency.	78
3.35 K^+ tracking efficiency.	79
3.36 K^- tracking efficiency.	79
3.37 π^+ tracking efficiency.	80
3.38 π^- tracking efficiency.	80
3.39 Background study for $D_s^+ \rightarrow K^+X$ momentum spectrum in real data.	81
3.40 Background study for $D_s^+ \rightarrow K^-X$ momentum spectrum in real data.	81
3.41 Background study for $D_s^+ \rightarrow \pi^+X$ momentum spectrum in real data.	82
3.42 Background study for $D_s^+ \rightarrow \pi^-X$ momentum spectrum in real data.	82
3.43 Charged kaon and pion laboratory momentum spectra after background subtractions and efficiency corrections: (a) $D_s^+ \rightarrow K^+X$, (b) $D_s^+ \rightarrow \pi^+X$, (c) $D_s^+ \rightarrow K^-X$, and (d) $D_s^+ \rightarrow \pi^-X$. Charge conjugate modes have been included on these plots. The points are obtained from data and solid line indicates the Monte Carlo after tuning. Good agreement between data and tuned Monte Carlo is found. Monte Carlo is normalized to data based on tag yield.	87
3.44 K_S^0 reconstruction efficiency. The corresponding number for each point is shown on the top of the plot. The colorful background of the number indicate how to define the momentum bin. The bins with same color have been merged into a big bin.	88
3.45 K_S^0 momentum spectra. Left plot is before efficiency correction and right one is after efficiency correction. Red rectangle points are obtained from data and blue histogram is Monte Carlo. The branching fraction shown on the right plot includes only statistical error.	89
3.46 π^0 invariant mass distributions, for π^0 momenta from 0.0 to 0.6 GeV/ c .	90
3.47 π^0 invariant mass distributions, for π^0 momenta from 0.6 to 1.2 GeV/ c .	91
3.48 π^0 invariant mass distribution, summed over all momenta.	92
3.49 π^0 invariant mass distribution sideband scaling factor.	93
3.50 Background study for true π^0 but from K_S^0 decay.	93
3.51 π^0 reconstruction efficiency.	94

3.52 π^0 momentum spectra. Left plot is before efficiency correction and right one is after efficiency correction. Red rectangle points are obtained from data and blue histogram is Monte Carlo. The branching fraction shown on the right plot includes only statistical error.	94
3.53 $D_s^+ \rightarrow \eta X$ decay study.	96
3.54 $D_s^+ \rightarrow \eta' X$ decay study..	97
3.55 $D_s^+ \rightarrow \phi X$ decay study.	99
3.56 $D_s^+ \rightarrow \omega X$ decay study. MC signal plot is from the generic MC sample with ω on the signal side. MC background plot is from the generic MC sample without ω on the signal side. Data S.S. is the data plot after D_s tag sideband subtraction. We get signal and background shape parameters from the fits to MC signal and MC background respectively and apply them in the fit to data. The data-MC comparison is shown on Data-MC plot, Monte Carlo is normalized to data based on tag yield.	100
3.57 $D_s^+ \rightarrow f_0(980)X$ decay study.	101
3.58 $D_s^+ \rightarrow K_S^0 K_S^0 X$ decay study.	102
3.59 $D_s^+ \rightarrow K_S^0 K^+ X$ decay study.	102
3.60 $D_s^+ \rightarrow K_S^0 K^- X$ decay study.	103
3.61 $D_s^+ \rightarrow K^+ K^- X$ decay study.	103
3.62 $D_s^+ \rightarrow K^+ K^+ X$ decay study.	104
3.63 $D_s^+ \rightarrow K^- K^- X$ decay study.	104
3.64 $D_s^+ \rightarrow K_L^0 X$ decay study.	106
3.65 $D_s^+ \rightarrow K_L^0 K_S^0 X$ decay study.	107
3.66 $D_s^+ \rightarrow K_L^0 K^+ X$ decay study.	108
3.67 $D_s^+ \rightarrow K_L^0 K^- X$ decay study.	109
3.68 $D_s^+ \rightarrow \eta \eta X$ decay study.	111
3.69 $D_s^+ \rightarrow \eta \eta' X$ decay study.	112
3.70 $D_s^+ \rightarrow \eta \phi X$ decay study.	113
3.71 $D_s^+ \rightarrow \eta \omega X$ decay study.	114
3.72 Systematic study for π^0 from $D_s^{*+} \rightarrow D_s^+ \pi^0$ decay.	118
3.73 D_s tag invariant mass distributions, for some of the signal side processes.121	

3.74 D_s tag invariant mass distributions, for the rest of the signal side processes.	122
4.1 The typical Feynman diagrams of D_s^+ decays: (a) Cabibbo-favored decay, (b) single-Cabibbo-suppressed decay, (c) single-Cabibbo-suppressed decay, (d) double-Cabibbo-suppressed decay, (e) short-range annihilation decay, (f) long-range annihilation decay.	128
5.1 $D_s^+ \rightarrow \pi^+ \pi^0 \omega$ decay study.	141
5.2 Two dimensions plot of $M_{\pi^+ \pi^0}$ vs. $M_{\pi^+ \pi^- \pi^0}$. Clear $\rho^+ \eta$ and $\rho^+ \phi$ bands are found. The red histogram on the right plot is the $\pi^+ \pi^0$ invariant mass distribution after the corresponding ω mass sideband subtraction. The blue histogram is from the phase space $\pi^+ \pi^0 \omega$ Monte Carlo. The green histogram is from the $\rho^+ \omega$ Monte Carlo.	142
5.3 Fit data to sum of phase space $\pi^+ \pi^0 \omega$ MC and $\rho^+ \omega$ MC to extract the $\rho^+ \omega$ contribution to $D_s^+ \rightarrow \pi^+ \pi^0 \omega$ decay.	143
5.4 $D_s^+ \rightarrow \pi^+ \omega$ decay study	145
5.5 $D_s^+ \rightarrow \pi^+ \eta \omega$ decay study	146
5.6 $D_s^+ \rightarrow K^+ \pi^0 \omega$ decay study	148
5.7 $D_s^+ \rightarrow K^+ \omega$ decay study	149
5.8 $D_s^+ \rightarrow K^+ \eta \omega$ decay study.	150
5.9 Data and Monte Carlo comparison plot of $\pi^+ \pi^- \pi^0$ invariant mass distribution. Blue solid histogram is obtained from our generic Monte Carlo and scaled to data according to D_s tag yield. Red points with error bars are from real data. Clear η and ϕ peaks are found in both data and Monte Carlo. The ω peak only shows up in data but not in Monte Carlo.	152
5.10 $D_s^+ \rightarrow \eta X, \eta \rightarrow \pi^+ \pi^- \pi^0$ decay study. MC signal plot is from the generic MC sample with η on the signal side. MC Total plot is from the whole generic MC sample. Data S.S. is the data plot after D_s tag sideband subtraction. We get signal and background shape parameters from the fits to MC signal and MC Total respectively and apply them in the fit to data. The data-MC comparison is shown on Data-MC plot, Monte Carlo is normalized to data based on tag yield.	153

5.11 $D_s^+ \rightarrow \phi X, \phi \rightarrow \pi^+ \pi^- \pi^0$ decay study. MC signal plot is from the generic MC sample with ϕ on the signal side. MC Total plot is from the whole generic MC sample. Data S.S. is the data plot after D_s tag sideband subtraction. We get signal and background shape parameters from the fits to MC signal and MC Total respectively and apply them in the fit to data. The data-MC comparison is shown on Data-MC plot, Monte Carlo is normalized to data based on tag yield.	154
5.12 The data and Monte Carlo comparison plot for $D_s^+ \rightarrow \pi^+ \pi^0 \omega$.	156
5.13 The data and Monte Carlo comparison plot for $D_s^+ \rightarrow \pi^+ \omega$.	156
5.14 The data and Monte Carlo comparison plot for $D_s^+ \rightarrow \pi^+ \eta \omega$.	157
5.15 The data and Monte Carlo comparison plot for $D_s^+ \rightarrow K^+ \pi^0 \omega$.	157
5.16 The data and Monte Carlo comparison plot for $D_s^+ \rightarrow K^+ \omega$.	158
5.17 The data and Monte Carlo comparison plot for $D_s^+ \rightarrow K^+ \eta \omega$.	158
6.1 ΔE and M_{bc} distributions from signal MC for $D^0 \rightarrow \pi^+ \pi^-$, $D^0 \rightarrow K^- \pi^+$, $D^0 \rightarrow K^+ K^-$, and $D^0 \rightarrow K_S^0 \pi^0$ modes.	167
6.2 ΔE and M_{bc} distributions from signal MC for $D^0 \rightarrow K_S^0 \eta$, $D^0 \rightarrow \pi^0 \pi^0$, $D^0 \rightarrow K_S^0 \eta'$, and $D^0 \rightarrow K_S^0 K_S^0$ modes.	168
6.3 ΔE and M_{bc} distributions from signal MC for $D^0 \rightarrow \eta \eta$, $D^0 \rightarrow \pi^0 \eta$, $D^0 \rightarrow \eta \eta'$, and $D^0 \rightarrow \pi^0 \eta'$ modes.	169
6.4 ΔE and M_{bc} distributions from signal MC for $D^+ \rightarrow K^+ \pi^0$, $D^+ \rightarrow K_S^0 \pi^+$, $D^+ \rightarrow K_S^0 K^+$, and $D^+ \rightarrow \pi^+ \pi^0$ modes.	170
6.5 ΔE and M_{bc} distributions from signal MC for $D^+ \rightarrow K^+ \eta'$, $D^+ \rightarrow \pi^+ \eta$, $D^+ \rightarrow \pi^+ \eta'$, and $D^+ \rightarrow K^+ \eta$ modes.	171
6.6 $M(D_s)$, $M_{\text{recoil}}(D_s)$, and $M_{\text{recoil}}(D_s + \gamma)$ distributions from signal MC for $D_s^+ \rightarrow \pi^+ \eta$, $D_s^+ \rightarrow K_S^0 K^+$, $D_s^+ \rightarrow \pi^+ \eta'$, and $D_s^+ \rightarrow \pi^+ \pi^0$ modes.	176
6.7 $M(D_s)$, $M_{\text{recoil}}(D_s)$, and $M_{\text{recoil}}(D_s + \gamma)$ distributions from signal MC for $D_s^+ \rightarrow K^+ \eta$, $D_s^+ \rightarrow K_S^0 \pi^+$, $D_s^+ \rightarrow K^+ \eta'$, and $D_s^+ \rightarrow K^+ \pi^0$ modes.	177
6.8 $D^0 \rightarrow K^- \pi^+$ decay study.	183
6.9 $D^0 \rightarrow K_S^0 \pi^0$ decay study.	184
6.10 $D^0 \rightarrow \pi^+ \pi^-$ decay study.	185
6.11 $D^0 \rightarrow K^+ K^-$ decay study.	186
6.12 $D^0 \rightarrow \pi^0 \pi^0$ decay study.	187

6.13 $D^0 \rightarrow K_S^0 K_S^0$ decay study.	188
6.14 $D^0 \rightarrow K_S^0 \eta$ decay study.	189
6.15 $D^0 \rightarrow K_S^0 \eta'$ decay study.	190
6.16 $D^0 \rightarrow \pi^0 \eta$ decay study.	191
6.17 $D^0 \rightarrow \pi^0 \eta'$ decay study.	192
6.18 $D^0 \rightarrow \eta \eta$ decay study.	193
6.19 $D^0 \rightarrow \eta \eta'$ decay study.	194
6.20 $D^+ \rightarrow K^- \pi^+ \pi^+$ decay study.	195
6.21 $D^+ \rightarrow K_S^0 \pi^+$ decay study.	196
6.22 $D^+ \rightarrow \pi^+ \pi^0$ decay study.	197
6.23 $D^+ \rightarrow K^+ \pi^0$ decay study.	198
6.24 $D^+ \rightarrow K_S^0 K^+$ decay study.	199
6.25 $D^+ \rightarrow \pi^+ \eta$ decay study.	200
6.26 $D^+ \rightarrow K^+ \eta$ decay study.	201
6.27 $D^+ \rightarrow K^+ \eta'$ decay study.	202
6.28 $D^+ \rightarrow \pi^+ \eta'$ decay study.	203
6.29 $D_s^+ \rightarrow K_S^0 K^+$ decay study.	204
6.30 $D_s^+ \rightarrow \pi^+ \pi^0$ decay study.	205
6.31 $D_s^+ \rightarrow \pi^+ \eta$ decay study.	206
6.32 $D_s^+ \rightarrow \pi^+ \eta'$ decay study.	207
6.33 $D_s^+ \rightarrow K_S^0 \pi^+$ decay study.	208
6.34 $D_s^+ \rightarrow K^+ \pi^0$ decay study.	209
6.35 $D_s^+ \rightarrow K^+ \eta$ decay study.	210
6.36 $D_s^+ \rightarrow K^+ \eta'$ decay study.	211

Chapter 1

Introduction

The goal of high energy particle physics is to understand the most fundamental particles and interactions: the building blocks of the Universe.

1.1 The Standard Model

Physicists have spent decades developing the Standard Model [1], a set of theories that describe in detail the fundamental particles that make up the universe and the forces at work between them. These elementary particles make up all visible matter in the universe. The Standard Model is a gauge theory of the electroweak and strong interactions with the gauge group $SU(3) \times SU(2) \times U(1)$.

In 1963, Sheldon Glashow discovered a way to combine the electromagnetic and weak interactions, this was the first step towards the Standard Model. After that, in 1967, Steven Weinberg and Abdus Salam incorporated the Higgs mechanism into Glashow's electroweak theory, giving it its modern form [1]. The Higgs mechanism is also believed to give rise to the rest masses of all the elementary particles the Standard Model accounts for, the W and Z bosons, and the fermions, the latter broken down into quarks and leptons. Different particles feel the Higgs field in different ways, and thus acquire different masses.

The electroweak theory became widely accepted after the discovery of neutral weak currents caused by Z boson exchange at CERN [2]. The W and Z bosons were discovered experimentally in 1981, and their masses were found to be as the Standard Model predicted.

The theory of the strong interaction, to which many contributed, acquired its modern form around 1973-74, when experiments confirmed that the hadrons were composed of fractionally charged quarks.

Numerous experiments carried out since the mid-20th century have yielded findings consistent with the Standard Model. The Standard Model falls short of being a complete theory of fundamental interactions because it does not include gravity and because it is incompatible with the recent observation of neutrino oscillations which provided some experimental evidence consistent with neutrinos having mass, which the Standard Model does not allow. Many new theories have been put forth to describe physics beyond the Standard Model. For example, Supersymmetry, SUSY, that could provide a way to unify three of the four fundamental forces: the electromagnetic; weak; and strong forces.

1.2 Elementary Particles

An elementary particle or fundamental particle is a particle not known to have substructure; that is, it is not known to be made up of smaller particles. If an elementary particle truly has no substructure, then it is one of the basic building blocks of the universe from which all other particles are made. In the Standard Model, the leptons, quarks, and gauge bosons are elementary particles.

All elementary particles are either bosons or fermions (depending on their spin). The spin-statistics theorem identifies the resulting quantum statistics that differentiates fermions from bosons. According to this methodology: particles normally associated with matter are fermions, having half-integer spin; they are divided into twelve flavours. Particles associated with fundamental forces are bosons, having integer spin.

- Fermions:
 - Leptons: electron neutrino, electron, muon neutrino, muon, tauon neutrino, tauon
 - Quarks: up, down, charm, strange, top, bottom
- Bosons:

- Gauge bosons: gluon, W and Z bosons, photon
- Other bosons: Higgs boson, graviton

1.2.1 Leptons

Leptons are a family of elementary particles, alongside quarks and gauge bosons (also known as force carriers). Leptons are fermions and are subject to the electromagnetic force, the gravitational force, and weak interaction. But leptons do not participate in the strong interaction.

There are six flavours of leptons, forming three generations

$$\begin{array}{cccc} 0 & \left(\begin{array}{c} \nu_e \\ e^- \end{array} \right) & \left(\begin{array}{c} \nu_\mu \\ \mu^- \end{array} \right) & \left(\begin{array}{c} \nu_\tau \\ \tau^- \end{array} \right) \\ -e & & & \end{array}$$

The first generation is the electronic leptons, comprising electrons (e^-), and electron neutrinos (ν_e); the second is the muonic leptons, comprising muons (μ^-), and muon neutrinos (ν_μ); and the third is the tauonic leptons, comprising tauons (τ^-), and tauon neutrinos (ν_τ). Each lepton has a corresponding antiparticle, these antiparticles are known as antileptons.

Leptons are an important part of the Standard Model, especially the electrons which are one of the components of atoms, alongside protons and neutrons. Exotic atoms with muons and tauons instead of electrons can also be synthesized.

The members of each generation's weak isospin doublet are assigned leptonic numbers that are conserved under the Standard Model. Electrons and electron neutrinos have an electronic number of $L_e = 1$, while muons and muon neutrinos have a muonic number of $L_\mu = 1$, while tauons and tauon neutrinos have a tauonic number of $L_\tau = 1$. The antileptons have their respective generation's leptonic numbers of -1 .

Conservation of the leptonic numbers means that the number of leptons of the same type remains the same, when particles interact. This implies that leptons and antileptons must be created in pairs of a single generation. However, neutrino oscillations are known to violate the conservation of the individual leptonic numbers. Such a violation is considered to be smoking gun evidence for physics beyond the

Standard Model. A much stronger conservation law is the conservation of the total number of leptons (L), conserved even in the case of neutrino oscillations, but even it is still violated by a tiny amount by the chiral anomaly.

1.2.2 Quarks

Similarly as leptons, there are six flavours of quarks, forming three generations

$$\begin{array}{c} +\frac{2}{3}e \\ -\frac{1}{3}e \end{array} \quad \begin{pmatrix} u \\ d \end{pmatrix} \quad \begin{pmatrix} c \\ s \end{pmatrix} \quad \begin{pmatrix} t \\ b \end{pmatrix}$$

Each quark has a corresponding antiquark. Quarks and antiquarks have never been detected to be isolated, a fact explained by confinement. Every quark carries one of three color charges of the strong interaction; antiquarks similarly carry anti-color. Color charged particles interact via gluon exchange in the same way that charged particles interact via photon exchange. However, gluons are themselves color charged, resulting in an amplification of the strong force as color charged particles are separated. Unlike the electromagnetic force which diminishes as charged particles separate, color charged particles feel increasing force.

However, color charged particles may combine to form color neutral composite particles called hadrons. A quark may pair up to an antiquark: the quark has a color and the antiquark has the corresponding anticolor. The color and anticolor cancel out, forming a color neutral meson. Alternatively, three quarks can exist together, one quark being “red”, another “blue”, another “green”. These three colored quarks together form a color-neutral baryon. Symmetrically, three antiquarks with the colors “antired”, “antiblue”, and “antigreen” can form a color-neutral antibaryon.

Quarks also carry fractional electric charges, but since they are confined within hadrons whose charges are all integral, fractional charges have never been isolated. Note that quarks have electric charges of either $+2/3$ or $-1/3$, whereas antiquarks have corresponding electric charges of either $-2/3$ or $+1/3$.

Evidence for the existence of quarks comes from deep inelastic scattering: firing electrons at nuclei to determine the distribution of charge within nucleons (which are baryons). If the charge is uniform, the electric field around the proton should be uniform and the electron should scatter elastically. Low-energy electrons do scatter

in this way, but above a particular energy, the protons deflect some electrons through large angles. The recoiling electron has much less energy and a jet of particles is emitted. This inelastic scattering suggests that the charge in the proton is not uniform but split among smaller charged particles: quarks.

1.2.3 Bosons

In the Standard Model, vector (spin-1) bosons (gluons, photons, and the W and Z bosons) mediate forces, while the Higgs boson (spin-0) is responsible for particles having intrinsic mass.

Gluons are the mediators of the strong interaction and carry both color and anticolor. Although gluons are massless, they are never observed in detectors due to color confinement; rather, they produce jets of hadrons, similar to single quarks. The first evidence for gluons came from annihilations of electrons and antielectrons at high energies which sometimes produced three jets: a quark, an antiquark, and a gluon.

There are three weak gauge bosons: W^+ , W^- , and Z^0 , these mediate the weak interaction. The massless photon mediates the electromagnetic interaction.

The Higgs boson (nicknamed the God particle) is a massive scalar elementary particle predicted to exist by the Standard Model, but has not yet been observed. The discovery of the Higgs boson from experiment would help explain how massless elementary particles can have mass. More specifically, the Higgs boson would explain the difference between the massless photon, which mediates electromagnetism, and the massive W and Z bosons, which mediate the weak force.

The details of elementary particles are shown in Figure 1.1 [3]. The 12 fundamental fermionic flavours are divided into three generations of four particles each. The three generations of leptons and quarks are shown in first three columns. The last column shows force carrier bosons.

1.3 Fundamental interactions

There are four different forces in nature: gravity, electromagnetism, the weak force, and the strong force. In physics, a fundamental interaction or fundamental force is

	I	II	III	
mass→	2.4 MeV	1.27 GeV	171.2 GeV	Bosons (Forces)
charge→	$\frac{2}{3}$	$\frac{2}{3}$	$\frac{2}{3}$	
spin→	$\frac{1}{2}$	$\frac{1}{2}$	$\frac{1}{2}$	
name→	up	charm	top	
Quarks	u	c	t	photon
	4.8 MeV	104 MeV	4.2 GeV	g
	$-\frac{1}{3}$	$-\frac{1}{3}$	$-\frac{1}{3}$	gluon
	$\frac{1}{2}$	$\frac{1}{2}$	$\frac{1}{2}$	
	down	strange	bottom	
Leptons	d	s	b	
	<2.2 eV	<0.17 MeV	<15.5 MeV	Z⁰
	0	0	0	weak force
	$\frac{1}{2}$	$\frac{1}{2}$	$\frac{1}{2}$	
	v_e	v_μ	v_τ	
	electron neutrino	muon neutrino	tau neutrino	
	0.511 MeV	105.7 MeV	1.777 GeV	W⁺
	-1	-1	-1	weak force
	$\frac{1}{2}$	$\frac{1}{2}$	$\frac{1}{2}$	
	e	μ	τ	
	electron	muon	tau	

Figure 1.1: Elementary particles in the Standard Model [3]. Detailed information of each particle including mass, charge, spin and name are shown. The 12 fundamental fermionic flavours are divided into three generations of four particles each. The three generations of leptons and quarks are shown in first three columns. The last column shows force carrier bosons.

a process by which elementary particles interact with each other. An interaction is often described as a physical field, and is mediated by the exchange of gauge bosons between particles. An interaction is fundamental when it cannot be described in terms of other interactions.

1.3.1 Gravitation

Gravity is the most familiar, but it is also the weakest. Since gravity is so weak, it has no measurable effect on the subatomic particles discussed in this thesis. But it is important for macroscopic objects and over long distances.

There are elementary particles, such as neutrons and neutrinos, lacking electrostatic charge. Electrostatic attraction is not relevant for large celestial bodies, such as planets, stars, and galaxies, simply because such bodies contain equal numbers of protons and electrons and so have a net electric charge of zero. On the other hand, nothing “cancels” gravity. Hence all objects having mass are subject to gravitational force, which works in only one direction: attraction.

Because of its long range, gravity is responsible for such large-scale phenomena as the structure of galaxies, black holes, and the expansion of the universe. Gravity also explains astronomical phenomena on more modest scales, such as planetary orbits, as well as everyday experience: objects fall; heavy objects act as if they were glued to the ground; animals and humans can jump only so high.

1.3.2 Electromagnetism

The electromagnetic force is understood as the exchange of photons between two electrical charges. This is described by a theory called quantum electrodynamics (QED). An example of an electromagnetic interaction is the electron-positron scattering process. This reaction is called Bhabha scattering. The particle can either exchange a “virtual” photon, or the particle-antiparticle pair can annihilate to produce a “virtual” photon. The photon can then materialize into another electron-positron pair.

Electromagnetism is infinite-ranged like gravity, but vastly stronger, and therefore describes almost all macroscopic phenomena of everyday experience, ranging from the impenetrability of solids, friction, rainbows, lightning, and all human-made

devices using electric current, such as television, lasers, and computers. Electromagnetism fundamentally determines all macroscopic, and many atomic level, properties of the chemical elements, including all chemical bonding.

1.3.3 Weak Interaction

The weak interaction is actually another aspect of the same process which produces the electromagnetic interaction. There are many similarities between the forces. In particular, the Z^0 boson acts like a heavy photon. Processes involving the Z^0 are called neutral-current interactions, because the boson is not electrically charged. The W^+ and W^- bosons behave a bit differently. Instead of just being absorbed or radiated, these charged-current interactions actually change the properties of the particle. Electromagnetism and the weak force are now understood to be two aspects of a unified electroweak interaction. This discovery was the first step toward the unified theory known as the Standard Model. The weak interaction is the only known interaction which does not conserve parity; it is left-right asymmetric. The weak interaction even violates CP symmetry but does conserve CPT .

1.3.4 Strong Interaction

As implied by its name, the strong force is much stronger than the other interactions. The strong interaction, or strong nuclear force, is the most complicated interaction, mainly because of the way it varies with distance. At distances greater than 10 femtometers, the strong force is practically unobservable. Moreover, it holds only inside the nucleus. It binds quarks into composite particles called hadrons. The binding is so complete, that despite extensive searches, no free quarks have ever been observed. The quarks in a hadron are bound together in such a way that there is no net color. Gluons carry a color charge, so like the quarks, they are required to be in color-neutral particles. The fundamental theory of QCD (Quantum Chromodynamics) is simple models for the interactions of quarks.

Fundamental interactions are summarized in Table 1.1 [3]. Both magnitude (“relative strength”) and “range”, as given in the table, are meaningful only within a rather complex theoretical framework. The force carriers of fundamental interactions are listed in the third column.

Table 1.1: Fundamental interactions [3]. Both magnitude (“relative strength”) and “range”, given in the table, are meaningful only within a rather complex theoretical framework. The force carriers of fundamental interactions are listed in the third column.

Interaction	Current Theory	Mediators	Relative Strength	Long-Distance Behavior	Range(m)
Strong	Quantum chromodynamics (QCD)	gluons	10^{38}	1	10^{-15}
Electro-magnetic	Quantum electrodynamics (QED)	photons	10^{36}	$\frac{1}{r^2}$	∞ (infinite)
Weak	Electroweak Theory	W and Z bosons	10^{25}	$\frac{e^{-m_{W,Z}r}}{r}$	10^{-18}
Gravitation	General Relativity (GR)	gravitons (not yet discovered)	1	$\frac{1}{r^2}$	∞ (infinite)

1.4 Inclusive Decays of D_s^+ Meson

The D_s^+ meson, consisting of a c and \bar{s} quark, is the least extensively studied of the ground state charmed mesons. Studies of inclusive branching fractions will give an overview of D_s^+ decays and provide strong constraints on Monte Carlo simulation. In addition to providing an improved Monte Carlo decay table, measurements of inclusive decays of D_s^+ meson allow some comparisons with expectations. The study of inclusive ω production in D_s^+ decays is of interest in shedding light on mechanisms of weak decay and their interplay with long-distance (nonperturbative) physics. Additionally, the study of η and particularly η' inclusive production is relevant because fits based on flavor SU(3) have great difficulty in reproducing the large reported branching fractions $\mathcal{B}(D_s^+ \rightarrow \rho^+ \eta) = (13.2 \pm 2.2)\%$ and $\mathcal{B}(D_s^+ \rightarrow \rho^+ \eta') = (12.2 \pm 2.0)\%$ [4], preferring values a factor of 2 and 4 less, respectively. In this thesis, we present measurements of many inclusive yields from D_s^+ decays. A global fit on inclusive yields of D_s^+ decays is performed to get an estimate of D_s^+ annihilation decays.

The prediction of inclusive yields from D_s^+ decays is permitted by the availability of branching fractions for a large majority of D_s^+ decays. This is achieved with the help of a modest amount of input from an isospin statistical model applied to non-resonant multibody D_s^+ decays. The calculated inclusive branching fractions can be compared with our measurements of inclusive yields of D_s^+ decays and examined for specific final states which can shed light on strong and weak decay mechanisms. Ref [5] shows the detail on the theoretical calculation of inclusive yields from D_s^+ decays. The following section will briefly introduce the method that is used to predict inclusive yields of D_s^+ decays in Ref [5].

1.4.1 D_s^+ Meson Decays Through Weak Annihilation

Searching for new physics is always a hot topic in particle physics. The mechanisms responsible for decays of hadrons containing heavy quarks are of interest both as probes of the strong interactions and as sources of information on the underlying weak processes. A firm understanding of long-distance (nonperturbative) effects is very important for new physics searching in such processes.

In B meson decays, the “weak annihilation,” or WA [6], is known as an incompletely understood process. In principle, one could extract the Cabibbo-Kobayashi-

Maskawa (CKM) matrix element $|V_{ub}|$ from charmless semileptonic B decays. As $|V_{ub}/V_{cb}|^2 \simeq 1\%$ while phase space favors $b \rightarrow u\ell\nu$ over $b \rightarrow c\ell\nu$ by a factor of 2, the charmless semileptonic B decays constitute only 2% of all semileptonic B decays. The study of leptons with energies E_ℓ beyond the endpoint for $b \rightarrow c\ell\nu$ can be used to extract the small charmless semileptonic fraction. But the WA process can contaminate the endpoint signal: a B^+ can turn into a soft $I = 0$ hadronic system plus a vector $\bar{b}u$ which can then annihilate freely into $\ell\nu$. (Helicity arguments greatly suppress the annihilation of a pseudoscalar $\bar{b}u$ into $\ell\nu$.) The CLEO [7] and BaBar [8] Collaborations have placed upper limits for WA of a few percent of charmless semileptonic b decays, while theoretical estimates [9] lie somewhat lower. The WA process should be more visible in charm decays because it is supposed to be of order $1/m_Q^3$, where Q is the heavy quark. The semileptonic decay $D_s^+ \rightarrow \omega\ell^+\nu_\ell$ can be used to probe this WA process [10]. By comparing the decays $D_s^+ \rightarrow \omega\ell^+\nu_\ell$ and $D_s^+ \rightarrow \phi\ell^+\nu_\ell$ with the corresponding hadronic decays $D_s^+ \rightarrow \omega\pi^+$ and $D_s^+ \rightarrow \phi\pi^+$, one could anticipate a WA contribution to the branching fraction $\mathcal{B}(\omega\ell^+\nu_\ell)$ of order 10^{-3} , nearly an order of magnitude greater than one would expect from the process $D_s^+ \rightarrow \phi\ell^+\nu_\ell$ taking account of $\omega\phi$ mixing.

The hadronic decays of D_s^+ provide very useful information to understand the WA process. D_s^+ decays to VP final states (V = vector, P = pseudoscalar) dominated by the annihilation process $c\bar{s} \rightarrow u\bar{d}$ do not appear to be consistent with flavor SU(3) [4]. Within flavor SU(3) [4], the decay of $D_s^+ \rightarrow \omega\pi^+$ is expected to be suppressed and the decay of $D_s^+ \rightarrow \rho^0\pi^+$ is allowed. From experimental measurements, the branching fraction of the suppressed decay $D_s^+ \rightarrow \omega\pi^+$ was measured to be $(2.5 \pm 0.9) \times 10^{-3}$ [11], while the allowed mode $D_s^+ \rightarrow \rho^0\pi^+$ is not observed [11]. The contribution of the weak process $c\bar{s} \rightarrow u\bar{d}$ to the decay $D_s^+ \rightarrow \omega\pi^+$ is forbidden by G-parity. The decay $D_s^+ \rightarrow \omega\pi^+$ may proceed through pre-radiation of the ω , whether via violation of the Okubo-Zweig-Iizuka (OZI) rule [12] or rescattering. For example, the D_s^+ can dissociate into two-meson states such as $D^{(*)0}K^{(*)+}$ and $D^{(*)+}K^{(*)0}$ which rescatter strongly to $(c\bar{s})\omega$ while the virtual $c\bar{s}$ state decays weakly to π^+ . A possible signature for ordinary WA caused directly by $c\bar{s} \rightarrow u\bar{d}$ would be the decay $D_s^+ \rightarrow \omega\pi^+\pi^0$, where the $u\bar{d}$ current couples to $\omega\pi^+\pi^0$. The decays of $D_s^+ \rightarrow \omega\pi^+\eta$ and $D_s^+ \rightarrow \omega\pi^+\eta'$ would also be possible through the process, $c\bar{s}$ emits a $Q = 1$ vector weak current, which can couple to $\omega\pi^+$, a state $s\bar{s}$ is left over, which

can couple to η or η' . The decay $D_s^+ \rightarrow \omega\pi^+\eta'$ is quite limited by the phase space.

1.4.2 Statistical Isospin Model

In the absence of information on branching fractions to certain modes, a statistical isospin model is used to relate them to other known modes. Such a model may be constructed by coupling the internal subsystems to isospin amplitudes in all possible ways and then assuming the reduced amplitudes are equal in magnitude and incoherent in phase [13, 14, 15]. This technique is illustrated with two cases of total $I = I_3 = 1$, $K\bar{K}\pi$ and 3π , using particle orders consistent with those quoted for the isospin Clebsch-Gordan coefficients in Ref. [11]. The following examples and tables are quoted from Ref. [5].

A. Example of $(K\bar{K}\pi)_{I=I_3=1}$

1. $(K\bar{K})\pi$: We label the reduced amplitudes $A_I^{K\bar{K}}$ by $I_{K\bar{K}} = 0, 1$. Then

$$A(K^+K^-\pi^+) = \frac{1}{\sqrt{2}}A_0^{K\bar{K}} - \frac{1}{2}A_1^{K\bar{K}}, \quad (1.1)$$

$$A(K^0\bar{K}^0\pi^+) = -\frac{1}{\sqrt{2}}A_0^{K\bar{K}} - \frac{1}{2}A_1^{K\bar{K}}, \quad (1.2)$$

$$A(K^+\bar{K}^0\pi^0) = \frac{1}{\sqrt{2}}A_1^{K\bar{K}}, \quad (1.3)$$

so assuming incoherent and equal amplitudes $A_{0,1}^{K\bar{K}}$,

$$|A(K^+K^-\pi^+)|^2 : |A(K^0\bar{K}^0\pi^+)|^2 : |A(K^+\bar{K}^0\pi^0)|^2 = 3 : 3 : 2. \quad (1.4)$$

2. $(\pi K)\bar{K}$: We label the reduced amplitudes $A_I^{\pi K}$ by $I_{\pi K} = 3/2, 1/2$. Then

$$A(\pi^+K^+K^-) = \frac{\sqrt{3}}{2}A_{3/2}^{\pi K}, \quad (1.5)$$

$$A(\pi^+K^0\bar{K}^0) = -\frac{1}{2\sqrt{3}}A_{3/2}^{\pi K} + \sqrt{\frac{2}{3}}A_{1/2}^{\pi K}, \quad (1.6)$$

$$A(\pi^0K^+\bar{K}^0) = -\frac{1}{\sqrt{6}}A_{3/2}^{\pi K} - \frac{1}{\sqrt{3}}A_{1/2}^{\pi K}, \quad (1.7)$$

leading again to the ratios (1.4) if $A_{1/2,3/2}^{\pi K}$ are equal and incoherent.

3. $(\pi\bar{K})K$: We label the reduced amplitudes $A_I^{\pi\bar{K}}$ by $I_{\pi\bar{K}} = 3/2, 1/2$. Then

$$A(\pi^+ K^- K^+) = -\frac{1}{2\sqrt{3}} A_{3/2}^{\pi\bar{K}} + \sqrt{\frac{2}{3}} A_{1/2}^{\pi\bar{K}} , \quad (1.8)$$

$$A(\pi^+ \bar{K}^0 K^0) = \frac{\sqrt{3}}{2} A_{3/2}^{\pi\bar{K}} , \quad (1.9)$$

$$A(\pi^0 \bar{K}^0 K^+) = -\frac{1}{\sqrt{6}} A_{3/2}^{\pi\bar{K}} - \frac{1}{\sqrt{3}} A_{1/2}^{\pi\bar{K}} , \quad (1.10)$$

leading again to (1.4) if $A_{1/2,3/2}^{\pi\bar{K}}$ are equal and incoherent.

B. Example of $(3\pi)_{I=I_3=1}$

The only couplings to consider are $(\pi\pi)\pi$. For example, choosing a particular order,

$$A(\pi^+ \pi^+ \pi^-) = \sqrt{\frac{3}{5}} A_2 , \quad (1.11)$$

$$A(\pi^+ \pi^0 \pi^0) = -\sqrt{\frac{3}{20}} A_2 + \frac{1}{2} A_1 , \quad (1.12)$$

so if A_2 and A_1 are equal and incoherent,

$$|A(\pi^+ \pi^+ \pi^-)|^2 : |A(\pi^+ \pi^0 \pi^0)|^2 = 3 : 2 . \quad (1.13)$$

Coupling the pions in a different order one can encounter also an amplitude with $I_{\pi\pi} = 0$, but the same result is obtained.

Results for Cabibbo-favored D_s^+ decays are quoted from Ref. [14] for $(K\bar{K}n\pi)_{I=I_3=1}$ final states in Table 1.2 and for $(3\pi)_{I=I_3=1}$ in Table 1.3. Higher-multiplicity D_s^+ decays appear to account for a very small fraction of the total [11]. Results for singly-Cabibbo suppressed D_s^+ decays to $K + (n\pi)$ can be transcribed from Table I of Ref. [15], which applies to a statistical average of $I = 1/2$ and $I = 3/2$ states for $\bar{D}^0 \rightarrow K + (n\pi)$ arising from $\bar{s}\bar{u}du$. Here the $K + (n\pi)$ states arise from $\bar{s}\bar{d}ud$, which is related to $\bar{s}\bar{u}du$ by isospin reflection. The results are shown in Table 1.4.

An alternative quark-antiquark pair production model is used to obtain estimates for systematic theoretical uncertainties in predictions of the statistical model. Results for relative branching fractions obtained in the $q\bar{q}$ pair production model are

Table 1.2: Statistical model predictions for charge states in $(K\bar{K}n\pi)_{I=I_3=1}$ [5].

$n_{(\pi^++\pi^-)}$	0	1	2	3
$Q(\bar{K})$	0	—	0	—
$n_\pi = 0$	1	—	—	—
	1	1/4	3/8	3/8
	2	1/10	9/40	9/40
	3	1/30	7/60	7/60
			2/15	4/15
				1/6
				1/6

Table 1.3: Statistical model predictions for charge states in $(n\pi)_{I=I_3=1}$ [5].

$n_{(\pi^++\pi^-)}$	1	3	5
$n_\pi = 1$	1	—	—
2	1	—	—
3	2/5	3/5	—
4	1/5	4/5	—
5	3/35	22/35	10/35
6	1/28	12/28	15/28

shown in Tables 1.5, 1.6, and 1.7 quoted from Ref. [5]. The upper and lower parts of Tables 1.6 and 1.7, denoted T and C respectively, correspond to color-favored and color-suppressed amplitudes. For details about this model see Ref. [5].

1.4.3 Predicted Inclusive Yields for D_s^+ Decays

With predictions of the statistical model for unknown D_s^+ decays, we can summarize D_s^+ branching fractions to leptonic, semileptonic, and hadronic final states in Table. 1.8 quoted from Ref. [5]. With these branching fractions listed in Tables 1.8, it now becomes possible to calculate inclusive yields for D_s^+ Decays. The inclusive pion yields are summarized in Table 1.9, for kaons in Table 1.10, and for η , η' , ϕ , and ω in Table 1.11. All of these tables are quoted from Ref. [5]. These calculated inclusive yields can be compared with our measurements of inclusive yields of D_s^+ decays and examined for specific final states which can shed light on strong and weak decay mechanisms.

Table 1.4: Statistical model predictions for charge states in $K + (n\pi)$ arising from singly-Cabibbo-suppressed D_s^+ decays. A statistical average of contributions from $I = 1/2$ and $I = 3/2$ final states has been taken as in Table I of Ref. [15] [5].

$n_{(\pi^+ + \pi^-)}$	0	1	2	3
$n_\pi = 1$	1/2	1/2	–	–
2	3/20	8/20	9/20	–
3	3/45	9/45	21/45	12/45

Table 1.5: Predictions of the $q\bar{q}$ pair production model for charge states in $(n\pi)_{I=I_3=1}$ [5].

$n_{(\pi^+ + \pi^-)}$	1	3	5
$n_\pi = 1$	1	–	–
2	1	–	–
3	3/7	4/7	–
4	1/5	4/5	–
5	5/61	40/61	16/61

Table 1.6: Predictions of the $q\bar{q}$ pair production model for charge states in $(K\bar{K}n\pi)_{I=I_3=1}$, for color-favored (T) and color-suppressed (C) amplitudes [5].

$n_{(\pi^+ + \pi^-)}$		0	1	2	3
$Q(\bar{K})$		0	–	0	–
T	$n_\pi = 0$	1	–	–	–
	1	0	1/2	1/2	–
	2	0	3/10	3/10	1/5
	3	0	3/22	3/22	2/11
C	$n_\pi = 0$	1	–	–	–
	1	1/3	1/3	1/3	–
	2	1/9	2/9	2/9	4/27
	3	1/27	1/9	1/9	4/27
				8/27	–
				2/11	–
				4/27	4/27

Table 1.7: Predictions of the $q\bar{q}$ pair production model for charge states in $K + (n\pi)$, for color-favored (T) and color-suppressed (C) amplitudes [5].

		$n_{(\pi^+ + \pi^-)}$	0	1	2	3
T	$n_\pi = 1$	0	1	–	–	
	2	0	3/5	2/5	–	
	3	0	6/22	4/11	4/11	
C	$n_\pi = 1$	1	0	–	–	
	2	1/4	1/4	1/2	–	
	3	3/37	6/37	20/37	8/37	

Table 1.8: D_s^+ branching fractions to leptonic, semileptonic, and hadronic modes [11]. Values for bracketed modes are inferred from statistical model. Second errors are systematic uncertainties obtained by differences between predictions of the statistical isospin model and the model based on $q\bar{q}$ production. Modes with $\mathcal{B} < 10^{-3}$ are omitted [5].

(a). Leptonic and semileptonic modes

Mode f	$\mathcal{B}(D_s^+ \rightarrow f)$ (%)
$\tau^+\nu_\tau$	6.6 ± 0.6
$\eta\ell^+\nu_\ell$	5.8 ± 1.2
$\eta'\ell^+\nu_\ell$	2.04 ± 0.66
$\phi\ell^+\nu_\ell$	4.72 ± 0.52
Total	19.16 ± 1.58

(b). Hadronic modes

Mode f	$\mathcal{B}(D_s^+ \rightarrow f)$ (%)
$[K^+\bar{K}^0]$	2.98 ± 0.18
$K^+K^-\pi^+$	5.50 ± 0.28
$[K^0\bar{K}^0\pi^+]$	5.76 ± 0.96
$[K^+\bar{K}^0\pi^0]$	3.56 ± 0.67
$K^+K^-\pi^+\pi^0$	5.6 ± 0.5
$[K^0\bar{K}^0\pi^+\pi^0]$	4.36 ± 1.68
$[K^+\bar{K}^0\pi^+\pi^-]$	1.92 ± 0.26
$[K^0K^-\pi^+\pi^+]$	3.28 ± 0.24
$[K^+\bar{K}^0\pi^0\pi^0]$	0.80 ± 0.67
$K^+K^-\pi^+\pi^+\pi^-$	0.88 ± 0.16
$[K^0\bar{K}^0\pi^+\pi^+\pi^-]$	0.70 ± 0.21
$[K^+\bar{K}^0\pi^+\pi^-\pi^0]$	0.46 ± 0.34
$[K^0K^-\pi^+\pi^+\pi^0]$	0.23 ± 0.16
$[K^+K^-\pi^+\pi^0\pi^0]$	0.59 ± 0.16
$[K^0\bar{K}^0\pi^+\pi^0\pi^0]$	0.47 ± 0.15
$[K^+\bar{K}^0\pi^0\pi^0\pi^0]$	0.06 ± 0.06
$\pi^+\pi^+\pi^-$	1.11 ± 0.08
$[\pi^+\pi^0\pi^0]$	$0.74 \pm 0.05 \pm 0.09$
$[\pi^+\pi^+\pi^-\pi^0]$	0.67 ± 0.06
$\eta\pi^+$	1.58 ± 0.21
$\omega\pi^+$	0.25 ± 0.09
$3\pi^+2\pi^-$	0.80 ± 0.09
$[2\pi^+\pi^-2\pi^0]$	$3.00 \pm 0.41 \pm 0.24$
$[\pi^+4\pi^0]$	$0.24 \pm 0.03 \pm 0.01$
$\eta\rho^+$	13.0 ± 2.2
$[3\pi^+2\pi^-\pi^0]$	4.5 ± 3.2
$2\pi^+\pi^-3\pi^0$	0.12 ± 0.03
$\eta'\pi^+$	3.8 ± 0.4
$\eta'\rho^+$	12.2 ± 2.0
$[K^0\pi^+]$	0.25 ± 0.03
$K^+\pi^0$	0.08 ± 0.02
$K^+\eta$	0.141 ± 0.031
$K^+\eta'$	0.16 ± 0.05
$K^+\pi^+\pi^-$	0.69 ± 0.05
$[K^0\pi^+\pi^0]$	$0.61 \pm 0.04^{+0.43}_{-0.26}$
$[K^+\pi^0\pi^0]$	$0.23 \pm 0.02^{+0.12}_{-0.23}$
$[K^0\pi^+\pi^+\pi^-]$	0.60 ± 0.22
$[K^+\pi^+\pi^-\pi^0]$	$1.05 \pm 0.39 \pm 0.45$
$[K^0\pi^+\pi^0\pi^0]$	0.45 ± 0.17
$[K^+3\pi^0]$	$0.15 \pm 0.06^{+0.08}_{-0.15}$
Total	83.57 ± 5.05

Table 1.9: Inclusive yields of pions from various final states in D_s^+ decays [5].

Mode	$\mathcal{B}(\%)$	$\mathcal{B}(\pi^+)(\%)$	$\mathcal{B}(\pi^0)(\%)$	$\mathcal{B}(\pi^-)(\%)$
$\tau^+ \nu_\tau$	6.6 ± 0.6	5.11 ± 0.46	3.58 ± 0.33	0.98 ± 0.09
$\eta \ell^+ \nu_\ell$	5.8 ± 1.2	1.59 ± 0.33	6.98 ± 1.45	1.59 ± 0.33
$\eta' \ell^+ \nu_\ell$	2.04 ± 0.66	1.93 ± 0.63	2.51 ± 0.82	1.93 ± 0.63
$\phi \ell^+ \nu_\ell$	4.72 ± 0.52	0.74 ± 0.08	0.79 ± 0.09	0.74 ± 0.08
$K^+ K^- \pi^+$	5.50 ± 0.28	5.50 ± 0.28	0	0
$K^0 \bar{K}^0 \pi^+$	5.76 ± 0.96	5.76 ± 0.96	0	0
$K^+ \bar{K}^0 \pi^0$	3.56 ± 0.67	0	3.56 ± 0.67	0
$K^+ K^- \pi^+ \pi^0$	5.6 ± 0.5	5.6 ± 0.5	5.6 ± 0.5	0
$K^0 \bar{K}^0 \pi^+ \pi^0$	4.36 ± 1.68	4.36 ± 1.68	4.36 ± 1.68	0
$K^+ \bar{K}^0 \pi^+ \pi^-$	1.92 ± 0.26	1.92 ± 0.26	0	1.92 ± 0.26
$K^0 K^- \pi^+ \pi^+$	3.28 ± 0.24	6.56 ± 0.48	0	0
$K^+ \bar{K}^0 \pi^0 \pi^0$	0.80 ± 0.67	0	1.60 ± 1.34	0
$K^+ K^- \pi^+ \pi^+ \pi^-$	0.88 ± 0.16	1.76 ± 0.32	0	0.88 ± 0.16
$K^0 \bar{K}^0 \pi^+ \pi^+ \pi^-$	0.70 ± 0.21	1.40 ± 0.42	0	0.70 ± 0.21
$K^+ \bar{K}^0 \pi^+ \pi^- \pi^0$	0.46 ± 0.34	0.46 ± 0.34	0.46 ± 0.34	0.46 ± 0.34
$K^0 K^- \pi^+ \pi^+ \pi^0$	0.23 ± 0.16	0.46 ± 0.32	0.23 ± 0.16	0
$K^+ K^- \pi^+ \pi^0 \pi^0$	0.59 ± 0.16	0.59 ± 0.16	1.18 ± 0.32	0
$K^0 \bar{K}^0 \pi^+ \pi^0 \pi^0$	0.47 ± 0.15	0.47 ± 0.15	0.94 ± 0.30	0
$K^+ \bar{K}^0 \pi^0 \pi^0 \pi^0$	0.06 ± 0.06	0	0.18 ± 0.18	0
$\pi^+ \pi^+ \pi^-$	1.11 ± 0.08	2.22 ± 0.16	0	1.11 ± 0.08
$\pi^+ \pi^0 \pi^0$	0.74 ± 0.10	0.74 ± 0.10	1.48 ± 0.20	0
$\pi^+ \pi^+ \pi^- \pi^0$	0.67 ± 0.06	1.34 ± 0.12	0.67 ± 0.06	0.67 ± 0.06
$\eta \pi^+$	1.58 ± 0.21	2.01 ± 0.27	1.90 ± 0.25	0.43 ± 0.06
$\omega \pi^+$	0.25 ± 0.09	0.48 ± 0.17	0.25 ± 0.09	0.22 ± 0.08
$3\pi^+ 2\pi^-$	0.80 ± 0.09	2.40 ± 0.27	0	1.60 ± 0.18
$2\pi^+ \pi^- 2\pi^0$	3.00 ± 0.48	6.00 ± 0.96	6.00 ± 0.96	3.00 ± 0.48
$\pi^+ 4\pi^0$	0.24 ± 0.03	0.24 ± 0.03	0.96 ± 0.12	0
$\eta \rho^+$	13.0 ± 2.2	16.55 ± 2.80	28.65 ± 4.85	3.55 ± 0.60
$3\pi^+ 2\pi^- \pi^0$	4.5 ± 3.2	13.5 ± 9.6	4.5 ± 3.2	9.0 ± 6.4
$2\pi^+ \pi^- 3\pi^0$	0.12 ± 0.03	0.24 ± 0.06	0.36 ± 0.09	0.12 ± 0.03
$\eta' \pi^+$	3.8 ± 0.4	7.39 ± 0.79	4.67 ± 0.49	3.59 ± 0.38
$\eta' \rho^+$	12.2 ± 2.0	23.74 ± 3.89	27.21 ± 4.46	11.54 ± 1.89
$K^0 \pi^+$	0.25 ± 0.03	0.25 ± 0.03	0	0
$K^+ \pi^0$	0.08 ± 0.02	0	0.08 ± 0.02	0
$K^+ \eta$	0.141 ± 0.031	0.04 ± 0.01	0.17 ± 0.04	0.04 ± 0.01
$K^+ \eta'$	0.16 ± 0.05	0.15 ± 0.05	0.20 ± 0.06	0.15 ± 0.05
$K^+ \pi^+ \pi^-$	0.69 ± 0.05	0.69 ± 0.05	0	0.69 ± 0.05
$K^0 \pi^+ \pi^0$	0.61 ± 0.35	0.61 ± 0.35	0.61 ± 0.35	0
$K^+ \pi^0 \pi^0$	0.23 ± 0.18	0	0.46 ± 0.36	0
$K^0 \pi^+ \pi^+ \pi^-$	0.60 ± 0.22	1.20 ± 0.44	0	0.60 ± 0.22
$K^+ \pi^+ \pi^- \pi^0$	1.05 ± 0.60	1.05 ± 0.60	1.05 ± 0.60	1.05 ± 0.60
$K^0 \pi^+ \pi^0 \pi^0$	0.45 ± 0.17	0.45 ± 0.17	0.90 ± 0.34	0
$K^+ 3\pi^0$	0.15 ± 0.13	0	0.45 ± 0.39	0
Total		125.5 ± 11.1	112.5 ± 8.0	46.6 ± 6.8

Table 1.10: Inclusive yields of kaons from various final states in D_s^+ decays [5].

Mode	$\mathcal{B}(\%)$	$\mathcal{B}(K^+)(\%)$	$\mathcal{B}(K^0)(\%)$	$\mathcal{B}(K^-)(\%)$	$\mathcal{B}(\bar{K}^0)(\%)$
$\tau^+\nu_\tau$	6.6 ± 0.6	0.14 ± 0.01	0.10 ± 0.01	0.03	0.01
$\phi\ell^+\nu_\ell$	4.72 ± 0.52	2.32 ± 0.26	1.60 ± 0.18	2.32 ± 0.26	1.60 ± 0.18
$K^+\bar{K}^0$	2.98 ± 0.18	2.98 ± 0.18	0	0	2.98 ± 0.18
$K^+K^-\pi^+$	5.50 ± 0.28	5.50 ± 0.28	0	5.50 ± 0.28	0
$K^0\bar{K}^0\pi^+$	5.76 ± 0.96	0	5.76 ± 0.96	0	5.76 ± 0.96
$K^+\bar{K}^0\pi^0$	3.56 ± 0.67	3.56 ± 0.67	0	0	3.56 ± 0.67
$K^+K^-\pi^+\pi^0$	5.6 ± 0.5	5.6 ± 0.5	0	5.6 ± 0.5	0
$K^0\bar{K}^0\pi^+\pi^0$	4.36 ± 1.68	0	4.36 ± 1.68	0	4.36 ± 1.68
$K^+\bar{K}^0\pi^+\pi^-$	1.92 ± 0.26	1.92 ± 0.26	0	0	1.92 ± 0.26
$K^0K^-\pi^+\pi^+$	3.28 ± 0.24	0	3.28 ± 0.24	3.28 ± 0.24	0
$K^+\bar{K}^0\pi^0\pi^0$	0.80 ± 0.67	0.80 ± 0.67	0	0	0.80 ± 0.67
$K^+K^-\pi^+\pi^+\pi^-$	0.88 ± 0.16	0.88 ± 0.16	0	0.88 ± 0.16	0
$K^0\bar{K}^0\pi^+\pi^+\pi^-$	0.70 ± 0.21	0	0.70 ± 0.21	0	0.70 ± 0.21
$K^+\bar{K}^0\pi^+\pi^-\pi^0$	0.46 ± 0.34	0.46 ± 0.34	0	0	0.46 ± 0.34
$K^0K^-\pi^+\pi^+\pi^0$	0.23 ± 0.16	0	0.23 ± 0.16	0.23 ± 0.16	0
$K^+K^-\pi^+\pi^0\pi^0$	0.59 ± 0.16	0.59 ± 0.16	0	0.59 ± 0.16	0
$K^0\bar{K}^0\pi^+\pi^0\pi^0$	0.47 ± 0.15	0	0.47 ± 0.15	0	0.47 ± 0.15
$K^+\bar{K}^0\pi^0\pi^0\pi^0$	0.06 ± 0.06	0.06 ± 0.06	0	0	0.06 ± 0.06
$K^0\pi^+$	0.25 ± 0.03	0	0.25 ± 0.03	0	0
$K^+\pi^0$	0.08 ± 0.02	0.08 ± 0.02	0	0	0
$K^+\eta$	0.14 ± 0.03	0.14 ± 0.03	0	0	0
$K^+\eta'$	0.16 ± 0.05	0.16 ± 0.05	0	0	0
$K^+\pi^+\pi^-$	0.69 ± 0.05	0.69 ± 0.05	0	0	0
$K^0\pi^+\pi^0$	0.61 ± 0.35	0	0.61 ± 0.35	0	0
$K^+\pi^0\pi^0$	0.23 ± 0.18	0.23 ± 0.18	0	0	0
$K^0\pi^+\pi^+\pi^-$	0.60 ± 0.22	0	0.60 ± 0.22	0	0
$K^+\pi^+\pi^-\pi^0$	1.05 ± 0.60	1.05 ± 0.60	0	0	0
$K^0\pi^+\pi^0\pi^0$	0.45 ± 0.17	0	0.45 ± 0.17	0	0
$K^+3\pi^0$	0.15 ± 0.13	0.15 ± 0.13	0	0	0
Total		27.3 ± 1.4	18.4 ± 2.0	18.4 ± 0.7	22.7 ± 2.2

Table 1.11: Inclusive yields of η , η' , ϕ , and ω from various final states in D_s^+ decays [5].

Mode	$\mathcal{B}(\%)$	$\mathcal{B}(\eta)(\%)$	$\mathcal{B}(\eta')(\%)$	$\mathcal{B}(\phi)(\%)$	$\mathcal{B}(\omega)(\%)$
$\eta\ell^+\nu_\ell$	5.8 ± 1.2	5.8 ± 1.2	0	0	0
$\eta'\ell^+\nu_\ell$	2.04 ± 0.66	1.33 ± 0.43	2.04 ± 0.66	0	0.06 ± 0.02
$\phi\ell^+\nu^\ell$	4.72 ± 0.52	0.06 ± 0.01	0	4.72 ± 0.52	0
$\phi\pi^+$	4.38 ± 0.35	0.06 ± 0.01	0	4.38 ± 0.35	0
$\phi\rho^+$	8.13 ± 2.34	0.11 ± 0.03	0	8.13 ± 2.34	0
$\phi 2\pi^+\pi^-$	1.20 ± 0.22	0.02	0	1.20 ± 0.22	0
$\phi\pi^+2\pi^0$	0.80 ± 0.15	0.01	0	0.80 ± 0.15	0
$\eta\pi^+$	1.58 ± 0.21	1.58 ± 0.21	0	0	0
$\omega\pi^+$	0.25 ± 0.09	0	0	0	0.25 ± 0.09
$\eta\rho^+$	13.0 ± 2.2	13.0 ± 2.2	0	0	0
$\eta'\pi^+$	3.8 ± 0.4	2.48 ± 0.26	3.8 ± 0.4	0	0.11 ± 0.01
$\eta'\rho^+$	12.2 ± 2.0	7.97 ± 1.32	12.2 ± 2.0	0	0.37 ± 0.07
$K^+\eta$	0.141 ± 0.031	0.14 ± 0.03	0	0	0
$K^+\eta'$	0.16 ± 0.05	0.10 ± 0.03	0.16 ± 0.05	0	0
Total		32.7 ± 2.9	18.2 ± 2.1	19.2 ± 2.4	0.8 ± 0.1

1.5 D_s^+ Exclusive Hadronic Decays Involving ω

The substantial inclusive ω yield, $D_s^+ \rightarrow \omega X$, is indicated by measurements of inclusive decays of D_s^+ mesons that will be described in latter sections of this thesis. The only D_s^+ exclusive hadronic decay mode involving ω that has been observed is $D_s^+ \rightarrow \pi^+ \omega$ with branching fraction of $\mathcal{B}(D_s^+ \rightarrow \pi^+ \omega) = (0.25 \pm 0.09)\%$ [11]. Searching for D_s^+ exclusive hadronic decays involving ω will obtain important information for understanding specific decay mechanisms. The decay $D_s^+ \rightarrow \omega \pi^+ \pi^0$, represented by the quark annihilation process $c\bar{s} \rightarrow u\bar{d}$, could have a sizable branching ratio [5]. The decay $D_s^+ \rightarrow \omega \pi^+ \eta$ could arise either from WA or from the transition $c\bar{s} \rightarrow s\bar{s} +$ (charged weak vector current), where the charged weak vector current produces $\omega \pi^+$ [5]. In this thesis, we will report a broad search for D_s^+ exclusive hadronic decays involving ω .

1.6 Decays of Charmed Mesons to Pairs of Pseudoscalars

Measurements of the decays of charmed mesons D^0 , D^+ , and D_s^+ to pairs of light pseudoscalar mesons P allow the testing of flavor symmetry and the extraction of key amplitudes. CLEO has large data samples collected on $\psi(3770)$ resonance and near the $D_s^{*+} D_s^-$ peak production energy. In this thesis, we study the decays of all possible $D \rightarrow PP$ modes and report a bunch of branching fractions of Cabibbo-favored, singly-Cabibbo-suppressed, and doubly-Cabibbo-suppressed decays. We normalize against the Cabibbo-favored D modes, $D^0 \rightarrow K^-\pi^+$, $D^+ \rightarrow K^-\pi^+\pi^+$, and $D_s^+ \rightarrow K^+K_S^0$.

The application of flavor symmetries, notably SU(3), to charmed particle decays can shed light on such fundamental questions as the strong phases of amplitudes in these decays. Knowing the strong phases of amplitudes in charmed particle decays is useful. For example, the relative strong phase in $D^0 \rightarrow K^-\pi^+$ and $\overline{D}^0 \rightarrow K^-\pi^+$ is important in interpreting decays of B mesons to $D^0 X$ and $\overline{D}^0 X$ [16, 17]. Such strong phases are non-negligible even in B decays to pairs of pseudoscalar mesons (P), and can be even more important in $D \rightarrow PP$ decays. The extraction of strong phases from charmed particle decays using SU(3) flavor symmetry, primarily the U-spin

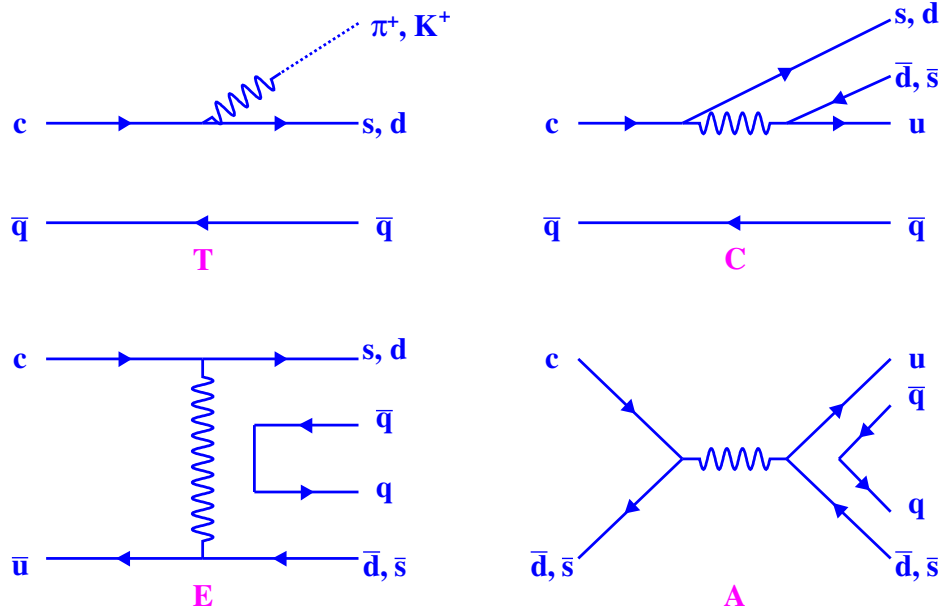


Figure 1.2: Flavor topologies for describing charm decays [18]. T : color-favored tree; C : color-suppressed tree; E : exchange; A : annihilation.

symmetry involving the interchange of s and d quarks, is illustrated in Ref. [18].

The flavor-topology language for charmed particle decays is first introduced by Chau and Cheng [19, 20] and used in Ref. [18]. These topologies, corresponding to linear combinations of $SU(3)$ -invariant amplitudes, are illustrated in Fig. 1.2. Cabibbo-favored amplitudes are proportional to the product $V_{ud}V_{cs}^*$ of Cabibbo-Kobayashi-Maskawa (CKM) factors; singly-Cabibbo-suppressed amplitudes are proportional to $V_{us}V_{cs}^*$ or $V_{ud}V_{cd}^*$; and doubly-Cabibbo-suppressed quantities are proportional to $V_{us}V_{cd}^*$. The relative hierarchy of these amplitudes is $1 : \lambda : -\lambda : -\lambda^2$, where $\lambda = \tan \theta_C$, θ_C is the Cabibbo angle.

Chapter 2

CESR and CLEO detector

Data for our analyses were taken at the Cornell Electron Storage Ring (CESR) using the CLEO-c general-purpose solenoidal detector.

The Cornell Electron Strong Ring (CESR) is a 122 m radius electron-positron storage ring run by the Laboratory of Elementary Particle Physics at Cornell University in Ithaca, NY. The ring itself is roughly 12 m beneath the Alumni athletic field, with the CLEO-c detector collecting data from e^+e^- collisions in the south end of the tunnel. The accelerator complex at Cornell consists of three main parts: a linear accelerator (linac), synchrotron, and storage ring (Fig. 2.1). The linac and synchrotron were built in the 1960's, with the capacity to accelerate electrons up to 12 GeV. The CESR storage ring was built in 1979 and was originally designed to run at center-of-mass energies up to 16 GeV.

The first CLEO detector was commissioned in 1979 to take advantage of the CESR storage ring to do B physics in the Υ region; the experiment's detector was upgraded in 1989 to CLEO II and again in 1995 to CLEO II.V. The CLEO III detector, commissioned in 1999, was designed to keep the previous electromagnetic calorimeter (along with the muon chambers and magnet) and to replace all other parts, improving and refining the components from previous incarnations to achieve even better performance.

When it became apparent that the asymmetric B -factories would outclass CESR and CLEO in B production, the detector and accelerator were modified to run at charm-threshold energies as CLEO-c and CESR-c. The CLEO-c detector required only a modest modification of the CLEO III infrastructure, replacing the central

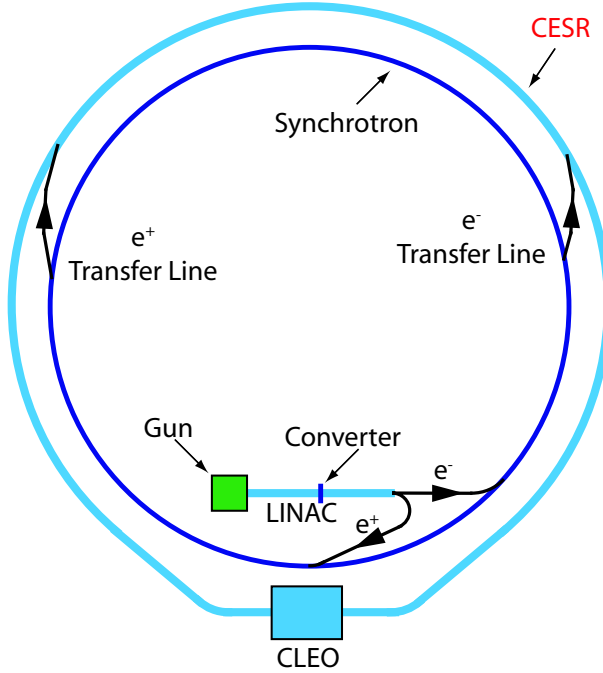


Figure 2.1: Cornell Electron Storage Ring (CESR). Figure from Ref. [21].

silicon strip detector with an additional wire tracking chamber and lowering the magnetic field strength in the tracking system. CESR required the installation of wiggler magnets to provide additional beam instability damping. Synchrotron radiation, the usual mechanism for damping, is inadequate when running so far below the design energy. The storage ring and CLEO-c detector modifications, as well as the motivation and physics reach of the project, are fully described in the document “CLEO-c and CESR-c: A New Frontier of Weak and Strong Interactions” [21] and in Ref. [22]. A briefer description follows below.

2.1 CESR

CESR is a symmetric e^+e^- collider capable of running at center-of-mass energies between approximately 3 and 11 GeV. While “CESR” can be taken to refer specifically to the storage ring, it can also refer to the entire apparatus used to create and accelerate positrons and electrons. The entire apparatus consists mainly of a linear accelerator (LINAC), synchrotron, and the storage ring. The storage ring stores

both electrons and positrons and has a circumference of 768 m.

Electrons are produced from a heated filament in an electron gun, and the electrons are collected in a “prebuncher” which compresses electrons into packets. The electron packets are accelerated in the LINAC using varying electric fields generated by radio frequency (RF) cavities. The electrons have an energy of approximately 300 MeV at the end of the 30 m LINAC. About half-way (15 m) down the LINAC, the electron beam may collide with a movable tungsten target. Collisions with the tungsten target create showers of many particles which will include positrons. The positrons are separated from other particles (mostly electrons, x-ray photons, and protons) and accelerated in the remainder of the LINAC to an energy of about 150 MeV.

Bunches of electrons and positrons from the LINAC are injected in opposite directions into the synchrotron. The synchrotron is a few meters smaller in radius than the storage ring and is located in the same tunnel. In the synchrotron, the particles are accelerated by four 3-meter long linear accelerators, and contained by a series of dipole bending magnets. The magnetic fields are increased as the energy of the particles is increased in order to continuously contain the particles. After reaching their final energy, the particles are transferred to the storage ring.

In the storage ring, electrons and positrons are guided by dipole bending magnets and are focused by a series of quadrupole and sextupole magnets. The beams lose energy by synchrotron radiation which occurs as charged particles move in a curved path, so superconducting RF cavities are used to maintain the beam energy, thus keeping the particles in their orbits. The electrons and positrons are stored in the same vacuum beam pipe, which means that care must be taken to avoid unwanted collisions. Electrostatic separators are used to bend the paths of electrons and positrons into trajectories which only intersect in the interaction region. The beams are maintained in so-called “pretzel” orbits to prevent the electron and positron beams from interacting except at the designed region (IR), as shown in Fig. 2.2. For low-energy running, “wiggler” magnets induce synchrotron radiation, but this has a minimal effect on the beam trajectory.

When an electron and a positron collide, they either annihilate, producing a virtual photon which decays into a pair of fermions, or scatter. The possible decay fermions depend on the beam energy, but are always produced in a matter-

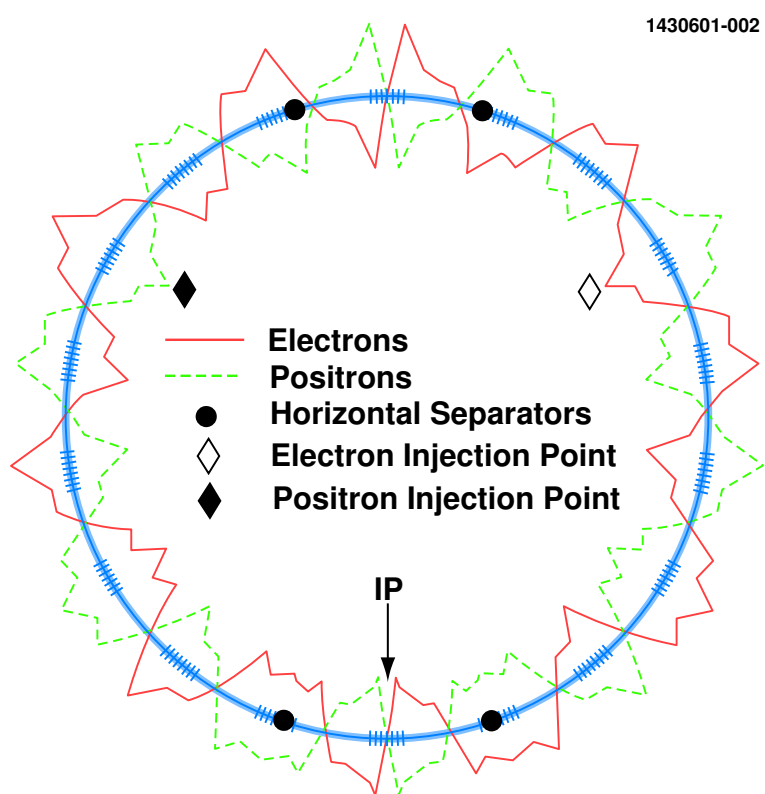


Figure 2.2: Exaggerated schematic of CESR beam orbits, showing the “pretzel” structure designed to keep beams separate [23].

antimatter pair. It is also possible that the initial electron and positron radiate two photons, which subsequently collide.

2.2 CLEO-c detector

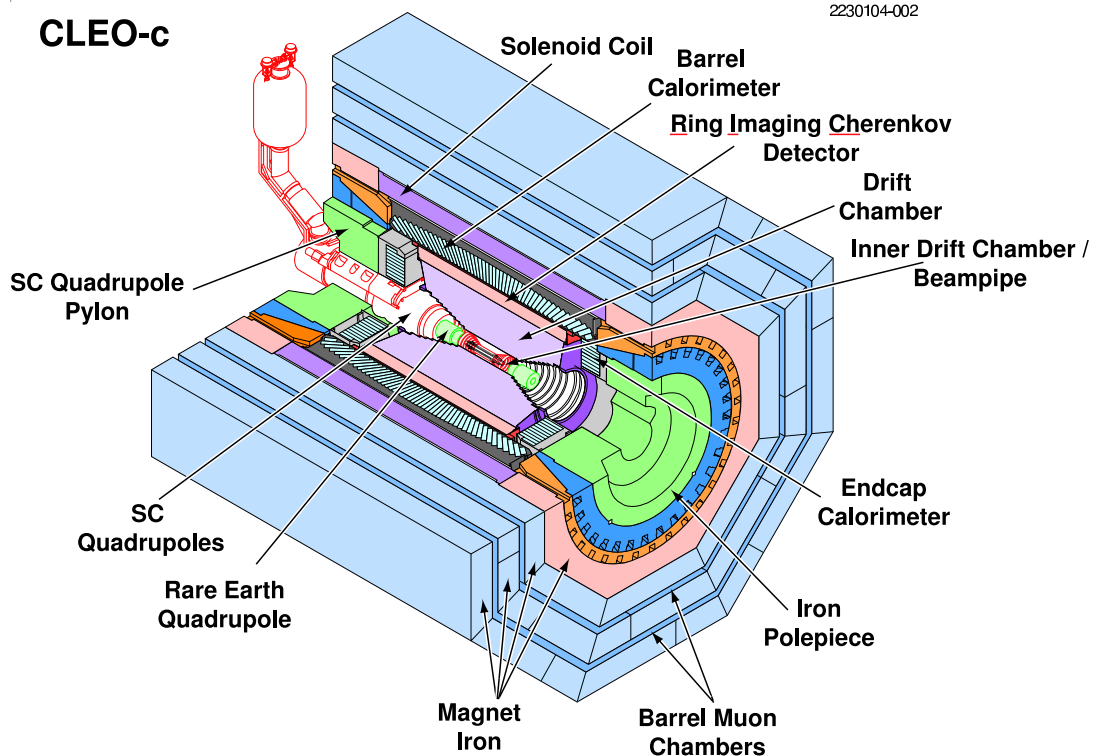


Figure 2.3: 3-D view of the CLEO-c detector [23].

The CLEO-c detector is described in detail elsewhere [24, 25, 26, 27]. The charged particle tracking system covers a solid angle of 93% of 4π and consists of a small-radius, six-layer, low-mass, stereo wire drift chamber, concentric with, and surrounded by, a 47-layer cylindrical central drift chamber. The chambers operate in a 1.0 T magnetic field and achieve a momentum resolution of $\sim 0.6\%$ at $p = 1 \text{ GeV}/c$. Photons are detected in an electromagnetic calorimeter consisting of 7800 cesium iodide crystals and covering 95% of 4π , which achieves a photon energy resolution of 2.2% at $E_\gamma = 1 \text{ GeV}$ and 6% at 100 MeV. We utilize two particle identification (PID) devices to separate charged kaons from pions: the central drift chamber, which provides measurements of ionization energy loss (dE/dx), and, surrounding

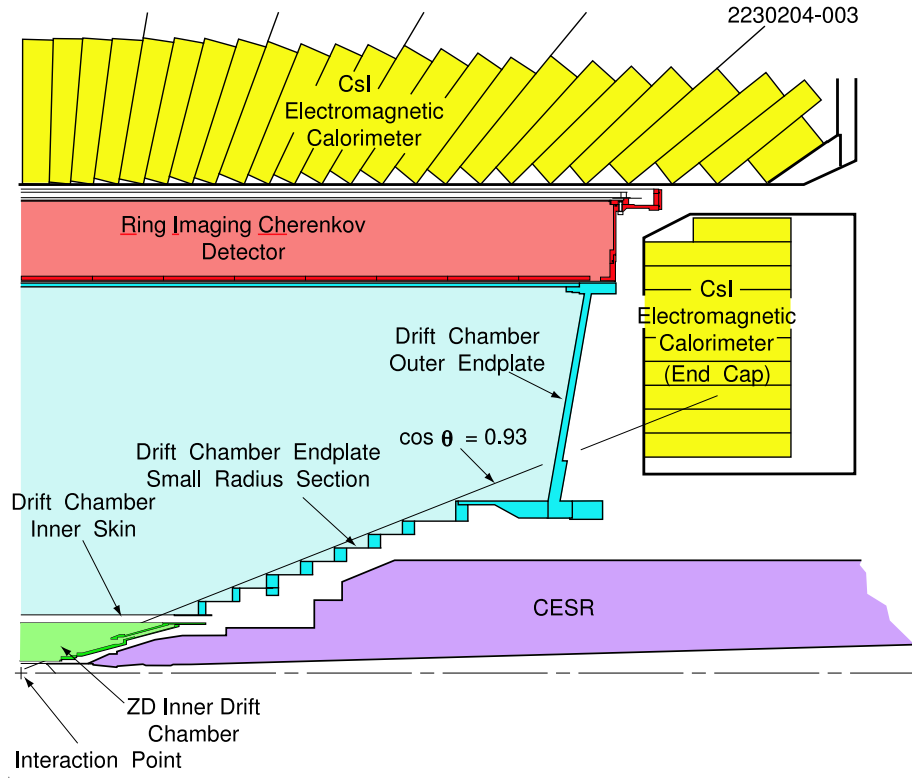


Figure 2.4: The CLEO-c detector [23].

this drift chamber, a cylindrical ring-imaging Cherenkov (RICH) detector, whose active solid angle is 80% of 4π . The combined PID system has a pion or kaon efficiency $> 85\%$ and a probability of pions faking kaons (or vice versa) $< 5\%$.

A 3-D view of the CLEO-c detector is shown in Fig. 2.3 while a 2-D view is shown in Fig. 2.4.

2.2.1 ZD

The silicon vertex detector was designed for CLEO III to allow the measurement of vertices of D daughters of B decays and also to provide precise directional information on tracks. For CLEO-c, however, the silicon vertex detector material would have significantly degraded the tracking through multiple scattering because the typical track momenta is lower than at CLEO III. Also, much of the motivation for the silicon detector is eliminated with the shift to running at lower energy. Since the CLEO-c D mesons are produced almost at rest, the flight paths would have been

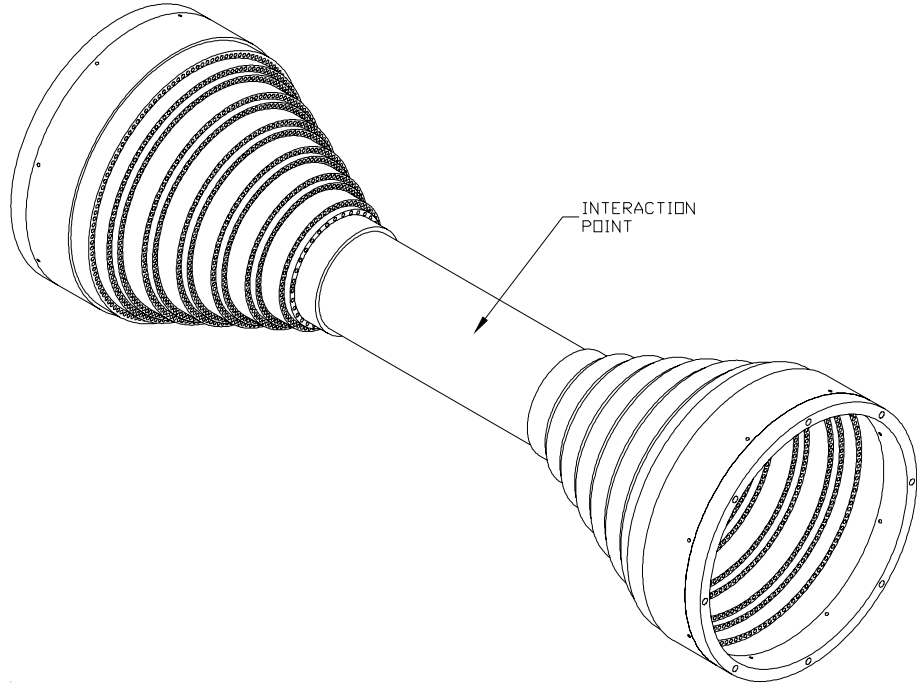


Figure 2.5: Schematic for ZD wire vertex chamber. Figure from Ref. [21].

too small to be measured by the silicon detector's vertex reconstruction capabilities. For these reasons, a replacement detector for CLEO-c was needed between the beampipe and the main drift chamber.

A new cylindrical wire vertex chamber (ZD) (Fig. 2.5) was constructed for the CLEO-c detector, filling the space between radii 4.1 cm and 11.8 cm. The ZD was built from materials similar to those in the main drift chamber, with gold-plated tungsten sense wires and gold-plated aluminum field wires. It has six layers of sense wires, all stereo, held at 1900 V relative to the field wires, that are grouped into 300 cells. The ZD is designed to provide position information on charged particles within $|\cos \theta| < 0.93$, where θ is defined with respect to the beam.

The electric charge (proportional to the energy deposited by the track) and the timing are recorded and contribute to track fitting by the main drift chamber. The z position resolution of the ZD wire vertex chamber is 680 microns, not nearly as good as the silicon vertex detector, but the momentum resolution is comparable on average and even better than in silicon at some energies.

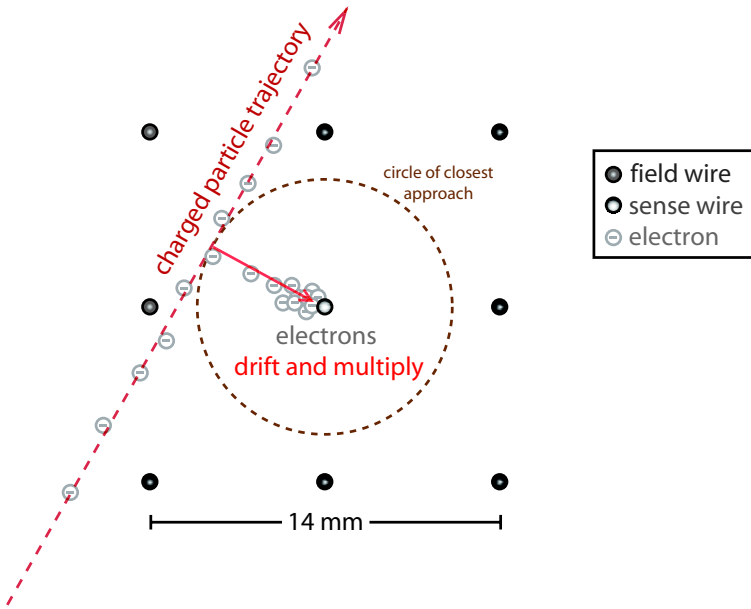


Figure 2.6: Charge collection and multiplication in the drift chamber. Figure from Ref. [21].

2.2.2 Drift chamber

Particle identification is very important for many physics goals of the CLEO-c program. The drift chamber and RICH subsystems complement each other extremely well to provide excellent hadron identification over the entire relevant momentum range. The measurement of specific ionization in the drift chamber provides good particle separation at low momenta.

The drift chamber covers the radial range from 12 cm to 82 cm, constrained on the inside by ZD and on the outside by the Ring Imaging Cherenkov counter (RICH). It consists of 47 sense wire layers. Of these, the first 16 are axial (wires parallel to the beam axis) and the remaining layers are grouped into superlayers of 4 layers each, with the superlayers alternating in stereo angle. The drift cells are nearly square with 3 field wires per sense wire and a maximum drift distance of about 7 mm. The gas is He:C₃H₈ (60:40), chosen for its long radiation length and our prior experience with CLEO II.V.

A charged particle will ionize the gas mixture when it passes through a cell, and the ionized electrons are then attracted to the sense wire. The electric field near the sense wire is very strong and causes the ionized electrons to ionize more atoms. This

creates an avalanche of electrons on the sense wire. A distance of closest approach to the sense wire can be calculated based on the transit time of the electron pulse from the wire, and the timing of collisions in the detector. The wire which carried the pulse is noted, and is used in combination with information from other wires to help determine the trajectory of the charged particle.

Like the ZD vertex chamber, the main drift chamber provides position and energy loss information when a charged particle ionizes gas in the drift chamber as it passes through. A track is reconstructed based on the wire hits from both drift chambers using pattern recognition software (the Billoir, or Kalman, algorithm). A fitted track yields momentum information based on the curvature of the trajectory in the magnetic field from the solenoid. The drift chamber has position resolution of 85 microns and momentum resolution (δ_p/p) of 0.6% at 1 GeV/ c .

The rate of energy loss (dE/dx) is compared to values for different particles to make an hypothesis as to particle identity. The nature of energy loss is the ionization or atomic excitation by moderately relativistic particles traveling through matter. At the energies of the CLEO experiment, dE/dx is a function of only the particle's speed, as determined by Bethe and Bloch. The deviation from the particle-hypothesis for a single measurement variable is defined as follows:

$$\chi_i \equiv \frac{dE/dx_i(\text{measured}) - dE/dx(\text{expected})}{\delta_i} \quad (2.1)$$

where δ_i is the uncertainty on the measurement. An overall χ^2 is formed for each particle identity hypothesis of electron, muon, pion, kaon, or proton by summing the χ_i^2 over many hits. Typically dE/dx information can be used to distinguish two types of particles (the π and the K for example) by looking at the χ^2 difference $\Delta\chi^2$:

$$\Delta\chi^2 = \chi_K^2 - \chi_\pi^2, \quad (2.2)$$

where particles with $\Delta\chi^2 < 0$ are more likely to be kaons than pions.

The value of dE/dx is plotted against particle momentum for each charged particle in Fig. 2.7. The separation of pion and kaon, which are the most common particles in our detector, is greater than 5σ below 600 MeV/ c and is still greater than 3σ at 700 MeV/ c . At higher momenta, RICH information is needed for good particle identification.

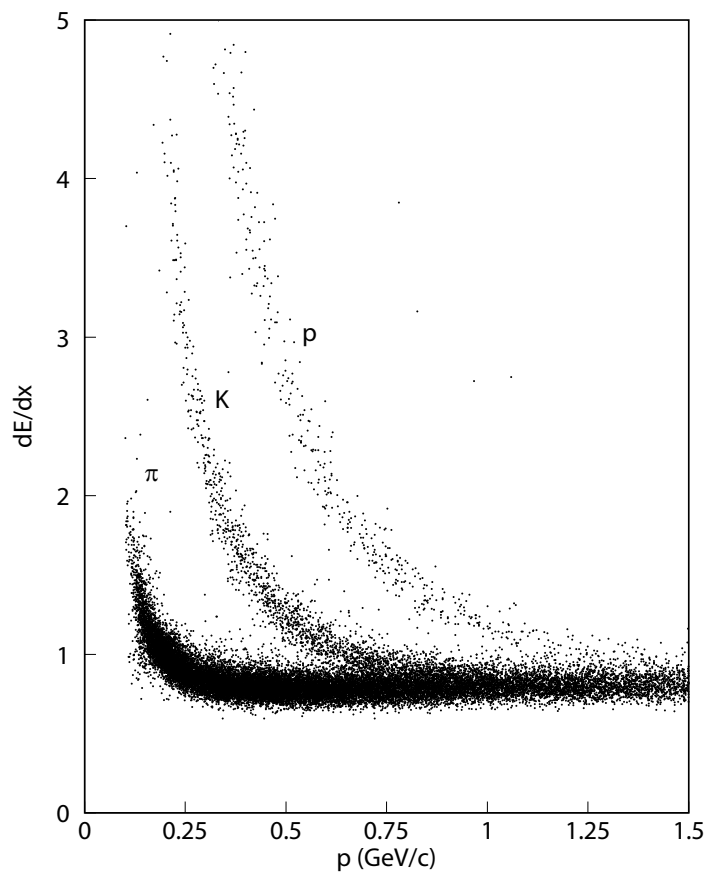


Figure 2.7: dE/dx vs. momentum scatter plots for different particles. Figure from Ref. [21].

2.2.3 RICH detector

The RICH detector separates hadrons at higher momenta as well as complementing low momentum particle-ID. The most significant improvement in the CLEO III upgrade was the insertion of a Ring Imaging Cherenkov (RICH) detector between the drift chamber and the crystal calorimeter. The solid angle coverage of the RICH is 83% of 4π , and tracks with transverse momentum above $0.12 \text{ GeV}/c$ will reach the RICH radiators when the magnetic field is lowered to 1 T.

Charged particles passing through 10 mm thick lithium fluoride crystals create a ring of Cherenkov photons that expands by traveling through a nitrogen expansion gap which is 16 cm in length. After traveling through the expansion gap, The Cherenkov photons are detected via conversion into photo-electrons by interaction with a methane-triethylamine mixture.

The RICH detector elements are shown in Fig. 2.8. Cherenkov radiation is electromagnetic radiation emitted when a charged particle (such as a electron) passes through an insulator at a speed greater than the speed of light in that medium.

While the speed of light in vacuum is a universal constant (c), the speed at which light propagates in a material may be significantly less than c . For example, the speed of the propagation of light in water is only $0.75 c$. Matter can be accelerated beyond this speed during nuclear reactions and in particle accelerators. Cherenkov radiation results when a charged particle travels through a dielectric (electrically insulating) medium with a speed greater than that at which light propagates in the same medium.

It is important to note, however, that the speed at which the photons travel is always the same. That is, the speed of light, commonly designated as c , does not change. The light appears to travel more slowly while traversing a medium due to the frequent interactions of the photons with matter. This is similar to a train that, while moving, travels at a constant velocity. If such a train were to travel on a set of tracks with many stops it would appear to be moving more slowly overall; i.e., have a lower average velocity, despite having a constant higher velocity while moving.

Charged tracks pass through LiF radiators (on average 1.7 cm thick) and produce Cherenkov photons. Out of 14 rows of LiF crystals the four central rows are equipped with “sawtooth” radiators to overcome total internal reflection of Cherenkov photons in the LiF radiator at near normal track incidence. Sawtooth radiators have

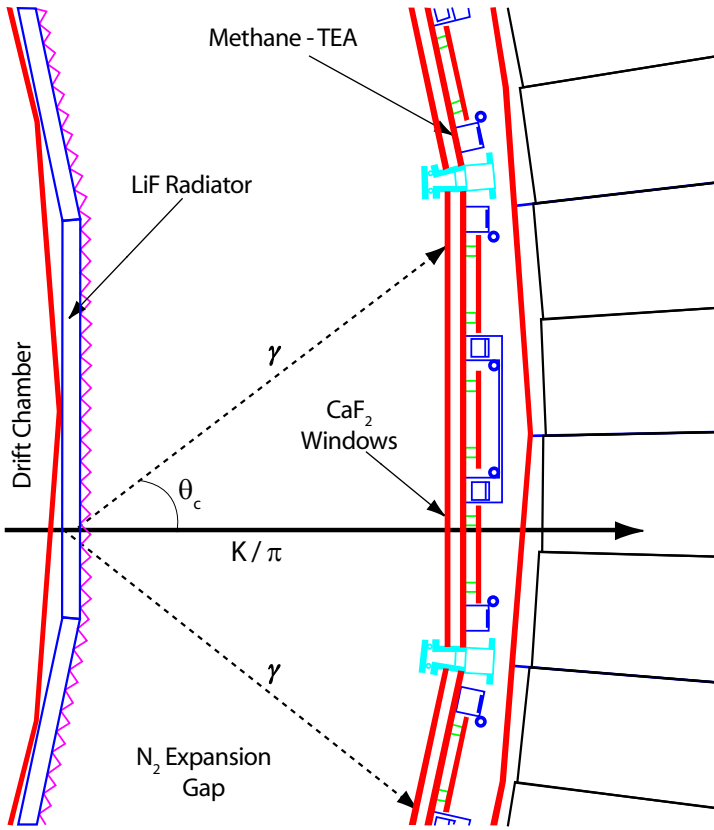


Figure 2.8: $r - \phi$ cross-section view of the CLEO RICH detector. Figure from Ref. [21].

triangular grooves on the surface. The photons travel through the expansion gap filled with nitrogen and enter the multi-wire proportional chambers through CaF_2 windows. The Cherenkov photons in a narrow VUV range (135-165 nm) are converted into photon-electrons. The charge is multiplied by the usual proportional wire chamber mechanism. The position of the photon conversion is measured via charge induced on cathode pads (there are 230,400 pads in total). Each cathode pad is input to a VA-RICH electronics chip residing on the detector where the pad signals are amplified, shaped and multiplied before being sent to the VME based digitization system. There the signals are digitized. Coherent noise is subtracted and the data are sparsified.

The resolution of the RICH depends on the polar angle of the track in question.

Averaged over Bhabha electrons the measured resolution is 12.2 (14.7) mrad for sawtooth (flat) radiators. To distinguish kaons from pions we use the likelihood ratio.

Cherenkov radiation is produced by the charged particles in the lithium fluoride Crystal at an angle θ_c to the trajectory of the track. The angle depends on the speed of the particle, v , and the index of refraction, $n = 1.5$, of the lithium fluoride as follows:

$$\cos \theta_c = \frac{c}{vn}. \quad (2.3)$$

It follows that the minimum velocity that a particle must have in order to radiate in the detector is approximately $2c/3$. The mass m of the particle can then be determined from θ_c and the measured magnitude of momentum p , since the relativistic momentum of the particle is given by:

$$p = \frac{mv}{\sqrt{1 - \frac{v^2}{c^2}}}. \quad (2.4)$$

Information from the RICH is used to determine a likelihood for a particular particle hypothesis. A likelihood L for each particle type is calculated from the number of photons which are within 5 standard deviations of the expected ring size for that particle type. An effective χ^2 for that particular particle type is $-2\ln(L)$. Thus, we can separate particles in a familiar way by using:

$$\Delta\chi^2_{RICH} = -2\ln(L_K) - (-2\ln(L_\pi)), \quad (2.5)$$

where particles with $\Delta\chi^2_{RICH} < 0$ are more likely to be kaons than pions. A typical cut on this χ^2 difference for kaons and pions of $\Delta\chi^2_{RICH} < 0$ identifies 92% of kaons with only an 8% fake rate for pions (Fig. 2.10).

The particle ID capabilities of dE/dx and the RICH fortunately compliment each other. In the case of K/π separation, RICH information is not good below a momentum of about 700 MeV/c because the kaons do not radiate in the RICH at lower momenta. The dE/dx separation is good below about 700 MeV/c, but is not very useful above 700 MeV/c. RICH and dE/dx information may be combined into

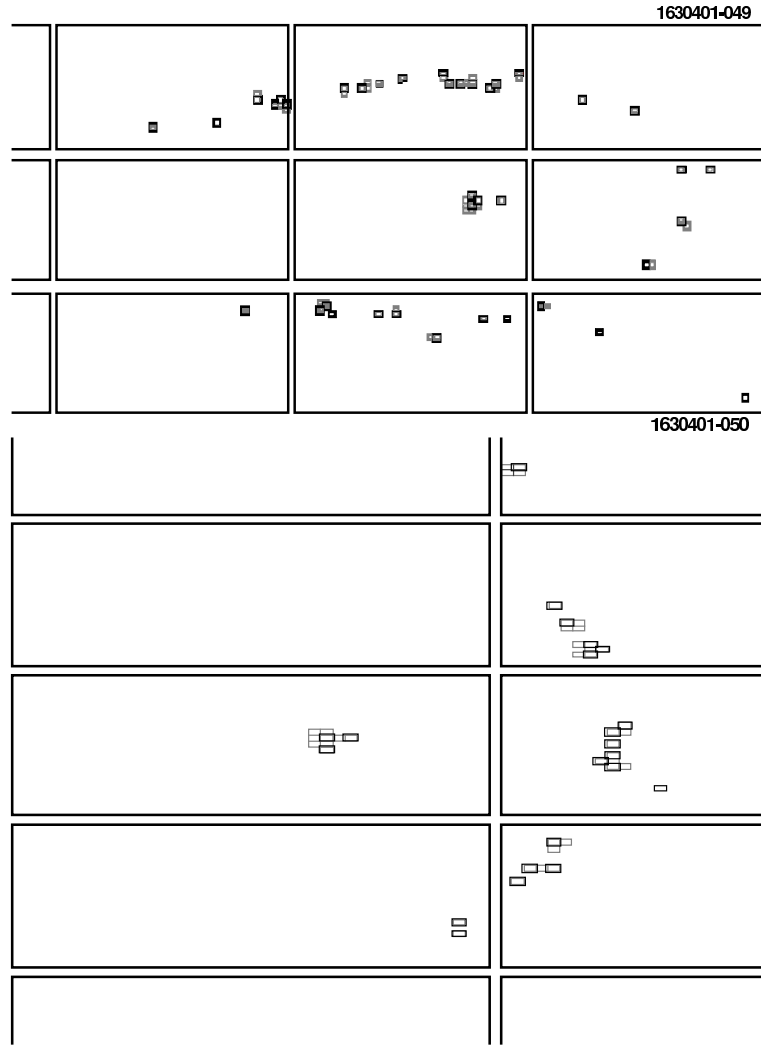


Figure 2.9: Cherenkov images produced by track crossing sawtooth (top) and flat (bottom) radiators [23]. The small squares indicate charge detected in pads of RICH wire chamber. Large rectangles outline 24×40 pad arrays. Hits in the middle of the images are due to the charged track crossing the wire chamber. The other hits are due to Cherenkov photons. The flat radiator image consists of half of the Cherenkov ring, with the other half trapped in the radiator by total internal reflection. The sawtooth radiator image consists of two Cherenkov images distorted by refraction on two sides of the tooth.

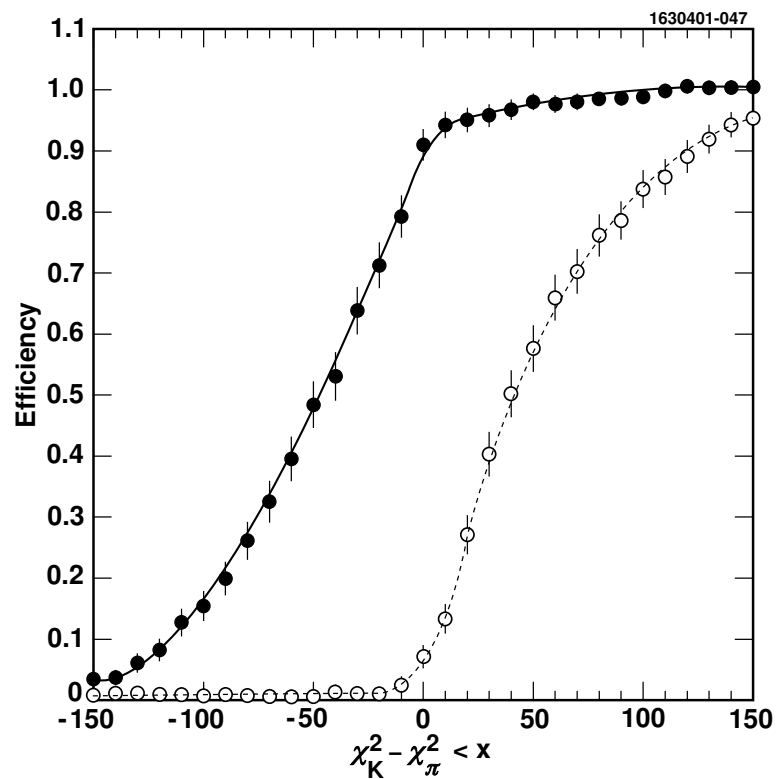


Figure 2.10: Kaon efficiency (filled circles) and pion fake rate (open circles) measured for various cuts on the χ^2 difference between kaon and pion mass hypotheses for tracks with momentum between 0.7 and 2.7 GeV/c [23].

a single overall χ^2 difference:

$$\Delta\chi^2 = -2\ln(L_K) - (-2\ln(L_\pi)) + \sigma_K^2 - \sigma_\pi^2, \quad (2.6)$$

where particles with $\Delta\chi^2 < 0$ are more likely to be kaons.

2.2.4 Crystal Calorimeter

The 7800-crystal CsI electromagnetic calorimeter is used mainly to find photons and identify electrons, and covers 93% of the 4π solid angle. A π^0 decays to two photons about 98.8% of the time, so when looking for a π^0 we aim to reconstruct it from these two photons. These photons interact with the calorimeter creating showers of charged particles and additional photons. The scintillation light from these showers is detected by silicon photo-diodes located on the back of each crystal, and the signal is used to determine the energy of the photon. Each crystal is 5×5 cm in cross section with a length of 30 cm. The crystals are oriented to point approximately towards the interaction region. The calorimeter has a mass resolution for $\pi^0 \rightarrow \gamma\gamma$ of approximately $6 \text{ MeV}/c^2$ depending on photon energies and locations. The calorimeter is optimized to capture all of the energy of electrons and photons which interact with it, as the length of each crystal is approximately 16 radiation lengths.

The CLEO-c CsI calorimeter is fully operational and an excellent match to the needs of tau-charm physics. The energy and position of each shower are used for the photon candidate momentum measurement, its position for matching to charged particle tracks, and its lateral shape for rejection of non-electromagnetic showers. The detector configuration provides minimally-obstructed, near-optimal-resolution coverage in the regions $|\cos\theta| < 0.8$ and $0.85 < |\cos\theta| < 0.93$. The narrow transition region ($0.80 < |\cos\theta| < 0.85$) has worse energy resolution because photons are obstructed by substantially more material than elsewhere.

Fig. 2.11 shows $\gamma\gamma$ mass distributions for moderate momentum ($p > 0.3 \text{ GeV}/c$) π^0 candidates in CLEO III $\Upsilon(4S)$ data, separately for barrel-barrel and barrel-endcap combinations. This momentum range is typical of the low multiplicity tau-charm decays. Note that the barrel-endcap resolution almost matches that of barrel-only photons and that barrel-endcap combinations add $\sim 8\%$ more π^0 's.

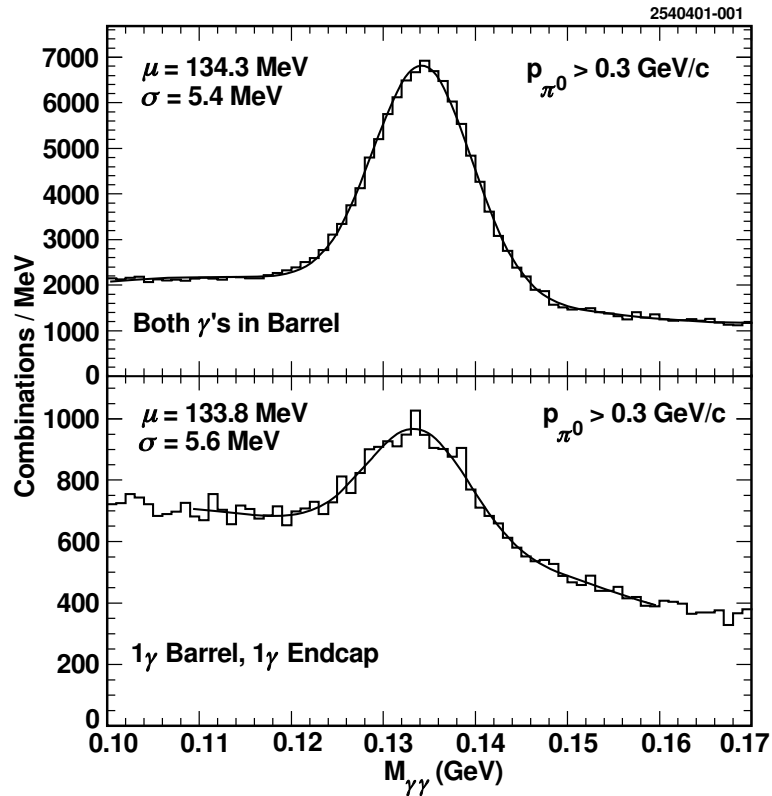


Figure 2.11: $M(\gamma\gamma)$ resolution for π^0 candidates [23].

2.2.5 Magnets

The CLEO III detector’s superconducting solenoid produced a field of 1.5 T within the detector. While this was superior for running at center-of-mass energies around 10 GeV, with average charged particle momentum of 530 MeV/ c , charm threshold energies produce tracks with a lower average momentum of 395 MeV/ c and a significant number of low momentum tracks. Lowering the magnetic field to 1.0 T in CLEO-c has two main benefits for low momentum tracks. First, low momentum tracks (60-80 MeV/ c) will penetrate deeper into the drift chamber, producing more hits and raising the detection efficiency. Second, it will reduce the number of “curlers”, or tracks that are associated with low-momentum particles that have trajectories with diameters smaller than the radius of the main drift chamber. At 1.5 T, these are particles with transverse momenta less than 180 MeV/ c . Curlers present a challenge because the pattern recognition is impaired for the entire event.

A reduced solenoidal field produces a larger radius of curvature, allowing the low momentum particles to escape the drift chamber.

2.2.6 Muon detector

The muon detector system consists of three “superlayers” which contain many plastic tubes surrounding anode wires. When a charged particle passes through the muon detector, an electrical signal is generated in a similar manner to those signals generated in the drift chamber. There are layers of iron which serve to stop most other particles which would also enter the muon chamber. Muons are able to penetrate the iron, and the depth to which the muon travels helps to identify it. About 85% of the solid angle is covered by the muon detectors.

However, the muon detectors are not much used for most CLEO-c analyses since it is designed for 1 GeV and higher energy muons, and the acceptance of the system is poor at the momentum range of muons produced at $\psi(3770)$ resonance.

2.3 Trigger and Data acquisition

Events are recorded by the Data Acquisition System (DAQ). All events can not be recorded because they happen at a rate which is much too fast to record. Also, many events are relatively uninteresting, and thus not worth recording. A relatively large amount of time is required to reconstruct the event and write the event information from the detector to disk, so only events that contain interesting physics are recorded.

In order to minimize dead time and to maximize the proportion of signal that is interesting physics, CLEO-c employs a global trigger that prescales events defined by preset trigger lines using decisions and information from the main drift chamber trigger and the electromagnetic calorimeter trigger. If an event is passed, a Level 1 pass signal is sent and the information is moved to storage by the DAQ; otherwise, the information is dropped to allow the next signal to be captured. Data from each component is processed in a separate VME crate to produce basic trigger primitives (track and shower counts, and the topologies of each) for use by the two hardware trigger systems.

2.3.1 Tracking trigger

The tracking components of the CLEO-c trigger consists of two distinct elements: axial and stereo. The tracking trigger checks the wire chamber output for signals of tracks and considers the axial and stereo portions of the drift chamber separately. The axial tracking looks at all 1696 axial wires in 16 radial layers for hit patterns indicating tracks with $p_{\perp} > 200$ MeV/c. At least one point in the track patterns must be within 5 mm of the beampipe. Tracking hits are binned in 42 ms intervals, or three times the bunch spacing in beam trains, which is sufficient for the trigger to determine the time of the interaction. The maximum drift time for a hit is 400 ns and all hits within 700 ns are used for the track, which is enough time for all hits from a track to register.

Track pattern recognition is performed by the axial tracking (AXTR) boards for the entire axial portion of the drift chamber at each time interval. An AXTR board covers 7 adjacent key wires, with signals from some wires shared between AXTR boards. Key wires are those in layer 9, where a hit is flagged as a track and wires above and below are checked for track reconstruction.

The stereo section of the main drift chamber has 8100 wires, which is more information than can be processed in the 42 ns time interval. Consequently, the wire hits are read out in 4×4 blocks, divided into eight U and V superlayers. The stereo wires are rotated with respect to the beam axis by a small angle ϕ .

A track is classified as “low momentum” if the curvature can be clearly identified as positive or negative, while “high momentum” tracks are those whose curvature is ambiguous. Timing in the tracking trigger has been thoroughly studied. Simulations for CLEO III indicated that most tracks have at least one hit that can be used to determine event timing.

2.3.2 Calorimeter trigger

The calorimetry subsystem of the CLEO trigger incorporates both analog and digital electronics to provide pipelined trigger information every 42 ns with a latency of approximately 2.5 μ s. Analog processing is employed to address the quantization error caused by split energy deposition in adjacent calorimeter cells, and digital field programmable gate arrays are used extensively to filter and categorize the

calorimeter energy topology. Timing, geographical, and energy information are all available for use in the calorimeter trigger.

The CLEO-c calorimeter comprises 1,656 doped CsI crystals in the detector “endcaps” and 6,144 crystals in the “barrel”. The light output from a crystal turns on rapidly, then decays with a 900 ns time constant. Four photodiodes are mounted on each crystal; each photodiode is viewed by a separate charge-sensitive integrating preamplifier. Preamp outputs are not cleared after an event, but decay exponentially to ground with a 180 μ s time constant. To reduce the difficulties associated with simulation of the trigger, and to increase its flexibility, the CC trigger was re-designed for CLEO-c. Complications associated with boundaries in the calorimeter are reduced by creating overlapping “tiles” by forming analog sums of signals from groups of 64 CsI crystals. A photon striking the calorimeter will deposit nearly all of its energy in at least one of the groups of crystals summed into a tile. Naturally, a signal in a single crystal will appear in four different tiles; it is the task tile processors (TPRO) to account for this. A diagram of the path for a single crystal’s signal through the CC trigger electronics is shown in Fig. 2.12.

The tile processor (TPRO) boards receive data from as many as 384 (overlapping) active tiles in the calorimeter barrel and 120 tiles in the endcaps. The first task of the tile processor is to filter event data so that overlapping, or adjacent, tiles which contain energy are reduced to a single hit. After filtering the data, the tile processor then determines the number of showers and their positions in the calorimeter. The algorithm run by the TPRO boards is a compromise between angular (and energy) resolution and the desire to limit the amount of information to be processed by the trigger. The tile processors remove all but the highest threshold tile in a group of contiguous or overlapping tiles, and project the two-dimensional tile information into one-dimensional distributions in θ (parallel to the electron/positron beams) and ϕ (around the circumference of the calorimeter barrel).

2.3.3 Global Level-1 Trigger

The Level 1 Decision and Data Flow Control system of the CLEO Trigger produce and distribute a trigger decision every 42 ns based on input from the calorimetry and tracking subsystems described above. Programmable trigger decision boards (L1TR)

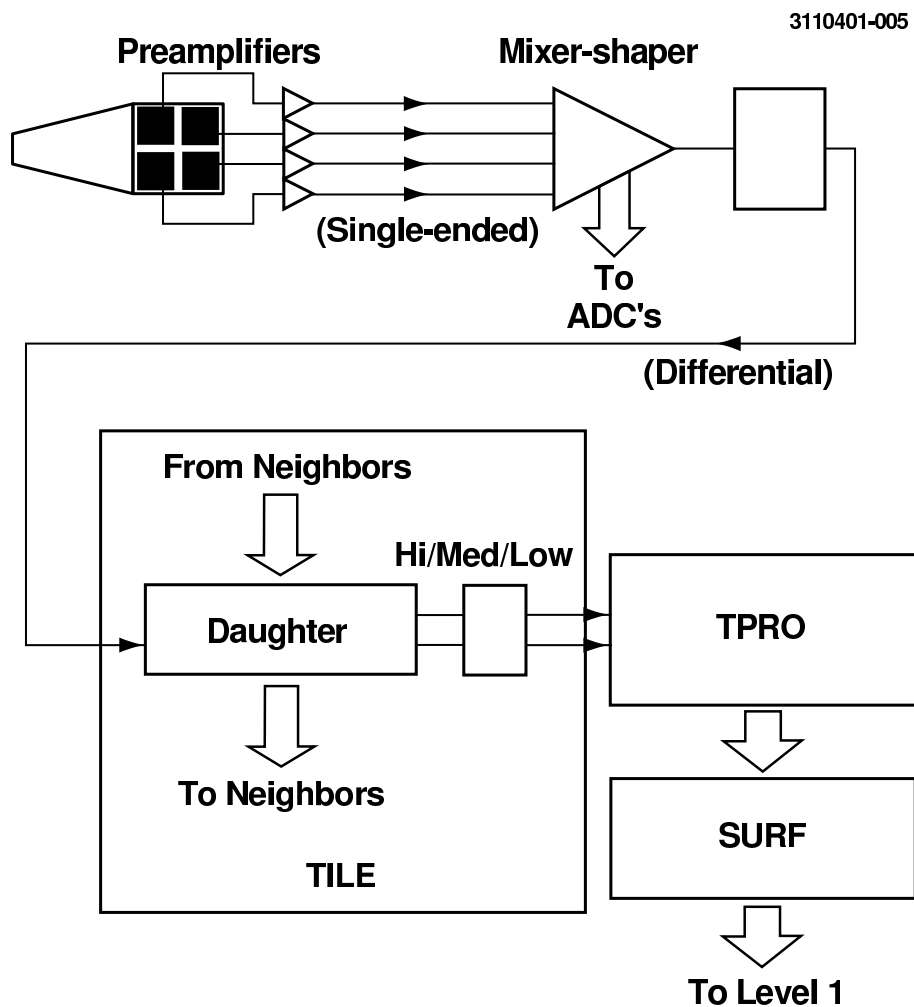


Figure 2.12: Flowchart for data within the calorimeter trigger [23].

monitor this information, and can be configured as desired to respond to a wide variety of trigger conditions. Tracking and calorimetry information is received and channeled through variable-depth pipelines to time-align the data; tracking is available in approximately $2\mu\text{s}$ while calorimetry requires over $2.5\ \mu\text{s}$. The time-aligned information is presented on a shared backplane, where several L1TR modules have access to the information for performing independent trigger condition evaluation.

All L1TR boards see the same input information on the Level-1 backplane. The Trigger Logic section allows the user to define 24 independent trigger “lines”, each is a (potentially complex) combinatoric function of the 179 inputs. Each of the 24 trigger lines is routed through a 24 bit prescaler to a 40 bit scaler.

2.3.4 The CLEO Data Acquisition System

A block diagram of the CLEO data acquisition system is shown in Fig. 2.13. For each event accepted by the trigger, approximately 400,000 detector channels have to be digitized. Front-end data conversion is performed in parallel and local buffers on each data-board hold the data for later asynchronous readout by the data acquisition system. Data sparsification is performed directly on the data-boards. The Data-Mover, a dedicated module in each front-end crate, assures transfer times below $500\ \mu\text{s}$ and provides a second buffer level. Both Fastbus and VME are supported at this level. Approximately 30 front-end crates are needed for the CLEO detector. Using inexpensive data links based on the Fast Ethernet protocol a fraction of the data is sent to a final trigger stage (Level 3) implemented in software on a fast workstation. The Level 3 decision is sent back to the front-end crates. Upon acceptance by Level 3, the event fragments are transmitted from the crates to the Event-Builder. Completely assembled events are transferred to mass storage and a fraction of the data is analyzed online by a monitor program to quickly discover problems with the CLEO detector and to ensure the quality of the data written to tape. The flow of event data through the data collection system is controlled by a simple control protocol. The basic philosophy is to re-arm the experiment to wait for the next trigger only when sufficient buffer space is available to receive a new event. In the architecture adopted for CLEO this means a free slot at the data-board level. Independent from the main data path, a slow control system monitors the individual

detector components. Run control as well as the initialization of the detector sub-systems are also be part of slow control.

2.4 Event reconstruction

After an event is read out, the next step is to process the data into a form useful for analysis. This analysis process is performed by an off-line computer code called “Pass2”, which performs the full reconstruction and fitting of the tracks, and the clustering of calorimeter showers (there is also a step called “Pass1” which is performed on the data as it is taken, but this is mostly to ensure the quality of the data).

The first step is to determine the set of calibration constants for the events, which help convert the raw information from the detector into meaningful physical quantities, and which can also help remove noise from the detector. After this step, higher level reconstruction occurs. This includes building the tracks and showers, and matching them. Quantities which are used for identifying tracks, such as dE/dx and RICH information, are also calculated.

Pass2 also reconstructs short lived particles such as the π^0 which decay into two photons that are only detected in the calorimeter. Showers from the calorimeter are combined to determine if the showers had the right energy to be a π^0 . A list of these particles is created for data analysis.

2.5 Monte Carlo simulation

In order to prevent bias due to selection criteria, examine sources of background, and determine detector efficiency, particle experimentalists need the ability to create a simulated data sample, which we call “Monte Carlo” (MC).

Creation of Monte Carlo is done in two stages. The first stage, using simulation program EvtGen, simulates the e^+e^- collision and primary decays of the particles at the particular beam energy and initial conditions of the beam. The Monte Carlo uses a decay file that gives the probability of each possible decay of a particle, and one of the decay chains is randomly selected based on these probabilities.

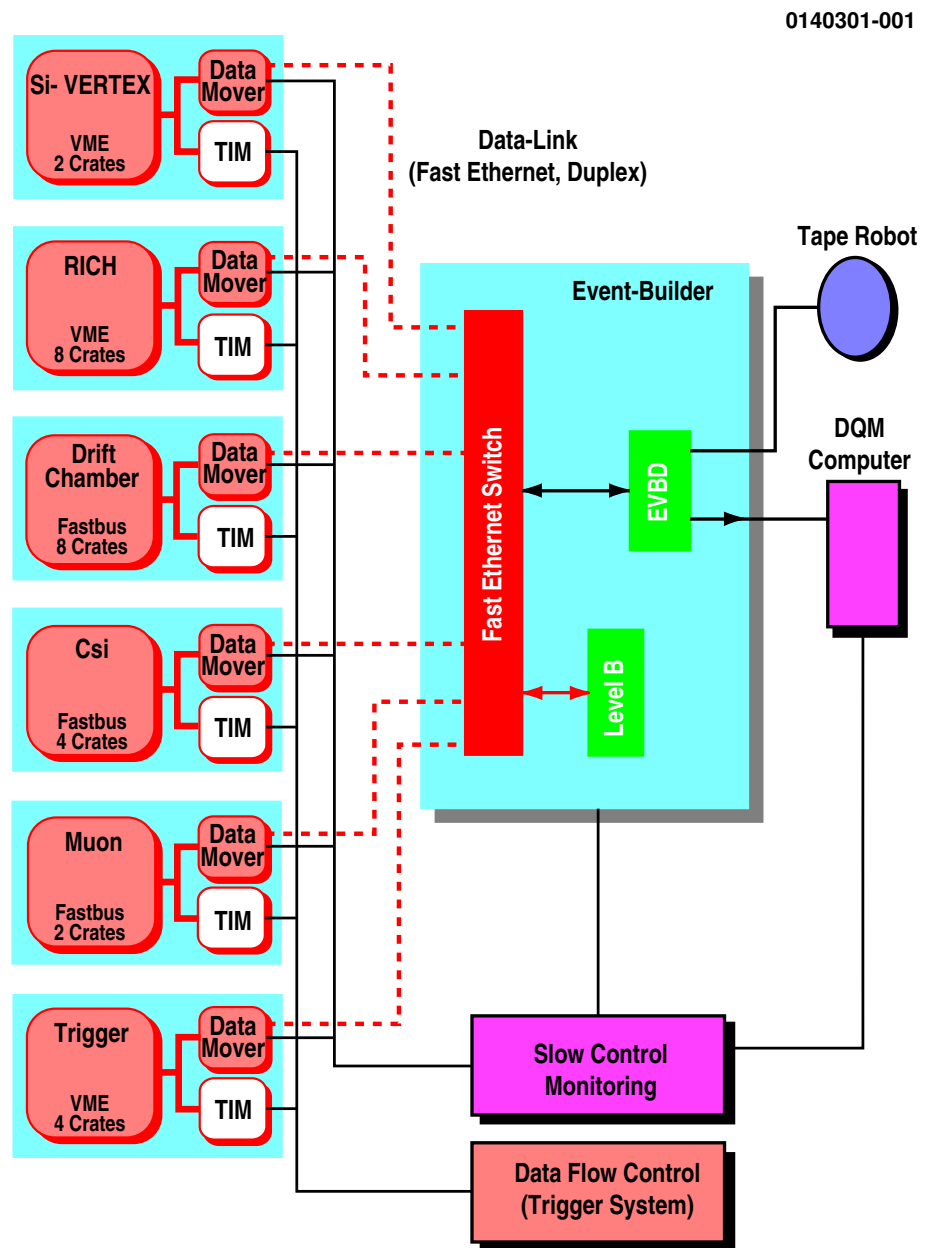


Figure 2.13: Architecture of the CLEO Data Acquisition System [23].

The output of EvtGen is the four-momentum of each daughter particle. The next simulation program, GEANT, takes the EvtGen particles and runs them through a simulation of the detector. All of the interactions of the particles in the detector are simulated, including bremsstrahlung radiation and interactions with material. GEANT also accounts for resolution effects, detector efficiencies, and noise. GEANT can be set to use the same calibration constants as any particular set of recorded events, so that different detector settings may be used to generate MC samples in order to represent the recorded data more accurately.

All of the simulated detector responses are put into a file which looks very much like the one that is stored to the DAQ for real events, except that it also contains information from EvtGen. This means that for simulated data, we can have the information about which particles decayed and what they decayed into. With real data we can only make hypotheses. The simulation can then be run through Pass2, just like real events, and the MC can be analyzed in the same way as the data.

Chapter 3

Inclusive Yields for D_s^+ Decays

The D_s^+ meson, consisting of c and \bar{s} quark, is the least extensively studied of the ground state charmed mesons. Cabibbo-favored decays of D_s^+ contain the $s\bar{s}$ component that goes to a KK pair, η , η' , or ϕ . (To the extent that ω contains some small $s\bar{s}$ component, Cabibbo-favored decays will occasionally go to ω .) Singly Cabibbo-suppressed decays contain only one \bar{s} quark or a s quark plus two \bar{s} quarks. Doubly Cabibbo-suppressed decays have two \bar{s} quarks. In annihilation decays, there is no s or \bar{s} quark in the final state. Typical Feynman diagrams are shown in Fig. 3.1. We study the inclusive decays of D_s^+ mesons, using data collected near the $D_s^{*+}D_s^-$ peak production energy $E_{\text{cm}} = 4170$ MeV by the CLEO-c detector. We report the inclusive yields of D_s^+ decays to K^+X , K^-X , K_S^0X , π^+X , π^-X , π^0X , ηX , $\eta'X$, ϕX , ωX and $f_0(980)X$, and also decays into pairs of kaons, $D_s^+ \rightarrow K\bar{K}X$. Using these measurements, we obtain an overview of D_s^+ decays.

3.1 Data sample

We use 586 pb⁻¹ of data produced in e^+e^- collisions at CESR near the center-of-mass energy $\sqrt{s} = 4170$ MeV. Here the cross-section for the channel of interest, $D_s^{*+}D_s^-$ or $D_s^+D_s^{*-}$, is ~ 1 nb [28]. We select events in which the D_s^* decays to $D_s\gamma$ (94% branching fraction [11]). Other charm production totals ~ 7 nb [28], and the underlying light-quark “continuum” is about 12 nb.

Data sets used in this analysis are summarized in Table 3.1, we processed v2 [29] D -skim over data 39, 40, 41, 47 and 48.

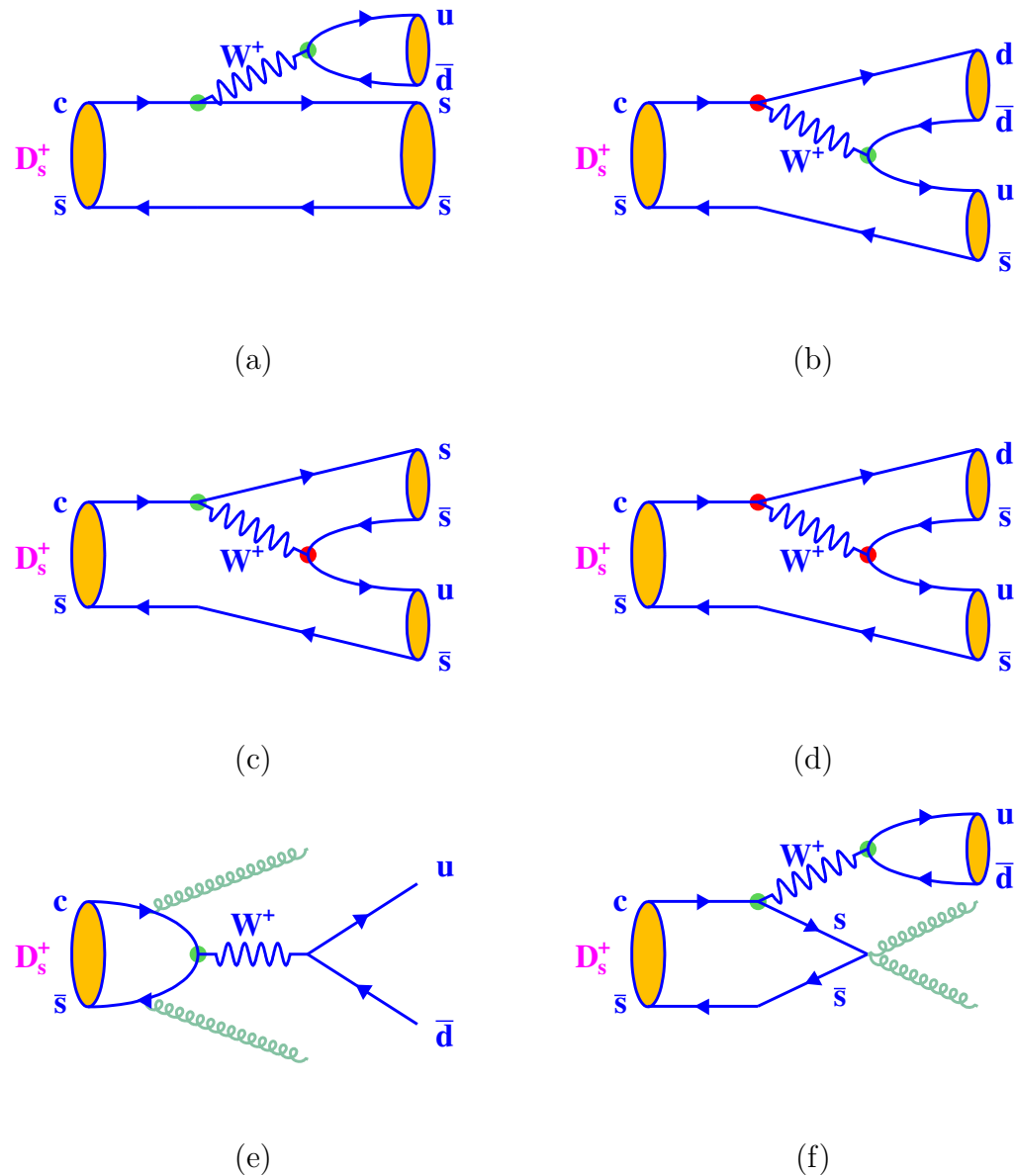


Figure 3.1: The typical Feynman diagrams of D_s^+ Cabibbo-favored decay (a), singly Cabibbo-suppressed decay (b) and (c), doubly Cabibbo-suppressed decay (d), and annihilation decays (e) and (f).

Table 3.1: Summary of data sets used in this analysis.

data set	\sqrt{s} (GeV)	$\mathcal{L}(\text{pb}^{-1})$ (RunInfo)
39	4170	55.049
40	4170	123.960
41	4170	119.126
47	4170	109.795
48	4170	178.269
Total		586.199

Generic mixture of $D\bar{D}$ Monte Carlo sample that contains events about 20 times luminosity of data is used to study efficiencies and possible background features.

3.2 D_s Tag Technique

3.2.1 Tag Selection

Here we employ a double-tagging technique. Single-tag (ST) events are selected by fully reconstructing a D_s^- , which we call a tag, in one of the following three two-body hadronic decay modes: $D_s^- \rightarrow K_S^0 K^-$, $D_s^- \rightarrow \phi \pi^-$, and $D_s^- \rightarrow K^{*0} K^-$. (Mention of a specific mode implies the use of the charge conjugate mode as well throughout this Paper.) Details on the tagging selection procedure are given in Ref. [29, 30, 31]. The tagged D_s^- candidate can be either the primary D_s^- or the secondary D_s^- from the decay $D_s^{*-} \rightarrow \gamma D_s^-$. We require the following intermediate states to satisfy these mass windows around the nominal mass [11]: $K_S^0 \rightarrow \pi^+ \pi^-$ (± 12 MeV), $\phi \rightarrow K^+ K^-$ (± 10 MeV) and $K^{*0} \rightarrow K^+ \pi^-$ (± 75 MeV). All charged particles must have momenta above 100 MeV/c to eliminate the soft pions from $D^* \bar{D}^*$ decays (through $D^* \rightarrow \pi D$).

In this analysis we use only these three D_s tag modes as shown in Table 3.2. These three “cleanest” D_s tag modes are much cleaner than other modes due to the additional sub-resonant mass requirements and have relatively good signal to noise ratios.

Table 3.2: Three cleanest tag modes. They are reproduced from the existing v2 D_s tag [29] modes by applying additional cuts on the sub-resonance states; ΔM_ϕ (± 10 MeV), ΔM_{K^*} (± 75 MeV). Mode numbers in the first column are re-defined mode number used in this analysis.

(Mode#)	Decay
400	$D_s^- \rightarrow K_S^0 K^-$, $K_S^0 \rightarrow \pi^+ \pi^-$
4011	$D_s^- \rightarrow \phi \pi^-$, $\phi \rightarrow K^+ K^-$
4012	$D_s^- \rightarrow K^- K^*(892)^0$, $K^*(892)^0 \rightarrow K^+ \pi^-$

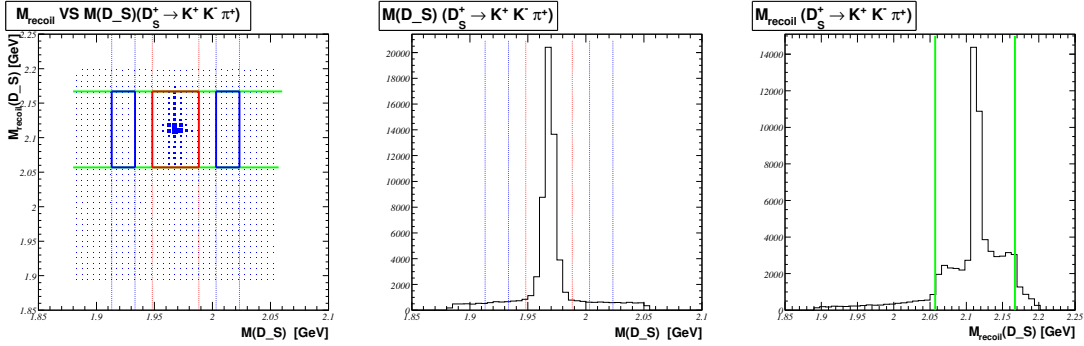


Figure 3.2: Typical M_{recoil} vs. $M(D_s)$ distribution obtained from signal Monte Carlo sample: $D_s^- \rightarrow \phi \pi^-$, $\phi \rightarrow K^+ K^-$.

3.2.2 Recoil Mass Against D_s Tag

We use the reconstructed invariant mass of the D_s candidate, $M(D_s)$, and the mass recoiling against the D_s candidate, $M_{\text{recoil}}(D_s) \equiv \sqrt{(E_0 - E_{D_s})^2 - (\vec{p}_0 - \vec{p}_{D_s})^2}$, as our primary kinematic variables to select a D_s candidate. Here (E_0, \vec{p}_0) is the net four-momentum of the e^+e^- beams, taking the finite beam crossing angle into account, \vec{p}_{D_s} is the momentum of the D_s candidate, $E_{D_s} = \sqrt{m_{D_s}^2 + \vec{p}_{D_s}^2}$, and m_{D_s} is the known D_s mass [11]. Typical mass distributions are shown in Fig. 3.2.

There are two components in the recoil mass distribution: a peak around the D_s^* mass if the tag is due to the primary D_s , and a broad flat distribution if the tag is due to the secondary D_s from D_s^* decays. The edges of $M_{\text{recoil}}(D_s)$ of the secondary D_s tag are kinematically determined (as a function of \sqrt{s} and known masses), *e.g.* at $\sqrt{s} = 4170$ MeV $\Delta M_{\text{recoil}}(D_s) \equiv M_{\text{recoil}}(D_s) - m_{D_s^*} = [-8.5, 29.8]$ MeV if the secondary D_s is from $D_s^{*-} \rightarrow D_s^- \pi^0$ decay and $\Delta M_{\text{recoil}}(D_s) = [-54.4, 57.1]$ MeV if the secondary D_s is from $D_s^{*-} \rightarrow D_s^- \gamma$ decay. We select tags within the range

$-55 \text{ MeV} < \Delta M_{\text{recoil}}(D_s) < +55 \text{ MeV}$ and look at the $M(D_s)$ distribution to get the number of D_s tags for further analysis. This loose window allows both primary and secondary D_s tags to be selected.

3.2.3 Second Recoil Mass Against D_s Tag

We also require a photon consistent with coming from $D_s^* \rightarrow \gamma D_s$ decay, by looking at the mass recoiling against the D_s candidate plus γ system, $M_{\text{recoil}}(D_s\gamma) \equiv \sqrt{(E_0 - E_{D_s} - E_\gamma)^2 - (\vec{p}_0 - \vec{p}_{D_s} - \vec{p}_\gamma)^2}$. For correct combinations, this recoil mass peaks at m_{D_s} , regardless of whether the candidate is due to a primary or a secondary D_s . We require $|M_{\text{recoil}}(D_s\gamma) - m_{D_s}| < 30 \text{ MeV}$.

3.2.4 Slow Track Veto and K_S^0 Flight Significance Cut

We noticed bump structures in the tag sideband region (especially in the high side tail) of $M(D_s)$, mainly caused by $D^{*+}D^{*-}$ events followed by $D^{*-} \rightarrow \pi^- D^0$ (dominant) decays or $D^{*-} \rightarrow \pi^0 D^-$ decays; and some additional contributions (but small) from $D^{*0}\bar{D}^{*0}$. Those events are rejected by applying a slow pion veto, rejecting the D_s candidates with pion momenta below $100 \text{ MeV}/c$ (we also apply the same momentum cut for charged kaon tracks used in reconstructing D_s candidates as there are not many real kaons below $100 \text{ MeV}/c$). The kinematically allowed region of slow pions from D^{*-} decays are beam-energy dependent and they are below $80.7 \text{ MeV}/c$ for charged pions at $\sqrt{s} = 4170 \text{ MeV}$. Unfortunately backgrounds from D^* cannot all be removed by slow track veto alone for $D_s^- \rightarrow K_S^0 K^-$ mode. Further, we require that the K_S^0 has traveled a measurable distance from the interaction point before decaying, *i.e.*, that the distance along the flight path, from interaction point to K_S^0 decay vertex, be greater than zero with a 3σ significance to remove the bump structure in high sideband region caused by false K_S^0 candidates (*i.e.* random combinations of charged pions). After the low-momentum track veto and K_S^0 flight significance requirement are applied, no bump structures remain as shown in Fig. 3.3.

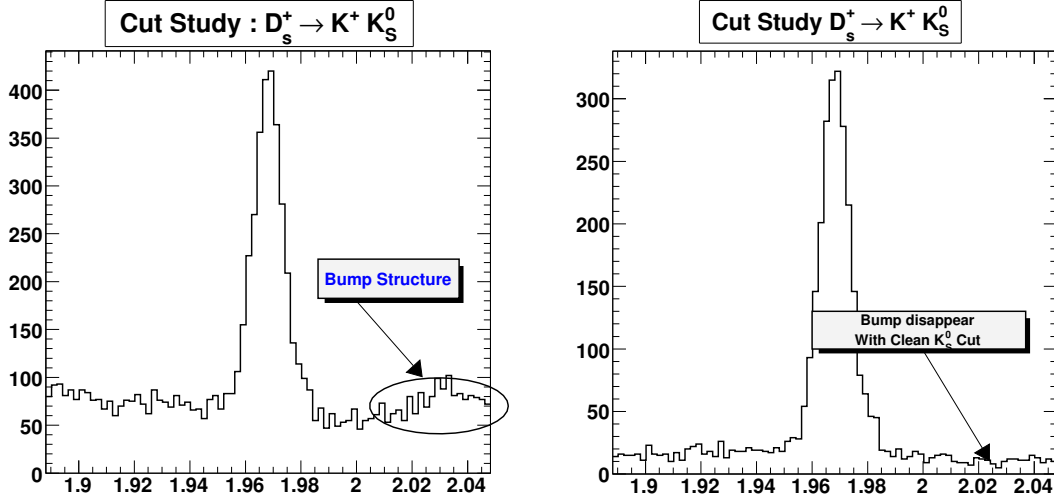


Figure 3.3: The left plot shows the clear bump structure in the high side tail of $M(D_s)$ distribution. After we apply the slow track veto and K_s^0 flight significance requirement, the bump disappears.

3.2.5 D_s Tag Yields

We use the ST invariant mass sidebands to estimate the background in our signal yields from combinatorial background under the ST mass peaks. The signal and sideband regions of invariant mass of D_s tag, $M(D_s)$, are defined as follows

- signal (resonance) region : $-20 < [M(D_s) - m_{D_s}] < +20$ MeV,
- sideband region : $-55 < [M(D_s) - m_{D_s}] < -35$ MeV and $+35 < [M(D_s) - m_{D_s}] < +55$ MeV,

where m_{D_s} is the world average mass of D_s [11]. We define the signal and sideband regions with the same size. The sideband scaling factor is used to handle a non-linear background shape.

The invariant mass distributions of D_s tag candidates for each tag mode in data are shown in Fig. 3.4. We fit $\Delta M(D_s)$ ($\equiv M(D_s) - m_{D_s}$) to a signal (double Gaussian) plus background (second degree polynomial) functions to get the sideband scaling factor:

$$f(x) = A_1 \left(G_1(x; \mu_1, \sigma_1) + \frac{A_2}{A_1} \cdot G_2(x; \mu_2, \sigma_2) \right) + (p_0 + p_1 \cdot x + p_2 \cdot x^2), \quad (3.1)$$

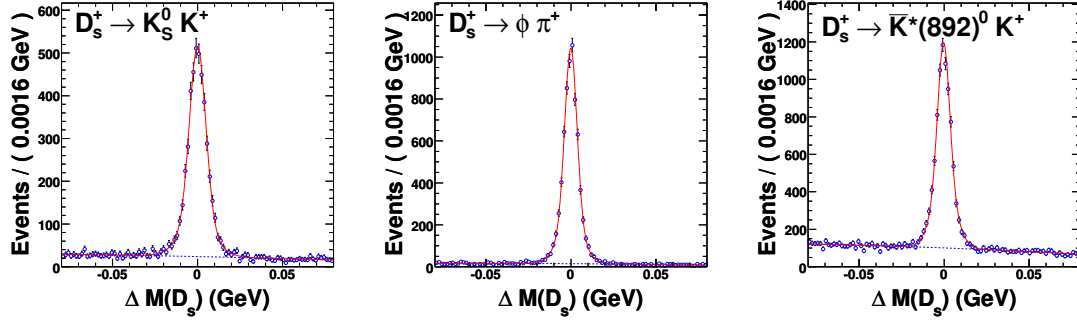


Figure 3.4: The mass difference $\Delta M(D_s) \equiv M(D_s) - m_{D_s}$ distributions in each tag mode after first recoil mass and second recoil mass cuts are applied. We fit the $\Delta M(D_s)$ distribution (open circle) to the sum (solid curve) of signal (double Gaussian) plus background (second degree polynomial, dashed curve) functions. Signal shape parameters ($A_1/A_2, \mu_1, \sigma_1, \mu_2$ and σ_2) are obtained from fits in mcDD-mix and fixed during the fit. Primary purpose of the fit is to obtain the sideband scaling factor.

Table 3.3: D_s tag yields. Here N_R is the yield in $M(D_s)$ signal (resonance) region, N_B is the yield in $M(D_s)$ sideband region, and s is the sideband scaling factor obtained from the fit to $\Delta M(D_s)$. N_{Tag} is the sideband-subtracted tag yield.

Tag Mode	N_R	N_B	s	N_{Tag}
$D_s^+ \rightarrow K^+ K_S^0, K_S^0 \rightarrow \pi^+ \pi^-$	4768	555	1.015 ± 0.024	4204.5 ± 74.3
$D_s^+ \rightarrow \phi \pi^+, \phi \rightarrow K^+ K^-$	7113	306	1.067 ± 0.029	6786.5 ± 86.8
$D_s^+ \rightarrow K^+ \bar{K}^{*0}, \bar{K}^{*0} \rightarrow K^- \pi^+$	10083	2441	1.019 ± 0.011	7594.8 ± 115.6
Total	18585.8 ± 162.6			

where $G(x; \mu, \sigma) = \frac{1}{\sqrt{2\pi}\sigma} e^{-\frac{(x-\mu)^2}{2\sigma^2}}$.

That is, we use the background fit result to get the sideband subtraction scaling factor. The number of D_s tag is computed as sideband-subtracted yield (cut and count followed by scaled sideband subtraction), not the fitted yield. When we fit real data distributions, the signal shape parameters are fixed to the values obtained from generic mcDD-mix samples. The tag yields of each D_s tag mode are listed in Table 3.3. We have 18586 ± 163 ST events that we use for further analysis.

3.3 Signal Selection

In each event where a tag is identified, we search for our signal modes recoiling against the tag.

3.3.1 Track Selection

On the signal side, charged tracks are required to satisfy criteria based on the track fit quality, have momenta above $50 \text{ MeV}/c$, and angles with respect to the beam line, θ , satisfying $|\cos \theta| < 0.80$. They must also be consistent with coming from the interaction point in three dimensions. The detailed track quality requirements are listed as follows:

- track fit o.k. and not fit abort
- $\chi^2 \leq 100000$
- hit fraction ≥ 0.5
- distance of closest approach to the interaction vertex in the bending plane $|d_0| \leq 5 \text{ mm}$
- distance of closest approach to the interaction vertex in the non-bending plane $|z_0| \leq 5 \text{ cm}$
- $|\cos \theta| < 0.80$
- track momentum: $0.05 \leq p_{\text{track}} < 2.0 \text{ GeV}/c$

3.3.2 Particle Identification

Pion and kaon candidates are required to have dE/dx measurements within three standard deviations (3σ) of the expected value. For tracks with momenta greater than $700 \text{ MeV}/c$, RICH information, if available, is combined with dE/dx . The details about PID are described in Ref. [32]. We define the following two observables:

$$PID_{\text{RICH}} = L_K - L\pi \quad (3.2)$$

The L_i are negative ln likelihoods given by the measured Cherenkov angles of photons in the RICH detector compared with the predicted Cherenkov angles for that particular particle type.

$$PID_{dE/dx} = \sigma_K^2 - \sigma_\pi^2 \quad (3.3)$$

The σ_i^2 are the difference between the measured dE/dx and the predicted dE/dx values divided by the error in the dE/dx determination for each particle type. Then, we can define the combined likelihood of dE/dx and RICH:

$$PID_{Comb} = PID_{RICH} + PID_{dE/dx} \quad (3.4)$$

For the signal side charged track, we consider the following cases:

- If dE/dx and RICH are both unavailable, don't use this track.
- dE/dx is available and RICH is not:

Make sure that the dE/dx is consistent with the particle hypothesis within three σ , and also require $PID_{dE/dx} > 0$ for pions and $PID_{dE/dx} < 0$ for kaons.

- dE/dx is unavailable and RICH is available:

Insist on at least three Cherenkov photons, and require $PID_{RICH} > 0$ for pions and $PID_{RICH} < 0$ for kaons.

- dE/dx and RICH are both available:

Use 3σ dE/dx consistency cut and insist on at least three Cherenkov photons, and require $PID_{Comb} > 0$ for pions and $PID_{Comb} < 0$ for kaons.

Candidate positrons (and electrons), selected with similar criteria, use in addition the ratio of calorimeter energy E to track momentum p . They are required to have momentum of at least 200 MeV/ c . We require $\mathcal{F}_{w/RICH}$ (one of the electron identification (EID) likelihood variable) to be greater or equal to 0.80. The details about EID are described in Ref. [33, 34, 35].

3.3.3 K_S^0 and π^0 Selection

The K_S^0 candidates are reconstructed in $K_S^0 \rightarrow \pi^+\pi^-$ decay. The two pions have no PID requirements, and a vertex fit is done to allow for the K_S^0 flight distance.

We identify π^0 candidates via $\pi^0 \rightarrow \gamma\gamma$, detecting the photons in the CsI calorimeter. Photons only in the good barrel region, $|\cos\theta| < 0.75$, are allowed, where θ is the angle of the photon with respect to the beam direction. We require that the calorimeter clusters have a measured energy above 30 MeV, have a lateral distribution consistent with that from photons, and not be matched to any charged track. The photon quality requirements are listed here:

- Photon energy is larger than 30 MeV
- No track matched
- E9o25 ok
- Not hot
- $|\cos\theta_\gamma| < 0.75$

The K_S^0 (or π^0) yield is extracted by defining a signal region and sideband regions in the invariant mass distribution of the pion (or photon) pair. The sideband scaling factor is obtained from Monte Carlo, thus allowing for a non-linear background shape. We treat π^0 from K_S^0 decay as a background for the decay $D_s^+ \rightarrow \pi^0 X$ and subtract it based on K_S^0 yields.

3.3.4 η , η' , ϕ , ω , and $f_0(980)$ Selection

For the η we use the $\gamma\gamma$ final state, which has a large branching fraction in η decays. To better handle the mild dependence of efficiency on η momentum, we separate the η sample into two momentum ranges to measure the inclusive yields, one below 300 MeV/ c and the other above. The η signal and background yields are determined by fits to a Crystal Ball function, to account for the peak and the low mass tail, and background polynomial. We reconstruct η' candidates in the the decay mode $\eta' \rightarrow \pi^+\pi^-\eta$ with the η subsequently decaying into $\gamma\gamma$. Candidates for η' are selected by combining η candidates within 3 r.m.s. widths of the nominal η mass, with a pair of $\pi^+\pi^-$. The mass difference between $\eta\pi^+\pi^-$ and η is then examined and fit to a Gaussian signal function and a background polynomial to extract the η' yields. The ϕ candidates are reconstructed in $\phi \rightarrow K^+K^-$ decay. We break the

ϕ sample into several momentum regions (200 MeV/ c bins) since the ϕ efficiency changes substantially with momentum. In each momentum region, the signals are fit with a sum of two Gaussian shapes and the background is fit to a polynomial. We reconstruct ω candidates in $\omega \rightarrow \pi^+ \pi^- \pi^0$ decay and extract the ω signal yields from the $\pi^+ \pi^- \pi^0$ invariant mass distribution. We form $f_0(980)$ candidates using $\pi^+ \pi^-$ pairs, $f_0(980) \rightarrow \pi^+ \pi^-$. The pions are subject to the standard pion PID requirements.

3.4 $D_s^+ \rightarrow K^+/K^-/\pi^+/\pi^- X$ Branching Fractions

3.4.1 Analysis Technique

The single tagging efficiency in generic D_s meson decays (ϵ_{tag}), *i.e.*, the efficiency for finding the tag, when the “other side” decays generically, is to a good approximation equal to the single tagging efficiency in inclusive decays (ϵ'_{tag}), *i.e.*, the efficiency for finding the tag, when the “other side” decays containing K^+ , or π^+ , or whatever particle’s inclusive yield is being measured. Thus, $\epsilon'_{\text{tag}}/\epsilon_{\text{tag}} \approx 1.0$. We make that assumption here, and study its validity in the section on systematics.

$$\begin{aligned} Y_\alpha &= \mathcal{B}_{\alpha X} \cdot (2 \times N_{D_s^{*+} D_s^-}) \cdot \epsilon_\alpha \epsilon'_{\text{tag}} \\ n_{D_s} &= (2 \times N_{D_s^{*+} D_s^-}) \cdot \epsilon_{\text{tag}} \\ \mathcal{B}_{\alpha X} &= \frac{Y_\alpha}{N_{D_s^{*+} D_s^-} \epsilon_\alpha \epsilon'_{\text{tag}}} \times \frac{N_{D_s^{*+} D_s^-} \epsilon'_{\text{tag}}}{n_{D_s}} = \frac{Y_\alpha / \epsilon_\alpha}{n_{D_s}}. \end{aligned}$$

The inclusive spectrum (or differential decay rate) can be expressed as

$$\frac{1}{\Gamma(D_s \rightarrow \text{all})} \cdot \frac{d\Gamma(D_s \rightarrow \alpha)}{dp} \equiv \frac{1}{\Gamma} \cdot \frac{d\Gamma_{D_s \rightarrow \alpha X}}{dp} \equiv \frac{d\mathcal{B}_{D_s \rightarrow \alpha X}}{dp} \quad (3.5)$$

$$= \frac{1}{n_{D_s}} \cdot \frac{\Delta n_\alpha}{\Delta p} \quad (3.6)$$

$$= \frac{1}{n_{D_s}} \cdot \frac{\Delta Y_\alpha / \epsilon_\alpha}{\Delta p}, \quad (3.7)$$

where n_{D_s} is the number of tag D_s , n_α is the number of signal particle after effi-

ciency correction and background subtraction (can be any of π^+ , π^- , K^+ , or K^-), Y_α is particle candidate yield, ϵ_α is detection efficiency, and p is the momentum (either in laboratory momentum p or D_s -rest frame momentum p^*). D_s inclusive branching fractions can be obtained by integrating the differential spectrum. $M(D_s)$ distribution is used to perform sideband subtraction method to obtain background-subtracted number of signal particle candidate yield ΔY_α for each momentum bin ($\Delta p(\Delta p^*) = 50$ MeV/c).

From the set of good tracks in momentum ($0.05 \leq p_{\text{track}} < 2.0$ GeV/c) and geometrical ($|\cos \theta_{\text{track}}| < 0.80$) acceptance we measure PID yields ($y_{i,j,s}(b)$) for each lab momentum bin i (p_{track}), D_s -rest frame momentum bin j (p_{track}^*), $M(D_s)$ signal and sideband bin s , and PID index b ($= e^+, e^-, K^+, K^-, \pi^+$, or π^-). The observed momentum spectra for $e^+, e^-, K^+, K^-, \pi^+$, and π^- are shown in Fig. 3.5.

For $D_s^+ \rightarrow K^+X$, $D_s^+ \rightarrow K^-X$, $D_s^+ \rightarrow \pi^+X$ and $D_s^+ \rightarrow \pi^-X$ modes, we count the numbers of charged kaons and pions recoiling against the tag where the tags are selected from both $M(D_s)$ signal and sideband regions. Thus the combinatoric background is subtracted by using $M(D_s)$ sideband events. The particle misidentification backgrounds among e , π and K are estimated by using the momentum-dependent particle misidentification rates determined from Monte Carlo and the e , π and K yields. Our identification can not distinguish between muons and pions. So, we assume the muon yield equals the electron yield, and subtract accordingly. For $D_s^+ \rightarrow \pi^+X$ and $D_s^+ \rightarrow \pi^-X$ modes, we treat π^\pm from K_S^0 decay as a background and subtract it based on K_S^0 yields. The momentum-dependent (50 MeV bins) efficiencies for track finding, track selection criteria, and particle identification are obtained from Monte Carlo simulation.

3.4.2 Background and Fake Rate Study

Using Monte Carlo, we study any possible background from many sources and cross fake rates among all kinds of particles (e , μ , K , and π). For Monte Carlo sample, we know the full information of a track (the information from both generator level and observed level). The detailed plots for Monte Carlo truth study are shown in Fig. 3.6 (for e^+), Fig. 3.7 (for e^-), Fig. 3.8 (for K^+), Fig. 3.9 (for K^-), Fig. 3.10 (for π^+), and Fig. 3.11 (for π^-). The Monte Carlo truth informations are shown on these plots.

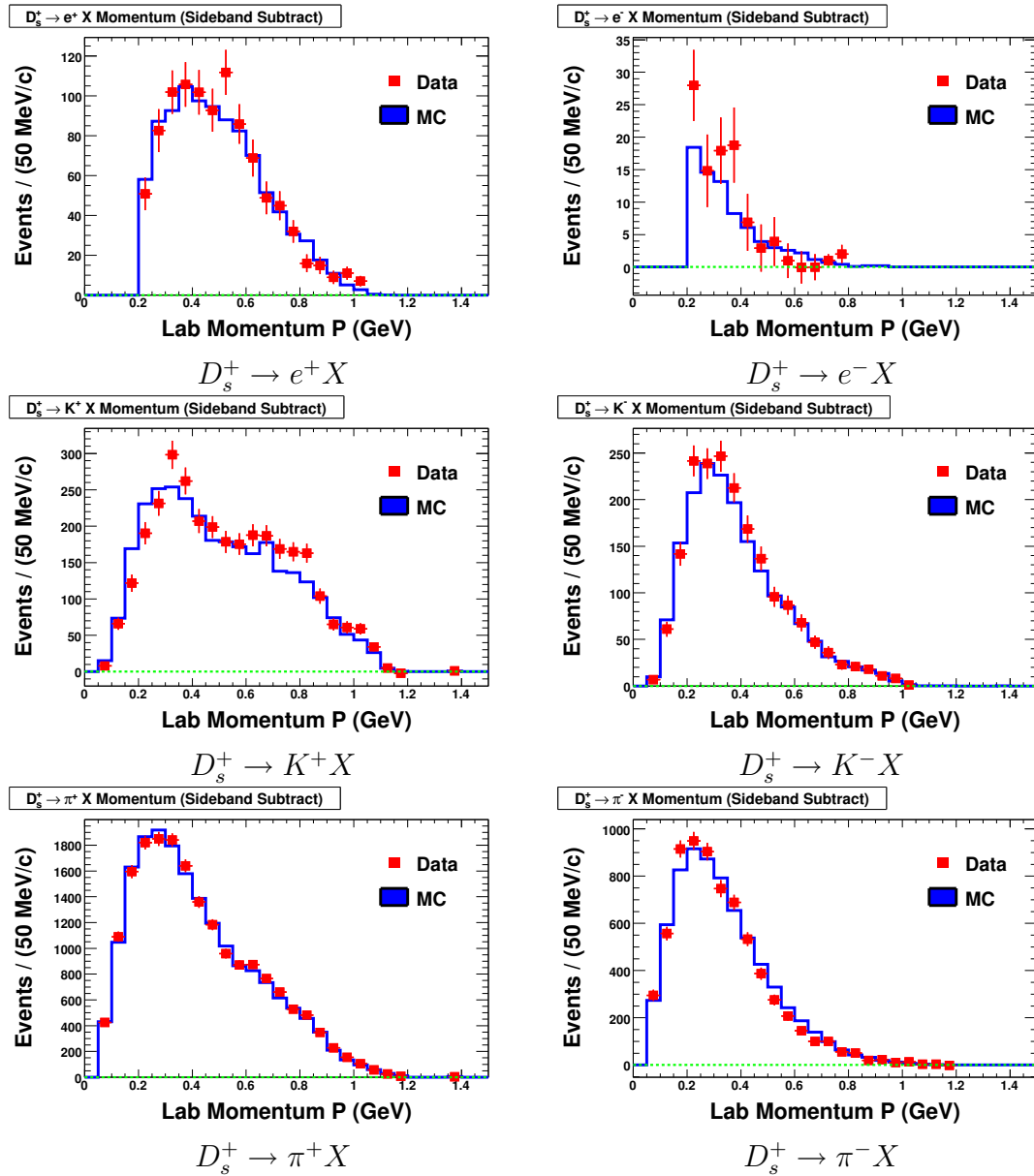
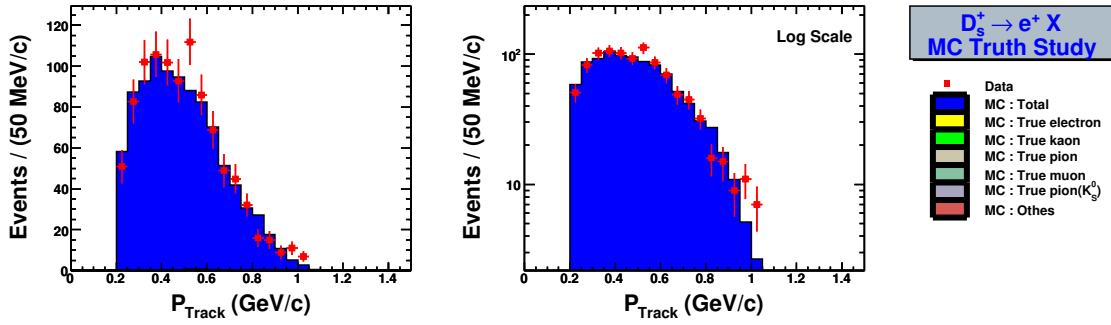
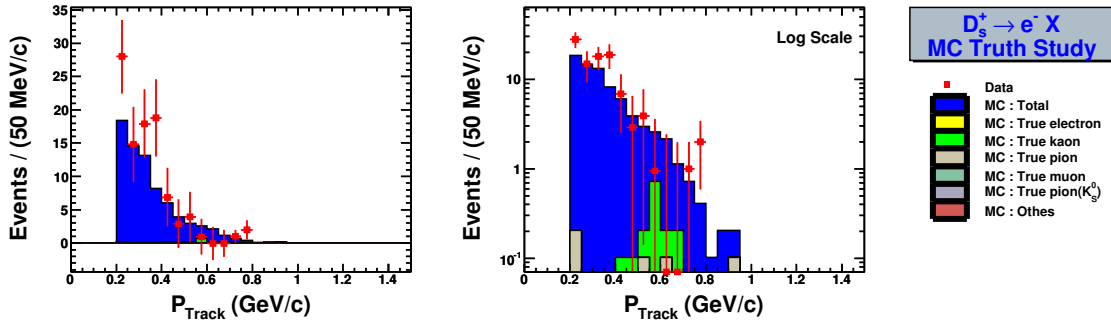
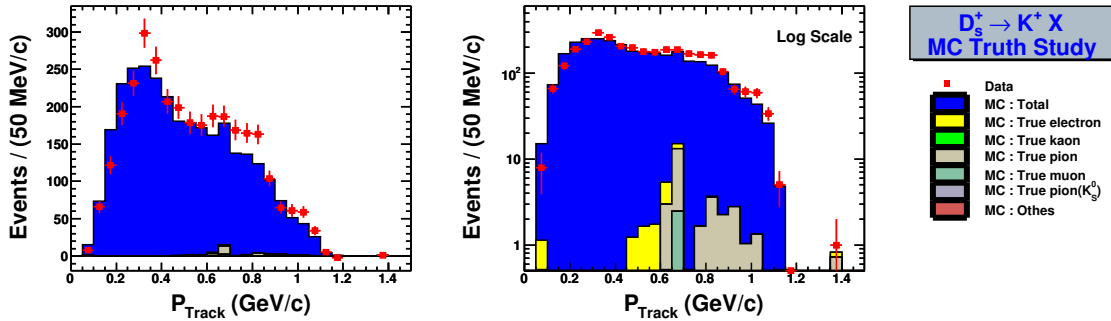
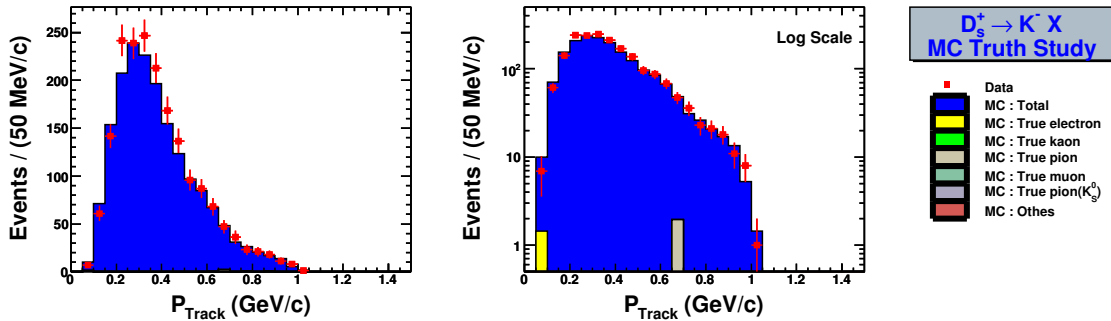
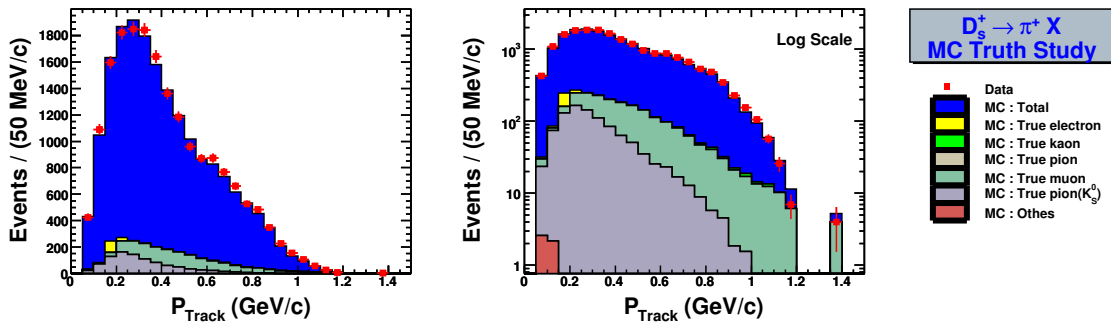


Figure 3.5: Observed momentum spectra of charged kaons, pions, and electrons. Red rectangles are obtained from data and blue solid histograms are Monte Carlo.

Figure 3.6: Monte Carlo truth information on e^+ momentum spectrum.Figure 3.7: Monte Carlo truth information on e^- momentum spectrum.

The red rectangle points are obtained from real data and blue solid histogram is from Monte Carlo. Different colorful histograms indicate different background sources. The left plot is in normal scale and the right plot is in log scale.

The cross-fake rates among all kinds of particles are momentum-dependent. Therefor we study the background and cross fake rates momentum bin by bin. To make sure there is enough statistics in each separate momentum bin for cross fake rate calculation and background estimation, we merge some low momentum bins and high momentum bins into a big bin. Fig. 3.12 shows how we merged the momentum bins for cross fake rate calculation and background study.

Figure 3.8: Monte Carlo truth information on K^+ momentum spectrum.Figure 3.9: Monte Carlo truth information on K^- momentum spectrum.Figure 3.10: Monte Carlo truth information on π^+ momentum spectrum.

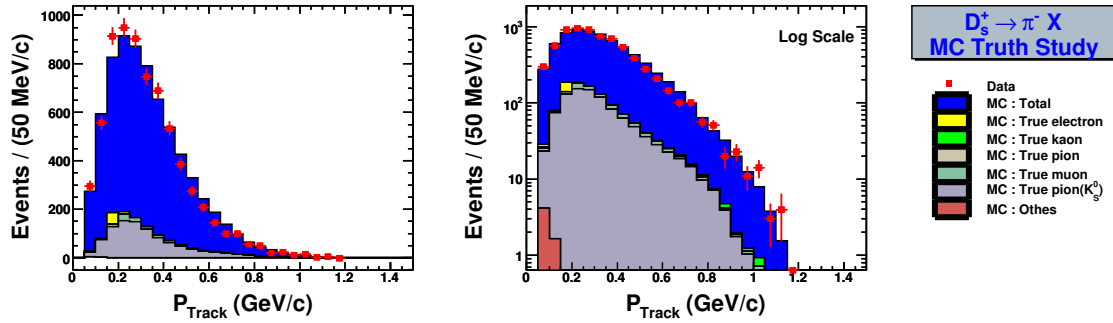


Figure 3.11: Monte Carlo truth information on π^- momentum spectrum.

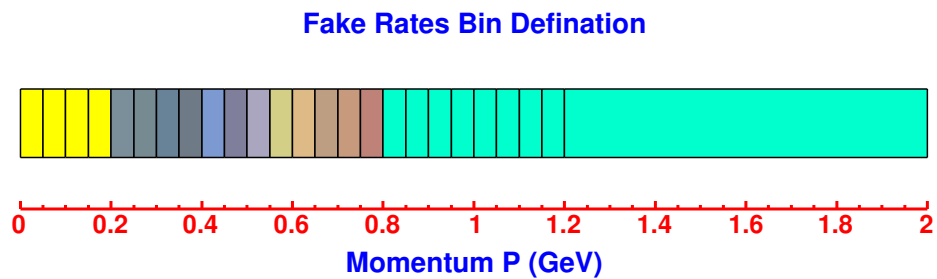


Figure 3.12: Momentum bin definitions for fake rates and background study. The separate boxes indicate the different momentum regions. We merge the bins with the same color into a big bin to make sure there is enough statistics in each bin for fake rates and background study.

3.4.3 The Cross-Fake Rates among e^\pm, K^\pm and π^\pm

In data, to estimate the backgrounds from any other particle faking to our signal particle, we define the cross-fake rates among all kinds of particles as

$$F_i^{a \rightarrow b} = \frac{\sum_j N_{i,j}^{a \rightarrow b \text{ (MC)}}}{\sum_j N_{i,j}^{\text{observed-}a \text{ (MC)}}} \quad (3.8)$$

Here, $F_i^{a \rightarrow b}$ is a particle faking to b particle rate in lab momentum bin i . $N_{i,j}^{a \rightarrow b \text{ (MC)}}$ is the number of Monte Carlo truth a particle, but is misidentified as b particle in lab momentum bin i and D_s -rest frame momentum bin j . $N_{i,j}^{\text{observed-}a \text{ (MC)}}$ is the number of observed a particle in lab momentum bin i and D_s -rest frame momentum bin j from Monte Carlo. Then the background number of a particle faking to b particle in lab momentum bin i and D_s -rest frame momentum bin j for data can be described as follow,

$$N_{i,j}^{a \rightarrow b \text{ (Data)}} = F_i^{a \rightarrow b} \times N_{i,j}^{\text{observed-}a \text{ (Data)}} \quad (3.9)$$

$$= \frac{\sum_j N_{i,j}^{a \rightarrow b \text{ (MC)}}}{\sum_j N_{i,j}^{\text{observed-}a \text{ (MC)}}} \times N_{i,j}^{\text{observed-}a \text{ (Data)}} \quad (3.10)$$

Here, $N_{i,j}^{\text{Data observed-}a}$ is the number of observed a particle in lab momentum bin i and D_s -rest frame momentum bin j from data.

When calculating the fake rate, for some particular lab momentum bins, the number of observed a particle can be zero ($\sum_j N_{i,j}^{\text{observed-}a \text{ (MC)}}$ is zero). For example, when we calculate e^+ fake to K^+ rate, there is a low momentum limit (200 MeV/c) for EID, the observed e^+ number from both data and Monte Carlo is zero in the lab momentum bin 1, 2, 3 and 4 (all of these four momentum bins are lower than 200 MeV/c). In this case, we directly estimate the a faking to b number in data by using Monte Carlo as the following formula shows us (normalized according to D_s tag yields from data and Monte Carlo),

$$N_{i,j}^{a \rightarrow b \text{ (Data)}} = N_{i,j}^{a \rightarrow b \text{ (MC)}} \times \frac{N_{D_s \text{ Tag}}^{\text{Data}}}{N_{D_s \text{ Tag}}^{\text{MC}}} \quad (3.11)$$

3.4.4 μ^\pm Fake to K^\pm and π^\pm

Muons can not be identified directly, there is no number of observed muons. Since right sign μ^+ and e^+ dominantly come from semileptonic decays, μ^+ and e^+ should have very similar behaviors. To estimate the effect of μ^+ faking to K^+ or π^+ in data, we use the number of observed e^+ to get the μ^+ faking to K^+ or π^+ rate shown as:

$$N_{i,j}^{\mu^+ \rightarrow K^+/\pi^+ \text{ (Data)}} = F_i^{\mu^+ \rightarrow K^+/\pi^+} \times N_{i,j}^{\text{observed } e^+ \text{ (Data)}} \quad (3.12)$$

$$= \frac{\sum_j N_{i,j}^{\mu^+ \rightarrow K^+/\pi^+ \text{ (MC)}}}{\sum_j N_{i,j}^{\text{observed } e^+ \text{ (MC)}}} \times N_{i,j}^{\text{observed } e^+ \text{ (Data)}} \quad (3.13)$$

For μ^- faking to K^- or π^- in data, we apply the directly estimating method instead of fake rate, since the μ^- and e^- don't have similar behaviors. The number of μ^- faking to K^- or π^- in data can be described as:

$$N_{i,j}^{\mu^- \rightarrow K^-/\pi^- \text{ (Data)}} = N_{i,j}^{\mu^- \rightarrow K^-/\pi^- \text{ (MC)}} \times \frac{N_{D_s \text{ Tag}}^{\text{Data}}}{N_{D_s \text{ Tag}}^{\text{MC}}} \quad (3.14)$$

3.4.5 π^\pm from K_S^0 Decay

We treat pion from K_S^0 decay as a source of background for inclusive π^\pm study. The number of π^\pm from K_S^0 decay in data is estimated by Monte Carlo and described as follows (normalized according to the K_S^0 yields from data and Monte Carlo).

$$N_{i,j}^{\pi^\pm \text{ From } K_S^0 \text{ (Data)}} = N_{i,j}^{\pi^\pm \text{ From } K_S^0 \text{ (MC)}} \times \frac{N_{K_S^0}^{\text{Data}}}{N_{K_S^0}^{\text{MC}}} \quad (3.15)$$

3.4.6 Other Background Sources

Monte Carlo study shows us there is a very tiny background contribution from other sources in addition to what we have considered above. We directly subtract them based on the Monte Carlo simulation. The background number from other sources is obtained by

$$N_{i,j}^{\text{Other} \rightarrow K^\pm/\pi^\pm \text{ (Data)}} = N_{i,j}^{\text{Other} \rightarrow K^\pm/\pi^\pm \text{ (MC)}} \times \frac{N_{D_s \text{ Tag}}^{\text{Data}}}{N_{D_s \text{ Tag}}^{\text{MC}}} \quad (3.16)$$

The cross fake rates are shown from Fig. 3.13 to Fig. 3.30. On the fake rate and background study plot, the corresponding number for each point is shown on the top of the plot. The colorful background of the number indicate how to define the momentum bin. The bins with same color have been merged into a big bin. The red text color means that number is a rate and blue text color means that number is the estimated background number in data.

Through this analysis, when we say K^+ , that means the K^+ from D_s^+ decay and also including K^- from D_s^- decay. When we say K^- , that means the K^- from D_s^+ decay and also including K^+ from D_s^- decay. Similarly for π^+ and π^- .

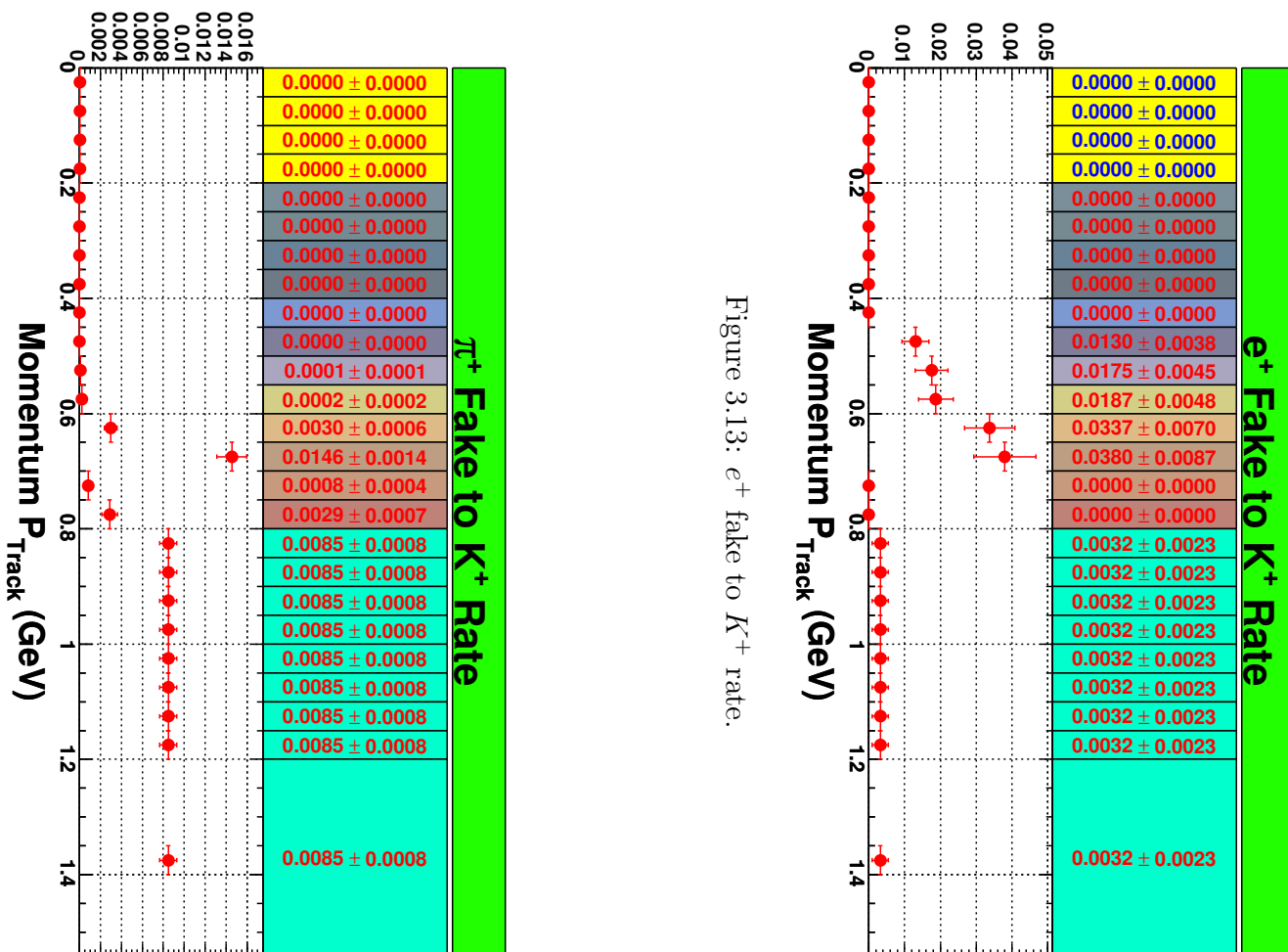


Figure 3.13: e^+ fake to K^+ rate.

Figure 3.14: π^+ fake to K^+ rate.

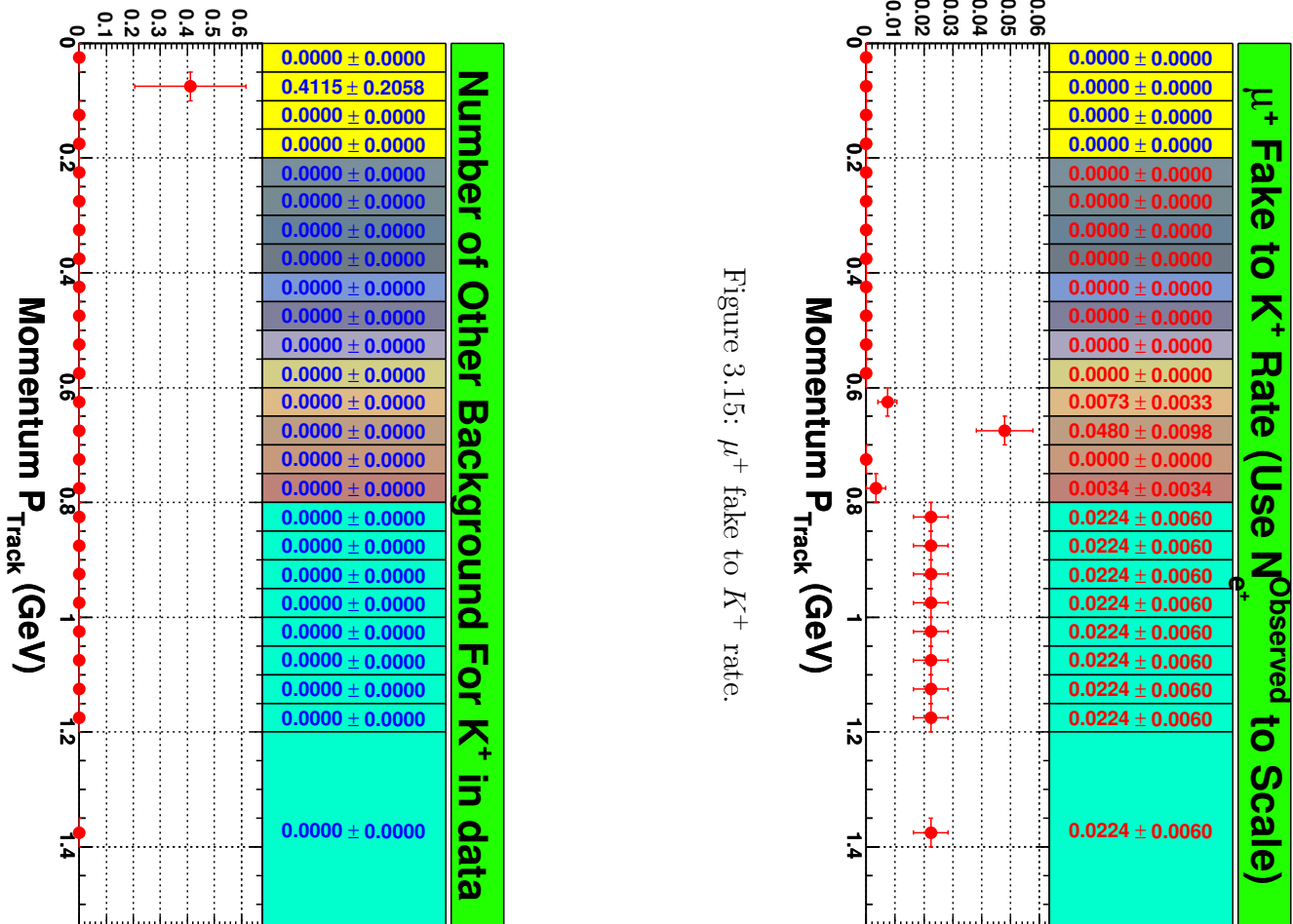


Figure 3.15: μ^+ fake to K^+ rate.

Figure 3.16: Other background fake to K^+ .

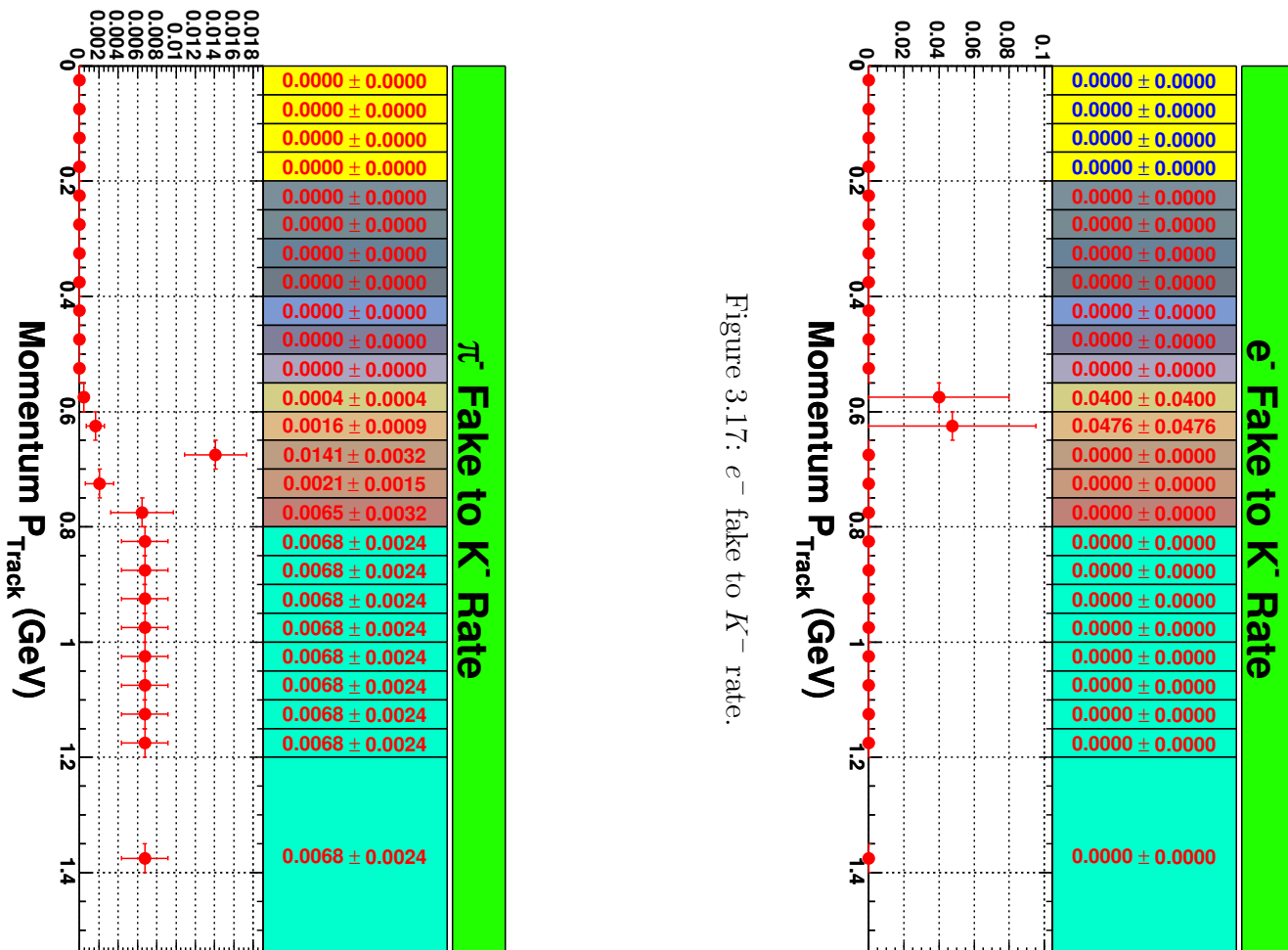


Figure 3.17: e^- fake to K^- rate.

Figure 3.18: π^- fake to K^- rate.

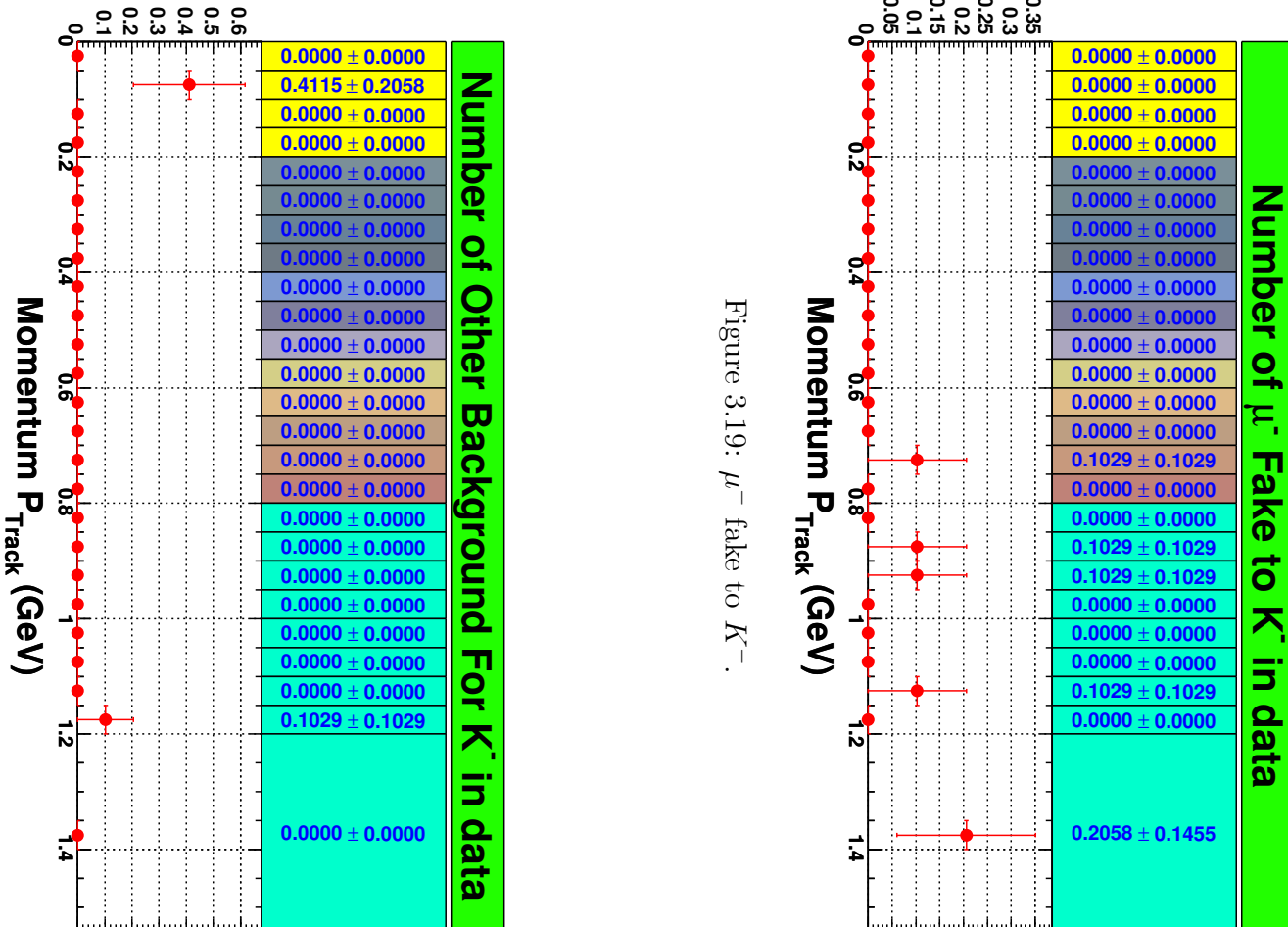


Figure 3.19: μ^- fake to K^- .

Figure 3.20: Other background fake to K^- .

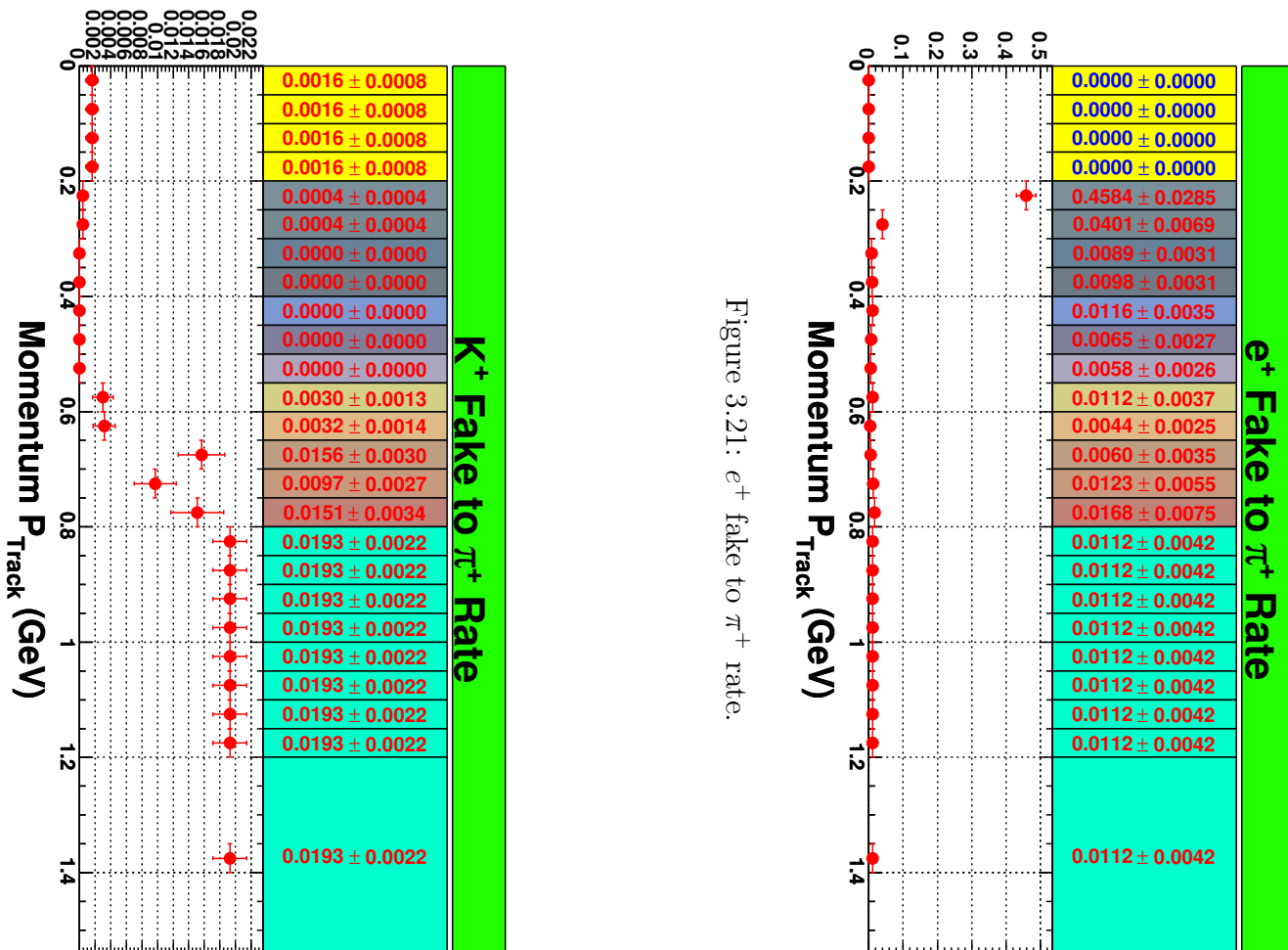
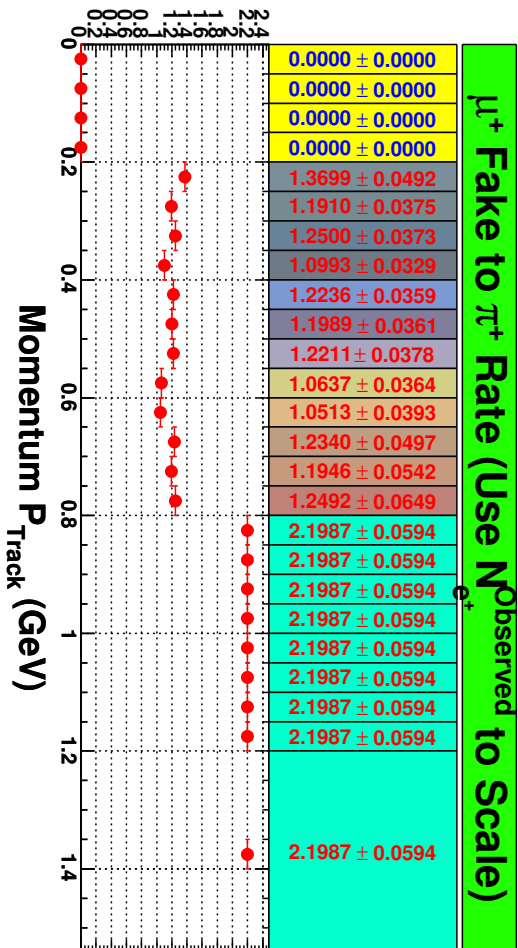
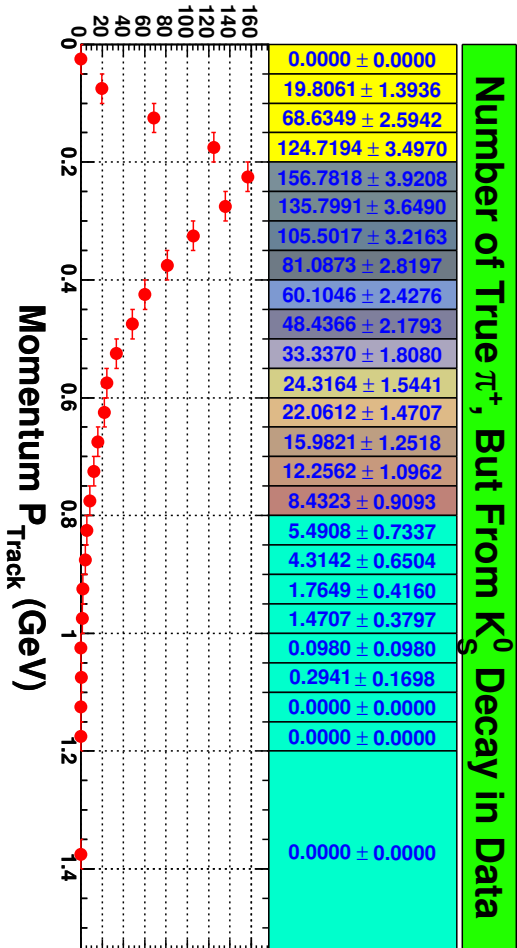


Figure 3.21: e^+ fake to π^+ rate.

Figure 3.22: K^+ fake to π^+ rate.

Figure 3.23: μ^+ fake to π^+ rate.Figure 3.24: Real π^+ background from K_S^0 decay.

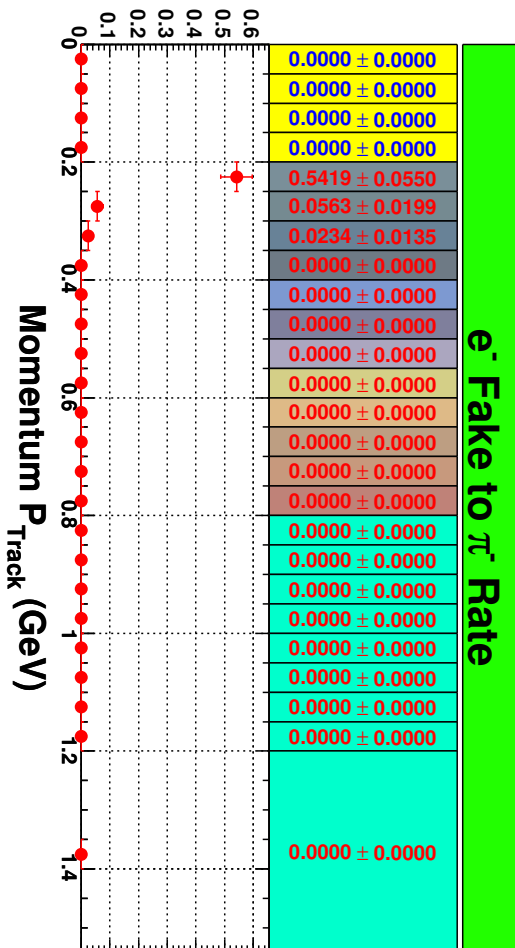
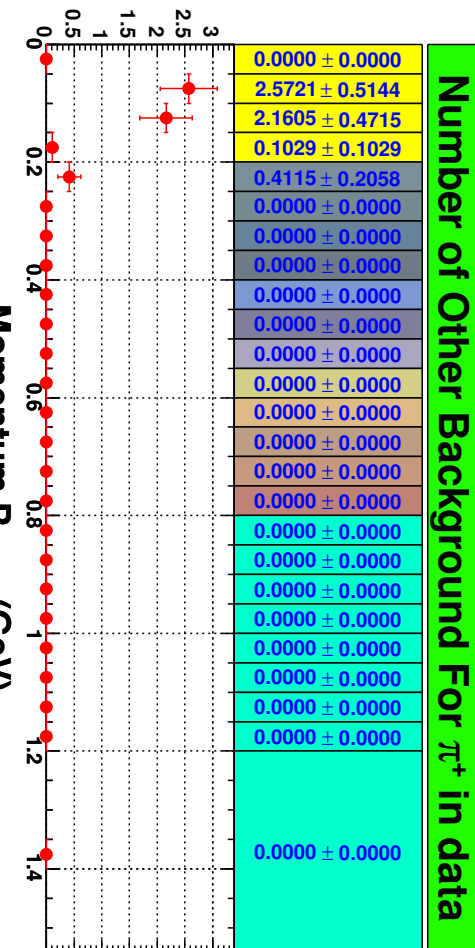
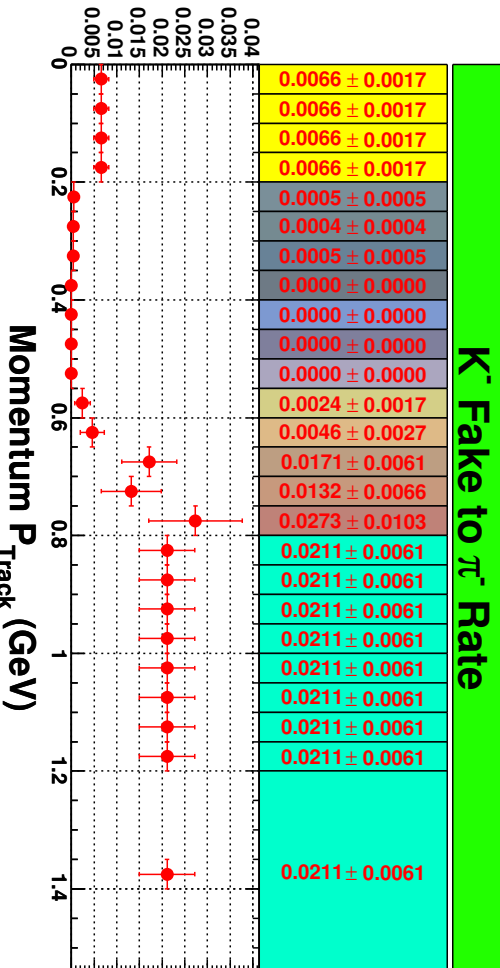
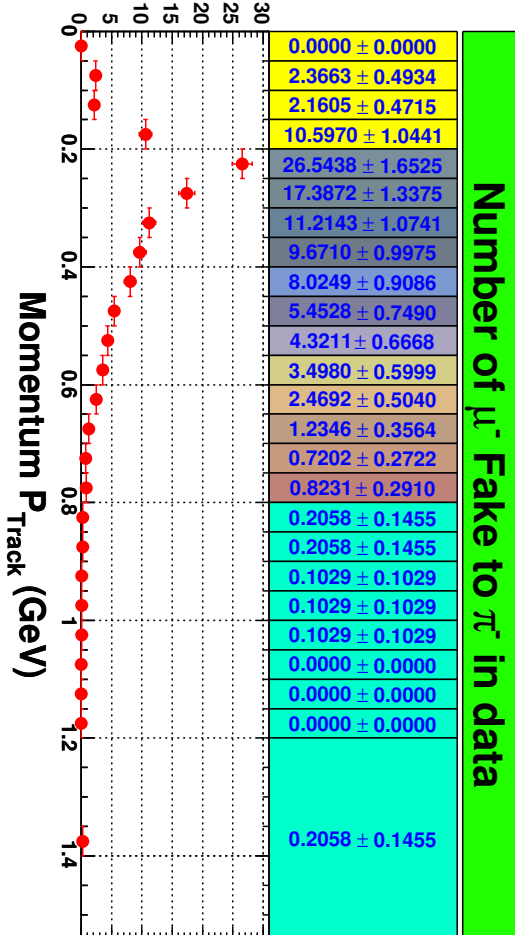


Figure 3.25: Other background fake to π^+ .



Figure 3.27: K^- fake to π^- rate.Figure 3.28: μ^- fake to π^- .

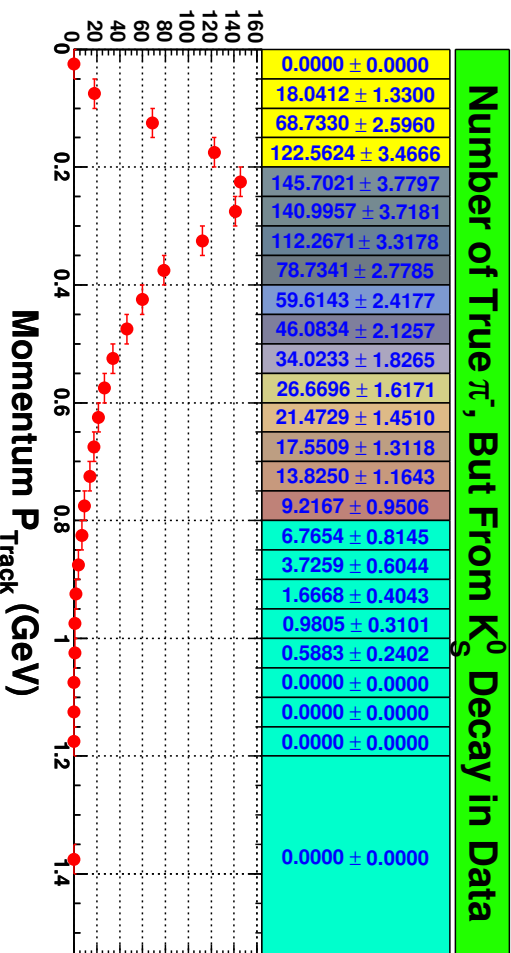


Figure 3.29: Real π^- background from K_S^0 decay.

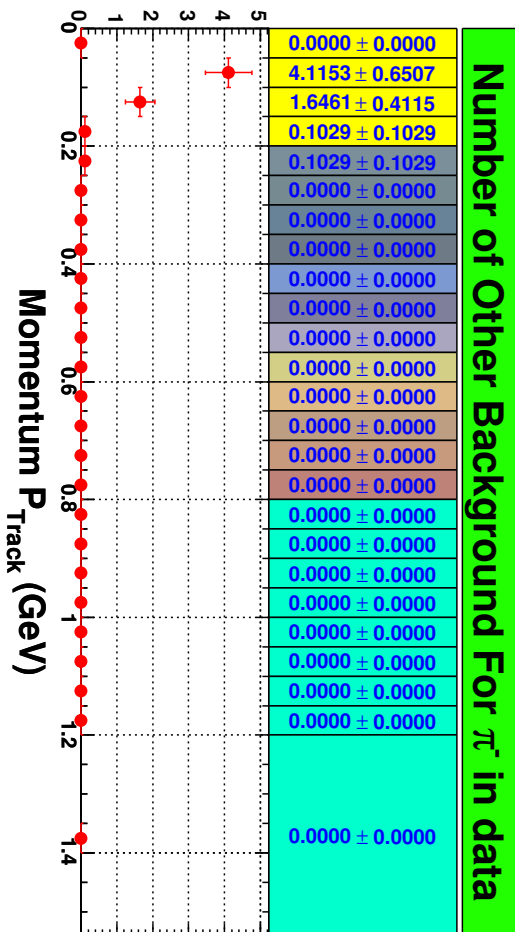


Figure 3.30: Other background fake to π^- .

3.4.7 K^\pm and π^\pm PID Efficiencies

We also study the K^\pm and π^\pm PID Efficiencies lab momentum bin by bin. The lab momentum bin definitions are same as before. The PID efficiency is defined as,

$$\epsilon_i^{K^\pm/\pi^\pm} = \frac{\sum_j N_{i,j}^{\text{MC Truth Identify as } K^\pm/\pi^\pm}}{\sum_j N_{i,j}^{\text{MC Truth Detected } K^\pm/\pi^\pm}} \quad (3.17)$$

Here, $N_{i,j}^{\text{MC Truth Identify as } K^\pm/\pi^\pm}$ is the number of K^\pm/π^\pm Monte Carlo truth matched and also identified as K^\pm/π^\pm , and $N_{i,j}^{\text{MC Truth Detected } K^\pm/\pi^\pm}$ is the total number of detected K^\pm/π^\pm with Monte Carlo truth match.

3.4.8 Tracking Efficiency

We include track finding, quality, radiation feed-down (due to material bremsstrahlung), and resolution effects into a total overall average efficiency. We also include geometrical acceptance ($|\cos \theta| < 0.80$) correction in this overall average efficiency. We call this overall efficiency as tracking efficiency. We study the tracking efficiency momentum bin by bin for each kind of signal particle.

Fig. 3.31 and Fig. 3.32 show the K^+ and K^- PID efficiencies, Fig. 3.33 and Fig. 3.34 show the π^+ and π^- PID efficiencies. Tracking efficiency plots are shown in Fig. 3.35 (for K^+), Fig. 3.36 (for K^-), Fig. 3.37 (for π^+), and Fig. 3.38 (for π^-).

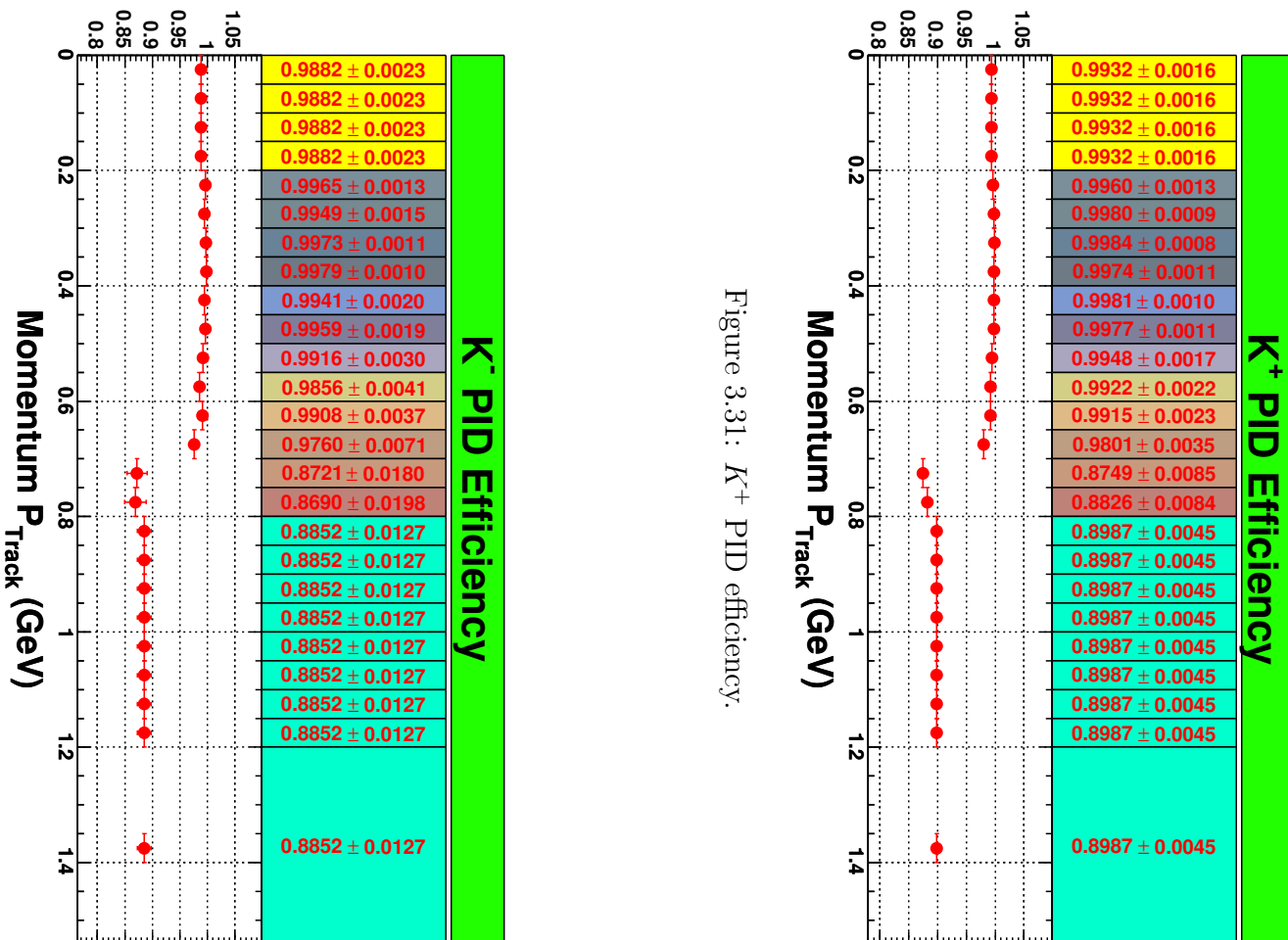


Figure 3.31: K^+ PID efficiency.

Figure 3.32: K –PID efficiency.

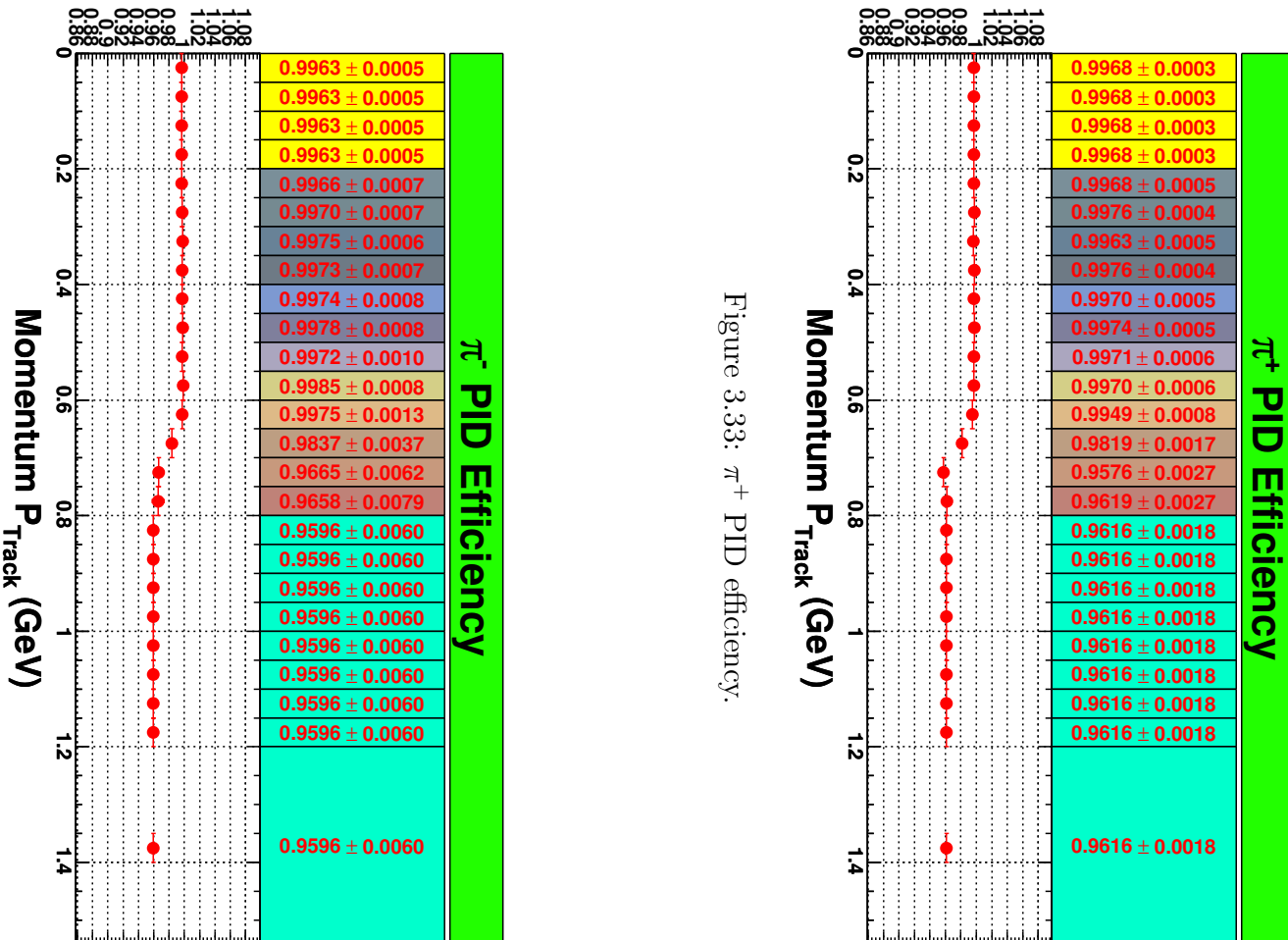


Figure 3.33: π^+ PID efficiency.

Figure 3.34: π^- PID efficiency.

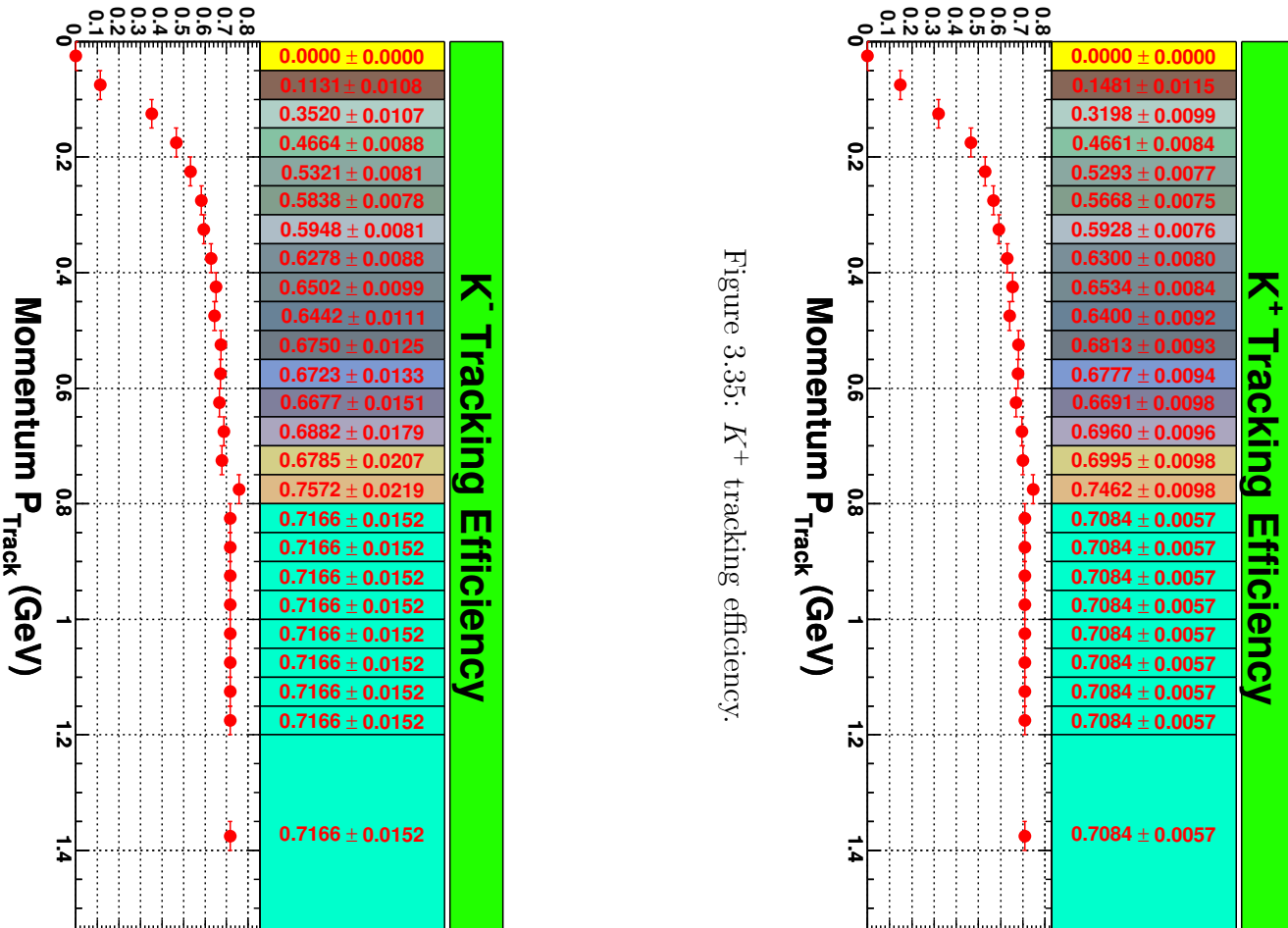


Figure 3.35: K^+ tracking efficiency.

Figure 3.36: K^- tracking efficiency.

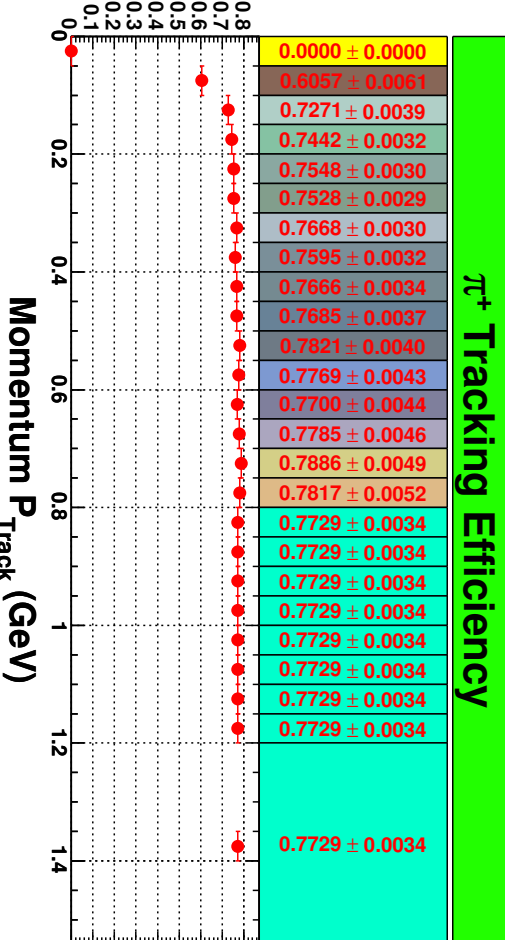


Figure 3.37: π^+ tracking efficiency.

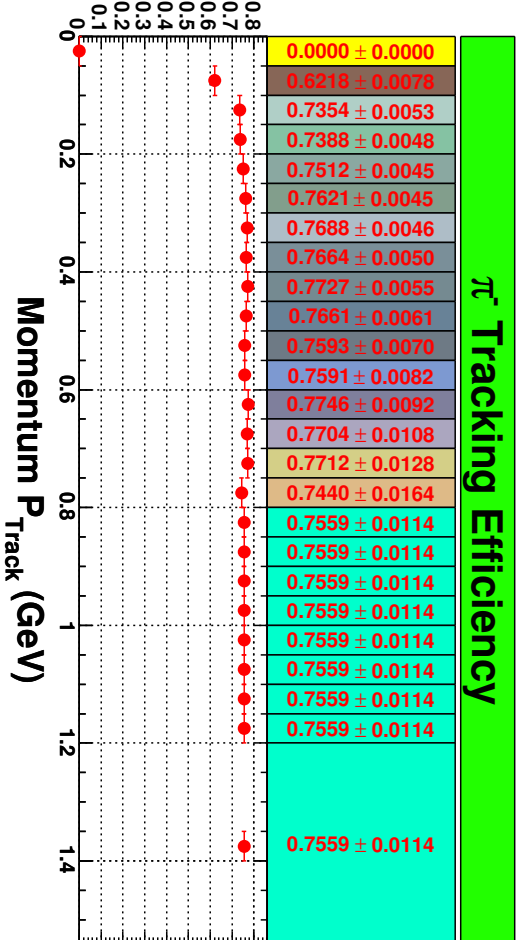


Figure 3.38: π^- tracking efficiency.

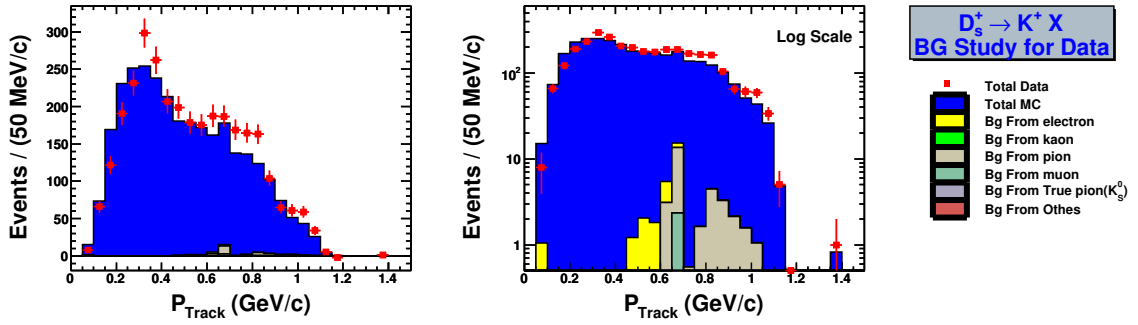


Figure 3.39: Background study for $D_s^+ \rightarrow K^+X$ momentum spectrum in real data.

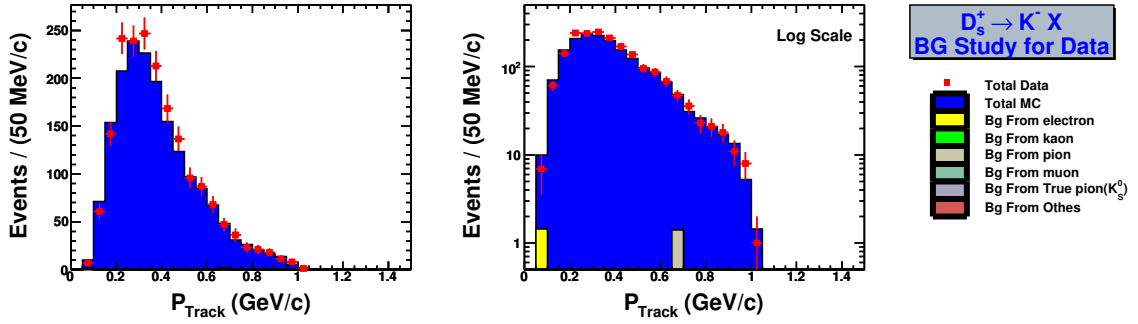


Figure 3.40: Background study for $D_s^+ \rightarrow K^-X$ momentum spectrum in real data.

3.4.9 $D_s^+ \rightarrow K^+/K^-/\pi^+/\pi^- X$ Branching Fractions

We use cross-fake rates to estimate background contributions from different sources in real data. The background study plots for data are shown in Fig. 3.39 (for $D_s^+ \rightarrow K^+X$), Fig. 3.40 (for $D_s^+ \rightarrow K^-X$), Fig. 3.41 (for $D_s^+ \rightarrow \pi^+X$), and Fig. 3.42 (for $D_s^+ \rightarrow \pi^-X$). The red rectangle points are obtained from real data and blue solid histogram is from Monte Carlo. Different colorful histograms indicate different sources. The left plot is in normal scale and the right plot is in log scale. The detailed background estimation numbers from different sources are listed in Table 3.4 (for $D_s^+ \rightarrow K^+X$), Table 3.5 (for $D_s^+ \rightarrow K^-X$), Table 3.6 (for $D_s^+ \rightarrow \pi^+X$), and Table 3.7 (for $D_s^+ \rightarrow \pi^-X$).

Momentum spectra are obtained by using 2-dimensional sideband-subtracted yield matrix $N(p, p^*)$, binned with lab momentum (p) and D_s -rest frame momentum (p^*) in 50×50 MeV/c bin size. We subtract all kinds of backgrounds bin by bin

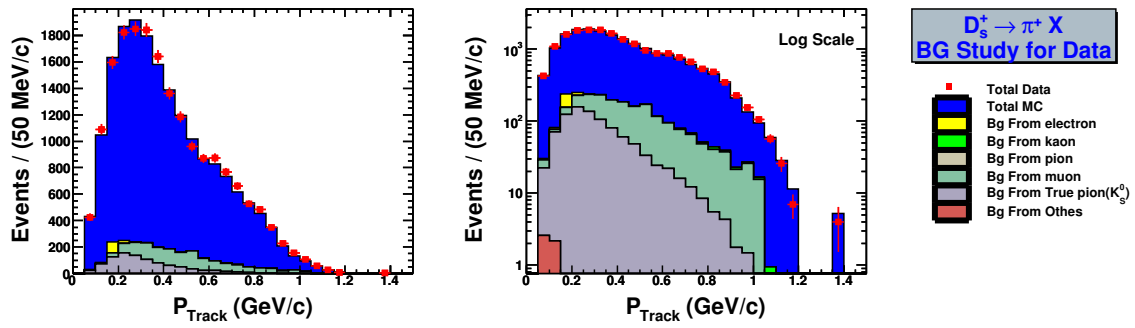


Figure 3.41: Background study for $D_s^+ \rightarrow \pi^+ X$ momentum spectrum in real data.

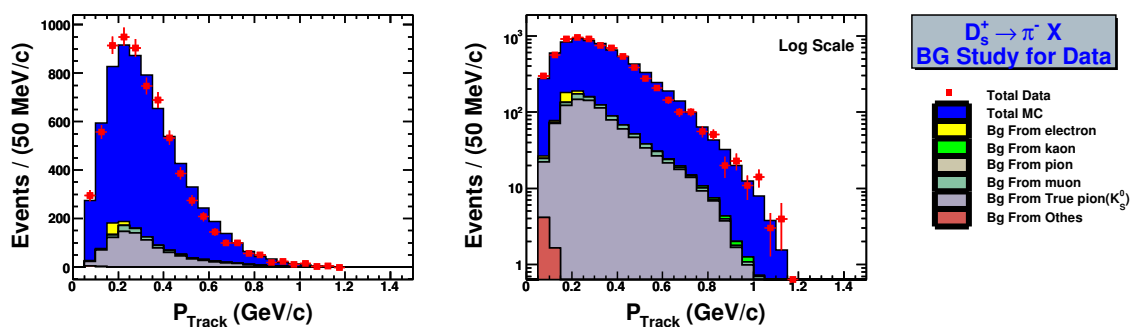


Figure 3.42: Background study for $D_s^+ \rightarrow \pi^- X$ momentum spectrum in real data.

Table 3.4: Estimated Backgrounds from all kinds of particles faking a K^+ .

p (GeV)	$N_{K^+}^{\text{In Data}}$	$N_{e^+ \rightarrow K^+}$	$N_{\pi^+ \rightarrow K^+}$	$N_{\mu^+ \rightarrow K^+}$	$N_{\text{Other} \rightarrow K^+}^{\text{In Data}}$
0.000—0.050	0.0000 ± 0.0000	0.0000 ± 0.0000	0.0000 ± 0.0000	0.0000 ± 0.0000	0.0000 ± 0.0000
0.050—0.100	7.9267 ± 4.0187	0.6173 ± 0.2520	0.0140 ± 0.0104	0.0000 ± 0.0000	0.4115 ± 0.2058
0.100—0.150	65.8943 ± 8.4981	0.0000 ± 0.0000	0.0361 ± 0.0252	0.0000 ± 0.0000	0.0000 ± 0.0000
0.150—0.200	121.6677 ± 11.9451	0.0000 ± 0.0000	0.0528 ± 0.0336	0.0000 ± 0.0000	0.0000 ± 0.0000
0.200—0.250	190.4195 ± 15.3039	0.0000 ± 0.0000	0.0000 ± 0.0000	0.0000 ± 0.0000	0.0000 ± 0.0000
0.250—0.300	231.4588 ± 16.9447	0.0000 ± 0.0000	0.0000 ± 0.0000	0.0000 ± 0.0000	0.0000 ± 0.0000
0.300—0.350	298.1508 ± 19.4109	0.0000 ± 0.0000	0.0000 ± 0.0000	0.0000 ± 0.0000	0.0000 ± 0.0000
0.350—0.400	262.1774 ± 18.3497	0.0000 ± 0.0000	0.0000 ± 0.0000	0.0000 ± 0.0000	0.0000 ± 0.0000
0.400—0.450	207.0151 ± 16.4332	0.0000 ± 0.0000	0.0000 ± 0.0000	0.0000 ± 0.0000	0.0000 ± 0.0000
0.450—0.500	198.7060 ± 15.0866	1.2103 ± 0.2149	0.0000 ± 0.0000	0.0000 ± 0.0000	0.0000 ± 0.0000
0.500—0.550	178.4457 ± 15.1705	1.9614 ± 0.3056	0.0971 ± 0.0438	0.0000 ± 0.0000	0.0000 ± 0.0000
0.550—0.600	175.4388 ± 14.7363	1.6085 ± 0.2678	0.2070 ± 0.0630	0.0000 ± 0.0000	0.0000 ± 0.0000
0.600—0.650	187.5230 ± 15.1981	2.3203 ± 0.3826	2.6118 ± 0.2494	0.5044 ± 0.1237	0.0000 ± 0.0000
0.650—0.700	186.8036 ± 14.4707	1.8557 ± 0.3623	11.1550 ± 0.6550	2.3440 ± 0.4451	0.0000 ± 0.0000
0.700—0.750	168.8189 ± 13.7611	0.0000 ± 0.0000	0.5530 ± 0.1102	0.0000 ± 0.0000	0.0000 ± 0.0000
0.750—0.800	164.8273 ± 13.1665	0.0000 ± 0.0000	1.5209 ± 0.1961	0.1077 ± 0.0541	0.0000 ± 0.0000
0.800—0.850	162.9115 ± 13.1598	0.0512 ± 0.0260	4.0931 ± 0.2822	0.3581 ± 0.1158	0.0000 ± 0.0000
0.850—0.900	103.8506 ± 10.5029	0.0478 ± 0.0211	2.9444 ± 0.2221	0.3346 ± 0.1068	0.0000 ± 0.0000
0.900—0.950	64.9461 ± 8.4327	0.0286 ± 0.0158	1.9281 ± 0.1601	0.2004 ± 0.0810	0.0000 ± 0.0000
0.950—1.000	60.8557 ± 8.4437	0.0353 ± 0.0174	1.3127 ± 0.1286	0.2468 ± 0.0829	0.0000 ± 0.0000
1.000—1.050	58.9847 ± 7.8123	0.0224 ± 0.0126	0.8893 ± 0.1019	0.1571 ± 0.0643	0.0000 ± 0.0000
1.050—1.100	33.9807 ± 6.0033	0.0000 ± 0.0000	0.4825 ± 0.0738	0.0000 ± 0.0000	0.0000 ± 0.0000
1.100—1.150	5.0000 ± 2.2361	0.0000 ± 0.0000	0.2190 ± 0.0536	0.0000 ± 0.0000	0.0000 ± 0.0000
1.150—1.200	-2.1341 ± 1.5096	0.0000 ± 0.0000	0.0593 ± 0.0227	0.0000 ± 0.0000	0.0000 ± 0.0000
1.200—2.000	1.0000 ± 1.0000	0.0000 ± 0.0000	0.0338 ± 0.0210	0.0000 ± 0.0000	0.0000 ± 0.0000

Table 3.5: Estimated Backgrounds from all kinds of particles faking a K^- .

p (GeV)	$N_{K^-}^{\text{In Data}}$	$N_{e^- \rightarrow K^-}$	$N_{\pi^- \rightarrow K^-}$	$N_{\mu^- \rightarrow K^-}^{\text{In Data}}$	$N_{\text{Other} \rightarrow K^-}^{\text{In Data}}$
0.000—0.050	0.0000 ± 0.0000	0.0000 ± 0.0000	0.0000 ± 0.0000	0.0000 ± 0.0000	0.0000 ± 0.0000
0.050—0.100	6.9136 ± 3.3434	1.0288 ± 0.3253	0.0000 ± 0.0000	0.0000 ± 0.0000	0.4115 ± 0.2058
0.100—0.150	60.9807 ± 7.9397	0.0000 ± 0.0000	0.0000 ± 0.0000	0.0000 ± 0.0000	0.0000 ± 0.0000
0.150—0.200	141.7347 ± 12.6707	0.0000 ± 0.0000	0.0000 ± 0.0000	0.0000 ± 0.0000	0.0000 ± 0.0000
0.200—0.250	241.6665 ± 16.5132	0.0000 ± 0.0000	0.0000 ± 0.0000	0.0000 ± 0.0000	0.0000 ± 0.0000
0.250—0.300	238.7223 ± 16.4186	0.0000 ± 0.0000	0.0000 ± 0.0000	0.0000 ± 0.0000	0.0000 ± 0.0000
0.300—0.350	246.6268 ± 16.6664	0.0000 ± 0.0000	0.0000 ± 0.0000	0.0000 ± 0.0000	0.0000 ± 0.0000
0.350—0.400	212.6471 ± 15.6757	0.0000 ± 0.0000	0.0000 ± 0.0000	0.0000 ± 0.0000	0.0000 ± 0.0000
0.400—0.450	168.4326 ± 14.7029	0.0000 ± 0.0000	0.0000 ± 0.0000	0.0000 ± 0.0000	0.0000 ± 0.0000
0.450—0.500	136.6858 ± 12.8702	0.0000 ± 0.0000	0.0000 ± 0.0000	0.0000 ± 0.0000	0.0000 ± 0.0000
0.500—0.550	95.7194 ± 10.7971	0.0000 ± 0.0000	0.0000 ± 0.0000	0.0000 ± 0.0000	0.0000 ± 0.0000
0.550—0.600	86.8495 ± 10.1640	0.0378 ± 0.1394	0.0881 ± 0.0428	0.0000 ± 0.0000	0.0000 ± 0.0000
0.600—0.650	67.8170 ± 9.0761	-0.0028 ± 0.1357	0.2378 ± 0.0666	0.0000 ± 0.0000	0.0000 ± 0.0000
0.650—0.700	46.9654 ± 7.1464	0.0000 ± 0.0000	1.4105 ± 0.2347	0.0000 ± 0.0000	0.0000 ± 0.0000
0.700—0.750	35.9034 ± 6.7968	0.0000 ± 0.0000	0.2074 ± 0.0718	0.1029 ± 0.1029	0.0000 ± 0.0000
0.750—0.800	22.9420 ± 5.3961	0.0000 ± 0.0000	0.3610 ± 0.0948	0.0000 ± 0.0000	0.0000 ± 0.0000
0.800—0.850	20.9614 ± 5.0078	0.0000 ± 0.0000	0.3438 ± 0.0767	0.0000 ± 0.0000	0.0000 ± 0.0000
0.850—0.900	18.0000 ± 4.2426	0.0000 ± 0.0000	0.1341 ± 0.0463	0.1029 ± 0.1029	0.0000 ± 0.0000
0.900—0.950	10.9807 ± 3.6110	0.0000 ± 0.0000	0.1546 ± 0.0469	0.1029 ± 0.1029	0.0000 ± 0.0000
0.950—1.000	8.0000 ± 2.8284	0.0000 ± 0.0000	0.0738 ± 0.0291	0.0000 ± 0.0000	0.0000 ± 0.0000
1.000—1.050	1.0000 ± 1.0000	0.0000 ± 0.0000	0.0947 ± 0.0321	0.0000 ± 0.0000	0.0000 ± 0.0000
1.050—1.100	0.0000 ± 0.0000	0.0000 ± 0.0000	0.0203 ± 0.0124	0.0000 ± 0.0000	0.0000 ± 0.0000
1.100—1.150	0.0000 ± 0.0000	0.0000 ± 0.0000	0.0269 ± 0.0176	0.1029 ± 0.1029	0.0000 ± 0.0000
1.150—1.200	0.0000 ± 0.0000	0.0000 ± 0.0000	-0.0072 ± 0.0077	0.0000 ± 0.0000	0.1029 ± 0.1029
1.200—2.000	0.0000 ± 0.0000	0.0000 ± 0.0000	0.0000 ± 0.0000	0.2058 ± 0.1455	0.0000 ± 0.0000

Table 3.6: Estimated Backgrounds from all kinds of particles faking a π^+ .

p (GeV)	$N_{\pi^+}^{\text{In Data}}$	$N_{e^+ \rightarrow \pi^+}$	$N_{K^+ \rightarrow \pi^+}$	$N_{\mu^+ \rightarrow \pi^+}$	$N_{\pi^+ \text{From } K_S^0}^{\text{In Data}}$	$N_{\text{Other} \rightarrow \pi^+}^{\text{In Data}}$
0.000—0.050	0.0000 ± 0.0000	0.0000 ± 0.0000	0.0000 ± 0.0000	0.0000 ± 0.0000	0.0000 ± 0.0000	0.0000 ± 0.0000
0.050—0.100	424.6983 ± 28.5887	1.5432 ± 0.3985	0.0127 ± 0.0076	6.3788 ± 0.8101	19.8061 ± 1.3936	2.5721 ± 0.5144
0.100—0.150	1090.0749 ± 39.5368	5.2470 ± 0.7347	0.1052 ± 0.0366	6.0701 ± 0.7903	68.6349 ± 2.5942	2.1605 ± 0.4715
0.150—0.200	1594.8982 ± 50.2468	84.9815 ± 2.9569	0.1943 ± 0.0694	29.9390 ± 1.7551	124.7194 ± 3.4970	0.1029 ± 0.1029
0.200—0.250	1820.2190 ± 53.0133	23.2860 ± 3.8606	0.0849 ± 0.0539	69.5883 ± 11.3455	156.7818 ± 3.9208	0.4115 ± 0.2058
0.250—0.300	1849.3408 ± 54.2287	3.3105 ± 0.5294	0.0946 ± 0.0553	98.3415 ± 12.9305	135.7991 ± 3.6490	0.0000 ± 0.0000
0.300—0.350	1840.7996 ± 51.5843	0.9054 ± 0.2002	0.0000 ± 0.0000	127.3219 ± 13.7533	105.5017 ± 3.2163	0.0000 ± 0.0000
0.350—0.400	1640.2307 ± 49.2202	1.0396 ± 0.2005	0.0000 ± 0.0000	116.2309 ± 12.3964	81.0873 ± 2.8197	0.0000 ± 0.0000
0.400—0.450	1359.4233 ± 45.1352	1.1811 ± 0.2190	0.0000 ± 0.0000	124.5511 ± 13.8769	60.1046 ± 2.4276	0.0000 ± 0.0000
0.450—0.500	1183.3525 ± 41.7500	0.6052 ± 0.1348	0.0000 ± 0.0000	111.2489 ± 12.9751	48.4366 ± 2.1793	0.0000 ± 0.0000
0.500—0.550	959.2308 ± 37.2635	0.6538 ± 0.1495	0.0000 ± 0.0000	136.5158 ± 13.9713	33.3370 ± 1.8080	0.0000 ± 0.0000
0.550—0.600	869.9224 ± 34.9988	0.9651 ± 0.1864	0.5256 ± 0.1118	91.3609 ± 10.6415	24.3164 ± 1.5441	0.0000 ± 0.0000
0.600—0.650	874.7518 ± 34.3654	0.3026 ± 0.0899	0.5949 ± 0.1269	72.3326 ± 9.7945	22.0612 ± 1.4707	0.0000 ± 0.0000
0.650—0.700	766.3698 ± 31.2824	0.2930 ± 0.0883	2.9205 ± 0.3362	60.2614 ± 10.1806	15.9821 ± 1.2518	0.0000 ± 0.0000
0.700—0.750	661.3054 ± 28.8198	0.5526 ± 0.1408	1.6366 ± 0.2654	53.6068 ± 8.7828	12.2562 ± 1.0962	0.0000 ± 0.0000
0.750—0.800	527.5489 ± 25.6527	0.5387 ± 0.1479	2.4898 ± 0.3267	39.9731 ± 7.1332	8.4323 ± 0.9093	0.0000 ± 0.0000
0.800—0.850	482.7960 ± 24.2180	0.1791 ± 0.0646	3.1420 ± 0.3025	35.0945 ± 9.8686	5.4908 ± 0.7337	0.0000 ± 0.0000
0.850—0.900	347.3052 ± 20.5778	0.1673 ± 0.0573	2.0029 ± 0.2310	32.7909 ± 9.6378	4.3142 ± 0.6504	0.0000 ± 0.0000
0.900—0.950	227.4348 ± 16.4063	0.1002 ± 0.0434	1.2526 ± 0.1771	19.6411 ± 7.3448	1.7649 ± 0.4160	0.0000 ± 0.0000
0.950—1.000	154.8423 ± 13.1653	0.1234 ± 0.0453	1.1737 ± 0.1923	24.1859 ± 7.3013	1.4707 ± 0.3797	0.0000 ± 0.0000
1.000—1.050	104.8921 ± 10.8268	0.0785 ± 0.0344	1.1376 ± 0.1847	15.3910 ± 5.8224	0.0980 ± 0.0980	0.0000 ± 0.0000
1.050—1.100	56.9074 ± 8.1968	0.0000 ± 0.0000	0.6554 ± 0.1338	0.0000 ± 0.0000	0.2941 ± 0.1698	0.0000 ± 0.0000
1.100—1.150	25.8363 ± 6.1917	0.0000 ± 0.0000	0.0964 ± 0.0438	0.0000 ± 0.0000	0.0000 ± 0.0000	0.0000 ± 0.0000
1.150—1.200	7.0000 ± 2.6458	0.0000 ± 0.0000	-0.0412 ± 0.0293	0.0000 ± 0.0000	0.0000 ± 0.0000	0.0000 ± 0.0000
1.200—2.000	3.9847 ± 2.4559	0.0000 ± 0.0000	0.0193 ± 0.0194	0.0000 ± 0.0000	0.0000 ± 0.0000	0.0000 ± 0.0000

Table 3.7: Estimated Backgrounds from all kinds of particles faking a π^- .

p (GeV)	$N_{\pi^-}^{\text{In Data}}$	$N_{e^- \rightarrow \pi^-}$	$N_{K^- \rightarrow \pi^-}$	$N_{\mu^- \rightarrow \pi^-}^{\text{In Data}}$	$N_{\pi^- \text{From } K_S^0}^{\text{In Data}}$	$N_{\text{Other} \rightarrow \pi^-}^{\text{In Data}}$
0.000—0.050	0.0000 ± 0.0000	0.0000 ± 0.0000	0.0000 ± 0.0000	0.0000 ± 0.0000	0.0000 ± 0.0000	0.0000 ± 0.0000
0.050—0.100	295.1047 ± 23.8492	2.0577 ± 0.4601	0.0455 ± 0.0238	2.3663 ± 0.4934	18.0412 ± 1.3300	4.1153 ± 0.6507
0.100—0.150	556.7959 ± 28.9010	4.1153 ± 0.6507	0.4014 ± 0.0932	2.1605 ± 0.4715	68.7330 ± 2.5960	1.6461 ± 0.4115
0.150—0.200	914.7670 ± 36.4010	47.4291 ± 2.2090	0.9329 ± 0.1665	10.5970 ± 1.0441	122.5624 ± 3.4666	0.1029 ± 0.1029
0.200—0.250	949.5027 ± 38.1051	15.1627 ± 3.1549	0.1199 ± 0.0758	26.5438 ± 1.6525	145.7021 ± 3.7797	0.1029 ± 0.1029
0.250—0.300	903.8648 ± 36.9170	0.8344 ± 0.3757	0.1028 ± 0.0627	17.3872 ± 1.3375	140.9957 ± 3.7181	0.0000 ± 0.0000
0.300—0.350	747.2606 ± 35.8126	0.4201 ± 0.1794	0.1121 ± 0.0633	11.2143 ± 1.0741	112.2671 ± 3.3178	0.0000 ± 0.0000
0.350—0.400	688.7240 ± 32.8115	0.0000 ± 0.0000	0.0000 ± 0.0000	9.6710 ± 0.9975	78.7341 ± 2.7785	0.0000 ± 0.0000
0.400—0.450	533.2984 ± 29.4468	0.0000 ± 0.0000	0.0000 ± 0.0000	8.0249 ± 0.9086	59.6143 ± 2.4177	0.0000 ± 0.0000
0.450—0.500	387.0894 ± 25.7348	0.0000 ± 0.0000	0.0000 ± 0.0000	5.4528 ± 0.7490	46.0834 ± 2.1257	0.0000 ± 0.0000
0.500—0.550	275.4628 ± 22.4814	0.0000 ± 0.0000	0.0000 ± 0.0000	4.3211 ± 0.6668	34.0233 ± 1.8265	0.0000 ± 0.0000
0.550—0.600	207.8353 ± 19.7626	0.0000 ± 0.0000	0.2111 ± 0.0753	3.4980 ± 0.5999	26.6696 ± 1.6171	0.0000 ± 0.0000
0.600—0.650	144.7247 ± 16.2690	0.0000 ± 0.0000	0.3125 ± 0.0905	2.4692 ± 0.5040	21.4729 ± 1.4510	0.0000 ± 0.0000
0.650—0.700	100.0747 ± 13.3012	0.0000 ± 0.0000	0.8045 ± 0.1731	1.2346 ± 0.3564	17.5509 ± 1.3118	0.0000 ± 0.0000
0.700—0.750	99.5383 ± 11.8723	0.0000 ± 0.0000	0.4740 ± 0.1385	0.7202 ± 0.2722	13.8250 ± 1.1643	0.0000 ± 0.0000
0.750—0.800	55.6796 ± 9.5214	0.0000 ± 0.0000	0.6273 ± 0.1900	0.8231 ± 0.2910	9.2167 ± 0.9506	0.0000 ± 0.0000
0.800—0.850	50.8363 ± 7.9584	0.0000 ± 0.0000	0.4421 ± 0.1300	0.2058 ± 0.1455	6.7654 ± 0.8145	0.0000 ± 0.0000
0.850—0.900	19.8342 ± 6.1918	0.0000 ± 0.0000	0.3796 ± 0.1132	0.2058 ± 0.1455	3.7259 ± 0.6044	0.0000 ± 0.0000
0.900—0.950	22.8597 ± 5.7697	0.0000 ± 0.0000	0.2316 ± 0.0881	0.1029 ± 0.1029	1.6668 ± 0.4043	0.0000 ± 0.0000
0.950—1.000	10.9136 ± 3.8960	0.0000 ± 0.0000	0.1687 ± 0.0672	0.1029 ± 0.1029	0.9805 ± 0.3101	0.0000 ± 0.0000
1.000—1.050	14.0000 ± 3.7417	0.0000 ± 0.0000	0.0211 ± 0.0220	0.1029 ± 0.1029	0.5883 ± 0.2402	0.0000 ± 0.0000
1.050—1.100	3.0000 ± 1.7321	0.0000 ± 0.0000	0.0000 ± 0.0000	0.0000 ± 0.0000	0.0000 ± 0.0000	0.0000 ± 0.0000
1.100—1.150	3.9807 ± 2.4575	0.0000 ± 0.0000	0.0000 ± 0.0000	0.0000 ± 0.0000	0.0000 ± 0.0000	0.0000 ± 0.0000
1.150—1.200	-1.0670 ± 1.0674	0.0000 ± 0.0000	0.0000 ± 0.0000	0.0000 ± 0.0000	0.0000 ± 0.0000	0.0000 ± 0.0000
1.200—2.000	0.0000 ± 0.0000	0.0000 ± 0.0000	0.0000 ± 0.0000	0.2058 ± 0.1455	0.0000 ± 0.0000	0.0000 ± 0.0000

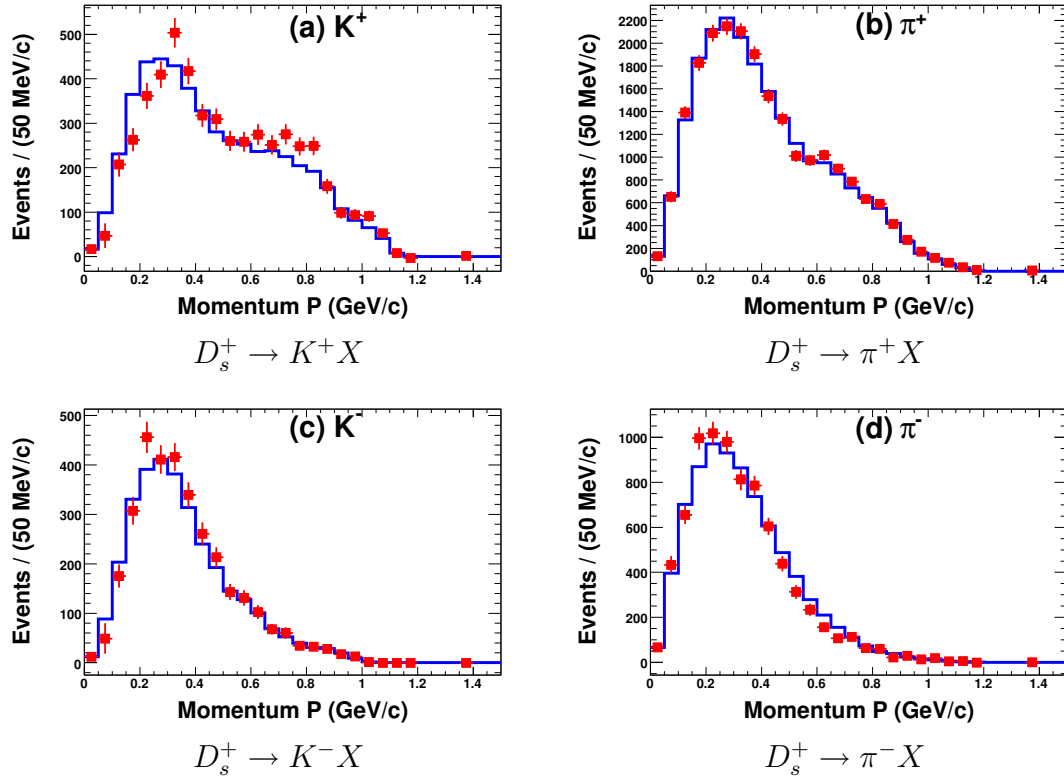


Figure 3.43: Charged kaon and pion laboratory momentum spectra after background subtractions and efficiency corrections: (a) $D_s^+ \rightarrow K^+ X$, (b) $D_s^+ \rightarrow \pi^+ X$, (c) $D_s^+ \rightarrow K^- X$, and (d) $D_s^+ \rightarrow \pi^- X$. Charge conjugate modes have been included on these plots. The points are obtained from data and solid line indicates the Monte Carlo after tuning. Good agreement between data and tuned Monte Carlo is found. Monte Carlo is normalized to data based on tag yield.

and then apply the PID efficiency and tracking efficiency corrections as a function of lab momentum. There is a 50 MeV/c minimum momentum cut for our tracks. We estimate the number of tracks with momentum lower than 50 MeV/c by using Monte Carlo. The lab momentum spectra are obtained by projecting the yield matrix to p bins. Obtained momentum spectra are compared to MC in Fig. 3.43.

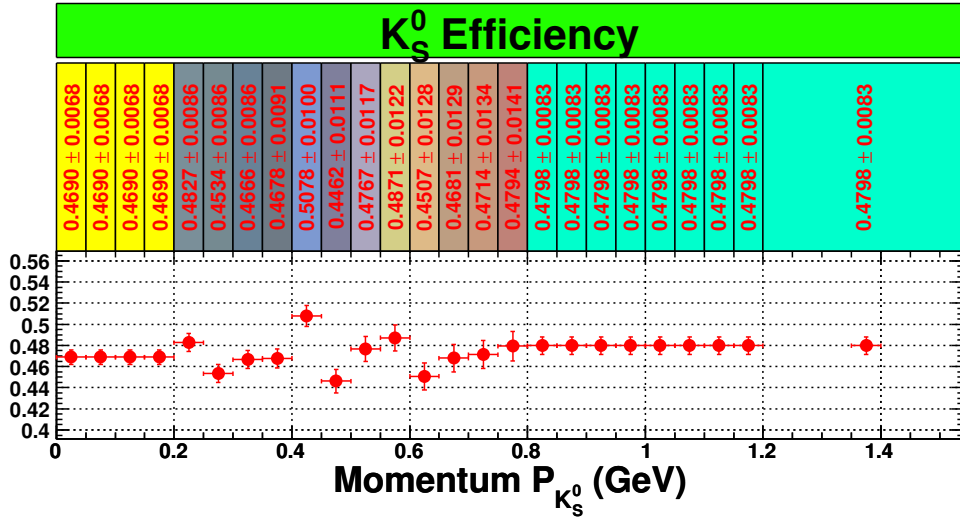


Figure 3.44: K_S^0 reconstruction efficiency. The corresponding number for each point is shown on the top of the plot. The colorful background of the number indicate how to define the momentum bin. The bins with same color have been merged into a big bin.

3.5 $D_s^+ \rightarrow K_S^0/\pi^0/\eta/\eta'/\phi/\omega/f_0(980)$ X Branching Fractions

3.5.1 $D_s^+ \rightarrow K_S^0 X$ Branching Fraction

The K_S^0 yield is extracted by defining a signal region and sideband regions in the invariant mass distribution of the pion pair. The sideband scaling factor is obtained from Monte Carlo. The momentum-dependent efficiency is shown in Fig. 3.44. The momentum spectra before the efficiency correction (left plot) and after the efficiency correction (right plot) are shown in Fig. 3.45.

3.5.2 $D_s^+ \rightarrow \pi^0 X$ Branching Fraction

We apply sideband subtraction on π^0 invariant mass distribution to extract π^0 yield. Unfortunately, Monte Carlo studies show that the background shape of low momentum π^0 is not flat. We utilize generic Monte Carlo samples to get the sideband scaling factor for π^0 invariant mass distribution, and apply this scaling factor to

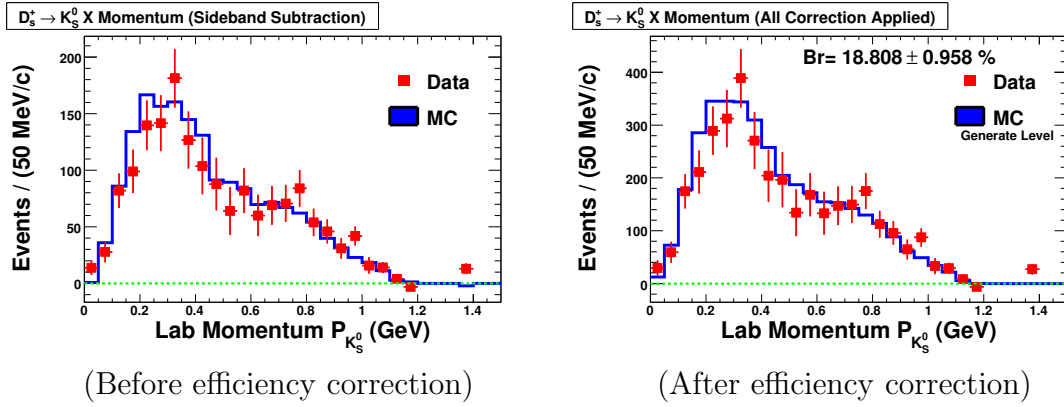


Figure 3.45: K_S^0 momentum spectra. Left plot is before efficiency correction and right one is after efficiency correction. Red rectangle points are obtained from data and blue histogram is Monte Carlo. The branching fraction shown on the right plot includes only statistical error.

data. Fig. 3.46 and Fig. 3.47 show the comparison plots between data and Monte Carlo in different π^0 momentum bins. Fig. 3.48 shows the π^0 invariant mass distribution in whole momentum region. The sideband scaling factors are shown in Fig. 3.49.

We treat π^0 from K_S^0 decay as a background for the decay $D_s^+ \rightarrow \pi^0 X$ as shown in Fig. 3.50 and subtract it based on K_S^0 yield. The momentum-dependent π^0 efficiency is shown in Fig. 3.51. The π^0 momentum spectra before the efficiency correction (left plot) and after the efficiency correction (right plot) are shown in Fig. 3.52.

3.5.3 $D_s^+ \rightarrow \eta X$ Branching Fraction

The η efficiency is constant above 300 MeV/ c and increase slowly below [36]. To measure the inclusive branching fractions, we define two η momentum bins. The low momentum bin is below 300 MeV/ c , and the other one is above 300 MeV/ c .

In Fig. 3.53, we show the two-photon invariant mass in two momentum intervals from both D_s tag signal and sideband regions respectively. The η yields from either D_s tag signal region or sideband region are extracted by fits to a Crystal Ball [37] signal function, to account for the low mass tail and a second degree polynomial background function. For the signal D_s region, the two tail part parameters of Crystal Ball function are fixed to the values obtained by Monte Carlo simulation,

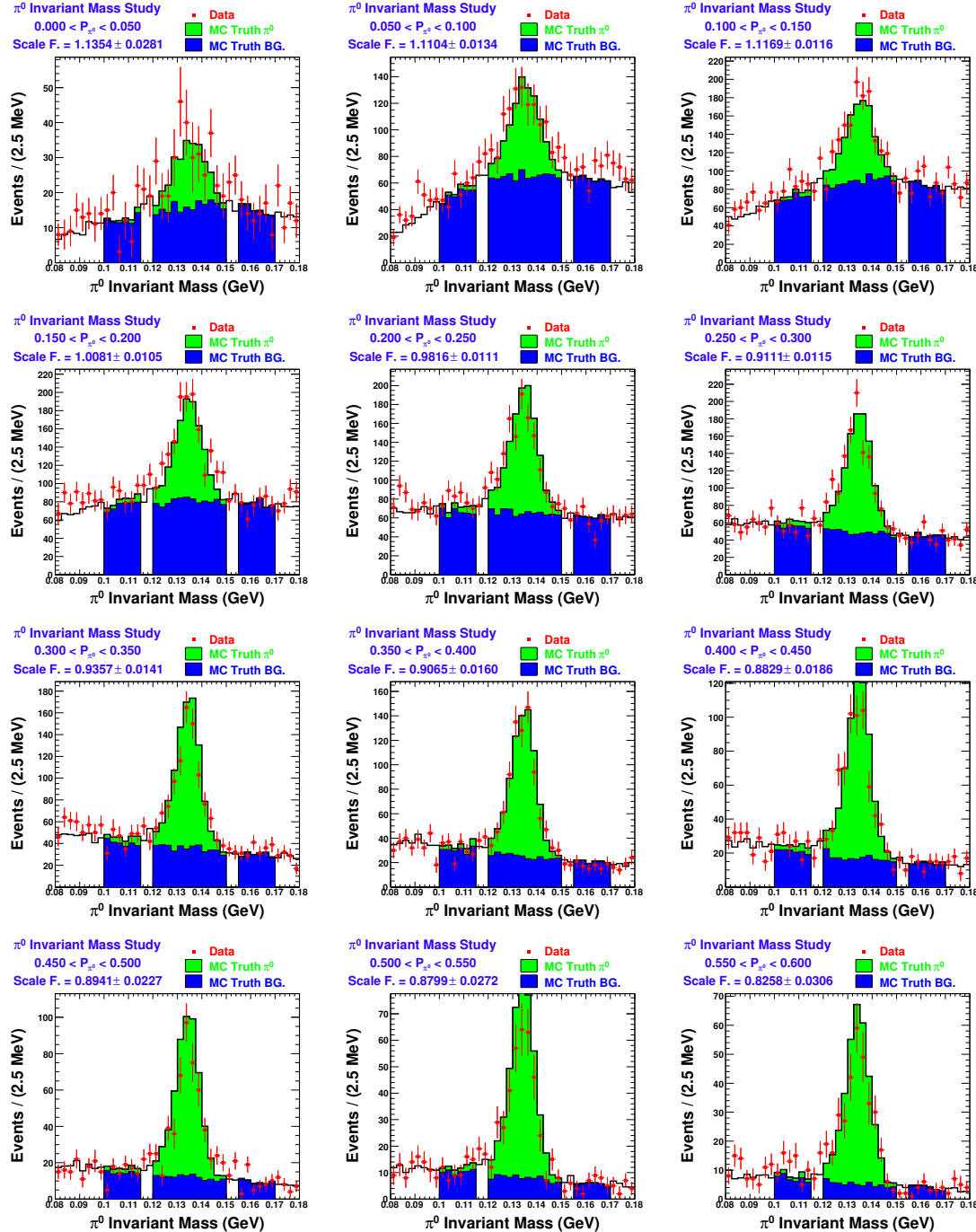


Figure 3.46: π^0 invariant mass distributions, for π^0 momenta from 0.0 to 0.6 GeV/c .

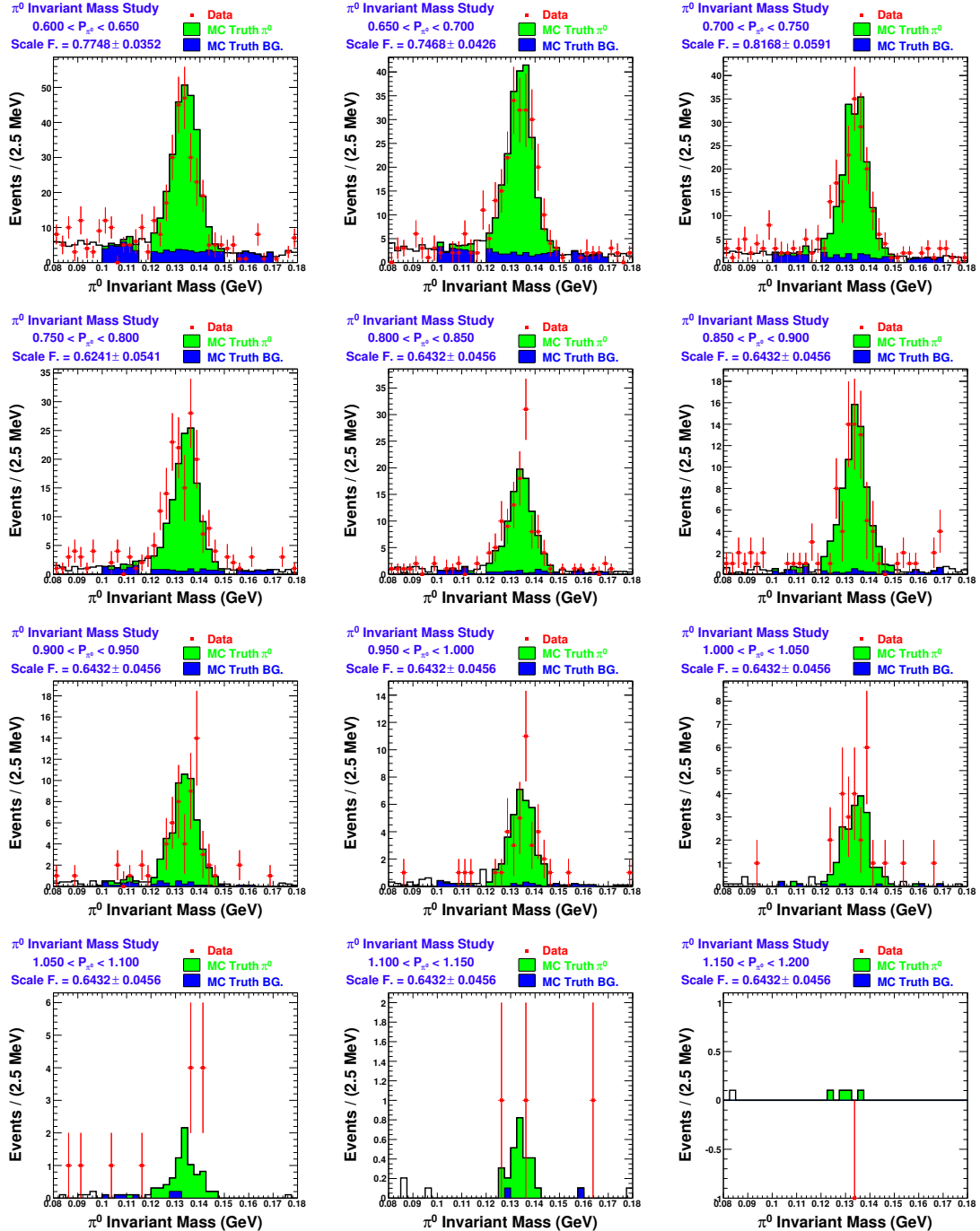


Figure 3.47: π^0 invariant mass distributions, for π^0 momenta from 0.6 to 1.2 GeV/c .

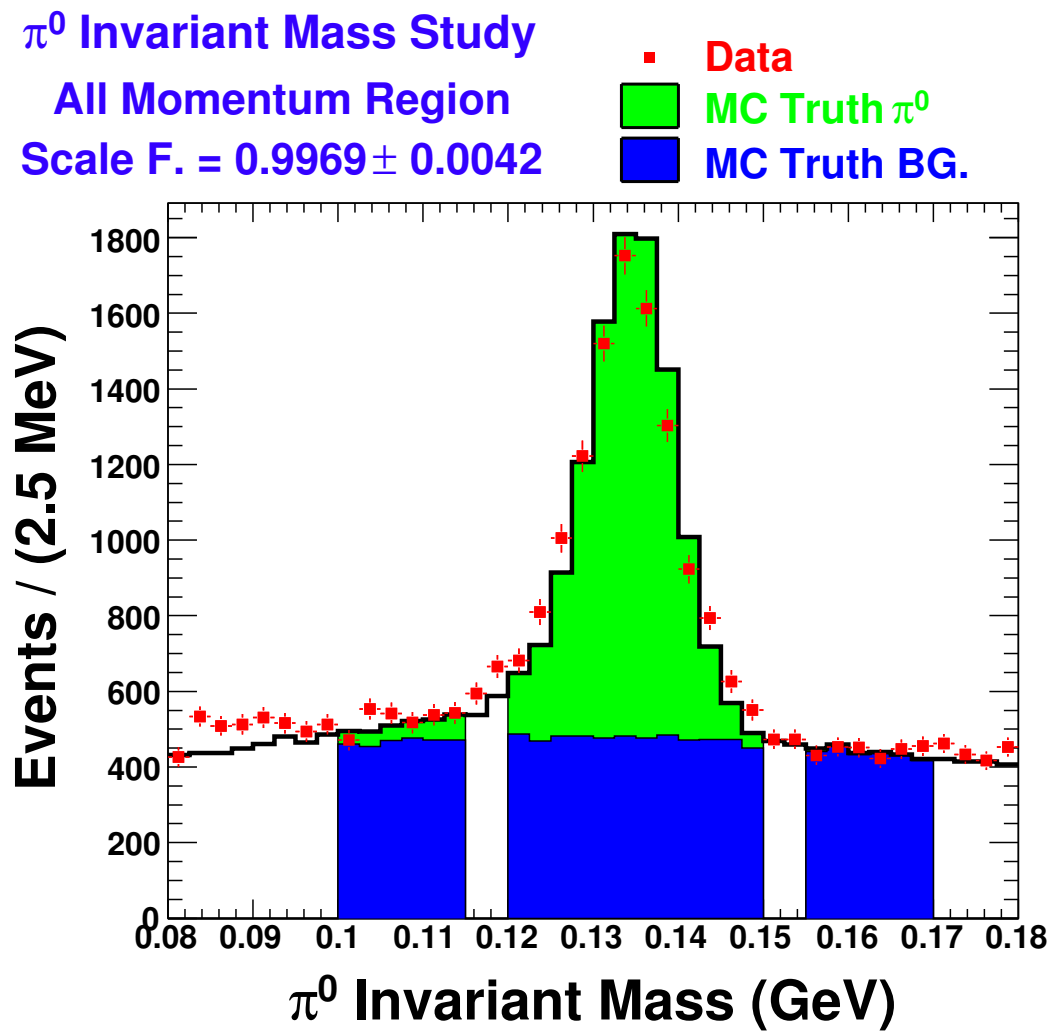


Figure 3.48: π^0 invariant mass distribution, summed over all momenta.

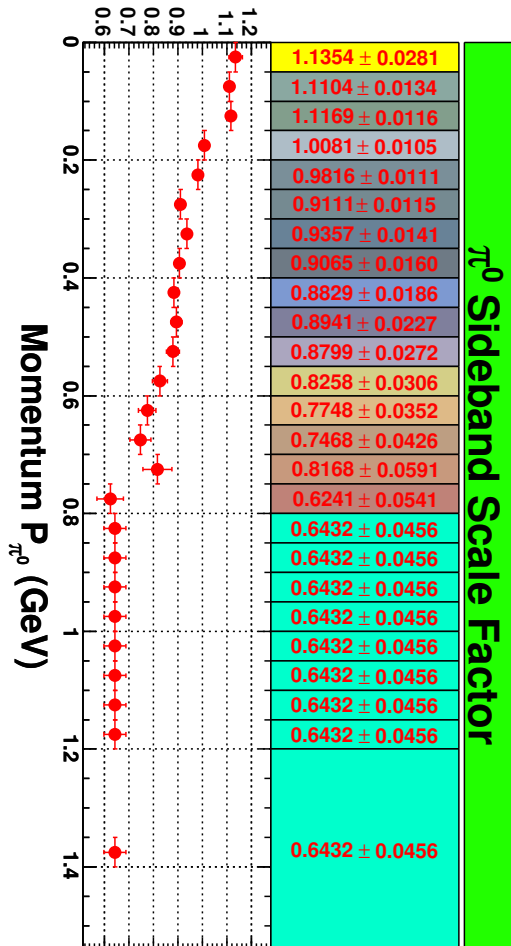


Figure 3.49: π^0 invariant mass distribution sideband scaling factor.

$D_s^+ \rightarrow \pi^0 \times$ Background Study

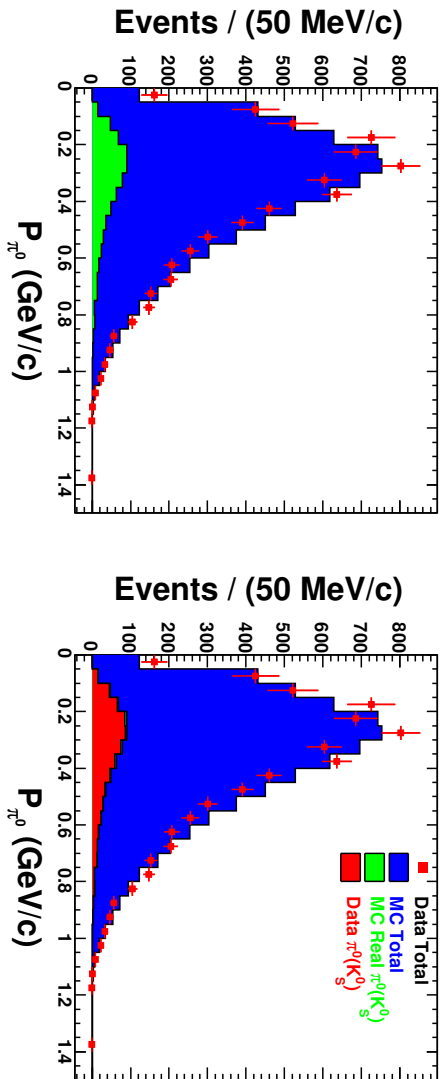


Figure 3.50: Background study for true π^0 but from K_S^0 decay.

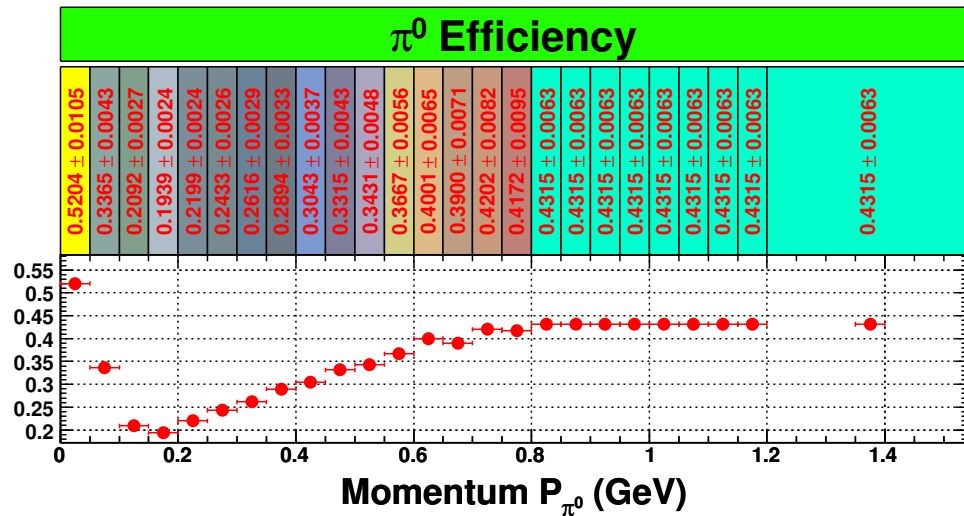


Figure 3.51: π^0 reconstruction efficiency.

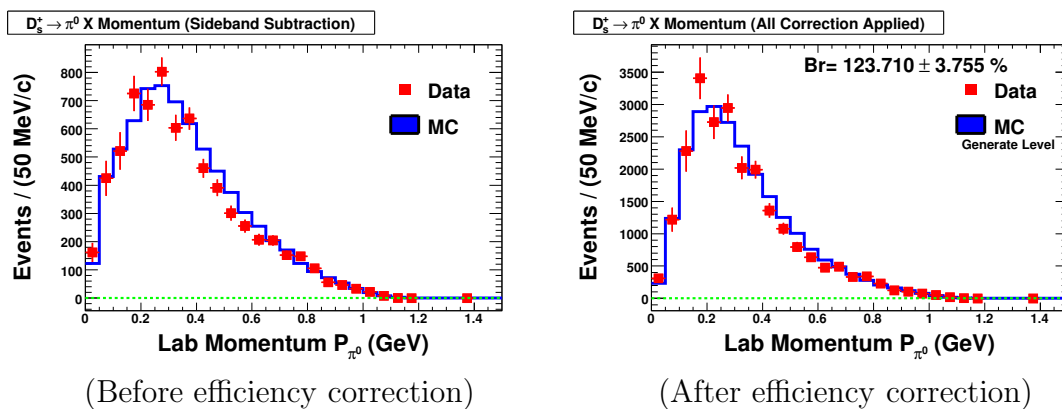


Figure 3.52: π^0 momentum spectra. Left plot is before efficiency correction and right one is after efficiency correction. Red rectangle points are obtained from data and blue histogram is Monte Carlo. The branching fraction shown on the right plot includes only statistical error.

the mean and the width are allowed to float. These values of parameters are then used for the D_s sideband regions. The yields from D_s tag signal and sideband regions, the sideband subtracted yield, the detection efficiency and the branching fractions in each momentum interval are given in Fig. 3.53.

3.5.4 $D_s^+ \rightarrow \eta' X$ Branching Fraction

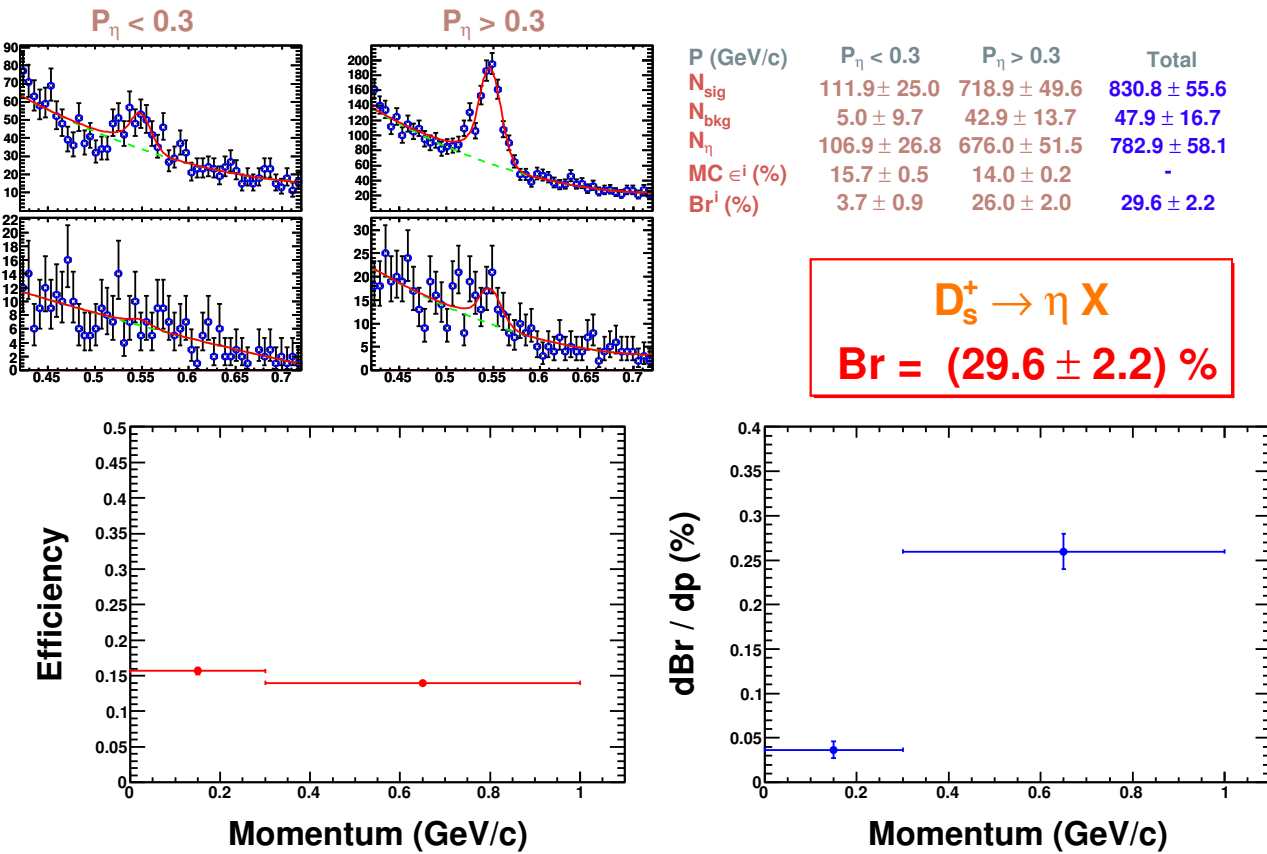
The η' has constant efficiency with momentum [36], so we don't need to separate the η' sample into different momentum intervals. The distributions of $\eta\pi^+\pi^- - \eta$ mass difference in the tag signal and sideband regions are shown in Fig. 3.54 and fitted to a Gaussian signal shape and a polynomial background where the signal shape parameters are allowed to float for the signal distribution and fixed to the values obtained there in the sideband region. The detailed yield numbers, reconstruction efficiency of η' and branching fraction are shown in Fig. 3.54.

3.5.5 $D_s^+ \rightarrow \phi X$ Branching Fraction

The ϕ efficiency, on the other hand, decreases drastically with decreasing momentum [36] and therefore we separate the ϕ sample into several momentum regions. The decrease in the ϕ efficiency is understood however from the fact that as the ϕ becomes less energetic, it becomes more probable that it decays to slow kaons (with momentum below 0.2 GeV/c), and these particles have very low detection efficiencies as they have large energy losses in the beam pipe and detector.

The Fig. 3.55 shows the K^+K^- invariant mass in five different momentum intervals from both signal and sideband regions for D_s tag respectively. The signals are fit with a sum of two Gaussian shapes and the background is fit to the second degree polynomial. The signal shapes are fixed to the values obtained by Monte Carlo simulation. The signal, background, and background subtracted yields, the detection efficiencies, and the branching fractions in each momentum interval are given in Fig. 3.55. The momentum distributions of the branching fractions are also shown in Fig. 3.55.

In the lowest momentum interval, $0.0 < p < 0.2$ GeV/c, the detection efficiency of ϕ is very small due to the tracking detection limit where two low momentum kaon tracks need to be found. We estimate the partial branching fraction in the


 Figure 3.53: $D_s^+ \rightarrow \eta X$ decay study.

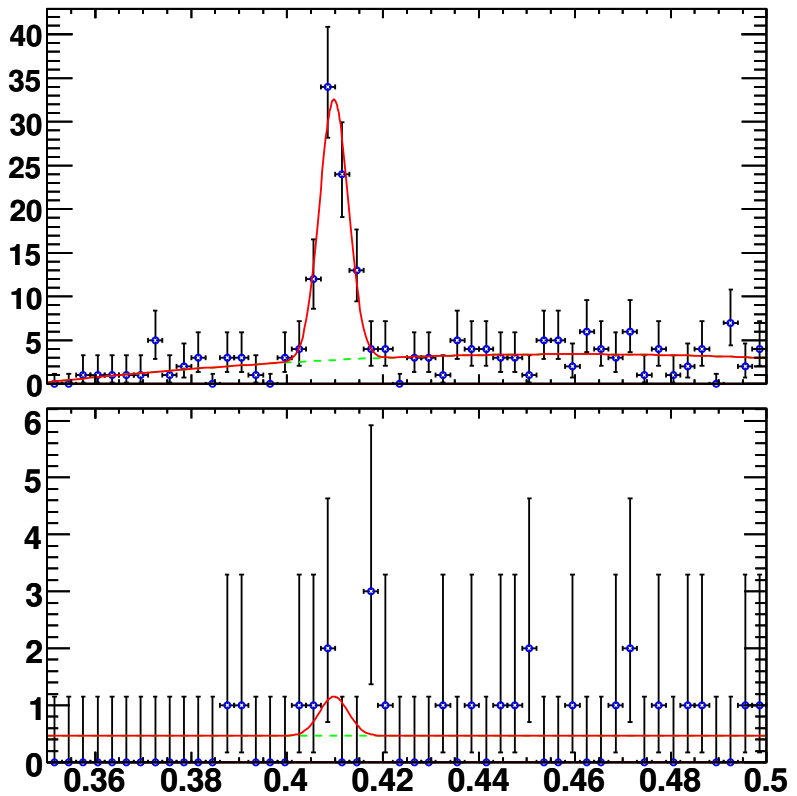


Figure 3.54: $D_s^+ \rightarrow \eta' X$ decay study..

N_{sig}	74.7 ± 9.8
N_{bkg}	1.7 ± 2.0
$N_{\eta'}$	73.0 ± 10.0
$\text{MC} \in (\%)$	3.52 ± 0.14
$\text{Br} (\%)$	11.1 ± 1.6

$D_s^+ \rightarrow \eta' X$
 $\text{Br} = (11.1 \pm 1.6) \%$

$0.0 < p < 0.2$ GeV/ c interval in a different way. Here, we modeled the partial branching ratio by taking the fraction of ϕ yield in the first momentum interval to ϕ yield in the rest of the momentum intervals in data to be equal to the same fraction from the Monte Carlo simulation, and assign an error equal to its value.

3.5.6 $D_s^+ \rightarrow \omega X$ Branching Fraction

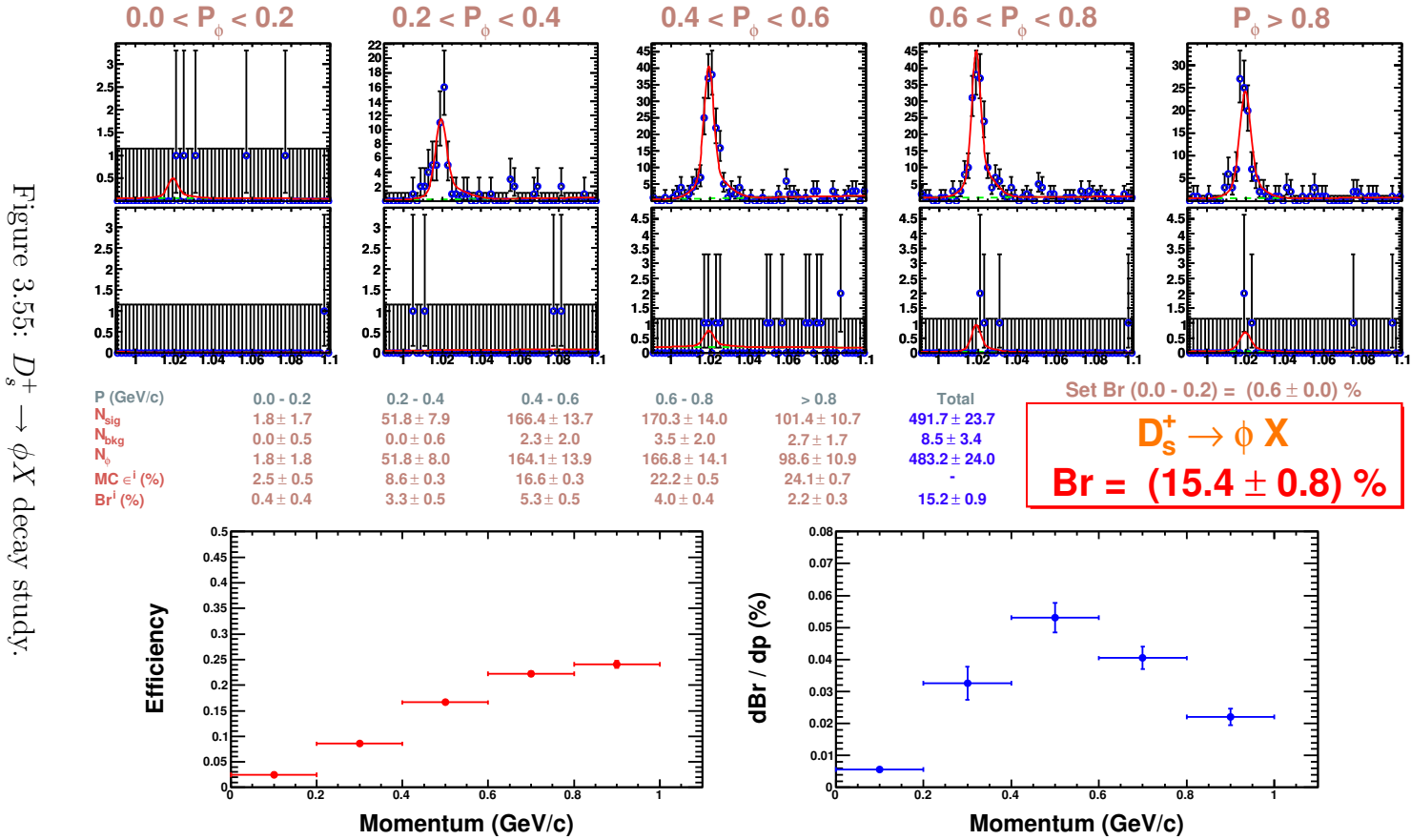
The ω candidates are reconstructed in the $\omega \rightarrow \pi^+ \pi^- \pi^0$ mode. Fig. 3.56 shows the details of $D_s^+ \rightarrow \omega X$ decay study. We fit the $\pi^+ \pi^- \pi^0$ invariant mass distribution to a Crystal Ball signal shape and a polynomial background. The Monte Carlo efficiency, fit yield, and branching fraction are also shown in Fig. 3.56.

3.5.7 $D_s^+ \rightarrow f_0(980)X$ Branching Fraction

We form $f_0(980)$ candidates using $\pi^+ \pi^-$ pairs, $f_0(980) \rightarrow \pi^+ \pi^-$ as shown in Fig. 3.57. The pions are subject to the standard pion PID requirements. We find no significant evidence for the decay $D_s^+ \rightarrow f_0(980)X$. We fit the invariant mass distribution of $\pi^+ \pi^-$ pairs to the Gaussian signal plus second-degree polynomial background functions to obtain a yield of 30 ± 47 (corresponding branching fraction is 0.35%). The 90% confidence level upper limit is $\mathcal{B}(D_s^+ \rightarrow f_0(980)X) \mathcal{B}(f_0(980) \rightarrow \pi^+ \pi^-) < 1.1\%$ (statistical uncertainty only). Systematic errors are 6.8% for the efficiency estimation, 5.6% for the signal and background shape parameters, and other smaller errors, leading to a combined relative systematic error of 8.8%. We conservatively increase the upper limit by 1.28 times the combined systematic errors, giving a upper limit, including systematic errors, of $\mathcal{B}(D_s^+ \rightarrow f_0(980)X) \mathcal{B}(f_0(980) \rightarrow \pi^+ \pi^-) < 1.3\%$.

3.6 Inclusive Yields of D_s^+ into Two Kaons

We also measure the inclusive yields of D_s^+ mesons into two kaons. After a tag is identified, we search for the best kaon pair, based on particle identification likelihood or K_S^0 mass, per mode recoiling against the tag. The kaon pair modes can be any of $K_S^0 K_S^0$, $K_S^0 K^+$, $K_S^0 K^-$, $K^+ K^-$, $K^+ K^+$, or $K^- K^-$. For $D_s^+ \rightarrow K_S^0 K^+ X$ and $D_s^+ \rightarrow K_S^0 K^- X$, we apply the sideband subtraction on K_S^0 candidate invariant mass distribution to remove the nonresonant decay background and get the signal


 Figure 3.55: $D_s^+ \rightarrow \phi X$ decay study.

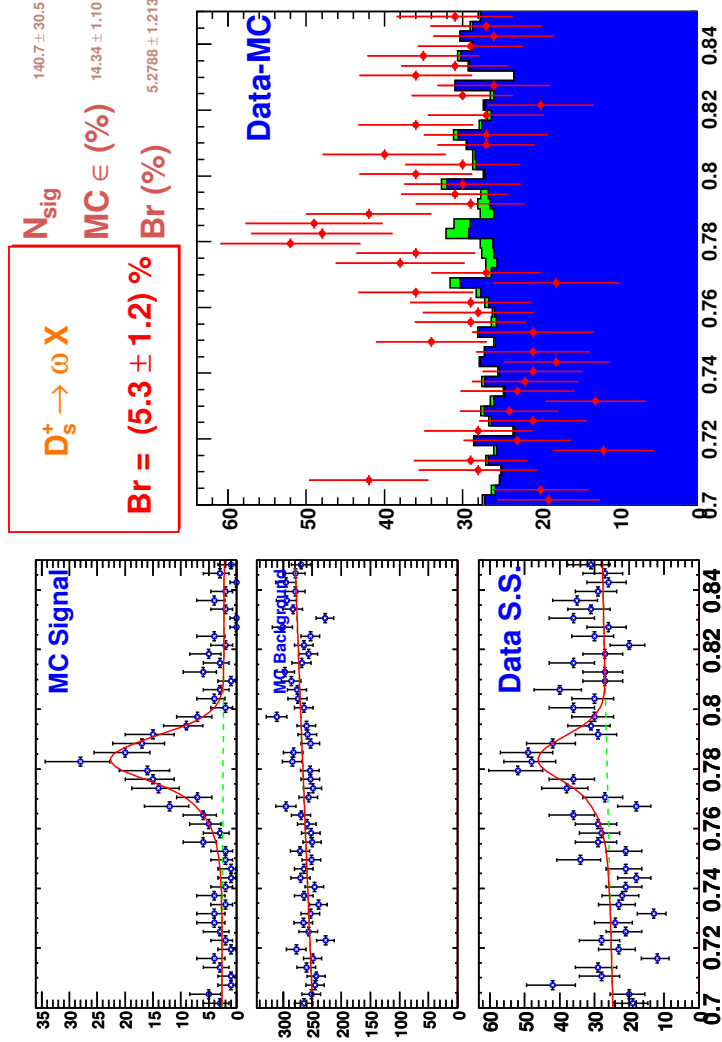
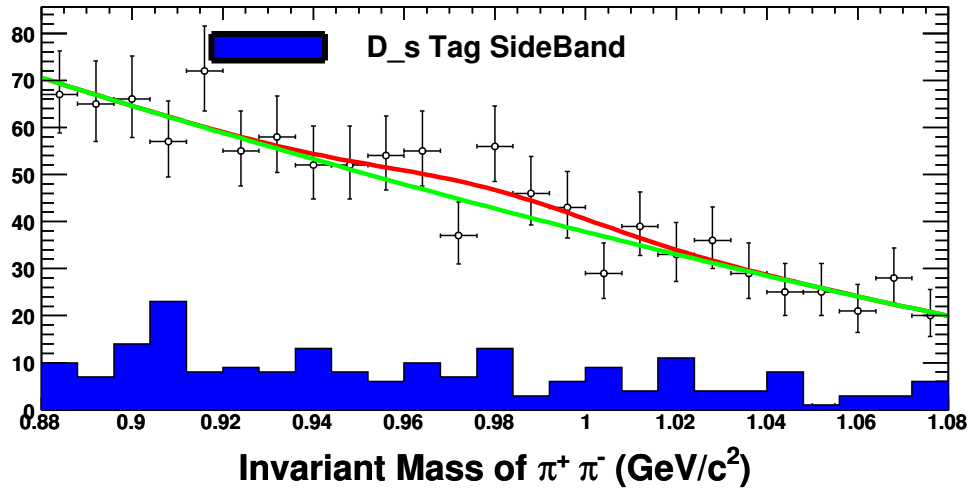
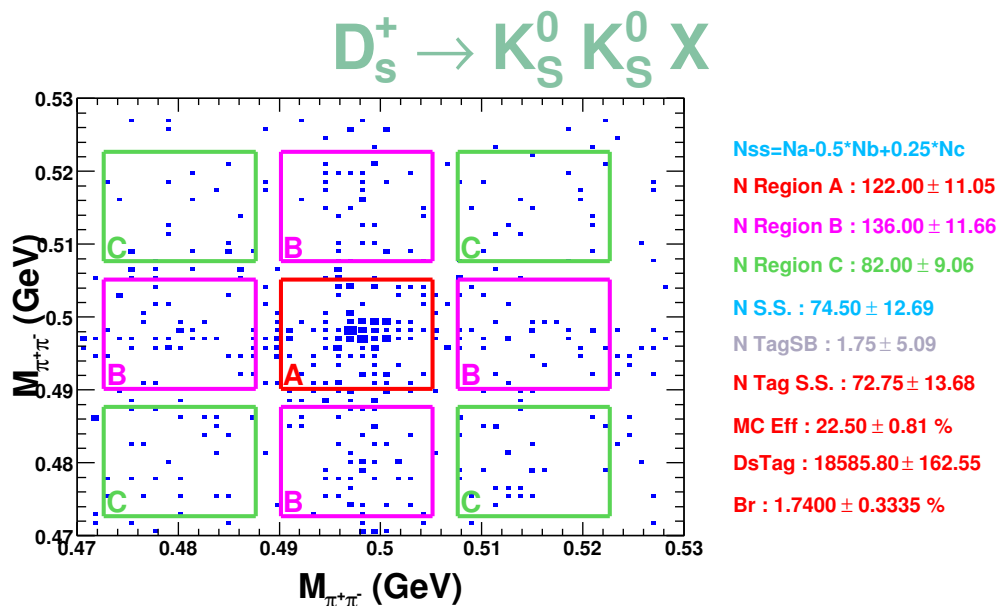
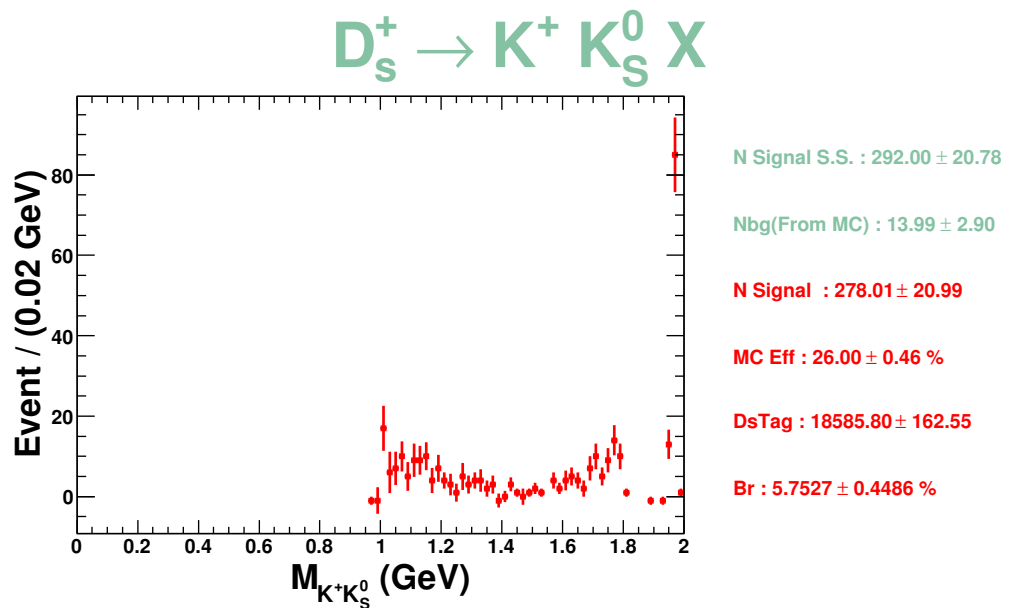
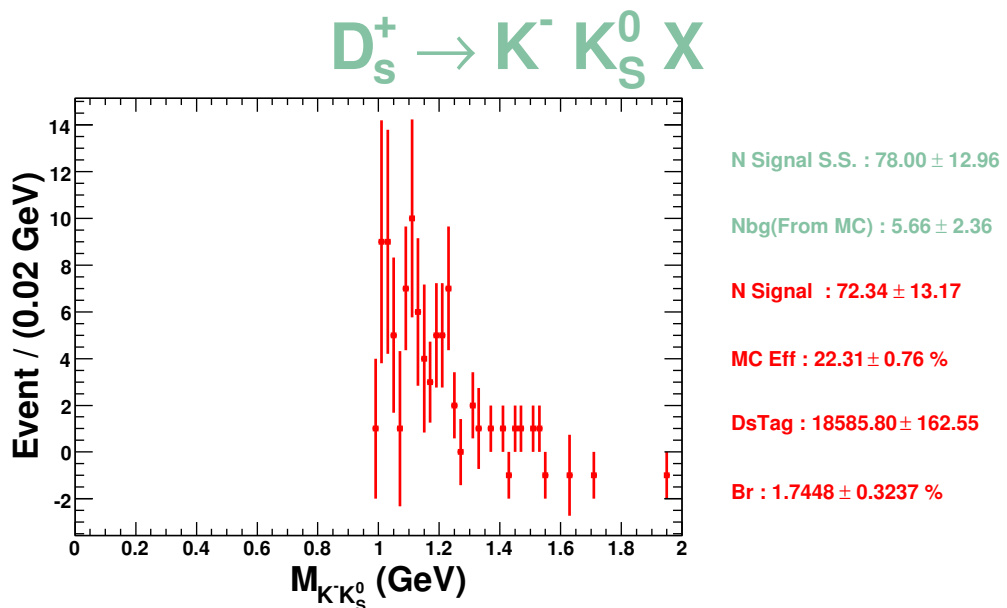
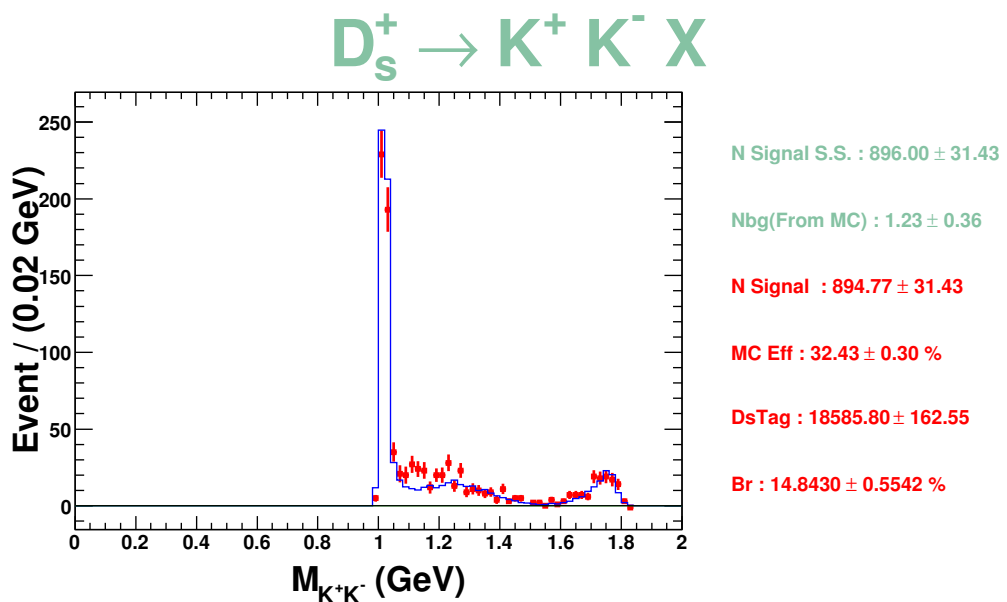


Figure 3.56: $D_s^+ \rightarrow \omega X$ decay study. MC signal plot is from the generic MC sample with ω on the signal side. MC background plot is from the generic MC sample without ω on the signal side. Data S.S. is the data plot after D_s tag sideband subtraction. We get signal and background shape parameters from the fits to MC signal and MC background respectively and apply them in the fit to data. The data-MC comparison is shown on Data-MC plot, Monte Carlo is normalized to data based on tag yield.

Figure 3.57: $D_s^+ \rightarrow f_0(980)X$ decay study.

yields. The $D_s^+ \rightarrow K_S^0 K_S^0 X$ signal yield is extracted by defining a signal region on the scatter plot for the two K_S^0 candidate invariant masses. In order to account for $D_s^+ \rightarrow K_S^0 \pi^+ \pi^- X$ and $D_s^+ \rightarrow \pi^+ \pi^- \pi^+ \pi^- X$ entering into the signal region of $D_s^+ \rightarrow K_S^0 K_S^0 X$, we perform a background subtraction which has two components. For all the two charged kaons modes, we count the event numbers where at least two charged kaons are found recoiling against the tag. In order to subtract the combinatoric background, we repeat the same procedure for each mode where the tags are selected from $M(D_s)$ sidebands. The other possible backgrounds from general D_s decay are studied using Monte Carlo and found to be negligible. Fig. 3.58 shows the scatter plot for the two K_S^0 candidate invariant masses. The invariant mass distributions of two kaons are shown in Fig. 3.59, Fig. 3.60, Fig. 3.61, Fig. 3.62, and Fig. 3.63 for each mode. Detailed numbers that are used to calculate inclusive branching fractions are shown on these plots. Branching fractions shown here include only statistical error. Table 3.8 lists the observed numbers, estimated background numbers, and signal yields for all inclusive two kaon modes.

Figure 3.58: $D_s^+ \rightarrow K_S^0 K_S^0 X$ decay study.Figure 3.59: $D_s^+ \rightarrow K_S^0 K^+ X$ decay study.

Figure 3.60: $D_s^+ \rightarrow K_S^0 K^- X$ decay study.Figure 3.61: $D_s^+ \rightarrow K^+ K^- X$ decay study.

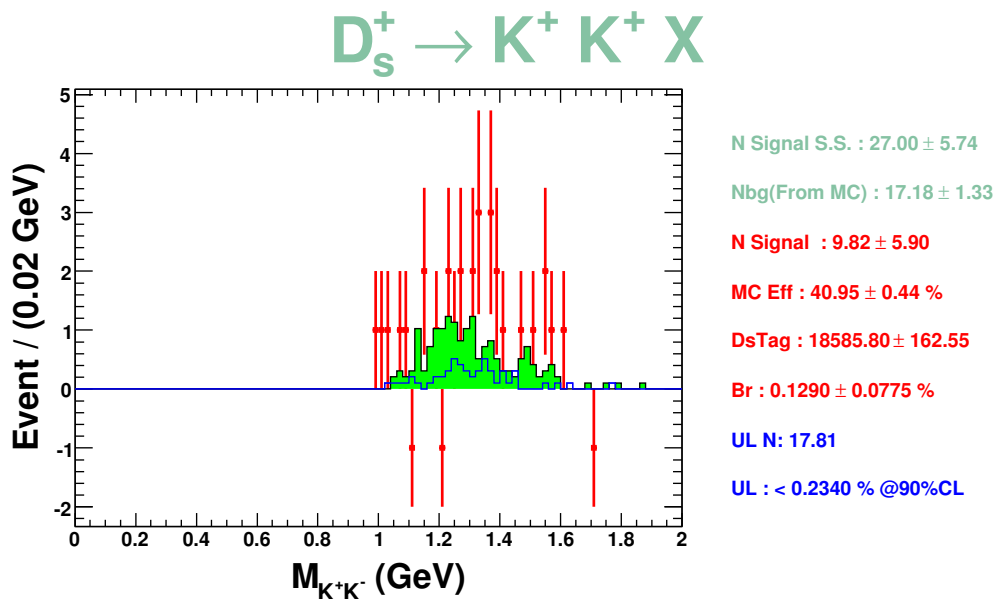
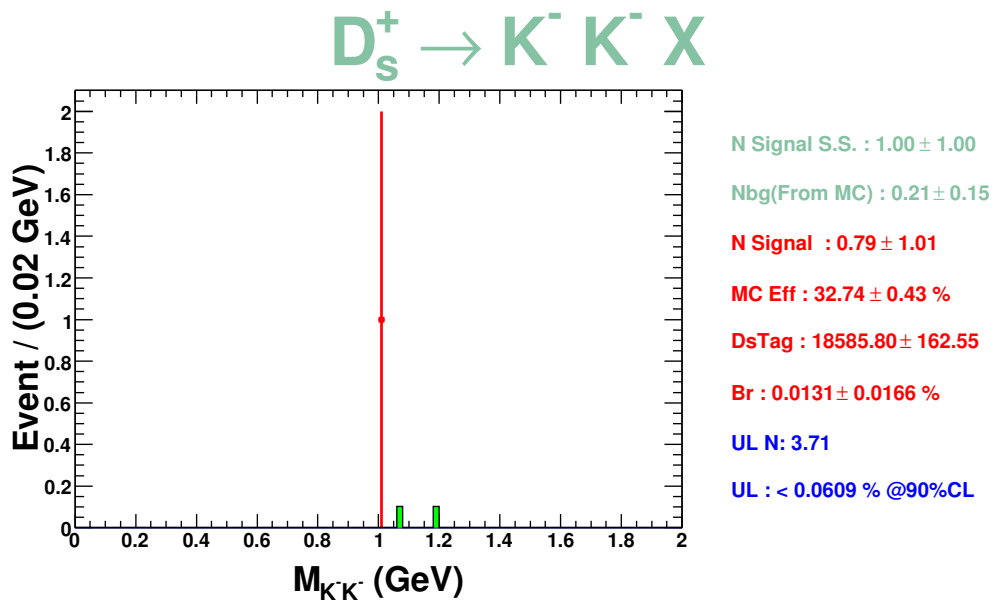
Figure 3.62: $D_s^+ \rightarrow K^+ K^+ X$ decay study.Figure 3.63: $D_s^+ \rightarrow K^- K^- X$ decay study.

Table 3.8: The observed numbers, estimated background numbers, and signal yields for all inclusive two kaon modes.

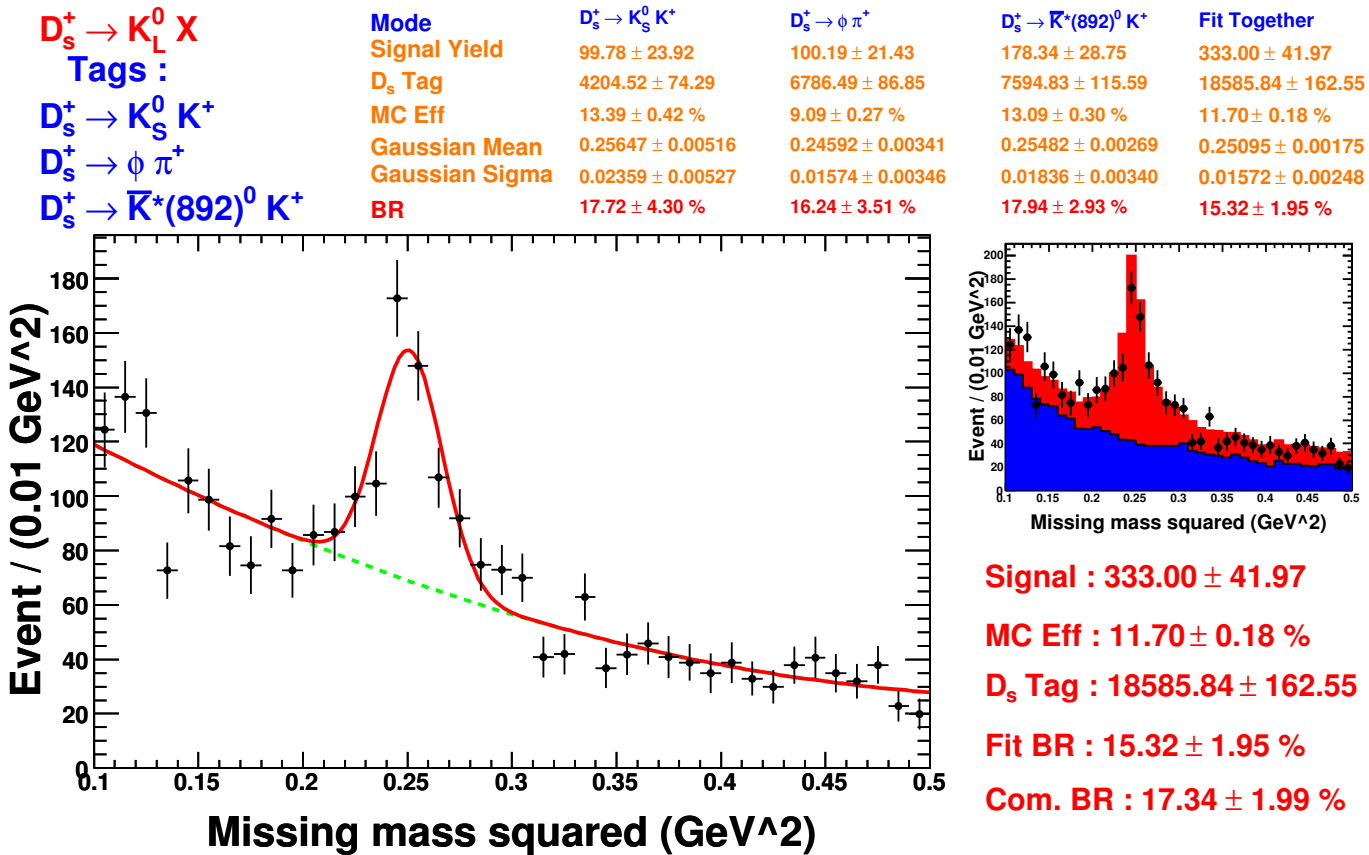
Mode	N_{obv}			N_{bkg}		Yield			
$D_s^+ \rightarrow K_S^0 K_S^0 X$	75	\pm	13	2	\pm	5	73	\pm	14
$D_s^+ \rightarrow K_S^0 K^+ X$	292	\pm	21	14	\pm	3	278	\pm	21
$D_s^+ \rightarrow K_S^0 K^- X$	78	\pm	13	6	\pm	2	72	\pm	13
$D_s^+ \rightarrow K^+ K^- X$	896	\pm	31	1.2	\pm	0.4	895	\pm	31
$D_s^+ \rightarrow K^+ K^+ X$	27	\pm	6	17	\pm	1	10	\pm	6
$D_s^+ \rightarrow K^- K^- X$	1	\pm	1	0.2	\pm	0.2	0.8	\pm	1.0

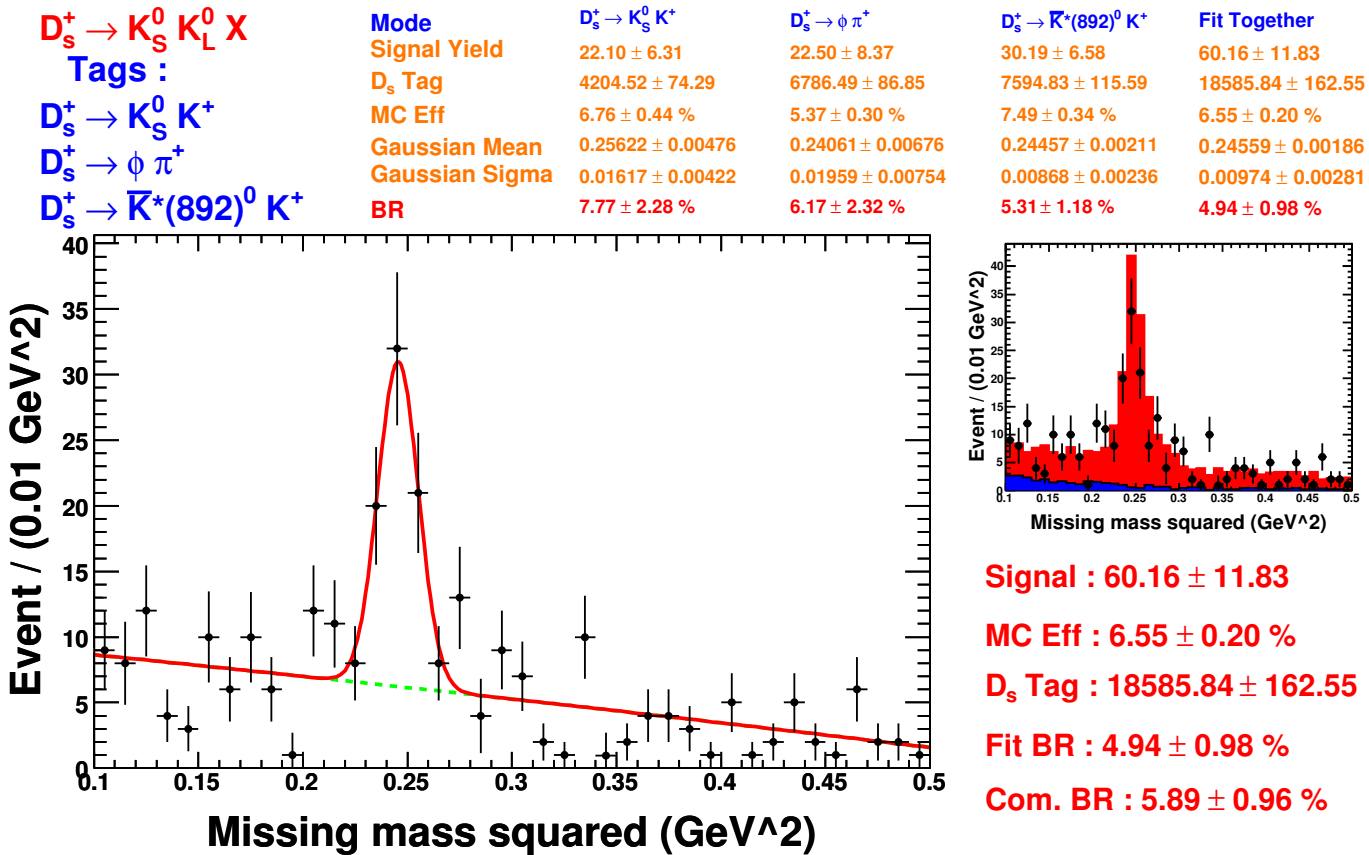
3.7 D_s^+ Inclusive K_L^0 Decays

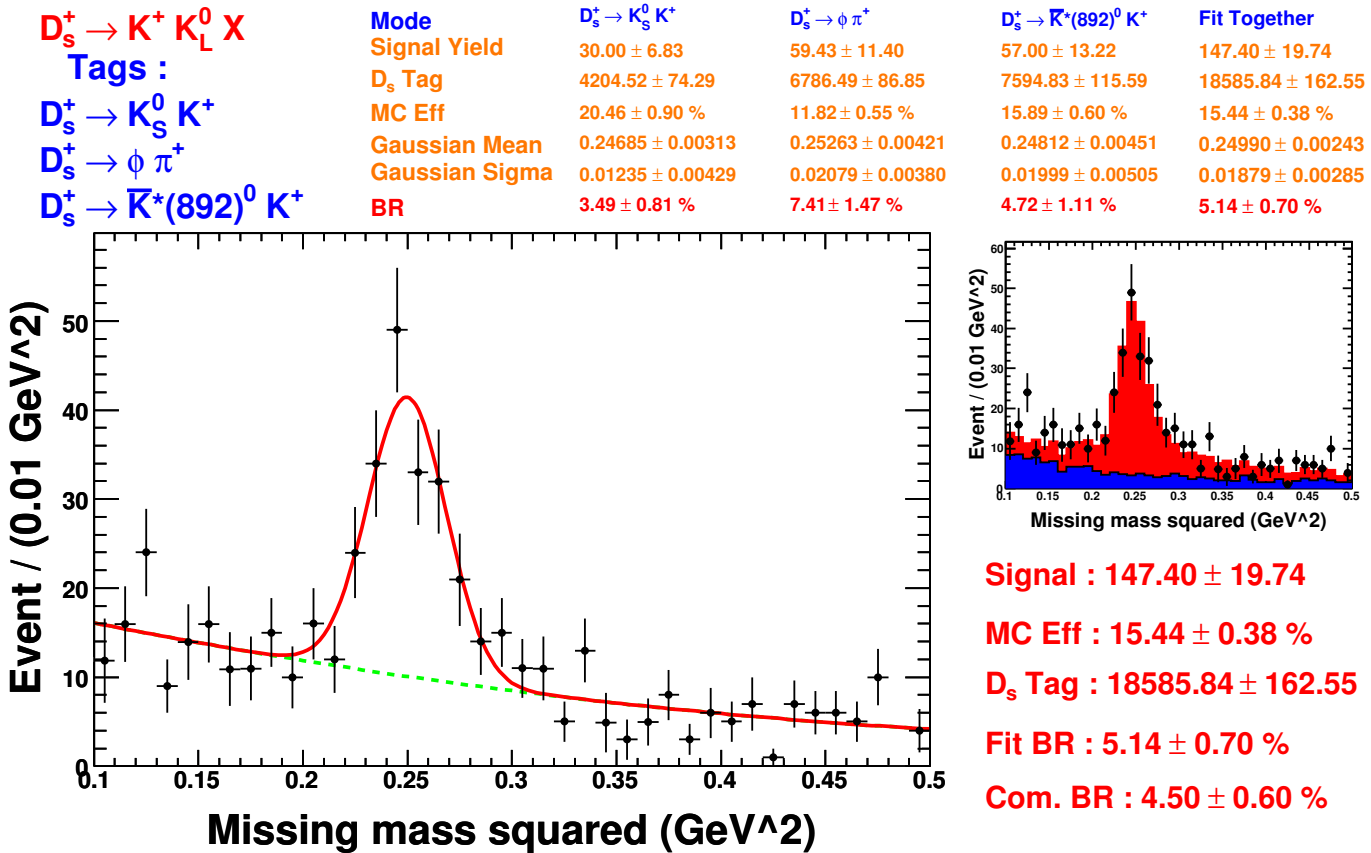
The double-tagging technique allows us to measure the inclusive yields for the decay $D_s^+ \rightarrow K_L^0 X$ without directly detecting the K_L^0 . Instead, we reconstruct all particles in the event except the single K_L^0 and infer the presence of a K_L^0 from the missing four-momentum. Our signal is a peak in the missing mass squared distribution at the K_L^0 mass squared. Similar missing-mass-squared techniques are used for $D_s^+ \rightarrow K_L^0 K_S^0 X$, $D_s^+ \rightarrow K_L^0 K^+ X$, and $D_s^+ \rightarrow K_L^0 K^- X$ modes by requiring there must be a K_S^0 , K^+ , or K^- recoiling against the tag. Note that if the D_s decay contains two or more K_L^0 's, we do not find any K_L^0 . Due to the low statistics and large systematic uncertainties, we quote the inclusive K_L^0 results only as a check for K_S^0 . Detailed plots and results are shown in Fig. 3.64 ($D_s^+ \rightarrow K_L^0 X$), Fig. 3.65 ($D_s^+ \rightarrow K_L^0 K_S^0 X$), Fig. 3.66 ($D_s^+ \rightarrow K_L^0 K^+ X$), and Fig. 3.67 ($D_s^+ \rightarrow K_L^0 K^- X$). We fit missing mass squared distributions to Gaussian signal plus 2nd degree polynomial function to extract signal yields. The branching fractions shown on these plots include only statistical error.

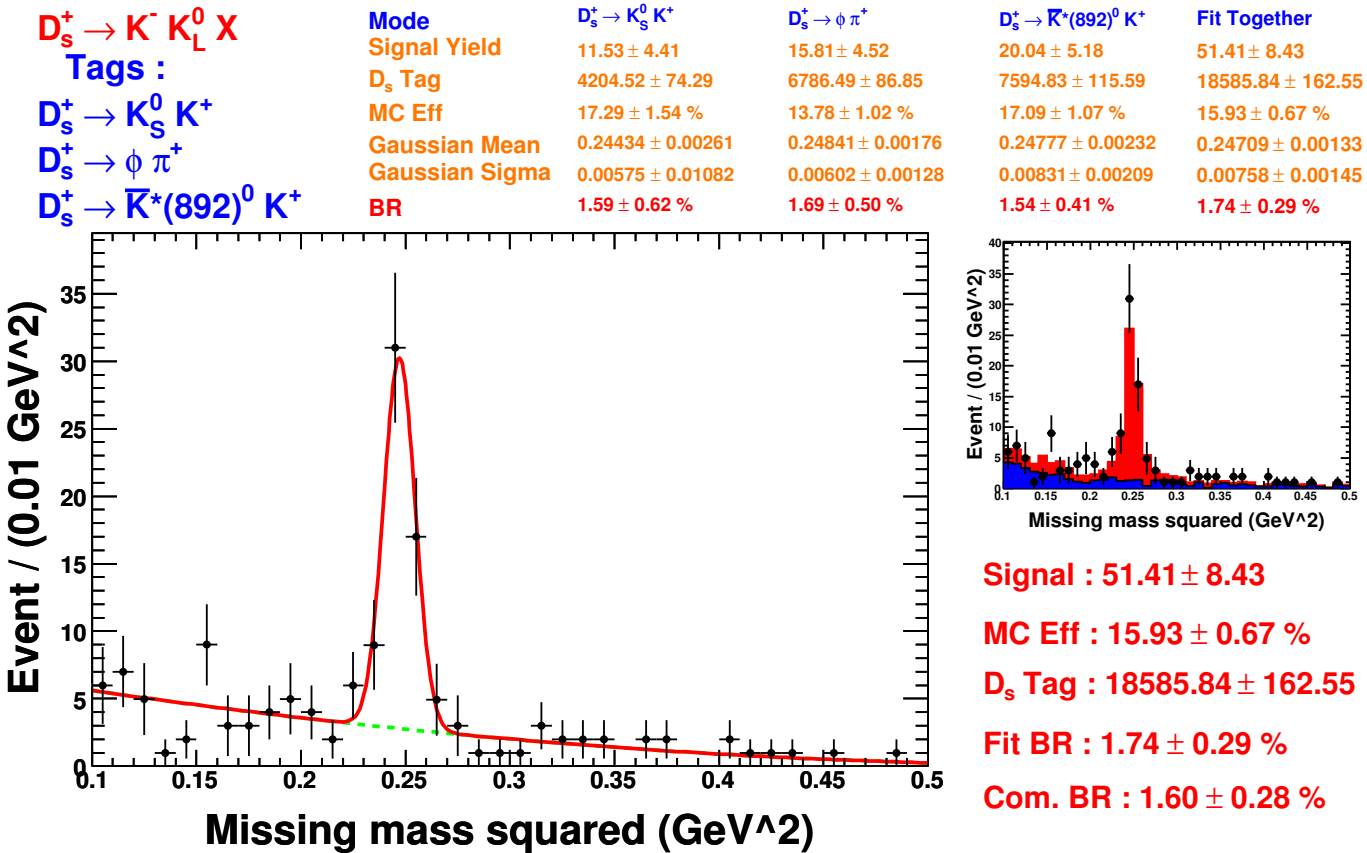
3.8 D_s^+ Inclusive $\eta\eta X$, $\eta\eta' X$, $\eta\phi X$ and $\eta\omega X$ Decays

We also search for the possible decay modes $D_s^+ \rightarrow \eta\eta X$, $D_s^+ \rightarrow \eta\eta' X$, $D_s^+ \rightarrow \eta\phi X$, and $D_s^+ \rightarrow \eta\omega X$ as shown in Fig. 3.68 ($D_s^+ \rightarrow \eta\eta X$), Fig. 3.69 ($D_s^+ \rightarrow \eta\eta' X$), Fig. 3.70 ($D_s^+ \rightarrow \eta\phi X$), and Fig. 3.71 ($D_s^+ \rightarrow \eta\omega X$). Signal yields are extracted by defining a signal region on the scatter plot of the η candidate invariant


 Figure 3.64: $D_s^+ \rightarrow K_L^0 X$ decay study.


 Figure 3.65: $D_s^+ \rightarrow K_L^0 K_S^0 X$ decay study.


 Figure 3.66: $D_s^+ \rightarrow K_L^0 K^+ X$ decay study.


 Figure 3.67: $D_s^+ \rightarrow K_L^0 K^- X$ decay study.

mass vs. the other η (or η' , ϕ , ω) candidate invariant mass. In order to account for non-resonance background events entering into the signal region, we perform a background subtraction which has two components. Scatter plots from signal Monte Carlo sample, generic Monte Carlo sample, and data are shown on these figures, up-left plot is from signal Monte Carlo sample, up-right plot is generic Monte Carlo, down-left plot is from D_s tag signal region and down-right plot is from D_s tag sideband region. No significant evidence is found in any of these modes. We set the 90% confidence level upper limit for each mode.

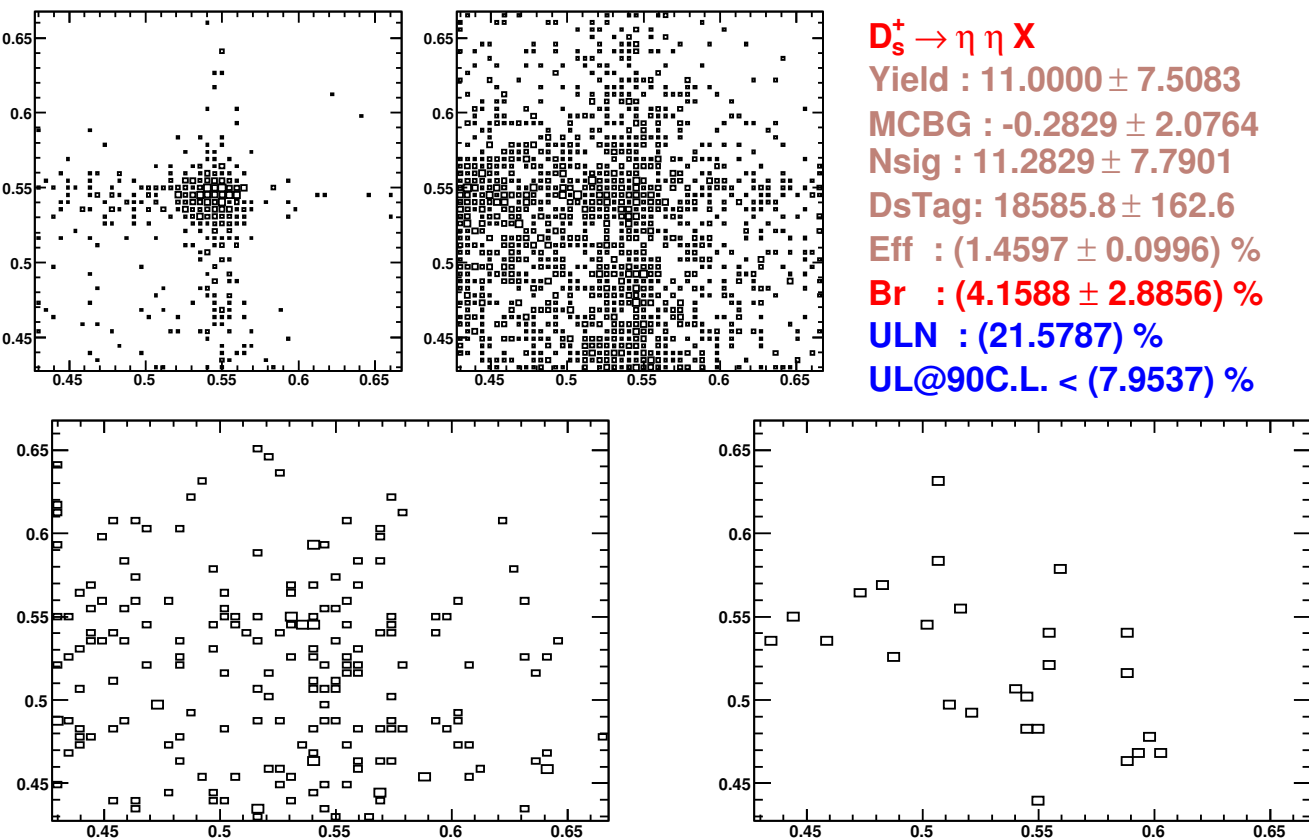


Figure 3.68: $D_s^+ \rightarrow \eta\eta X$ decay study.

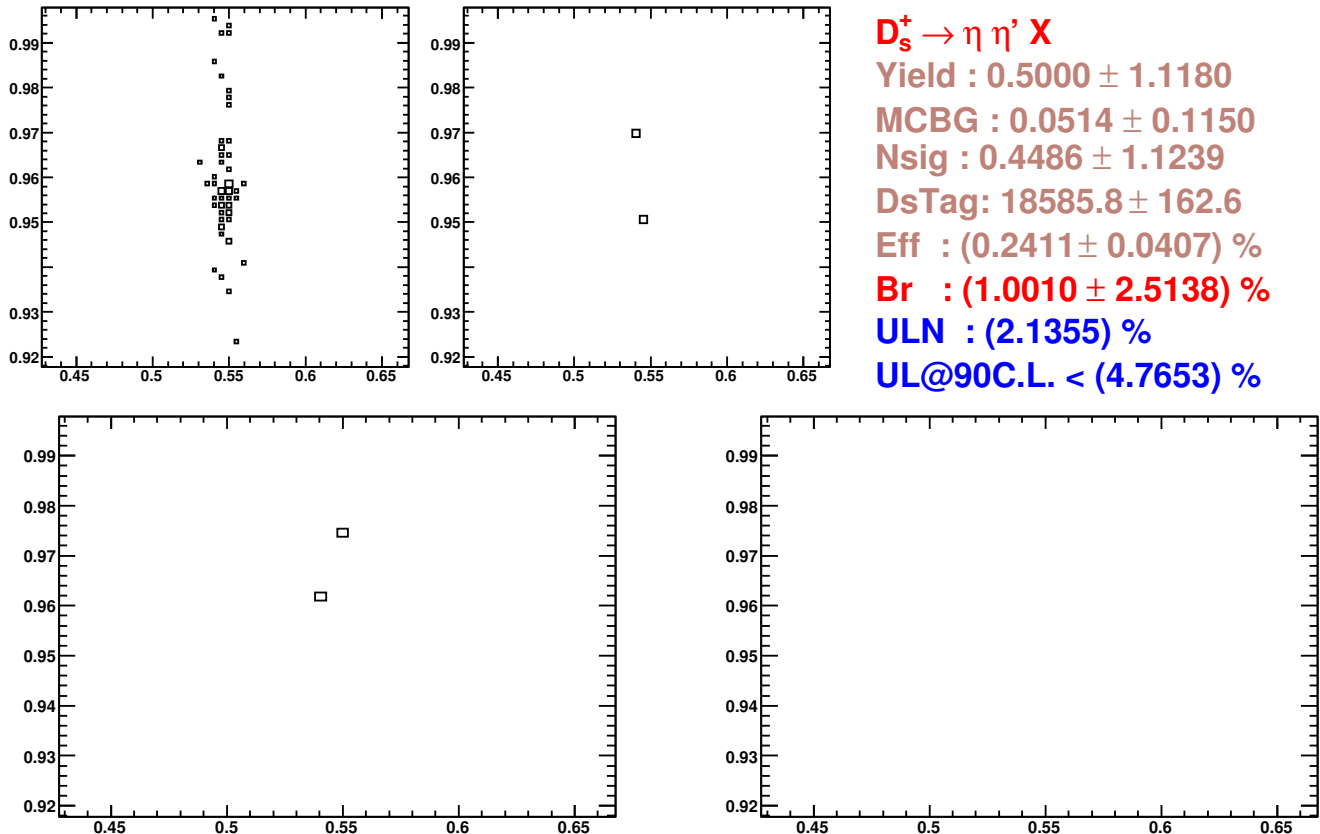


Figure 3.69: $D_s^+ \rightarrow \eta\eta'X$ decay study.

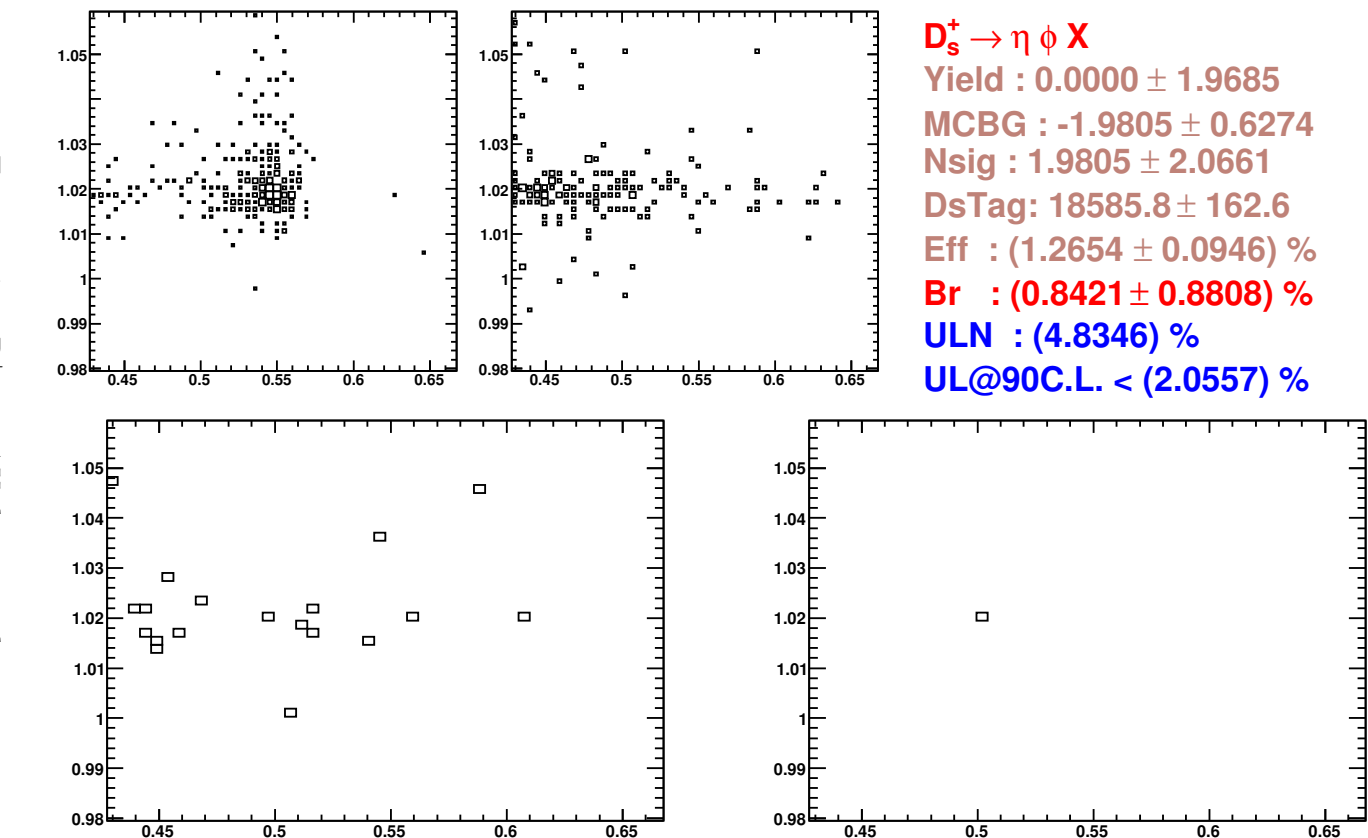


Figure 3.70: $D_s^+ \rightarrow \eta \phi X$ decay study.

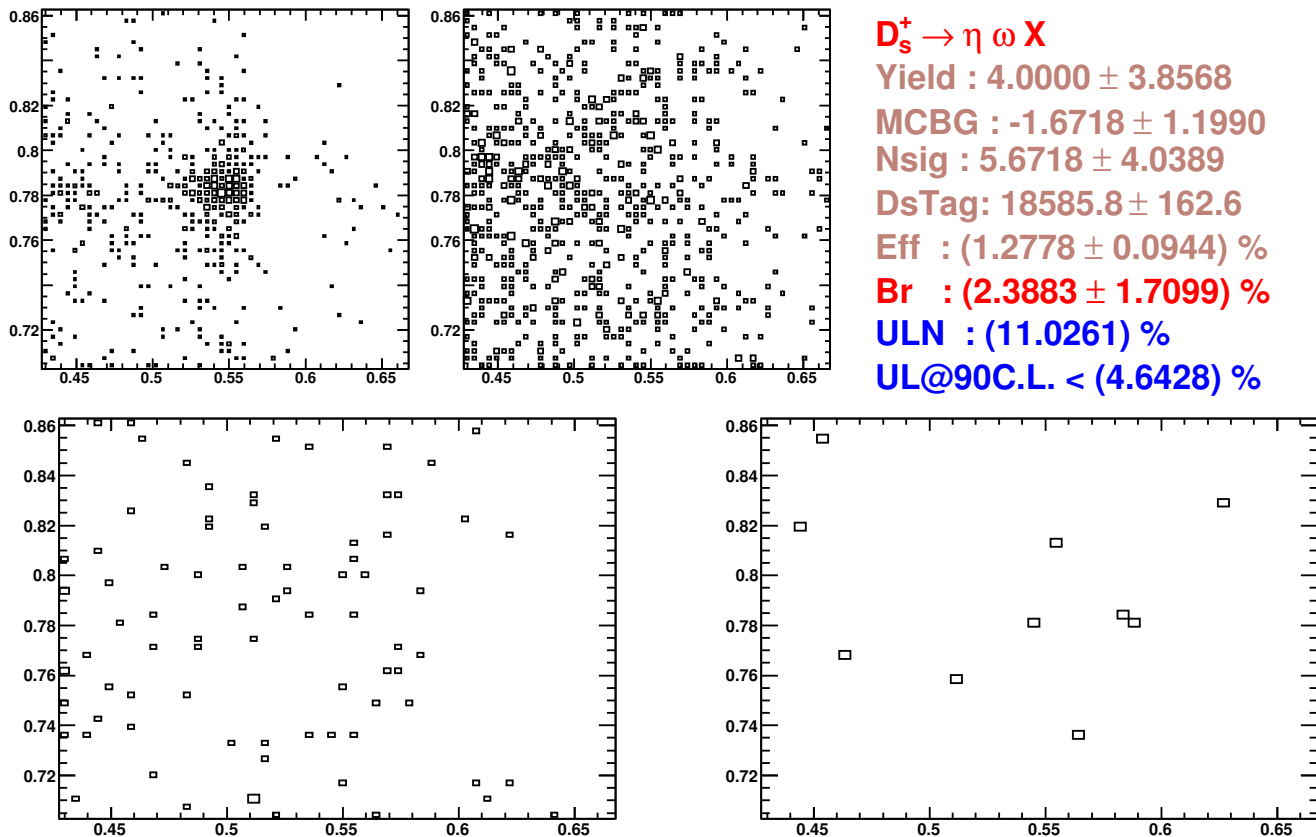


Figure 3.71: $D_s^+ \rightarrow \eta\omega X$ decay study.

3.9 Systematics

We have considered several sources of systematic uncertainties.

3.9.1 D_s Tag Systematics

Through this analysis, we use a double-tag method. We require full reconstruction of the D_s tag and the additional photon (from $D_s^{*+} \rightarrow D_s^+ \gamma$ decay). For this reason, many of the systematics from the D_s tag side cancel in the final inclusive branching fractions. The error in total D_s tag yield is 0.87% and has been included in the statistical errors of the inclusive branching fractions.

3.9.2 MC Efficiency Statistical Error

Uncertainties in Monte Carlo efficiencies arise due to finite Monte Carlo staticstics. We use about $20 \times$ mcDD-mix Monte Carlo samples to estimate the efficiencies. The expected uncertainties in efficiencies also have been included in the statistical errors.

3.9.3 Tracking and PID

Uncertainty in track reconstruction efficiencies has been evaluated by the DTag group and is 0.3% per charged particle, an additional 0.6% systematic uncertainty for each kaon track is added [38]. The particle identification efficiencies of kaons (pions) are found to be overestimated in Monte Carlo by 1.0% (0.5%) per particle, and the corresponding systematic errors of PID are 0.3% (0.25%). We assign 1.8% as the systematic uncertainty for K_S^0 , 4.0% for π^0 , and 5.6% for η .

3.9.4 e, K, π Production Rate

When we estimate the cross-fake backgrounds among all kinds of particles, we use the observed paticle number as the normalization number. The observed number of the particle can be effected by other particles (*e.g.* observed number of particle a can be effected by number of paticle b due to b faking to a). We estimate the cross-fake rate by using the generic Monte Carlo. If the production rates of e, K, π are very

different between Monte Carlo and data, the fake rate can be different. We define the following variable to estimate how big this production rate can effect the final inclusive branching fraction, and take the value of this variable as the systematic error for e, K, π production rate.

$$\delta_{a \rightarrow b} = \frac{N_a^{\text{Data}}}{N_b^{\text{Data}}} \times F^{a \rightarrow b} \times \left(1 - \frac{\epsilon^a + N_b^{\text{MC}}/N_a^{\text{MC}} \times F^{b \rightarrow a} + N_c^{\text{MC}}/N_a^{\text{MC}} \times F^{c \rightarrow a}}{\epsilon^a + N_b^{\text{Data}}/N_a^{\text{Data}} \times F^{b \rightarrow a} + N_c^{\text{Data}}/N_a^{\text{Data}} \times F^{c \rightarrow a}}\right)$$

Here, N is the number of any kind of particle, a, b, c indicate different kind of particles, they can be e, K, π . F is the fake rate and ϵ is the PID efficiency. Due to the good agreement between data and Monte Carlo, the correction factor ($1 - \frac{\epsilon^a + N_b^{\text{MC}}/N_a^{\text{MC}} \times F^{b \rightarrow a} + N_c^{\text{MC}}/N_a^{\text{MC}} \times F^{c \rightarrow a}}{\epsilon^a + N_b^{\text{Data}}/N_a^{\text{Data}} \times F^{b \rightarrow a} + N_c^{\text{Data}}/N_a^{\text{Data}} \times F^{c \rightarrow a}}$) for the difference of production rate among e, K, π is very tiny. Then the systematic errors due to the difference of e, K, π production rate between data and Monte Carlo are very tiny as shown in Table. 3.9 (less than 0.01%). We can ignore them.

3.9.5 e, K, π PID Effect on Cross-Fake Rate

The PID efficiency systematic error not only can effect the signal particle yield, but also can effect the fake background. Such as, the PID efficiency systematic error of particle a can effect particle b yield through:

$$\delta_{a \rightarrow b} = \frac{N_a^{\text{Data}}}{N_b^{\text{Data}}} \times F^{a \rightarrow b} \times \delta_{\epsilon^a} \quad (3.18)$$

These systematic uncertainties are also tiny due to the tiny fake rates. All of these systematic uncertainties are less than 0.07% as shown in Table. 3.9, we ignore these systematic errors.

3.9.6 Uncertainty for $D_s^+ \rightarrow f_0(980)X$

The parameters of the signal shape function are fixed to the values obtained from Monte Carlo simulation. We also determine the signal line shape parameters by using $D_s^+ \rightarrow \pi^+ f_0(980)$, $f_0(980) \rightarrow \pi^+ \pi^-$ decay in real data. Fix the parameters to the values obtained from data and get the changes in yield to set the systematic uncertainty for signal fitting. We repeat the fit to data with different bin size and

Table 3.9: Systematic uncertainties from fake rates.

Source	Value (%)			
	K^+X	K^-X	π^+X	π^-X
$F^{e \rightarrow K/\pi}$	0.000078	0.000044	0.000040	0.000552
$F^{K \rightarrow \pi}$	—	—	0.000120	0.000013
$F^{\pi \rightarrow K}$	0.000468	0.000030	—	—
$F^{\mu \rightarrow K/\pi}$	0.000027	—	0.001405	—
EID (e fake)	0.003719	0.000142	0.001895	0.001773
KID (K fake)	—	—	0.000280	0.000123
PiID (π fake)	0.001690	0.000439	—	—
EID (μ fake)	0.001296	—	0.066614	—

observe the changes in yield to set systematic uncertainty for different bin size. The $f_0(980)$ efficiency may be different due to the different contribution modes to $f_0(980)X$. We generate different Monte Carlo samples to study the $f_0(980)$ efficiency, and set the difference as the systematic associated with efficiency.

3.9.7 Branching Fraction Truncation

We estimate the number of signal track below 50 MeV/ c by using Monte Carlo directly. We take a half of the number of signal in the first low momentum bin as the systematic uncertainty for truncating momentum spectra. For $D_s^+ \rightarrow \phi X$, we modeled the partial branching ratio in first momentum bin by taking the fraction of ϕ yield in the first momentum interval to ϕ yield in the rest of the momentum intervals in data to be equal to the same fraction from the Monte Carlo simulation, and assign systematic uncertainty equal to its value.

3.9.8 The Effect from $D_s^{*+} \rightarrow D_s^+ \pi^0$ Decay

For the $D_s^+ \rightarrow \pi^0 X$ decay, if the tag comes from $D_s^{*+} \rightarrow D_s^+ \pi^0$ event, the π^0 from $D_s^{*+} \rightarrow D_s^+ \pi^0$ decay could affect our inclusive π^0 branching fraction. To understand this systematic, we generate two Monte Carlo samples, one only contains $D_s^{*+} \rightarrow D_s^+ \gamma$ and the other only contains $D_s^{*+} \rightarrow D_s^+ \pi^0$. The branching fraction of $D_s^{*+} \rightarrow D_s^+ \pi^0$ is about 6% [11], the systematic associated with π^0 from $D_s^{*+} \rightarrow D_s^+ \pi^0$ decay is 1.45%. The details for this systematic study are shown on Fig. 3.72.

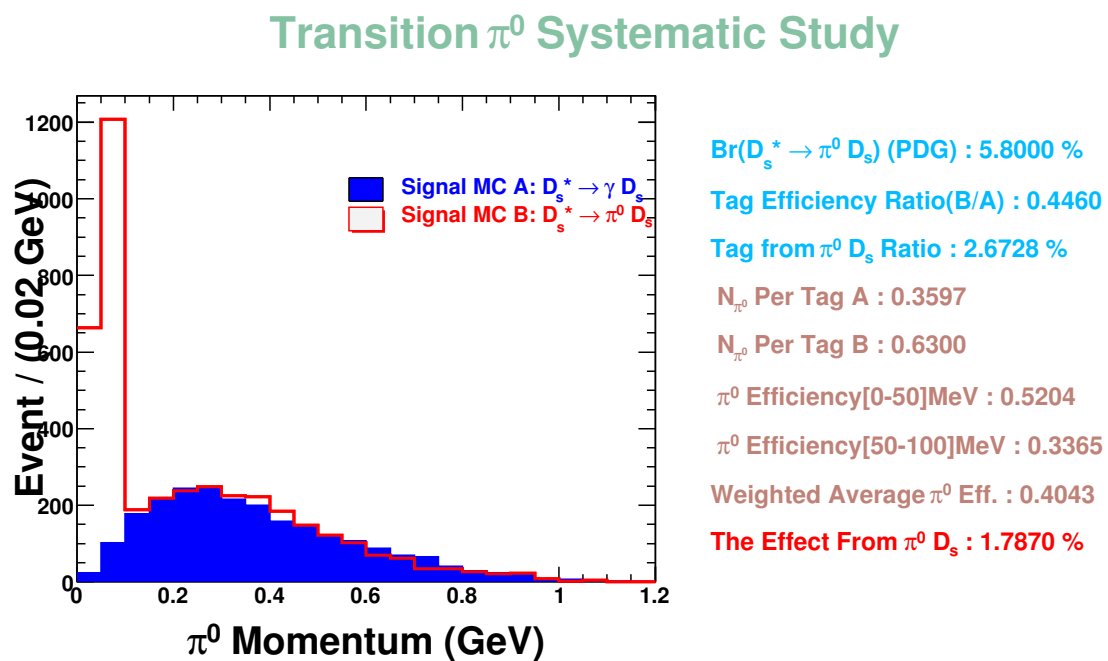


Figure 3.72: Systematic study for π^0 from $D_s^{*+} \rightarrow D_s^+ \pi^0$ decay.

3.9.9 $D_s^+ \rightarrow K^+ K^+ X$ Monte Carlo Efficiency

For the $D_s^+ \rightarrow K^+ K^+ X$ decay, actually our generic Monte Carlo only contains $D_s^+ \rightarrow K^+ K^+ K^-$. There is another possible contribution to $D_s^+ \rightarrow K^+ K^+ X$ decay, it is $D_s^+ \rightarrow K^+ K^+ \pi^-$. We generate this sample to study the efficiency difference between these two possible modes and set this difference as the systematic.

3.9.10 D_s Single Tag Efficiency

The single tagging efficiency in generic D_s meson decays (ϵ_{tag}), *i.e.*, the efficiency for finding the tag, where the “other side” decays generically, is to a good approximation equal to the single tagging efficiency in inclusive decays (ϵ'_{tag}), *i.e.* the efficiency for finding the tag, when the “other side” decays containing K^+ , or π^+ , or whatever particle’s inclusive yield is being measured. thus, $\epsilon'_{\text{tag}}/\epsilon_{\text{tag}} \approx 1.0$. The small differences between single tagging efficiency ϵ_{tag} and ϵ'_{tag} are studied by using our generic Monte Carlo sample. The invariant mass distributions of D_s tags from different MC samples are shown in Fig. 3.73 and Fig. 3.74. We took the central value of $\epsilon'_{\text{tag}}/\epsilon_{\text{tag}}$ as the correction factor and the error of $\epsilon'_{\text{tag}}/\epsilon_{\text{tag}}$ as the systematic. The efficiencies and correction factors are summarized in Table. 3.10.

3.9.11 Correction Factor and Systematic Summary

We apply the correction factors for PID, π^0 finding and η finding. They are 0.5% for π^\pm PID and 1% for K^\pm PID. The correction factor for π^0 and η finding is 6%. The correction factor for each mode is listed in the last column of Table 3.11. Table 3.11 also shows main systematic uncertainties that have been considered for this analysis.

3.10 Results

In summary, we report several measurements of D_s^+ inclusive decays with significantly better precision than current world averages. The inclusive yields are listed in Table 3.12. The first error is the statistical error and the second error is the systematic error. For the upper limits, we conservatively increase the quoted upper limits by 1.28 times the systematic errors from Table 3.11. For the K_S^0 modes, the corre-

Table 3.10: Single tag efficiencies and correction factors.

Mode	eff(%)	$\epsilon'_{\text{tag}}/\epsilon_{\text{tag}}$	Systematic (%)
$D_s^+ \rightarrow \text{Generic}$	26.605 ± 0.063	—	—
$D_s^+ \rightarrow K^+ X$	25.827 ± 0.117	0.971	0.510
$D_s^+ \rightarrow K^- X$	25.294 ± 0.145	0.951	0.618
$D_s^+ \rightarrow K_S^0 X$	26.321 ± 0.144	0.989	0.596
$D_s^+ \rightarrow \pi^+ X$	26.686 ± 0.070	1.003	0.352
$D_s^+ \rightarrow \pi^- X$	26.392 ± 0.100	0.992	0.445
$D_s^+ \rightarrow \pi^0 X$	27.948 ± 0.081	1.051	0.374
$D_s^+ \rightarrow \eta X$	28.000 ± 0.125	1.052	0.503
$D_s^+ \rightarrow \eta' X$	27.219 ± 0.206	1.023	0.792
$D_s^+ \rightarrow \phi X$	26.601 ± 0.157	1.000	0.634
$D_s^+ \rightarrow \omega X$	24.787 ± 0.822	0.932	3.325
$D_s^+ \rightarrow K_L^0 X$	26.148 ± 0.144	0.983	0.600
$D_s^+ \rightarrow K_S^0 K_S^0 X$	26.985 ± 0.525	1.014	1.958
$D_s^+ \rightarrow K_S^0 K^+ X$	26.456 ± 0.275	0.994	1.064
$D_s^+ \rightarrow K_S^0 K^- X$	24.415 ± 0.452	0.918	1.864
$D_s^+ \rightarrow K^+ K^- X$	25.500 ± 0.162	0.958	0.678
$D_s^+ \rightarrow K_L^0 K_S^0 X$	26.459 ± 0.216	0.995	0.849
$D_s^+ \rightarrow K_L^0 K^+ X$	26.341 ± 0.276	0.990	1.072
$D_s^+ \rightarrow K_L^0 K^- X$	24.560 ± 0.453	0.923	1.860

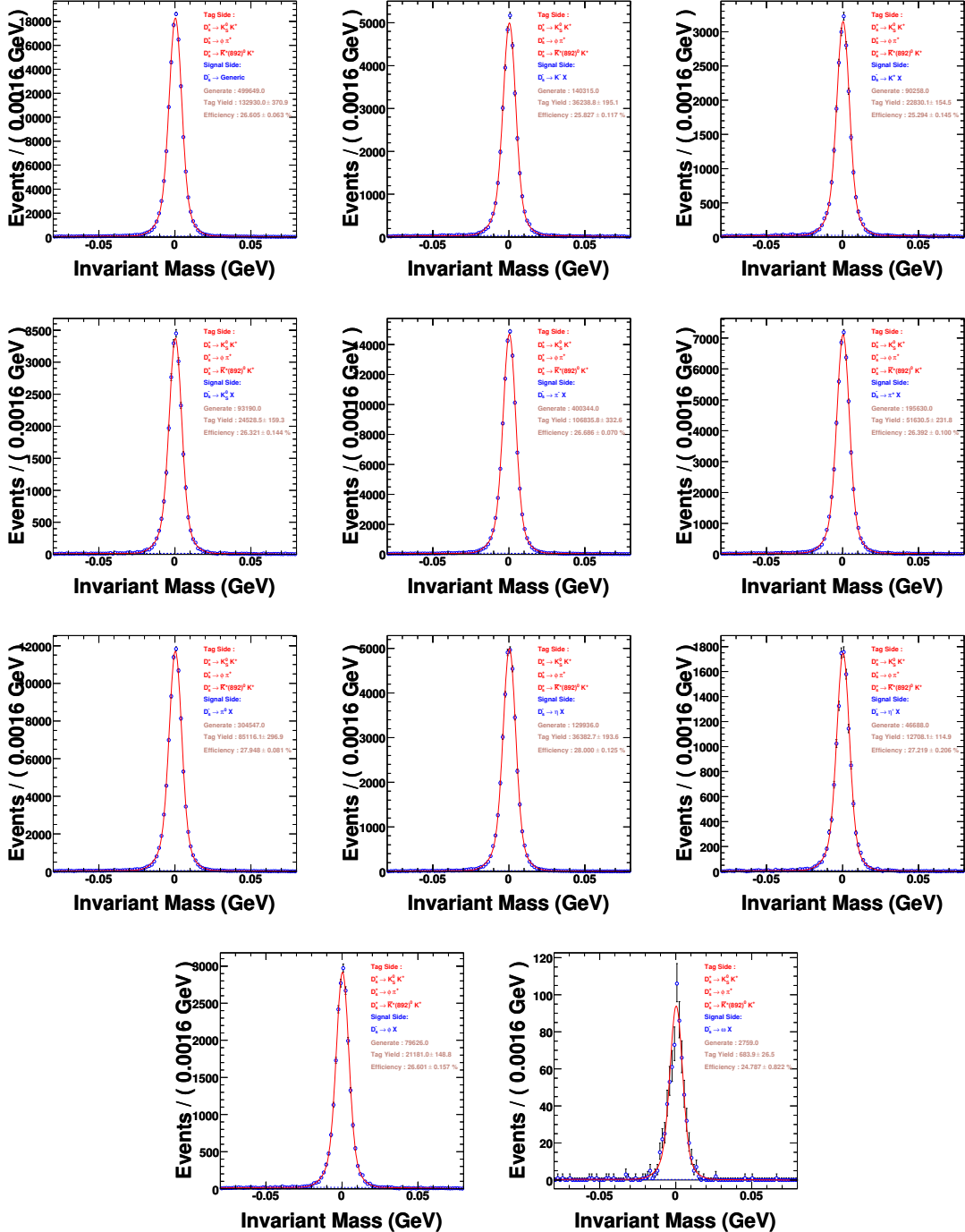


Figure 3.73: D_s tag invariant mass distributions, for some of the signal side processes.

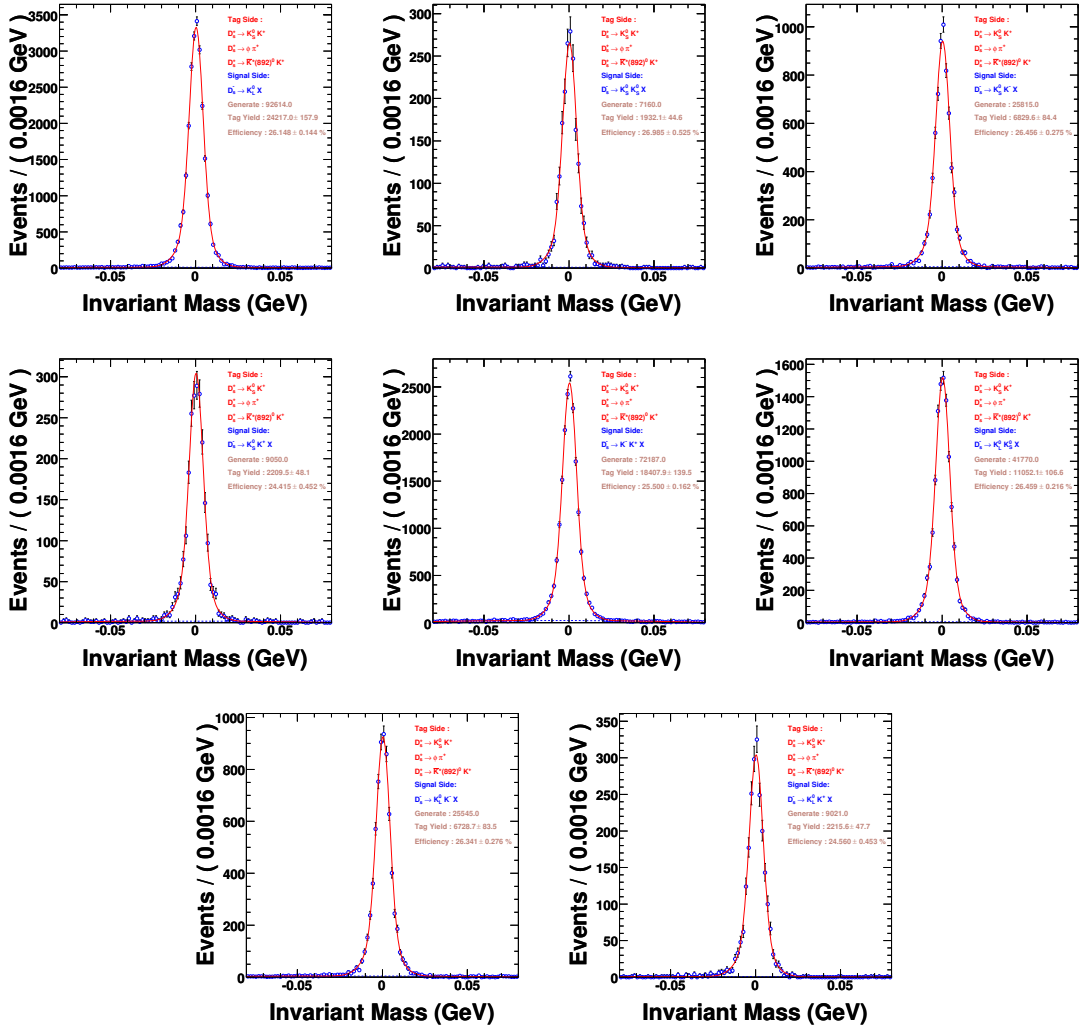


Figure 3.74: D_s tag invariant mass distributions, for the rest of the signal side processes.

Table 3.11: Systematic summary.

Mode	Value (%)											C. F.		
	Tracking	K^\pm	Trk	K^\pm	ID	π^\pm	ID	K_S^0, π^0, f_0, η	Truncate	Tag	Eff	Other		
$\pi^+ X$	0.300	—	—	0.250	—	—	—	0.295	0.352	—	—	0.603	0.998	
$\pi^- X$	0.300	—	—	0.250	—	—	—	0.421	0.445	—	—	0.727	0.987	
$\pi^0 X$	—	—	—	—	—	—	—	4.000	—	0.374	1.466	4.276	0.988	
$K^+ X$	0.300	0.600	0.300	—	—	—	—	—	0.158	0.510	—	—	0.908	0.961
$K^- X$	0.300	0.600	0.300	—	—	—	—	—	0.186	0.618	—	—	0.978	0.941
ηX	—	—	—	—	—	—	—	5.600	—	0.503	—	—	5.623	0.989
$\eta' X$	0.600	—	—	0.500	—	—	—	5.600	—	0.792	—	—	5.709	0.951
ϕX	0.600	1.200	0.600	—	—	—	—	—	3.653	0.634	—	—	3.988	0.980
ωX	0.600	—	—	0.500	—	—	—	4.000	—	3.325	—	—	5.260	0.867
$f_0(980) X$	0.600	—	—	0.500	—	—	—	5.620	—	—	6.748	—	8.817	0.990
$K_S^0 X$	0.600	—	—	—	—	—	—	1.800	—	0.596	—	—	1.989	0.989
$K_S^0 K_S^0 X$	1.200	—	—	—	—	—	—	3.600	—	1.958	—	—	4.270	1.014
$K_S^0 K^+ X$	0.900	0.600	0.300	—	—	—	—	1.800	—	1.064	—	—	2.373	0.984
$K_S^0 K^- X$	0.900	0.600	0.300	—	—	—	—	1.800	—	1.864	—	—	2.824	0.909
$K^+ K^- X$	0.600	1.200	0.600	—	—	—	—	—	—	0.678	—	—	1.619	0.939
$K^+ K^+ X$	0.600	1.200	0.600	—	—	—	—	—	—	—	6.227	—	6.398	0.980
$K^- K^- X$	0.600	1.200	0.600	—	—	—	—	—	—	—	—	—	1.470	0.980

sponding K_L^0 modes are listed as a comparison. The value of the decay $D_s^+ \rightarrow K_L^0 X$ is only for D_s^+ decaying into a single K_L^0 . So one should not directly compare the values of $D_s^+ \rightarrow K_S^0 X$ and $D_s^+ \rightarrow K_L^0 X$ in Table 3.12. One can correct the single K_L^0 inclusive yield by adding two times the inclusive yield of $D_s^+ \rightarrow K_L^0 K_L^0 X$ (assuming $\mathcal{B}(D_s^+ \rightarrow K_L^0 K_L^0 X) = \mathcal{B}(D_s^+ \rightarrow K_S^0 K_S^0 X)$). All the K_L^0 modes are consistent with K_S^0 modes. In the last column of Table 3.12, we show PDG [11] averages, when available.

Table 3.12: D_s inclusive yield results. Uncertainties are statistical and systematic, respectively. The inclusive K_L^0 results are only used as a check for K_S^0 . PDG [11] averages are shown in the last column, when available.

Mode	Yield(%)				K_L^0 Mode	Yield(%)				$\mathcal{B}(\text{PDG})(\%)$		
$D_s^+ \rightarrow \pi^+ X$	119.3	\pm	1.2	\pm	0.7							
$D_s^+ \rightarrow \pi^- X$	43.2	\pm	0.9	\pm	0.3							
$D_s^+ \rightarrow \pi^0 X$	123.4	\pm	3.8	\pm	5.3							
$D_s^+ \rightarrow K^+ X$	28.9	\pm	0.6	\pm	0.3					20	$^{+18}_{-14}$	
$D_s^+ \rightarrow K^- X$	18.7	\pm	0.5	\pm	0.2					13	$^{+14}_{-12}$	
$D_s^+ \rightarrow \eta X$	29.9	\pm	2.2	\pm	1.7							
$D_s^+ \rightarrow \eta' X$	11.7	\pm	1.7	\pm	0.7							
$D_s^+ \rightarrow \phi X$	15.7	\pm	0.8	\pm	0.6							
$D_s^+ \rightarrow \omega X$	6.1	\pm	1.4	\pm	0.3							
$D_s^+ \rightarrow f_0(980) X, f_0(980) \rightarrow \pi^+ \pi^-$	< 1.3% (90% CL)											
$D_s^+ \rightarrow K_S^0 X$	19.0	\pm	1.0	\pm	0.4	$D_s^+ \rightarrow K_L^0 X$	15.6	\pm	2.0	20	\pm	14
$D_s^+ \rightarrow K_S^0 K_S^0 X$	1.7	\pm	0.3	\pm	0.1	$D_s^+ \rightarrow K_L^0 K_S^0 X$	5.0	\pm	1.0			
$D_s^+ \rightarrow K_S^0 K^+ X$	5.8	\pm	0.5	\pm	0.1	$D_s^+ \rightarrow K_L^0 K^+ X$	5.2	\pm	0.7			
$D_s^+ \rightarrow K_S^0 K^- X$	1.9	\pm	0.4	\pm	0.1	$D_s^+ \rightarrow K_L^0 K^- X$	1.9	\pm	0.3			
$D_s^+ \rightarrow K^+ K^- X$	15.8	\pm	0.6	\pm	0.3							
$D_s^+ \rightarrow K^+ K^+ X$	< 0.26% (90% CL)											
$D_s^+ \rightarrow K^- K^- X$	< 0.06% (90% CL)											

Chapter 4

General Discussions on D_s Decays

4.1 Measurements Summary

Table 4.1 shows the measurements summary. We have several measurements, such as $\mathcal{B}(D_s^+ \rightarrow \eta X)$, $\mathcal{B}(D_s^+ \rightarrow \eta' X)$, $\mathcal{B}(D_s^+ \rightarrow \phi X)$, $\mathcal{B}(D_s^+ \rightarrow K\bar{K}X)$, $\mathcal{B}(D_s^+ \rightarrow KX)$, and $\mathcal{B}(D_s^+ \rightarrow \omega X)$. From other CLEO measurements, we already know the branching fractions of $D_s^+ \rightarrow \tau^+ \nu$ [39] and $D_s^+ \rightarrow \mu^+ \nu$ [40]. Using these measurements, we obtain an overview of D_s^+ decays.

4.2 Variable Definitions and Notations

4.2.1 Classify “Quark-Level Final States”

The quark-level diagrams contributing to D_s^+ decay are shown in Fig. 4.1. We classify “quark-level final states” as $s\bar{s}$ (as would come from Fig. 4.1-a), \bar{s} (Fig. 4.1-b), $s\bar{s}\bar{s}$ (Fig. 4.1-c), $\bar{s}\bar{s}$ (Fig. 4.1-d), and “no strange quarks” (Fig. 4.1-e and Fig. 4.1-f). The $s\bar{s}$ final state is Cabibbo-favored. The \bar{s} and $s\bar{s}\bar{s}$ final states are singly-Cabibbo-suppressed, the $\bar{s}\bar{s}$ final state is doubly-Cabibbo-suppressed, and the “no strange quarks” final state arises from short-range (Fig. 4.1-e) and long-range (Fig. 4.1-f) annihilation diagrams (While Fig. 4.1-f shows the $s\bar{s}$ annihilating into gluons, here we also include its rescattering into $u\bar{u}$ or $d\bar{d}$).

The $s\bar{s}$ final state can hadronize as $K\bar{K}X$, but also as ηX , $\eta' X$, or ϕX . The \bar{s} final state will hadronize as KX . The $s\bar{s}\bar{s}$ final state in principle can hadronize

Table 4.1: Measurements summary.

(a).Total kaon branching fractions

Value(%)	Mode
(28.914 ± 0.697)	(K^+X)
(18.679 ± 0.554)	(K^-X)
(19.017 ± 1.040)	(K_S^0X)
(19.017 ± 1.040)	$(K_L^0X = K_S^0X)$
(85.627 ± 2.263)	$D_s^+ \rightarrow KX$

(b).Total kaon pair branching fractions.

Value(%)	Mode
$2 \times (1.716 \pm 0.337)$	$(K_S^0K_S^0X = K_L^0K_L^0X)$
$2 \times (5.846 \pm 0.477)$	$(K_S^0K^+X = K_L^0K^+X)$
$2 \times (1.920 \pm 0.361)$	$(K_S^0K^-X = K_L^0K^-X)$
(15.810 ± 0.643)	(K^+K^-X)
(0.130 ± 0.130)	(K^+K^+X)
(0.032 ± 0.032)	(K^-K^-X)
(4.965 ± 0.985)	$(K_L^0K_S^0X)$
(39.901 ± 1.813)	$D_s^+ \rightarrow KX$

(c).Inclusive branching fractions summary.

D_s^+ Mode	Measurement	\mathcal{B} (%)
$\tau^+\nu$	CLEO-c Measurment [39]	5.62 ± 0.44
$\mu^+\nu$	CLEO-c Measurment [40]	0.565 ± 0.048
ηX		29.933 ± 2.790
$\eta' X$		11.667 ± 1.809
ϕX		15.714 ± 1.029
ωX		6.090 ± 1.437
KKX	Sum of kaon-pair branching fractions	39.901 ± 1.813
KX	Sum of kaon branching fractions	85.627 ± 2.263
$(S)K^+X$	$K^+ - K^+K^- - 2 \times K_S^0K^+ - 2 \times K^+K^+$	1.152 ± 1.370
$(S)K^-X$	$K^- - K^+K^- - 2 \times K_S^0K^- - 2 \times K^-K^-$	-1.035 ± 1.116
$(S)K_S^0X$	$K_S^0 - K_S^0K^+ - K_S^0K^- - K_S^0K_L^0 - 2 \times K_S^0K_S^0$	2.854 ± 1.895

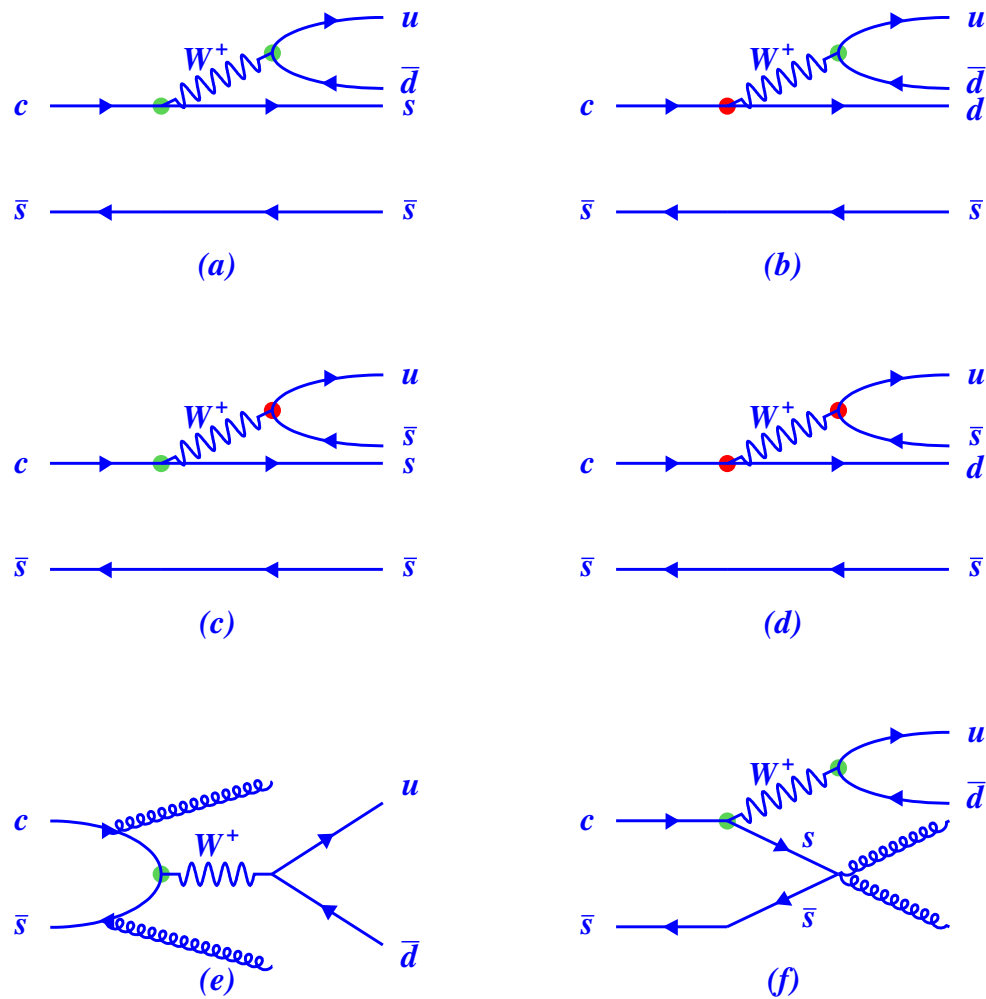


Figure 4.1: The typical Feynman diagrams of D_s^+ decays: (a) Cabibbo-favored decay, (b) single-Cabibbo-suppressed decay, (c) single-Cabibbo-suppressed decay, (d) double-Cabibbo-suppressed decay, (e) short-range annihilation decay, (f) long-range annihilation decay.

as $KK\bar{K}X$, but there will be limited phase space for this, so $K\eta X$, $K\eta'X$, $K\phi X$ are probably more likely. The $s\bar{s}$ final state will hadronize as KKX , but being doubly-Cabibbo-suppressed, can probably be ignored.

4.2.2 Cabibbo-Favored Decays with $s\bar{s}$ in Final States

We have performed a global fit to our measurements. For this, we have branching fractions $\mathcal{B}(XX)$. In particular, for $s\bar{s}$ quark-level final states, we write $\mathcal{B}(D_s \rightarrow s\bar{s}) \equiv \mathcal{B}(s\bar{s})$, $\mathcal{B}(D_s \rightarrow s\bar{s} \rightarrow \eta X) \equiv \mathcal{B}(\eta)$, $\mathcal{B}(D_s \rightarrow s\bar{s} \rightarrow \eta'X) \equiv \mathcal{B}(\eta')$, $\mathcal{B}(D_s \rightarrow s\bar{s} \rightarrow \phi X) \equiv \mathcal{B}(\phi)$, and $\mathcal{B}(D_s \rightarrow s\bar{s} \rightarrow K\bar{K}X) \equiv \mathcal{B}(K\bar{K})$. Thus $\mathcal{B}(s\bar{s}) = \mathcal{B}(\eta) + \mathcal{B}(\eta') + \mathcal{B}(\phi) + \mathcal{B}(K\bar{K})$. Note that $\mathcal{B}(D_s \rightarrow s\bar{s} \rightarrow \eta X)$ is the branching fraction for *primary* production of η (*not* from η' decay), from the quark-level state $s\bar{s}$. The free parameters in our fit are $\mathcal{B}(\eta)$, $\mathcal{B}(\eta')$, $\mathcal{B}(\phi)$, and $\mathcal{B}(K\bar{K})$, which we adjust to obtain the best fit.

4.2.3 Singly-Cabibbo-Suppressed Decays with \bar{s} in Final States

For the \bar{s} quark-level final state, we note that $\mathcal{B}(D_s \rightarrow \bar{s}) \equiv \mathcal{B}(\bar{s}) \approx |V_{cd}/V_{cs}|^2 \times \mathcal{B}(s\bar{s})$. Thus, we do not adjust $\mathcal{B}(\bar{s})$ in the fit, but write $\mathcal{B}(\bar{s}) = C_1 \times |V_{cd}/V_{cs}|^2 \times \mathcal{B}(s\bar{s})$, where C_1 is a phase space correction factor, probably a bit larger than 1.0. We take C_1 to be 1.25 ± 0.25 .

4.2.4 Singly-Cabibbo-Suppressed Decays with $s\bar{s}\bar{s}$ in Final States

We break the $s\bar{s}\bar{s}$ quark-level final state into 4 separate pieces, as we have done with the $s\bar{s}$ final state. Thus $\mathcal{B}(D_s \rightarrow s\bar{s}\bar{s}) \equiv \mathcal{B}(s\bar{s}\bar{s})$ is made up of $\mathcal{B}(D_s \rightarrow s\bar{s}\bar{s} \rightarrow \eta\bar{s}X) \equiv \mathcal{B}(\eta\bar{s})$, $\mathcal{B}(D_s \rightarrow s\bar{s}\bar{s} \rightarrow \eta'\bar{s}X) \equiv \mathcal{B}(\eta'\bar{s})$, $\mathcal{B}(D_s \rightarrow s\bar{s}\bar{s} \rightarrow \phi\bar{s}X) \equiv \mathcal{B}(\phi\bar{s})$, and $\mathcal{B}(D_s \rightarrow s\bar{s}\bar{s} \rightarrow K\bar{K}\bar{s}X) \equiv \mathcal{B}(K\bar{K}\bar{s})$. Thus $\mathcal{B}(s\bar{s}\bar{s}) = \mathcal{B}(\eta\bar{s}) + \mathcal{B}(\eta'\bar{s}) + \mathcal{B}(\phi\bar{s}) + \mathcal{B}(K\bar{K}\bar{s})$. We note that $\mathcal{B}(s\bar{s}\bar{s}) \approx |V_{us}/V_{ud}|^2 \times \mathcal{B}(s\bar{s})$. So again, we do not adjust any of the pieces making up $\mathcal{B}(s\bar{s}\bar{s})$, but rather write

$$\mathcal{B}(\eta\bar{s}) = C_2 \times |V_{us}/V_{ud}|^2 \times \mathcal{B}(\eta) \quad (4.1)$$

$$\mathcal{B}(\eta' \bar{s}) = C_2 \times |V_{us}/V_{ud}|^2 \times \mathcal{B}(\eta') \quad (4.2)$$

$$\mathcal{B}(\phi \bar{s}) = C_2 \times |V_{us}/V_{ud}|^2 \times \mathcal{B}(\phi) \quad (4.3)$$

$$\mathcal{B}(K \bar{K} \bar{s}) = C_2 \times |V_{us}/V_{ud}|^2 \times \mathcal{B}(K \bar{K}) \quad (4.4)$$

The quantity C_2 , like C_1 , is a phase space correction factor, expected to be smaller than 1.0. We take it to be 0.75 ± 0.25 . Assuredly the true phase space correction factors would be different for η , η' , ϕ , and $K \bar{K}$. We neglect this in our fit, allowing for it as a systematic error.

4.2.5 Doubly-Cabibbo-Suppressed Decays with $\bar{s}\bar{s}$ in Final States

For the doubly-Cabibbo-suppressed decays, we estimate $\mathcal{B}(D_s \rightarrow \bar{s}\bar{s}) \equiv \mathcal{B}(\bar{s}\bar{s}) = C_3 \times |(V_{cd}/V_{cs})(V_{us}/V_{ud})|^2 \times \mathcal{B}(s\bar{s})$. This term is down a factor of 400 from the dominant term, and has essentially no effect on our fit. We take $C_3 = 1.0 \pm 1.0$.

4.2.6 Annihilation Decays without s or \bar{s} in Final States

Finally, there are annihilation diagrams. We write $\mathcal{B}(\text{Annihilation}) = \mathcal{B}(D_s^+ \rightarrow \mu^+ \nu) + \mathcal{B}(D_s^+ \rightarrow \tau^+ \nu) + \mathcal{B}(D_s^+ \rightarrow \text{Other Annihilation})$. One of our goals in performing the global fit is to get an estimate of $\mathcal{B}(D_s^+ \rightarrow \text{Other Annihilation})$. In our fit, we use $\mathcal{B}(D_s^+ \rightarrow \tau^+ \nu) = (5.62 \pm 0.41 \pm 0.16)\%$ [39], and $\mathcal{B}(D_s^+ \rightarrow \mu^+ \nu) = (0.565 \pm 0.045 \pm 0.017)\%$ [40].

4.2.7 Extra η Decays

It is possible for a D_s decay to contain more than one of η , η' , ϕ , $K \bar{K}$, *e.g.* $\eta\eta$, $\eta\phi$, etc. From energy conservation, one of an allowed pair must be η . So, we include a yield $\mathcal{B}(\text{extra } \eta)$ to allow for this. We searched for $D_s^+ \rightarrow \eta\eta X$, $D_s^+ \rightarrow \eta\eta' X$, and $D_s^+ \rightarrow \eta\phi X$. We found no clear signals, obtaining a summed yield of $(6.0 \pm 3.9)\%$. In our global fit, we take $\mathcal{B}(\text{extra } \eta)$ to be 6.0%, and include the $\pm 3.9\%$ in the systematic error.

4.2.8 η and η' from $D_s \rightarrow \bar{s}$ Decay

Another source of η and η' is the quark-level decay $D_s \rightarrow \bar{s}$ (Fig. 4.1-b). Here, the η or η' will come not from their $s\bar{s}$ component, but from their $u\bar{u}$ and $d\bar{d}$ components. At quark level, the decay is $D_s \rightarrow u\bar{d}d\bar{s}$, so making η or η' is natural. We assume that this diagram gives an η a fraction f_1 of the time, and an η' a fraction f_2 of the time, where $f_1 + f_2 \leq 1$. While one can make quark-level predictions of what to expect for f_1 and f_2 , we take the conservative position of allowing them the full range, $0 \leq f_1 + f_2 \leq 1$, and take $f_1 = f_2 = 1/4$, in the middle of the allowed range.

4.3 Build χ^2 for Our Global Fit

For our global fit, we write

$$\begin{aligned} \chi^2 = & \left(\frac{Y_\eta - (\mathcal{B}(\eta) + \mathcal{B}(\eta\bar{s}) + \mathcal{B}(\eta' \rightarrow \eta X) \times (\mathcal{B}(\eta') + \mathcal{B}(\eta'\bar{s}) + f_2 \times \mathcal{B}(\bar{s})) + \mathcal{B}(\text{extra } \eta) + f_1 \times \mathcal{B}(\bar{s}))}{\delta_{Y_\eta}} \right)^2 + \\ & \left(\frac{Y_{\eta'} - (\mathcal{B}(\eta') + \mathcal{B}(\eta'\bar{s}) + f_2 \times \mathcal{B}(\bar{s}))}{\delta_{Y_{\eta'}}} \right)^2 + \\ & \left(\frac{Y_\phi - (\mathcal{B}(\phi) + \mathcal{B}(\phi\bar{s}))}{\delta_{Y_\phi}} \right)^2 + \\ & \left(\frac{Y_{KK} - (\mathcal{B}(K\bar{K}) + \mathcal{B}(K\bar{K}\bar{s}) + \mathcal{B}(\phi \rightarrow K\bar{K}) \times (\mathcal{B}(\phi) + \mathcal{B}(\phi\bar{s})) + \mathcal{B}(\bar{s}\bar{s}))}{\delta_{Y_{KK}}} \right)^2 + \\ & \left(\frac{Y_K - (2 \times (\mathcal{B}(K\bar{K}) + \mathcal{B}(K\bar{K}\bar{s})) + 2 \times \mathcal{B}(\phi \rightarrow K\bar{K}) \times (\mathcal{B}(\phi) + \mathcal{B}(\phi\bar{s})) + \mathcal{B}(s\bar{s}\bar{s}) + \mathcal{B}(\bar{s}) + 2 \times \mathcal{B}(\bar{s}\bar{s}))}{\delta_{Y_K}} \right)^2 \end{aligned} \quad (4.5)$$

Here Y_i is the central value of a measurement, and δ_{Y_i} is the error on that measurement. As η' decays to η , and ϕ decays to $K\bar{K}$, our χ^2 needs the branching fractions for those decays, $\mathcal{B}(\eta' \rightarrow \eta X)$ and $\mathcal{B}(\phi \rightarrow K\bar{K})$. We take these from PDG [11]. Better than words, Eq. 4.5 gives the meaning of the various $\mathcal{B}(XX)$ parameters. Thus, the measured yield of η , Y_η , has contributions from primary production of η from the $s\bar{s}$ quark state ($\mathcal{B}(\eta)$), primary production of η from the $s\bar{s}\bar{s}$ quark state ($\mathcal{B}(\eta\bar{s})$), primary production of η from the \bar{s} quark state ($f_1 \times \mathcal{B}(\bar{s})$), production of η from decay of η' , the η' being from the $s\bar{s}$ quark state ($\mathcal{B}(\eta') \times \mathcal{B}(\eta' \rightarrow \eta X)$), or the η' being from the $s\bar{s}\bar{s}$ quark state ($\mathcal{B}(\eta'\bar{s}) \times \mathcal{B}(\eta' \rightarrow \eta X)$), or from the \bar{s} quark state ($f_2 \times \mathcal{B}(\bar{s}) \times \mathcal{B}(\eta' \rightarrow \eta X)$), and finally of “extra η ’s”, η that accompanies an η , η' , or ϕ already recorded ($\mathcal{B}(\text{extra } \eta)$). The measured yields for η' and ϕ , while not as complicated, have some of the same features. Note that, as described earlier, our measured yield of di-kaons, Y_{KK} , includes $K\bar{K}$ and KK and $\bar{K}\bar{K}$ pairs. There

Table 4.2: Results from the global fit. The central values of parameters are listed in the second column. The errors: δ_1 is statistical uncertainty, δ_2 is from phase space factor $C_1 = 1.25 \pm 0.25$, δ_3 is from phase space factor $C_2 = 0.75 \pm 0.25$, δ_4 is from $f_1 + f_2 = 0.5 \pm 0.5$, and δ_5 is from the $\mathcal{B}(\text{extra } \eta) = (6.0 \pm 3.9)\%$.

Parameter	Value(%)	Error(%)				
		δ_1	δ_2	δ_3	δ_4	δ_5
$\mathcal{B}(D_s \rightarrow s\bar{s} \rightarrow \eta X)$	14.7	2.9	0.2	0.2	1.0	3.7
$\mathcal{B}(D_s \rightarrow s\bar{s} \rightarrow \eta' X)$	10.3	1.7	0.2	0.1	1.0	0.1
$\mathcal{B}(D_s \rightarrow s\bar{s} \rightarrow \phi X)$	15.1	1.0	0.0	0.2	0.0	0.0
$\mathcal{B}(D_s \rightarrow s\bar{s} \rightarrow K\bar{K}X)$	25.4	1.2	0.3	0.6	0.1	0.1
$\mathcal{B}(D_s \rightarrow s\bar{s})$	65.6	2.7	0.7	1.0	1.8	3.5
$\mathcal{B}(\text{Other Annihilation})$	21.5	2.8	0.1	0.3	2.0	3.9

is a subtlety in the last line of Eq. 4.5. The decay $D_s \rightarrow s\bar{s}\bar{s}$ always makes at least one kaon, and when the decay is $D_s \rightarrow K\bar{K}\bar{s}$, i.e., $\mathcal{B}(K\bar{K}\bar{s})$, makes 2 more. Line 5, for the kaon yield, properly handles this.

4.4 Results from Global Fit

We minimize χ^2 by varying $\mathcal{B}(\eta)$, $\mathcal{B}(\eta')$, $\mathcal{B}(\phi)$, and $\mathcal{B}(K\bar{K})$. All other $\mathcal{B}(XX)$ parameters are fixed as previously described. Further, we have the unitarity requirement $\mathcal{B}(s\bar{s}) + \mathcal{B}(s\bar{s}\bar{s}) + \mathcal{B}(\bar{s}) + \mathcal{B}(\bar{s}\bar{s}) + \mathcal{B}(\text{Annihilation}) = 1.0$. Our fit gives $\mathcal{B}(\eta)$, $\mathcal{B}(\eta')$, $\mathcal{B}(\phi)$, $\mathcal{B}(K\bar{K})$, and hence $\mathcal{B}(s\bar{s})$, $\mathcal{B}(s\bar{s}\bar{s})$, $\mathcal{B}(\bar{s})$, and $\mathcal{B}(\bar{s}\bar{s})$. Unitarity then gives $\mathcal{B}(\text{Other Annihilation})$. Results are given in Table 4.2.

We have five measurements, and four free parameters. So it would appear that there is one degree of freedom. However, the single kaon and di-kaon measurements are highly correlated, so we effectively have more like four measurements. This is reflected in the χ^2 of the fit, 0.03. We have also made a fit leaving the di-kaon term out, and a fit leaving the single kaon term out. These fits give essentially the same result as the nominal fit with both terms included.

In interpreting the results in Table 4.2, it should be recognized that the decay products of the true “other annihilation” diagrams will include some $D_s \rightarrow$ gluons $\rightarrow s\bar{s}$ events, thus being treated as part of $\mathcal{B}(s\bar{s})$ rather than “other annihilation”. Also, the gluons will make $u\bar{u}$, $d\bar{d}$, which will sometimes make η , η' , again being treated

as a contribution to $\mathcal{B}(s\bar{s})$. Thus $\mathcal{B}(\text{Other Annihilation})$ should be viewed as a lower bound, $\mathcal{B}(\eta)$, $\mathcal{B}(\eta')$, $\mathcal{B}(\phi)$, $\mathcal{B}(K\bar{K})$ as upper bounds, on contributions from the various diagrams in Fig. 4.1. On the other hand, an overestimate of $\mathcal{B}(\text{extra } \eta)$ will give an overestimate of $\mathcal{B}(\text{Other Annihilation})$.

We can obtain a conservative lower bound on $\mathcal{B}(\text{Other Annihilation})$ by setting $f_1 = f_2 = 0$ and $\mathcal{B}(\text{extra } \eta) = 0$. That gives $\mathcal{B}(\text{Other Annihilation}) = 13.3 \pm 3.0\%$, i.e., $> 9.5\%$ at 90% C.L..

4.5 Singly-Cabibbo-Suppressed Decay Rate

We use our measurements of the total kaon yield and the total di-kaon yield to get a measurement of the singly-Cabibbo-suppressed rate. If there were no tri-kaon events, then (total kaon yield) minus $2 \times$ (total di-kaon yield) would give (single kaon yield) which would include the \bar{s} final state, and that fraction of the $s\bar{s}\bar{s}$ final state for which the $s\bar{s}$ component hadronized as η , η' , or ϕ . Tri-kaon events complicate the situation. As mentioned earlier, in counting di-kaons, a given charge pairing (K^+K^+ , $K^+K_S^0$, K^+K^- etc.) is counted once. Thus $K_S^0 K_S^0 K_S^0 X$ is counted as one di-kaon, while $K^+ K_S^0 K_S^0 X$ is counted as two, $K^+ K_S^0 K^- X$ as three. For the total kaon yield, a tri-kaon event is counted as 3 kaons, In taking (total kaon yield) minus $2 \times$ (total di-kaon yield) as a way of counting singly-Cabibbo-suppressed yield, the “right” answer for a tri-kaon event is +1, and what we actually obtain is +1, -1, and -3, for the different tri-kaon events, on average -1 instead of +1. Thus, our proposed procedure will underestimate the singly-Cabibbo-suppressed rate. To the extent that the tri-kaon rate is small, the underestimate is small. We estimate and apply a correction.

Our numbers are: total kaon yield is $(85.6 \pm 2.3)\%$, total di-kaon yield is $(39.9 \pm 1.8)\%$. The errors are *highly* correlated. Taking correlations into consideration, we find kaon - $2 \times$ di-kaon is $(5.8 \pm 2.2)\%$. Taking $\mathcal{B}(s\bar{s}\bar{s})/\mathcal{B}(s\bar{s})$ to be $\sim 1/20$, and $\mathcal{B}(s\bar{s}\bar{s} \rightarrow \text{tri-kaon})/\mathcal{B}(s\bar{s}\bar{s})$ to be $< \mathcal{B}(K\bar{K})/\mathcal{B}(s\bar{s}) = 0.39$, our correction factor for the presence of tri-kaon decays is $< (65.6 \times \frac{1}{20} \times 0.39 \times 2)\%$. Thus, the correction factor is $< 2.6\%$. Taking it to be $(1.3 \pm 1.3)\%$, the measured branching fraction for $D_s \rightarrow \text{single-Cabibbo-suppressed}$ is $(7.1 \pm 2.2 \pm 1.3)\%$. The expected branching fraction is $(|V_{us}/V_{ud}|^2 + |V_{cd}/V_{cs}|^2) \times \mathcal{B}(s\bar{s}) \approx \frac{1}{10} \times \mathcal{B}(s\bar{s})$. Taking $\mathcal{B}(s\bar{s})$ from Table 4.2,

we see fine agreement between expectations and measurements.

4.6 Minimum Yields of π^+ , π^- , and π^0

From our global fit, we can compute the minimum yields of π^+ , π^- , and π^0 for each category. For example, for the Cabibbo-favored decay $D_s^+ \rightarrow s\bar{s} \rightarrow \eta X$, with 14.7% yield, we compute the yields of π^+ , π^- , and π^0 that come from a 14.7% η yield. To this we add 14.7% π^+ yield, since that must be present to conserve charge. (This is an overestimate, because semileptonic decays have charge conserved via e^+ or μ^+ , consequently we perform a subtraction to allow for that.) For $D_s^+ \rightarrow s\bar{s}\bar{s} \rightarrow \eta\bar{s}X$, with 0.6% yield, similarly we compute the yields of π^+ , π^- , and π^0 that come from a 0.6% η yield. Charge conservation might be achieved by a π^+ , but also by a K^+ . Lacking any information on how much comes from π^+ , how much from K^+ , we assume half from each. Our global fit gives a single number $\mathcal{B}(K\bar{K}) = 25.4\%$, for the di-kaon yield. To determine the π^+ , π^0 , and π^- yields, we need yields for the separate di-kaon combinations, $K_S^0 K_S^0$, $K_S^0 K^+$, $K_S^0 K^-$, etc. For our calculation, we take the measured di-kaon yields from Table 3.12, and normalize them so their sum equals $\mathcal{B}(K\bar{K})$. (Where we have only an upper limit, we use half of it for the “measurement”).

The results of our computation are given in Table 4.3. There one sees that the yields of π^+ , π^- , and π^0 should be larger than 96.2%, 20.5%, and 46.8%, respectively. The observed yields are indeed larger than these numbers. Thus, on average, 1/4 of the D_s decays will contain an additional $\pi^+\pi^-$ pair, and 3/4 of the D_s decays will contain an additional π^0 (or 1/2 contain one additional π^0 , 1/8 contain two additional π^0 's).

For the 21.5% yield of $D_s \rightarrow$ Other Annihilation decays, we know nothing about the pion content other than that there will be one π^+ to conserve charge. One might reasonably expect that a substantial fraction of the 1/4 of the D_s decays containing an additional $\pi^+\pi^-$ pair would be in the “Other Annihilation” decays. As for the additional π^0 in 3/4 of the decays, that can appear any place, e.g., as converting a charge-conserving π^+ into a ρ^+ . They will probably appear disproportionately in the “Other Annihilation” decays, as these start (in our table) with fewer particles.

Table 4.3: The minimum yields of π^+ , π^- , and π^0 for each category. We compute the yields of π^+ , π^- , and π^0 that come from signal particles. In addition to that, we add charged pions to conserve charge. Semileptonic decays have charge conserved via e^+ or μ^+ , consequently we perform a subtraction to allow for that.

Mode	\mathcal{B} (%)	Charge Conservation		Particle Decay			Total Yields		
		π^+	π^-	π^+	π^-	π^0	π^+	π^-	π^0
ηX	14.7	14.7	0.0	4.0	4.0	17.7	18.7	4.0	17.7
$\eta \bar{s}X$	0.6	0.3	0.0	0.2	0.2	0.7	0.4	0.2	0.7
$\eta' X$	10.3	10.3	0.0	9.7	9.7	12.7	20.0	9.7	12.7
$\eta' \bar{s}X$	0.4	0.2	0.0	0.4	0.4	0.5	0.6	0.4	0.5
ϕX	15.1	15.1	0.0	2.4	2.4	2.5	17.5	2.4	2.5
$\phi \bar{s}X$	0.6	0.3	0.0	0.1	0.1	0.1	0.4	0.1	0.1
Extra ηX	6.0	0.0	0.0	1.6	1.6	7.2	1.6	1.6	7.2
$\bar{s}X$ (no η, η')	2.1	1.0	0.0	0.0	0.0	0.0	1.0	0.0	0.0
$\bar{s}X, X \rightarrow \eta$	1.0	0.5	0.0	0.3	0.3	1.2	0.8	0.3	1.2
$\bar{s}X, X \rightarrow \eta'$	1.0	0.5	0.0	1.0	1.0	1.3	1.5	1.0	1.3
$K_S^0 K_S^0 (K_L^0 K_L^0) X$	3.3	3.3	0.0	0.0	0.0	0.0	3.3	0.0	0.0
$K_S^0 K^+ (K_L^0 K^+) X$	11.4	0.0	0.0	0.0	0.0	0.0	0.0	0.0	0.0
$K_S^0 K^- (K_L^0 K^-) X$	3.7	7.5	0.0	0.0	0.0	0.0	7.5	0.0	0.0
$K^+ K^- (-\phi) X$	7.9	7.9	0.0	0.0	0.0	0.0	7.9	0.0	0.0
$K^+ K^+ X$	0.1	0.0	0.1	0.0	0.0	0.0	0.0	0.1	0.0
$K^- K^- X$	0.03	0.1	0.0	0.0	0.0	0.0	0.1	0.0	0.0
$K_S^0 K_L^0 (-\phi) X$	0.0	0.0	0.0	0.0	0.0	0.0	0.0	0.0	0.0
$e^+ (\mu^+) X$	10.7	-10.7	0.0	0.0	0.0	0.0	-10.7	0.0	0.0
$\tau^+ \nu$	5.6	0.0	0.0	4.1	0.8	2.9	4.1	0.8	2.9
$\mu^+ \nu$	0.6	0.0	0.0	0.0	0.0	0.0	0.0	0.0	0.0
Other Annih.	21.5	21.5	0.0	0.0	0.0	0.0	21.5	0.0	0.0
Minimum Yields							96.2	20.5	46.8
Observed Yields							119.3	43.2	123.4
Additional Yields							23.0	22.7	76.7

4.7 D_s Inclusive ω Decay

The inclusive ω yield, $D_s \rightarrow \omega X$, of $6.1 \pm 1.4\%$, is substantial. While ω has an $s\bar{s}$ component, it is *very* small, so it is unlikely that very much of the ω yield comes from the $s\bar{s}$ component of $D_s^+ \rightarrow s\bar{s}X$. At quark level, this is $D_s^+ \rightarrow s\bar{s}u\bar{d}$, and a decay $D_s^+ \rightarrow \pi^+ \eta\omega$ is quite possible. A decay $D_s^+ \rightarrow \pi^+ \eta'\omega$, from energy considerations, is just barely possible. From the decay $D_s^+ \rightarrow s\bar{s}\bar{s}$, ω could come from $D_s^+ \rightarrow K^+ \eta\omega$ (barely), but not from $D_s^+ \rightarrow K^+ \eta'\omega$. From $D_s^+ \rightarrow \bar{s}X$, it can come from $D_s^+ \rightarrow K^+ \omega X$, with lots of phase space. And from “Other Annihilation”, there are lots of possibilities.

Chapter 5

Search for D_s^+ Exclusive Hadronic Decays Involving ω

The inclusive ω yield, $D_s^+ \rightarrow \omega X$, is substantial. Up to now, the only D_s^+ exclusive hadronic decay mode involving ω that has been observed is $D_s^+ \rightarrow \pi^+ \omega$ with the branching fraction of $\mathcal{B}(D_s^+ \rightarrow \pi^+ \omega) = 0.25 \pm 0.09\%$ [11]. There is lots of room for D_s^+ exclusive hadronic decays involving ω . The study of ω production in D_s^+ decays is of interest in shedding light on mechanisms of weak decay and their interplay with long-distance (nonperturbative) physics. A search for D_s^+ *exclusive* decays involving ω will be presented in this section. The exclusive modes are listed as follows:

- $D_s^+ \rightarrow \pi^+ \pi^0 \omega$
- $D_s^+ \rightarrow \pi^+ \omega$
- $D_s^+ \rightarrow \pi^+ \eta \omega$
- $D_s^+ \rightarrow K^+ \pi^0 \omega$
- $D_s^+ \rightarrow K^+ \omega$
- $D_s^+ \rightarrow K^+ \eta \omega$

5.1 Data and Monte Carlo Samples

We use 586 pb^{-1} of data produced in e^+e^- collisions at CESR near the center-of-mass energy $\sqrt{s} = 4170 \text{ MeV}$ to search for D_s^+ exclusive decays involving ω , the same sample used for the D_s^+ inclusive analysis.

For each signal mode, a 50K signal Monte Carlo sample, one D_s decays in tag modes and the other D_s decays in our particular signal mode, was generated to calculate double-tag Monte Carlo efficiency. A single-tag Monte Carlo sample, one D_s decays in tag modes and the other D_s decays generically, was generated to get single-tag Monte Carlo efficiency. Corresponding $20 \times \text{mcDD-mix}$ sample with ISR (generic mixture of $D\bar{D}$ MC), is used to study the possible background features.

5.2 Event Selection

5.2.1 Double-Tagging Technique

Here we employ a double-tagging technique, the same as the technique that is used in the D_s^+ inclusive analysis. Three tag modes used in this analysis are $D_s^- \rightarrow K_S^0 K^-$, $D_s^- \rightarrow \phi \pi^-$, and $D_s^- \rightarrow K^{*0} K^-$, the same as in the D_s^+ inclusive analysis. The details on D_s tag selection have been presented in Chapter 3. We have 18586 ± 163 single-tag (ST) events for further analysis.

5.2.2 Good Track Selection and PID

Number of good tracks is required according to the requirement of each mode. Such as for $D_s^+ \rightarrow \pi^+ \pi^0 \omega, \omega \rightarrow \pi^+ \pi^- \pi^0$, we require there must be three and only three good tracks on the signal side. Mode dependent requirements on numbers of kaon and pion are applied on the signal side. For example, we require there must be exactly one kaon and two pions for $D_s^+ \rightarrow K^+ \omega, \omega \rightarrow \pi^+ \pi^- \pi^0$. Good track selection requirements and particle identification have been described in Chapter 3.

5.2.3 π^0 and η Selection

We identify π^0 and η candidates via $\pi^0 \rightarrow \gamma\gamma$ and $\eta \rightarrow \gamma\gamma$, detecting the photons in the CsI calorimeter. Standard Version-2 Dtag procedures [29] are used to select π^0 and η candidates. We require that the calorimeter clusters have a measured energy above 30 MeV, and not be matched to any charged track. We select best π^0 or η candidate based on the pull mass. For the modes with two π^0 's (or one π^0 and one η) in the final state, we select best two non-overlapping π^0 's (or one π^0 and one η) based on their pull masses.

5.3 Yields in Data

5.3.1 Absolute Branching Fractions

The absolute branching fractions of our interested modes are given by

$$\mathcal{B}_{\text{sig}} = \frac{N_{\text{DT}}}{N_{\text{ST}}} \times \frac{\epsilon_{\text{ST}}}{\epsilon_{\text{DT}}},$$

where N_{ST} is the single-tag yield, and N_{DT} is the double-tag yield. The ϵ_{ST} is the single-tag MC efficiency obtained from single-tag MC samples (one D_s decays in tag modes and the other D_s decays generically) and ϵ_{DT} is the double-tag efficiency obtained from signal MC samples (one D_s decays in tag modes and the other D_s decays in our particular signal mode). We get the single-tag and double-tag efficiencies from single-tag MC sample and signal MC sample respectively. Thus, the tag bias is automatically considered and corrected by this absolute branching fraction calculation procedure.

Single-tag yield is obtained from the D_s tag invariant mass distributions as we described in Chapter 3. Double-tag yields are extracted from the $\pi^+\pi^-\pi^0$ invariant mass distribution after requiring that both the tag- D_s and signal- D_s be in the D_s nominal mass region (20 MeV mass window on the tag side and 30 MeV mass window on the signal side due to π^0 or η on the signal side). The signal and sideband regions of $\pi^+\pi^-\pi^0$ invariant mass are defined as follows:

- signal region : $-20 < M_{\pi^+\pi^-\pi^0} - M_\omega < +20$ MeV.

- lower sideband region : $-80 < M_{\pi^+\pi^-\pi^0} - M_\omega < -40$ MeV.
- upper sideband region : $+40 < M_{\pi^+\pi^-\pi^0} - M_\omega < +80$ MeV.

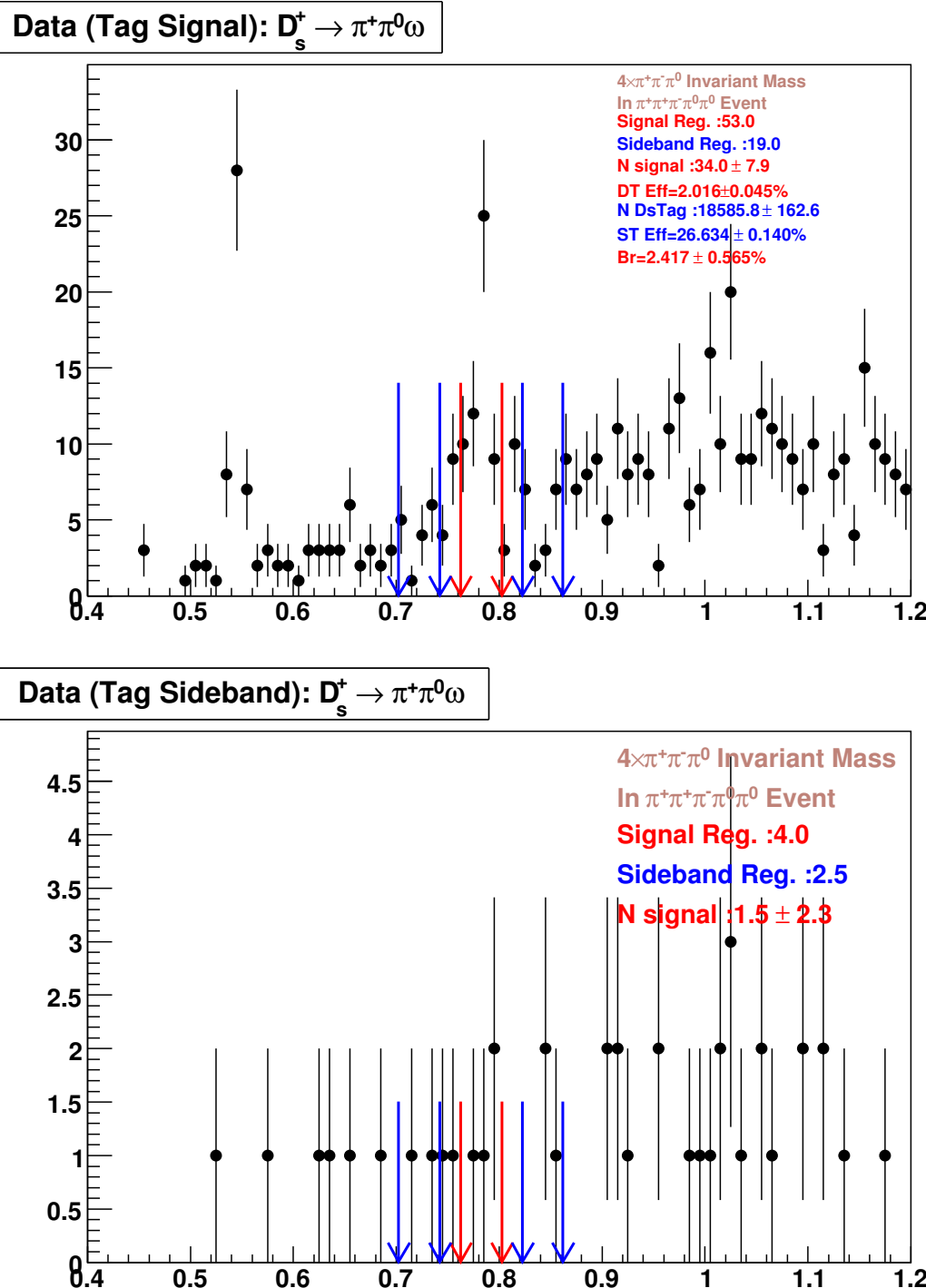
5.3.2 $D_s^+ \rightarrow \pi^+\pi^0\omega$

For $D_s^+ \rightarrow \pi^+\pi^0\omega$ mode, we require there must be three and only three charged pions against the D_s tag. Two non-overlapping best π^0 's are selected based on π^0 pull masses. The invariant mass distribution of all possible combinations of $\pi^+\pi^-\pi^0$ in $D_s^+ \rightarrow \pi^+\pi^0\omega, \omega \rightarrow \pi^+\pi^-\pi^0$ events is shown in Fig. 5.1 upper plot. The red lines indicate the signal region and blue lines indicate the upper and lower sideband regions. The detailed numbers of signal and sideband events, sideband-subtracted double-tag signal yield, single-tag yield, and efficiencies are shown in Fig. 5.1 upper plot. We find the clear $\eta \rightarrow \pi^+\pi^-\pi^0$ and $\phi \rightarrow \pi^+\pi^-\pi^0$ peaks in Fig. 5.1 upper plot. These two peaks come from $D_s^+ \rightarrow \rho^+(\pi^+\pi^0)\eta, \eta \rightarrow \pi^+\pi^-\pi^0$ and $D_s^+ \rightarrow \rho^+(\pi^+\pi^0)\phi, \phi \rightarrow \pi^+\pi^-\pi^0$ events. The lower plot of Fig. 5.1 shows the invariant mass distribution of $\pi^+\pi^-\pi^0$ in D_s tag sideband regions. No background from D_s tag sideband regions is found from this plot. In the D_s tag signal region (upper plot), a clear ω signal is found. We apply the ω mass sideband subtraction to obtain the double-tag yield.

The $D_s^+ \rightarrow \pi^+\pi^0\omega$ decay might come from $D_s^+ \rightarrow \rho^+(\pi^+\pi^0)\omega$. A two dimensions plot of $M_{\pi^+\pi^0}$ vs. $M_{\pi^+\pi^-\pi^0}$ is used to search for a ρ^+ component in $D_s^+ \rightarrow \pi^+\pi^0\omega$ decay as shown in Fig. 5.2. Clear $\rho^+\eta$ and $\rho^+\phi$ bands are found in Fig. 5.2. The red histogram on the right plot in Fig. 5.2 is the $\pi^+\pi^0$ invariant mass distribution after the corresponding ω mass sideband subtraction. The blue histogram is from the phase space $\pi^+\pi^0\omega$ Monte Carlo. The green histogram is from the $\rho^+\omega$ Monte Carlo. We fit data histogram to sum of phase space $\pi^+\pi^0\omega$ MC and $\rho^+\omega$ MC. The fit result suggests that half of the $D_s^+ \rightarrow \pi^+\pi^0\omega$ decay comes from the $D_s^+ \rightarrow \rho^+\omega, \rho^+ \rightarrow \pi^+\pi^0$ decay as shown in Fig. 5.3.

5.3.3 $D_s^+ \rightarrow \pi^+\omega$

The decay of $D_s^+ \rightarrow \pi^+\omega$ has been observed before and the branching fraction of this decay was measured to be $0.25 \pm 0.09\%$ [11]. To measure this decay, we require

Figure 5.1: $D_s^+ \rightarrow \pi^+ \pi^0 \omega$ decay study.

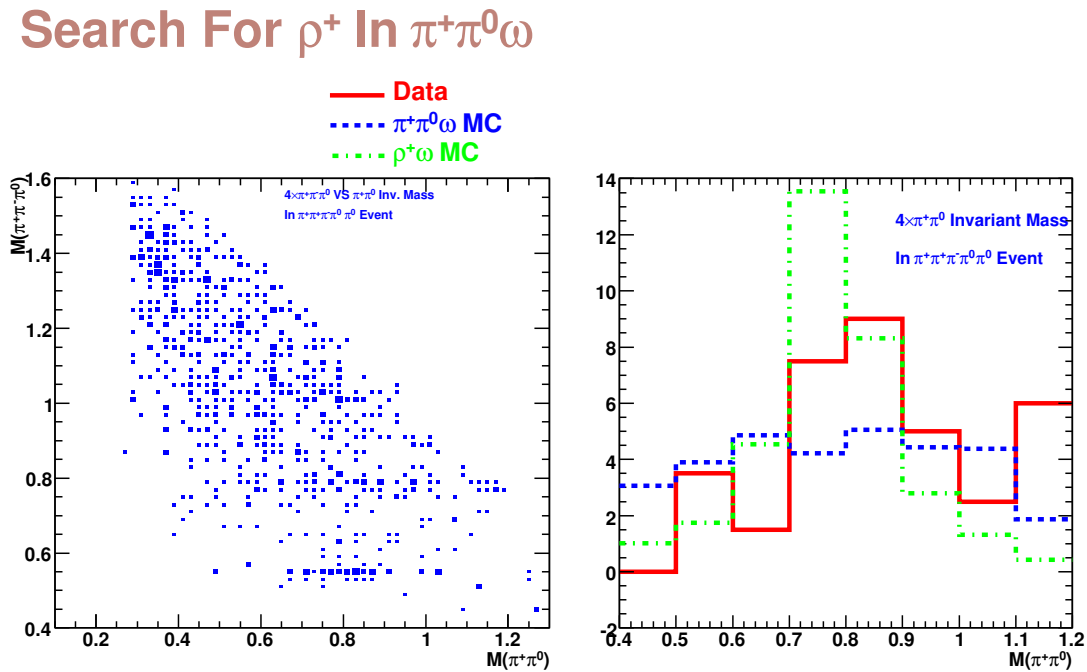


Figure 5.2: Two dimensions plot of $M_{\pi^+\pi^0}$ vs. $M_{\pi^+\pi^-\pi^0}$. Clear $\rho^+\eta$ and $\rho^+\phi$ bands are found. The red histogram on the right plot is the $\pi^+\pi^0$ invariant mass distribution after the corresponding ω mass sideband subtraction. The blue histogram is from the phase space $\pi^+\pi^0\omega$ Monte Carlo. The green histogram is from the $\rho^+\omega$ Monte Carlo.

Fit Plot for ρ^+ Searching In $\pi^+\pi^0\omega$

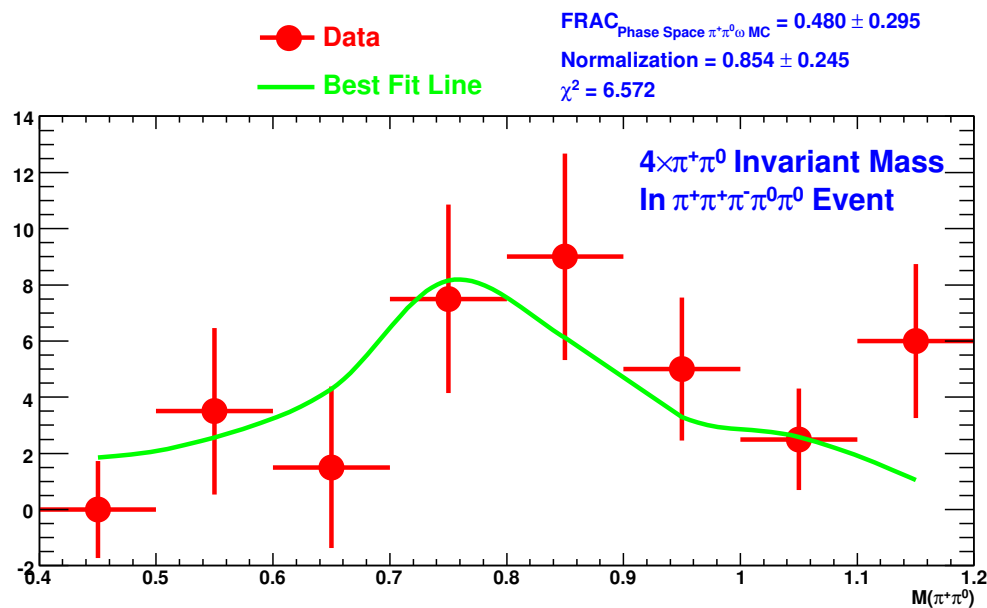
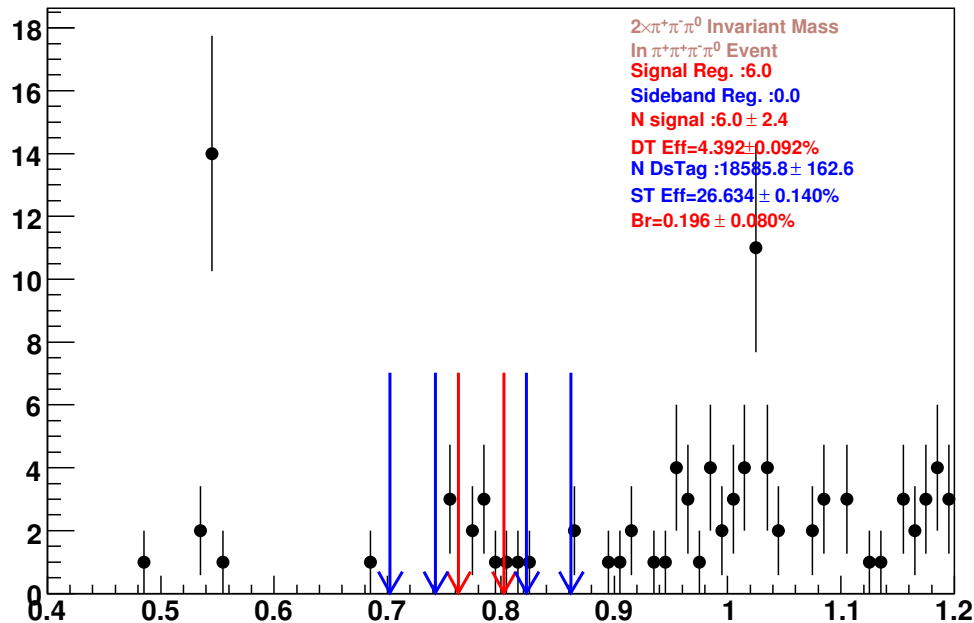
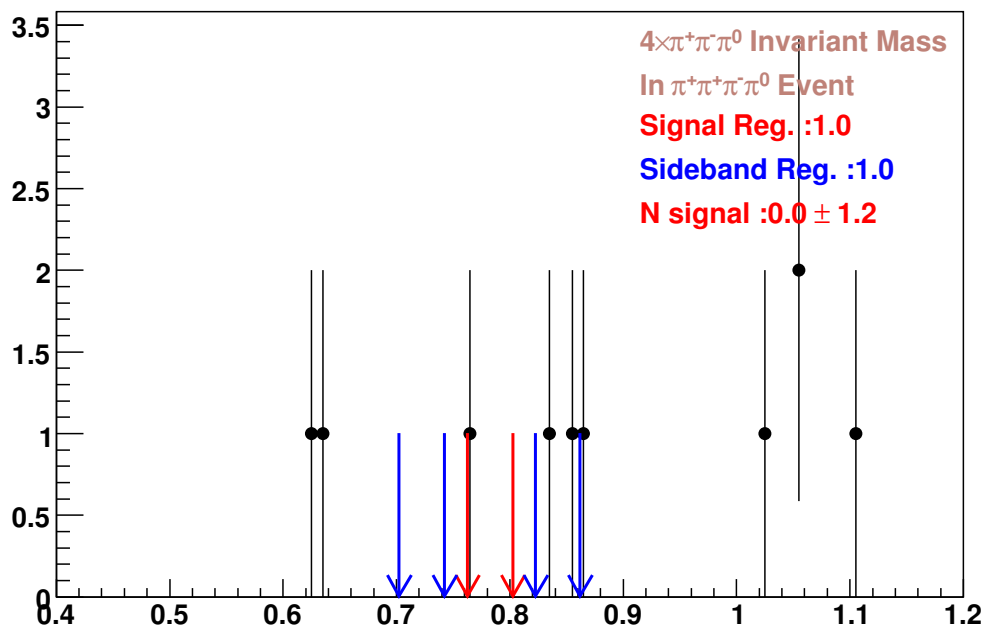


Figure 5.3: Fit data to sum of phase space $\pi^+\pi^0\omega$ MC and $\rho^+\omega$ MC to extract the $\rho^+\omega$ contribution to $D_s^+ \rightarrow \pi^+\pi^0\omega$ decay.

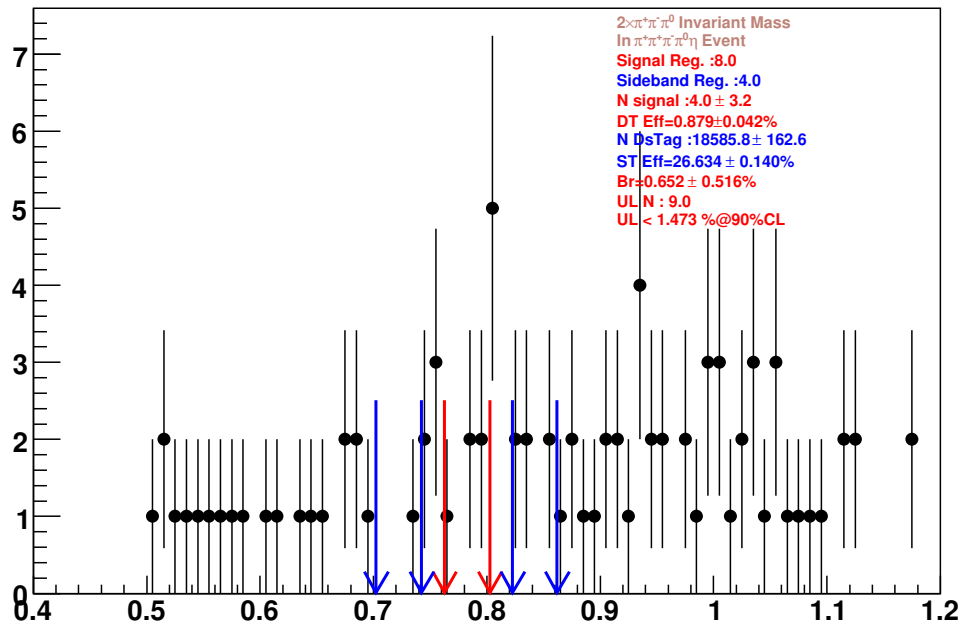
there must be three and only three charged pions on the signal side. One best π^0 has been selected based on its pull mass. The invariant mass distribution of all possible combinations of $\pi^+\pi^-\pi^0$ in $D_s^+ \rightarrow \pi^+\omega, \omega \rightarrow \pi^+\pi^-\pi^0$ events is shown in Fig. 5.4 upper plot. Same as before, the red lines indicate the signal region and blue lines indicate the upper and lower sideband regions. The detailed numbers of signal and sideband events, sideband-subtracted double-tag signal yield, single-tag yield, and efficiencies are shown in Fig. 5.4 upper plot. Clear $\eta \rightarrow \pi^+\pi^-\pi^0$ and $\phi \rightarrow \pi^+\pi^-\pi^0$ peaks in Fig. 5.4 upper plot come from $D_s^+ \rightarrow \pi^+\eta, \eta \rightarrow \pi^+\pi^-\pi^0$ and $D_s^+ \rightarrow \pi^+\phi, \phi \rightarrow \pi^+\pi^-\pi^0$ events. Both of these two decays are Cabibbo-favored and have big branching fractions [11]. The lower plot of Fig. 5.4 shows the invariant mass distribution of $\pi^+\pi^-\pi^0$ in D_s tag sideband regions. No background from D_s tag sideband regions is found from this plot. Signal evidence is found in the ω mass signal region and no background event has been found in the ω mass sideband regions.

5.3.4 $D_s^+ \rightarrow \pi^+\eta\omega$

We require there must be three and only three charged pions on the signal side when searching for $D_s^+ \rightarrow \pi^+\eta\omega$ decay. One best π^0 and one best η are selected based on their pull masses on the signal side. There are two possible combinations of $\pi^+\pi^-\pi^0$ in a $D_s^+ \rightarrow \pi^+\eta\omega, \omega \rightarrow \pi^+\pi^-\pi^0$ event. The invariant mass distribution of $\pi^+\pi^-\pi^0$ is shown in Fig. 5.5 upper plot. Red and blue lines indicate the ω mass signal and sideband regions. The detailed numbers of signal and sideband events, sideband-subtracted double-tag signal yield, single-tag yield, and efficiencies are also shown in Fig. 5.5 upper plot. The lower plot of Fig. 5.5 shows the invariant mass distribution of $\pi^+\pi^-\pi^0$ in D_s tag sideband regions. No background from D_s tag sideband regions is found from this plot. No clear signal evidence is found for $D_s^+ \rightarrow \pi^+\eta\omega$ decay. We set upper limit at 90% confidence level according to the number of observed events in the ω mass signal region and the expected background contribution by using ω mass sideband regions.

Data (Tag Signal): $D_s^+ \rightarrow \pi^+ \omega$ Data (Tag Sideband): $D_s^+ \rightarrow \pi^+ \omega$ Figure 5.4: $D_s^+ \rightarrow \pi^+ \omega$ decay study

Data (Tag Signal): $D_s^+ \rightarrow \pi^+ \eta \omega$



Data (Tag Sideband): $D_s^+ \rightarrow \pi^+ \eta \omega$

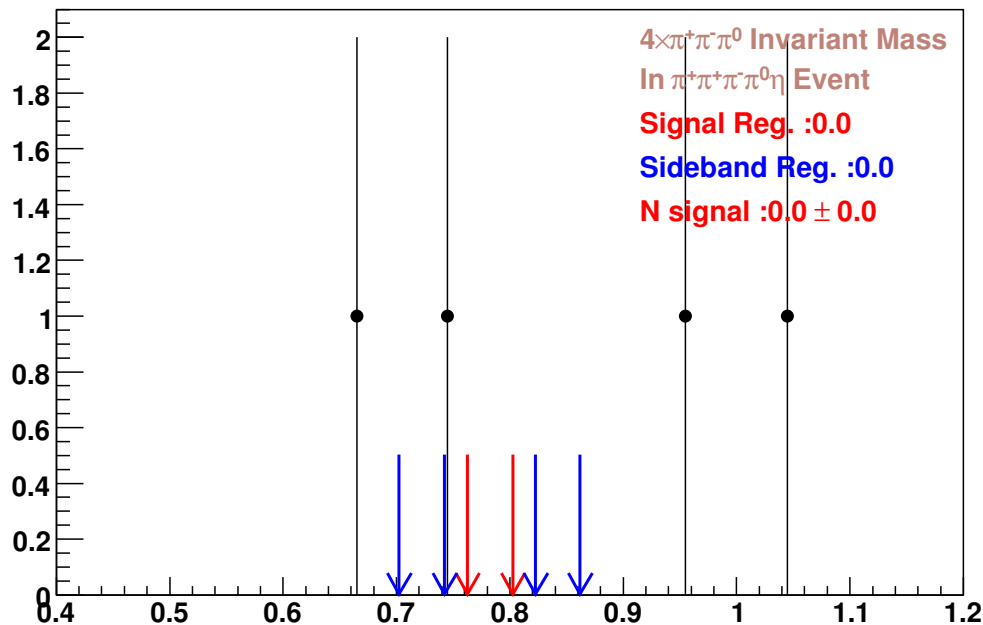


Figure 5.5: $D_s^+ \rightarrow \pi^+ \eta \omega$ decay study

5.3.5 $D_s^+ \rightarrow K^+ \pi^0 \omega$

To search for $D_s^+ \rightarrow K^+ \pi^0 \omega$ decay, we require there must be one and only one charged kaon, and two and only two charged pions on the signal side. Best two π^0 's are selected based on their pull masses on the signal side. The invariant mass distribution of $\pi^+ \pi^- \pi^0$ is shown in Fig. 5.6 upper plot. Red and blue lines indicate the ω mass signal and sideband regions. The detailed numbers are shown in Fig. 5.6 upper plot. No background from D_s tag sideband regions (lower plot) is found. No clear signal evidence is found for $D_s^+ \rightarrow K^+ \pi^0 \omega$ decay and an upper limit is set at 90% confidence level.

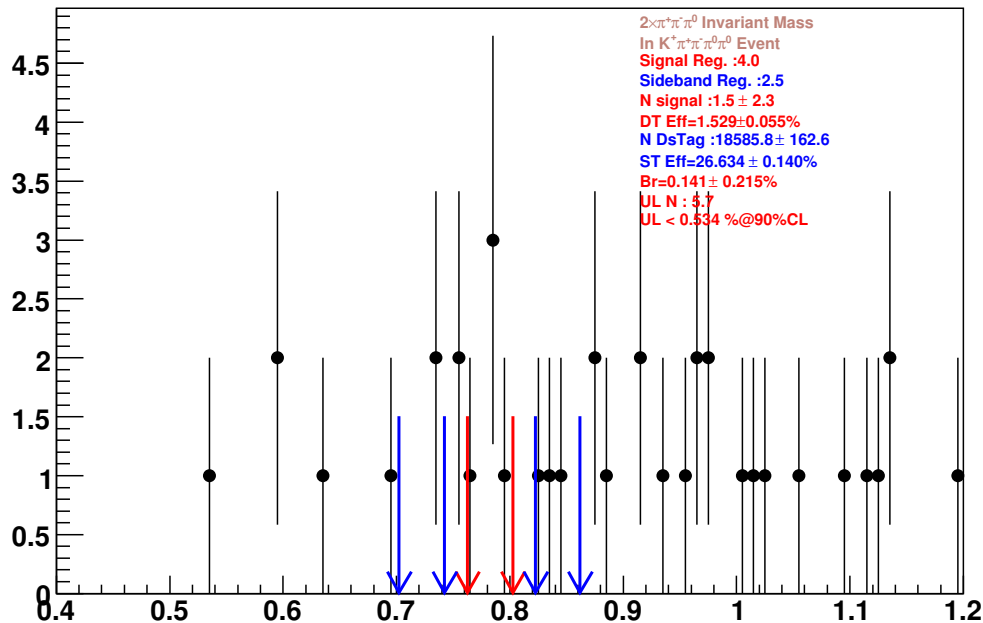
5.3.6 $D_s^+ \rightarrow K^+ \omega$

To search for $D_s^+ \rightarrow K^+ \omega$ decay, similarly we require there must be one and only one charged kaon, and two and only two charged pions on the signal side. One best π^0 is selected based on their pull masses on the signal side. The invariant mass distribution of $\pi^+ \pi^- \pi^0$, detailed numbers of yields, and efficiencies are shown in Fig. 5.7 upper plot. The lower plot of Fig. 5.7 shows there is no background from D_s tag sideband regions. No clear signal evidence is found for $D_s^+ \rightarrow K^+ \omega$ decay.

5.3.7 $D_s^+ \rightarrow K^+ \eta \omega$

We also search for $D_s^+ \rightarrow K^+ \eta \omega$ decay by requiring there must be one and only one charged kaon, and two and only two charged pions on the signal side. One best π^0 and one best η are selected based on their pull masses on the signal side. The invariant mass distribution of $\pi^+ \pi^- \pi^0$ is shown in Fig. 5.8 upper plot. Red and blue lines indicate the ω mass signal and sideband regions. The detailed numbers of signal and sideband events, sideband-subtracted double-tag signal yield, single-tag yield, and efficiencies are also shown in Fig. 5.8 upper plot. The lower plot of Fig. 5.8 shows the invariant mass distribution of $\pi^+ \pi^- \pi^0$ in D_s tag sideband regions. No background from D_s tag sideband regions is found from this plot. No signal evidence is found for $D_s^+ \rightarrow K^+ \eta \omega$ decay. We set upper limit at 90% confidence level according to the number of observed events in the ω mass signal region and the expected background contribution by using ω mass sideband regions.

Data (Tag Signal): $D_s^+ \rightarrow K^+ \pi^0 \omega$



Data (Tag Sideband): $D_s^+ \rightarrow K^+ \pi^0 \omega$

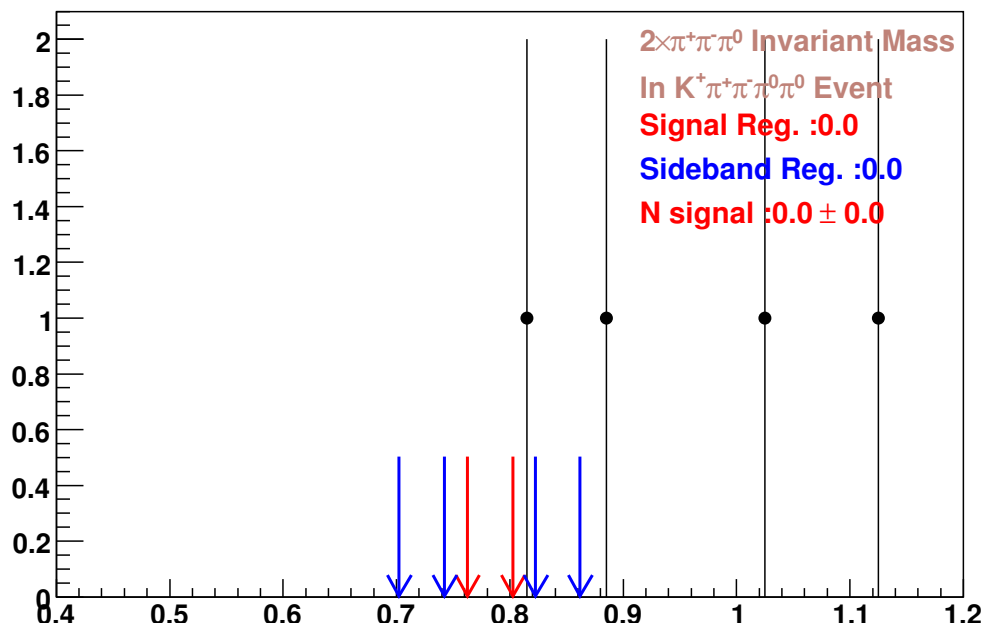
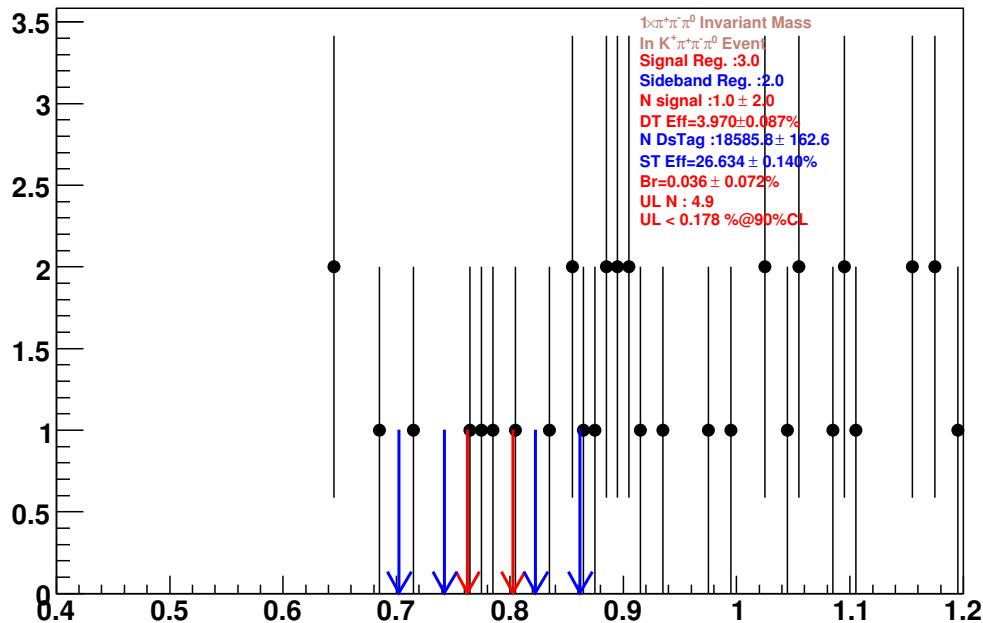
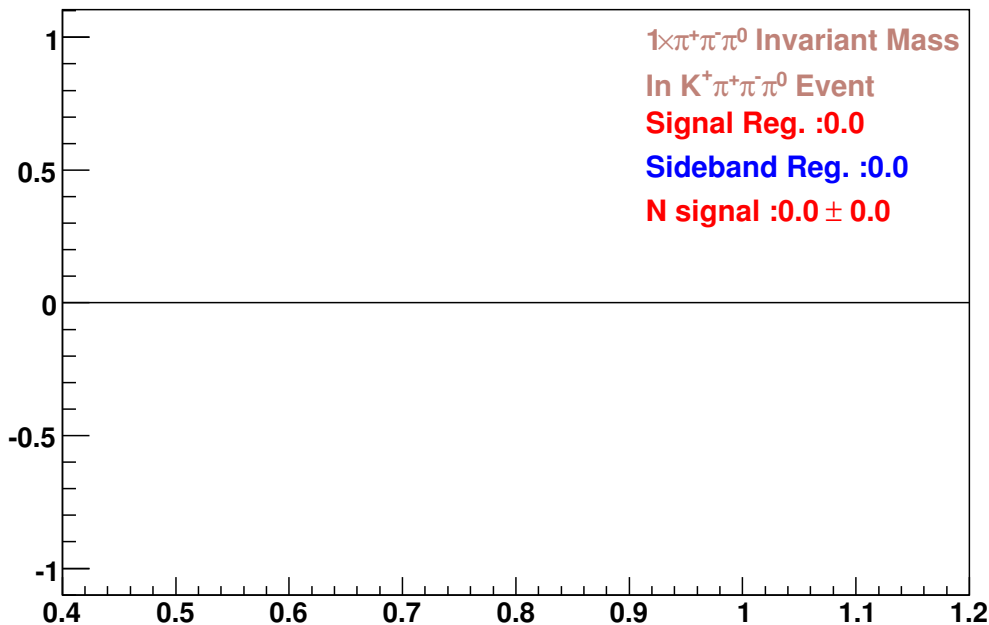
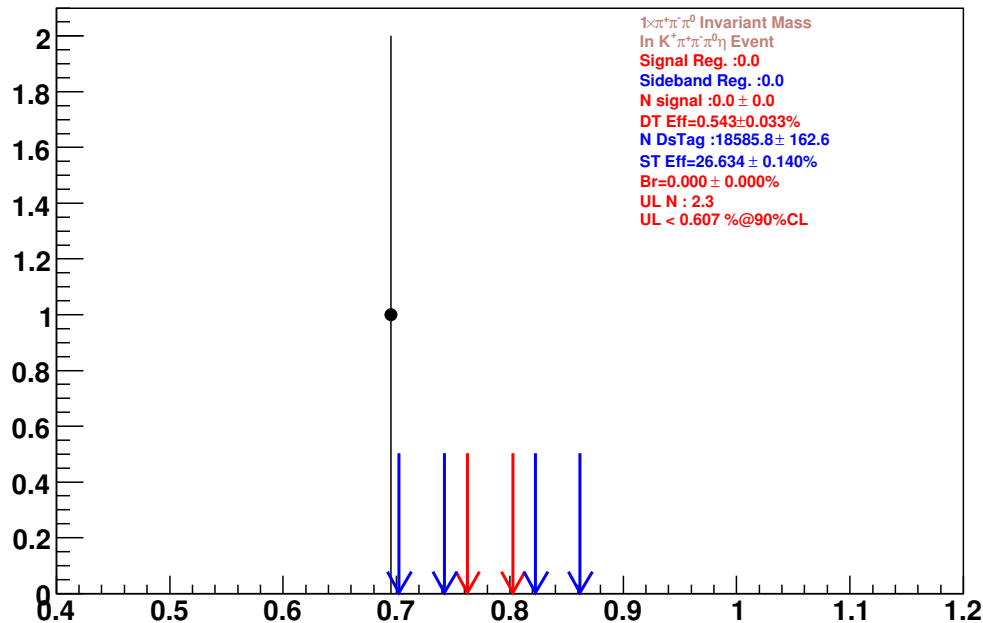


Figure 5.6: $D_s^+ \rightarrow K^+ \pi^0 \omega$ decay study

Data (Tag Signal): $D_s^+ \rightarrow K^+ \omega$

Data (Tag Sideband): $D_s^+ \rightarrow K^+ \omega$
Figure 5.7: $D_s^+ \rightarrow K^+ \omega$ decay study

Data (Tag Signal): $D_s^+ \rightarrow K^+ \eta \omega$



Data (Tag Sideband): $D_s^+ \rightarrow K^+ \eta \omega$

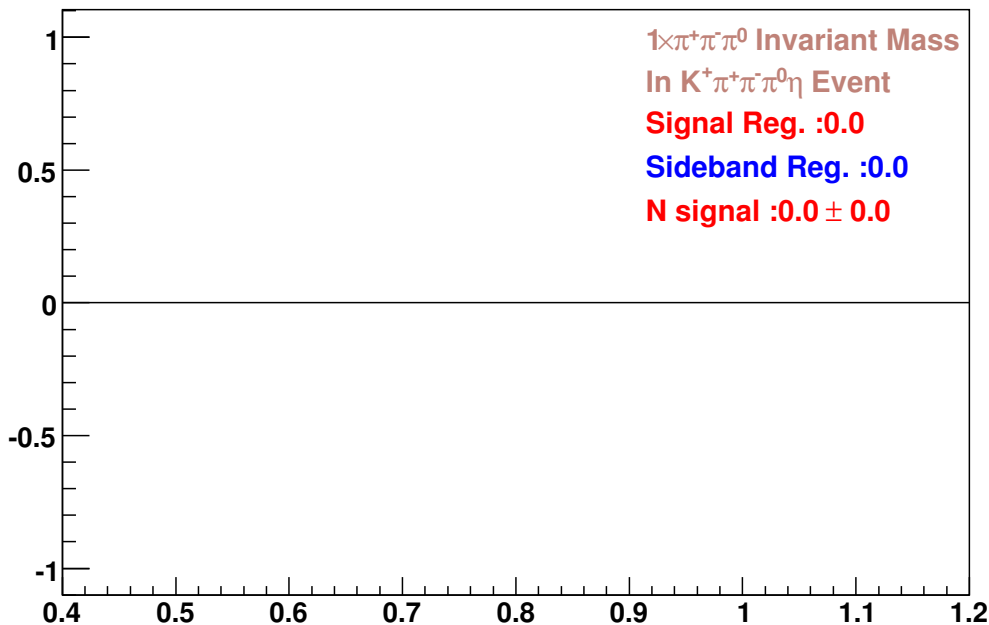


Figure 5.8: $D_s^+ \rightarrow K^+ \eta \omega$ decay study.

Table 5.1: The detailed yields. Here N_{Sg} is the observed event number from ω mass signal region, N_{Sd} is the scaled event number from ω mass sideband regions, N_{Ss} is the sideband-subtracted double-tag yield, and N_{Up} is the number that is used to set upper limit at 90% confidence level for low statistics modes.

Mode	N_{Sg}	N_{Sd}	N_{Ss}	N_{Up}	$\epsilon_{\text{DT}}(\%)$	$\mathcal{B}(\%)$
$D_s^+ \rightarrow \pi^+ \pi^0 \omega$	53.0	19.0	34.0 ± 7.9	—	2.016 ± 0.045	2.417 ± 0.565
$D_s^+ \rightarrow \pi^+ \omega$	6.0	0.0	6.0 ± 2.4	—	4.392 ± 0.092	0.196 ± 0.080
$D_s^+ \rightarrow \pi^+ \eta \omega$	8.0	4.0	4.0 ± 3.2	9.0	0.879 ± 0.042	< 1.473
$D_s^+ \rightarrow K^+ \pi^0 \omega$	4.0	2.5	1.5 ± 2.3	5.7	1.529 ± 0.055	< 0.534
$D_s^+ \rightarrow K^+ \omega$	3.0	2.0	1.0 ± 2.0	4.9	3.970 ± 0.087	< 0.178
$D_s^+ \rightarrow K^+ \eta \omega$	0.0	0.0	0.0 ± 0.0	2.3	0.543 ± 0.033	< 0.607

The detailed yields from ω mass signal and sideband regions for all modes are summarized in Table 5.1. Double-tag efficiency is also listed in Table 5.1. Branching fractions and upper limits listed here only include statistical error.

5.4 Double Check for D_s^+ Inclusive Decays

From the D_s^+ inclusive study analysis (Chapter 3), we found that the D_s^+ inclusive ω yield is substantial. But up to now, the only observed D_s^+ exclusive decay mode with ω in the final state is $D_s \rightarrow \pi^+ \omega$, $\mathcal{B}(D_s \rightarrow \pi^+ \omega) = 0.25 \pm 0.09\%$ [11]. To confirm our results, cross check has been performed. We extract inclusive ω yield from $\pi^+ \pi^- \pi^0$ invariant mass distribution. The $\eta \rightarrow \pi^+ \pi^- \pi^0$ and $\phi \rightarrow \pi^+ \pi^- \pi^0$ peaks should also show up in $\pi^+ \pi^- \pi^0$ invariant mass distribution. We can use this feature to perform the cross check for our procedure.

Fig. 5.9 shows the data and Monte Carlo comparison plot of $\pi^+ \pi^- \pi^0$ invariant mass distribution. Blue solid histogram is obtained from our generic Monte Carlo and scaled to data according to D_s tag yield. Red points with error bars are from real data. Clear η and ϕ peaks are found in both data and Monte Carlo. The agreement between data and Monte Carlo is fine. The ω peak only shows up in data but not in Monte Carlo because our generic Monte Carlo does not have much ω .

The D_s^+ inclusive η and ϕ yields can be measured by using $\eta \rightarrow \pi^+ \pi^- \pi^0$ and $\phi \rightarrow \pi^+ \pi^- \pi^0$ decays. Fig. 5.10 shows the details of the measurement of D_s^+ inclusive η decay through $\eta \rightarrow \pi^+ \pi^- \pi^0$ decay. Similar plots are shown in Fig. 5.11 for the

measurement of D_s^+ inclusive ϕ decay by using $\phi \rightarrow \pi^+\pi^-\pi^0$ decay. For both η and ϕ , good agreements with the corresponding measurements by using $\eta \rightarrow \gamma\gamma$ and $\phi \rightarrow K^+K^-$ decays are found. Same technique is used for the measurement of D_s^+ inclusive ω decay.

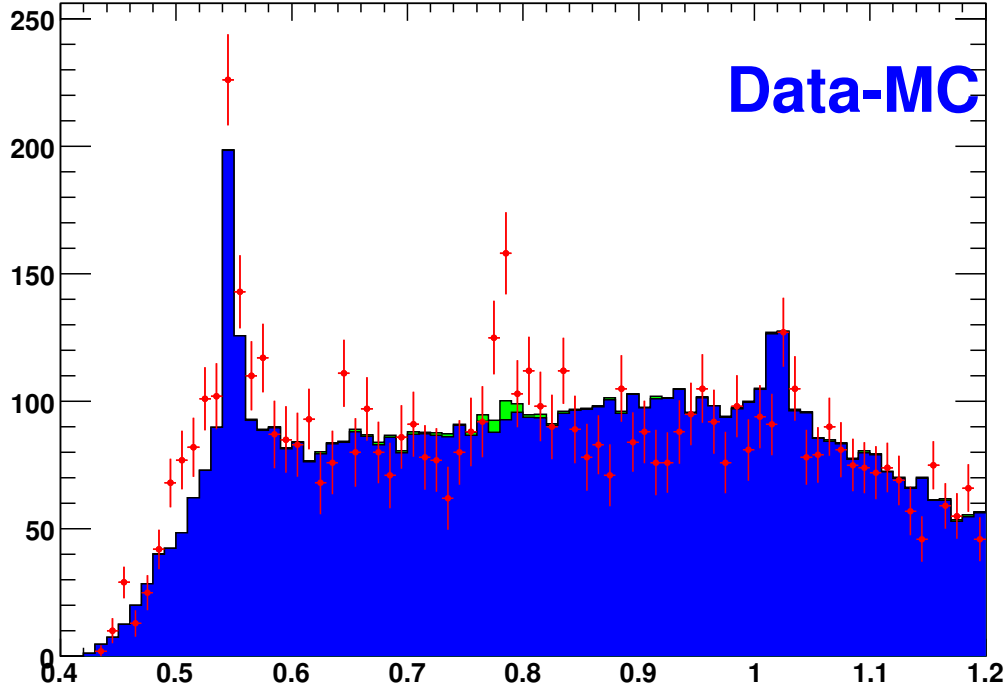


Figure 5.9: Data and Monte Carlo comparison plot of $\pi^+\pi^-\pi^0$ invariant mass distribution. Blue solid histogram is obtained from our generic Monte Carlo and scaled to data according to D_s tag yield. Red points with error bars are from real data. Clear η and ϕ peaks are found in both data and Monte Carlo. The ω peak only shows up in data but not in Monte Carlo.

5.5 Data and Monte Carlo Comparison

To understand any possible background contribution from generic D_s^+ decays, careful data and Monte Carlo comparison has been done for all of our signal modes. Fig. 5.12 to Fig. 5.17 show the data and Monte Carlo comparisons. Points with error bars are from real data and green shadow histogram is obtained from generic Monte Carlo.

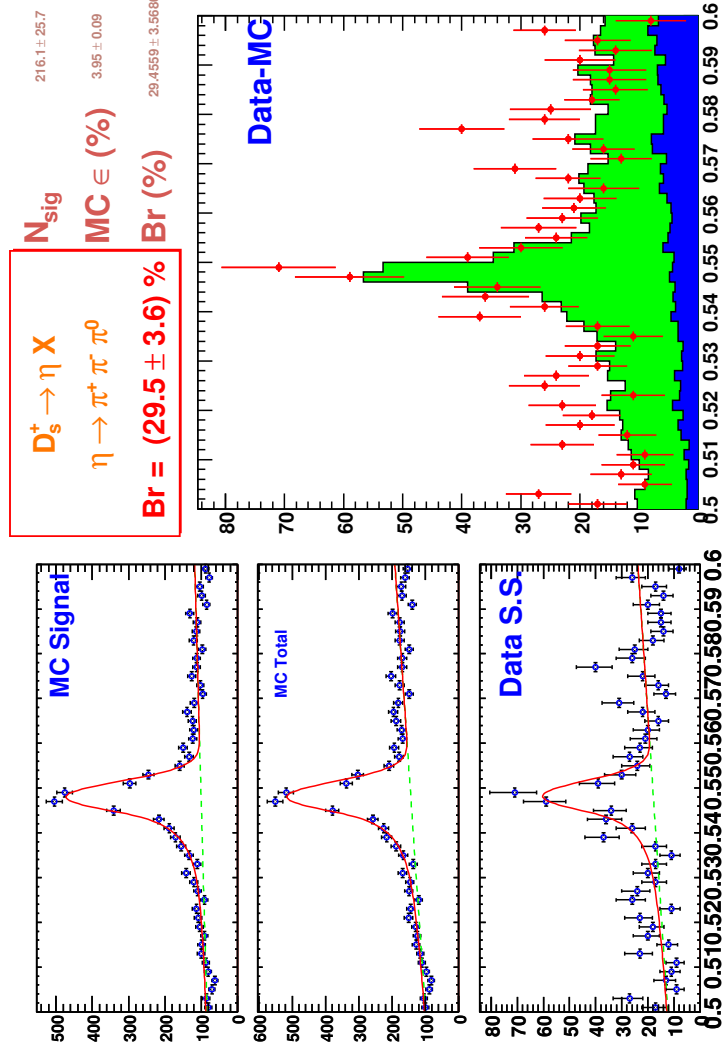


Figure 5.10: $D_s^+ \rightarrow \eta X, \eta \rightarrow \pi^+ \pi^- \pi^0$ decay study. MC signal plot is from the generic MC sample with η on the signal side. MC Total plot is from the whole generic MC sample. Data S.S. is the data plot after D_s tag sideband subtraction. We get signal and background shape parameters from the fits to MC signal and MC Total respectively and apply them in the fit to data. The data-MC comparison is shown on Data-MC plot, Monte Carlo is normalized to data based on tag yield.

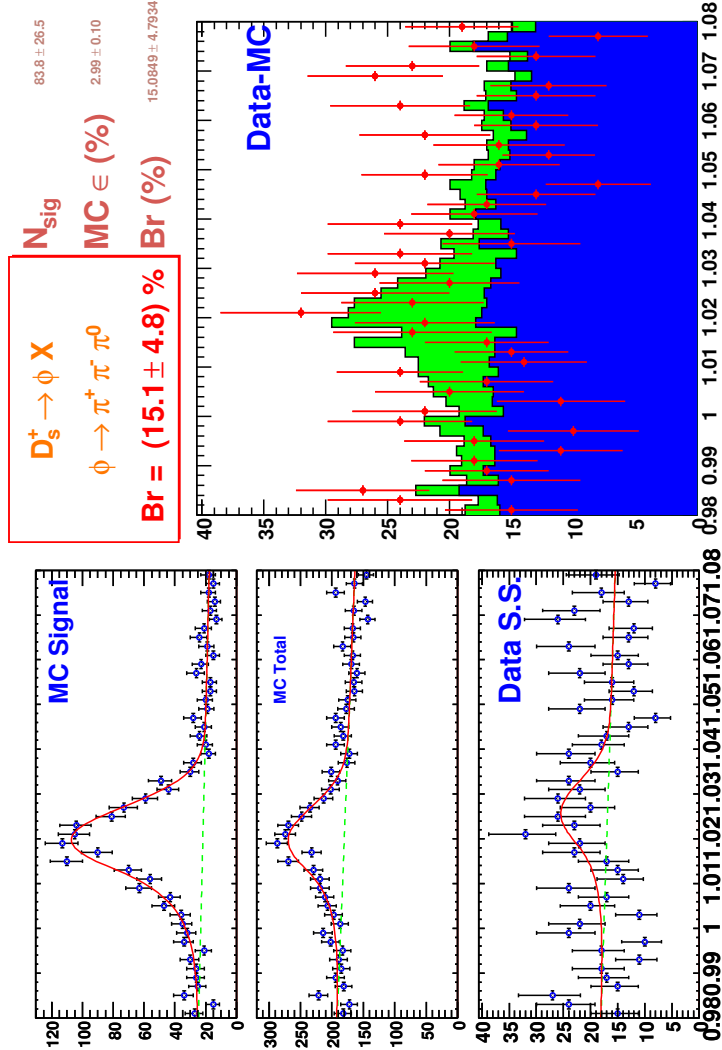


Figure 5.11: $D_s^+ \rightarrow \phi X, \phi \rightarrow \pi^+ \pi^- \pi^0$ decay study. MC signal plot is from the generic MC sample with ϕ on the signal side. MC Total plot is from the whole generic MC sample. Data S.S. is the data plot after D_s tag sideband subtraction. We get signal and background shape parameters from the fits to MC signal and MC Total respectively and apply them in the fit to data. The data-MC comparison is shown on Data-MC plot, Monte Carlo is normalized to data based on tag yield.

The Monte Carlo histogram has been scaled to real data according to the D_s tag yields in data and Monte Carlo.

Fig. 5.12 shows the data and Monte Carlo comparison plot of $D_s^+ \rightarrow \pi^+ \pi^0 \omega$. The input branching fractions in generic Monte Carlo are $\mathcal{B}(D_s^+ \rightarrow \pi^+ \pi^0 \omega) = 0\%$, $\mathcal{B}(D_s^+ \rightarrow \rho^+ \eta) = 7.58\%$ and $\mathcal{B}(D_s^+ \rightarrow \rho^+ \phi) = 7.35\%$. From the Fig. 5.12, we found that the rough peak size of η and ϕ is consistent between data and Monte Carlo. Clear ω peak is in data but not in generic Monte Carlo. Generic Monte Carlo also shows the flat background distribution in the $\pi^+ \pi^- \pi^0$ invariant mass.

The data and Monte Carlo comparison plot of $D_s^+ \rightarrow \pi^+ \omega$ is shown in Fig. 5.13. The input branching fractions in generic Monte Carlo are $\mathcal{B}(D_s^+ \rightarrow \pi^+ \omega) = 0.25\%$, $\mathcal{B}(D_s^+ \rightarrow \pi^+ \eta) = 1.54\%$ and $\mathcal{B}(D_s^+ \rightarrow \pi^+ \phi) = 2.06\%$. We found that the rough peak size of η , ϕ , and ω is consistent between data and Monte Carlo as shown in the Fig. 5.13.

The comparison plot of $D_s^+ \rightarrow \pi^+ \eta \omega$ is shown in Fig. 5.14. No clear signal is found in data, generic Monte Carlo shows flat $\pi^+ \pi^- \pi^0$ invariant mass distribution. Fig. 5.15 and Fig. 5.16 are the comparison plots of $D_s^+ \rightarrow K^+ \pi^0 \omega$ and $D_s^+ \rightarrow K^+ \omega$. Fig. 5.17 is for $D_s^+ \rightarrow K^+ \eta \omega$ decay, nothing has been found in either data or Monte Carlo.

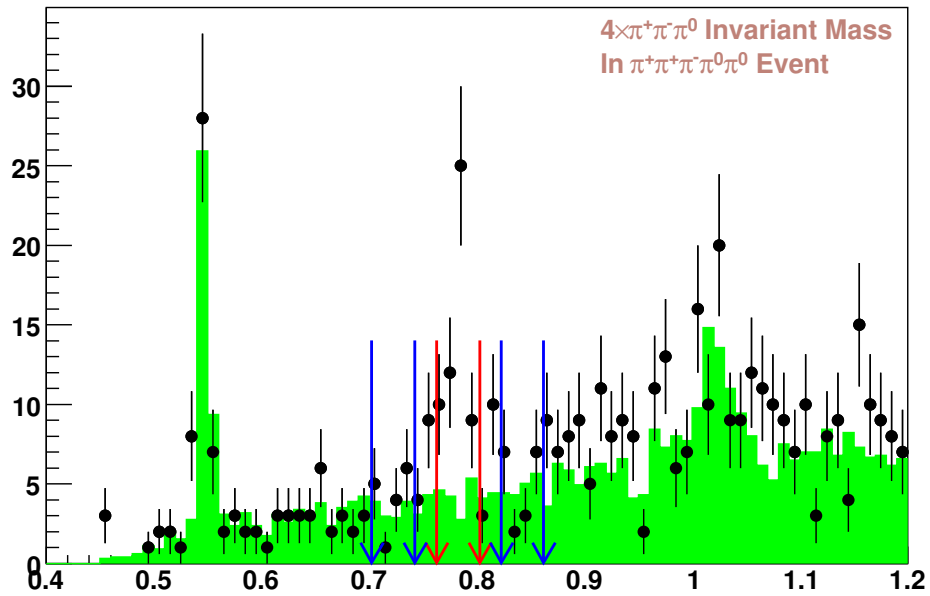
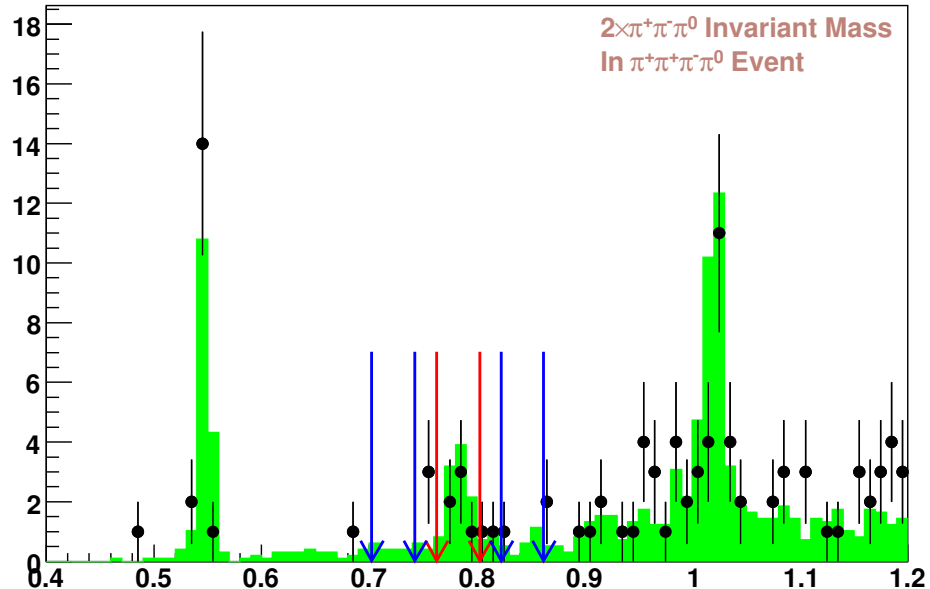
5.6 Systematics

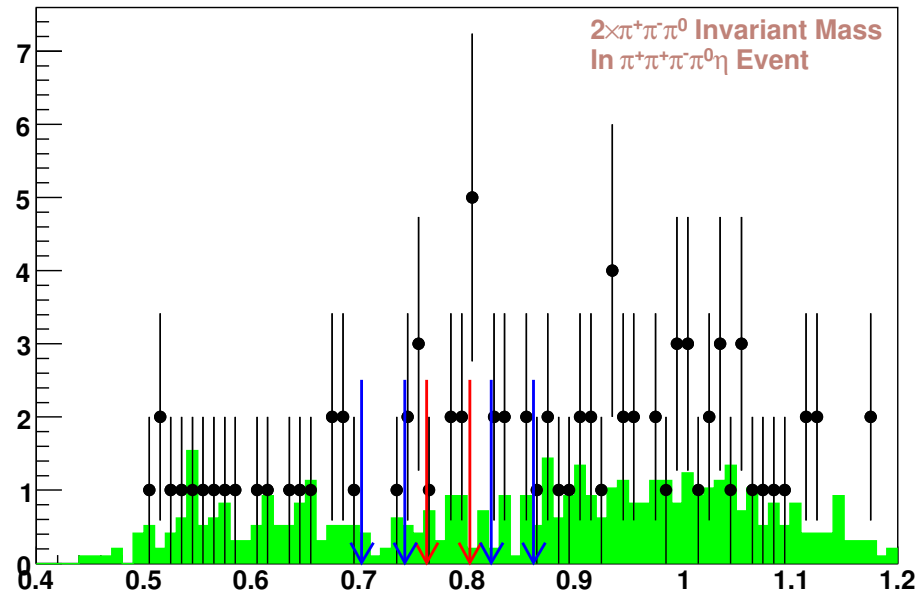
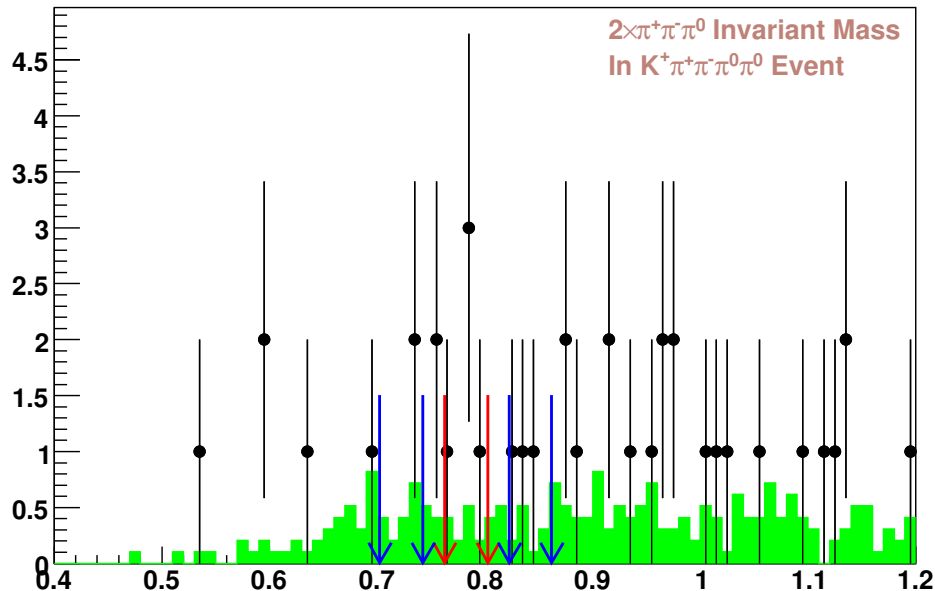
5.6.1 D_s Tag and MC Efficiency Statistical Errors

The error in total D_s tag yield is 0.87% and has been included in the statistical errors of branching fractions. Uncertainties in Monte Carlo efficiencies arise due to finite Monte Carlo staticstics. 50K signal Monte Carlo samples are generated to study the reconstruction efficiencies. The expected uncertainties in efficiencies also have been included in the statistical errors.

5.6.2 Tracking and PID

Uncertainties in track reconstruction and particle identification have been discussed in Chapter 3. We use the same numbers for this analysis.

Data V.S. MC: $D_s^+ \rightarrow \pi^+ \pi^0 \omega$ Figure 5.12: The data and Monte Carlo comparison plot for $D_s^+ \rightarrow \pi^+ \pi^0 \omega$.Data V.S. MC: $D_s^+ \rightarrow \pi^+ \omega$ Figure 5.13: The data and Monte Carlo comparison plot for $D_s^+ \rightarrow \pi^+ \omega$.

Data V.S. MC: $D_s^+ \rightarrow \pi^+ \eta \omega$ Figure 5.14: The data and Monte Carlo comparison plot for $D_s^+ \rightarrow \pi^+ \eta \omega$.Data V.S. MC: $D_s^+ \rightarrow K^+ \pi^0 \omega$ Figure 5.15: The data and Monte Carlo comparison plot for $D_s^+ \rightarrow K^+ \pi^0 \omega$.

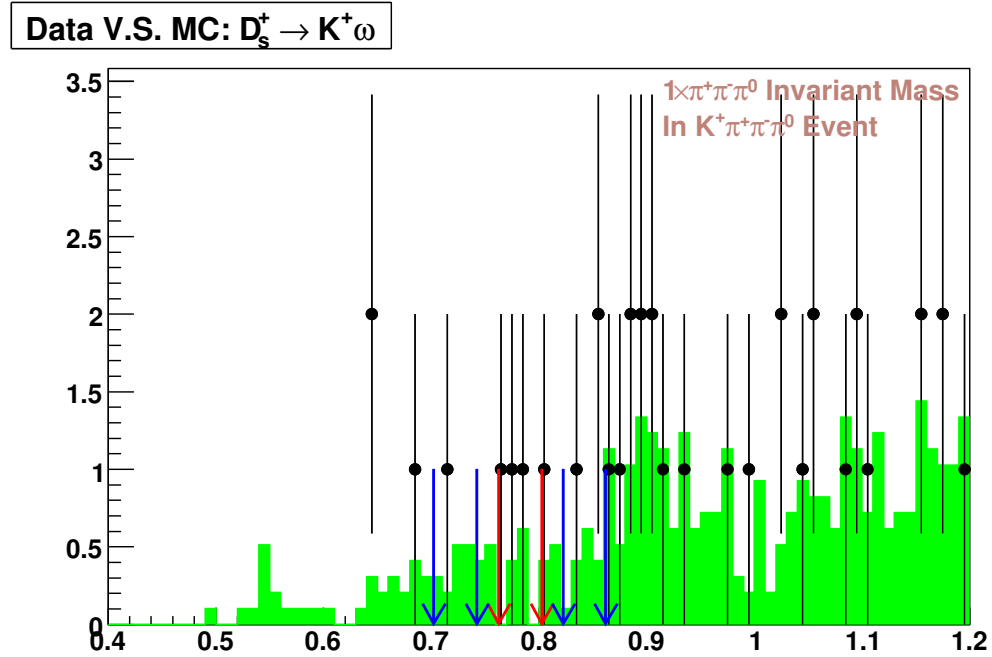


Figure 5.16: The data and Monte Carlo comparison plot for $D_s^+ \rightarrow K^+ \omega$.

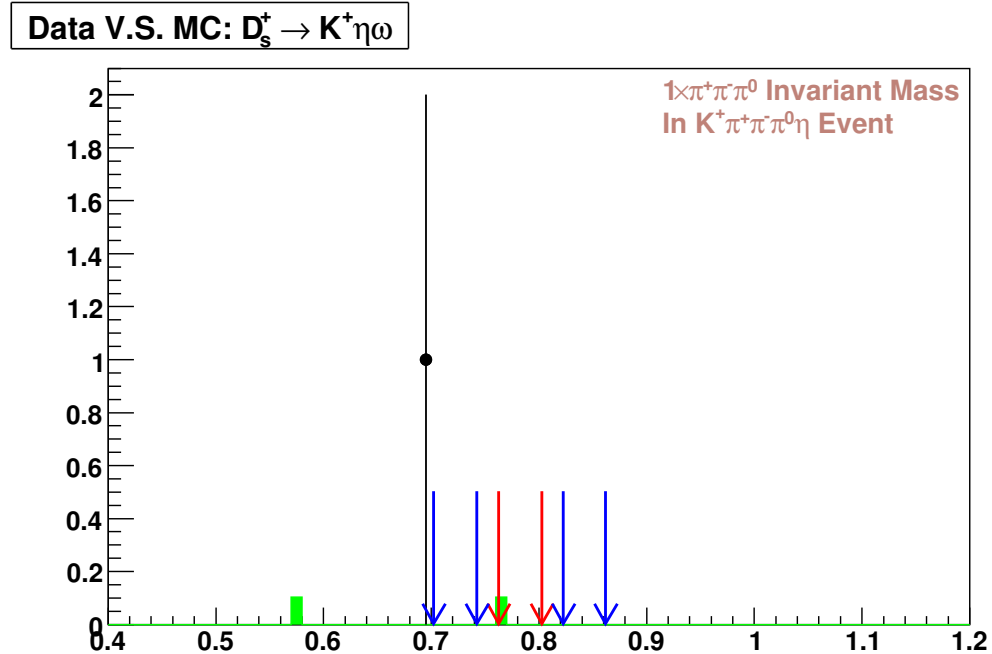


Figure 5.17: The data and Monte Carlo comparison plot for $D_s^+ \rightarrow K^+ \eta\omega$.

Uncertainty in track reconstruction efficiencies is 0.3% per charged particle, an additional 0.6% systematic uncertainty for each kaon track is added. Systematic error of PID is 0.3% (0.25%) per kaon (pion). We assign 4.0% as the systematic uncertainty for π^0 and 5.6% for η .

5.6.3 Background Contributions from D_s Tag Sideband

As shown before, the background contributions from D_s tag sideband regions are negligible in any of our signal modes.

5.6.4 Resonant Structure

For the $D_s^+ \rightarrow \pi^+ \pi^0 \omega$ decay, we fit data to sum of phase space $\pi^+ \pi^0 \omega$ MC and $\rho^+ \omega$ MC to extract how much from the sub-resonant decay of $D_s^+ \rightarrow \rho^+ \omega$, $\rho^+ \rightarrow \pi^+ \pi^0$ and how much from the non-resonant decay of $D_s^+ \rightarrow \pi^+ \pi^0 \omega$. A ratio of phase space $\pi^+ \pi^0 \omega$ decay to total was measured to be 0.480 ± 0.295 from the fit. For $D_s^+ \rightarrow \pi^+ \pi^0 \omega$ via phase space, we find an efficiency of $2.158 \pm 0.065\%$. For $D_s^+ \rightarrow \rho^+ \omega$, we find $1.900 \pm 0.061\%$. We use the central value of that ratio to calculate the branching fraction and take the error as a systematic uncertainty.

5.6.5 Region Definition

For the $D_s^+ \rightarrow \pi^+ \pi^0 \omega$ and $D_s^+ \rightarrow \pi^+ \omega$ decays, we redefine the sideband regions to study the effect and assign the difference in branching fractions as the systematic uncertainty.

5.6.6 Correction Factor

We apply the correction factors for PID, π^0 finding and η finding. They are 0.5% for π^\pm PID and 1% for K^\pm PID. The correction factor for π^0 and η finding is 6%.

5.6.7 Systematic Summary

We have considered several systematic uncertainties as shown upon. Table 5.2 shows the details of the main systematic uncertainties that effect this analysis. The cor-

Table 5.2: Main systematic uncertainties and correction factors.

Mode	Value (%)								C.F.
	Trk	K -Trk	K -ID	π -ID	π^0, η	MC- ϵ	R.D.	Total	
$\pi^+\pi^0\omega$	0.900	—	—	0.750	8.000	3.886	5.204	10.371	0.865
$\pi^+\omega$	0.900	—	—	0.750	4.000	—	17.248	17.744	0.925
$\pi^+\eta\omega$	0.900	—	—	0.750	6.882	—	—	6.981	0.865
$K^+\pi^0\omega$	0.900	0.600	0.300	0.500	8.000	—	—	8.094	0.860
$K^+\omega$	0.900	0.600	0.300	0.500	4.000	—	—	4.184	0.920
$K^+\eta\omega$	0.900	0.600	0.300	0.500	6.882	—	—	6.991	0.860

- R.D. is the systematic uncertainty from changing sideband region definition.

Table 5.3: Results of search for D_s^+ exclusive hadronic decays involving ω . Uncertainties are statistical and systematic, respectively.

Mode	$\mathcal{B}(\%)$
$D_s^+ \rightarrow \pi^+\pi^0\omega$	$2.794 \pm 0.653 \pm 0.290$
$D_s^+ \rightarrow \pi^+\omega$	$0.212 \pm 0.086 \pm 0.038$
$D_s^+ \rightarrow \pi^+\eta\omega$	< 1.855 (90% CL)
$D_s^+ \rightarrow K^+\pi^0\omega$	< 0.685 (90% CL)
$D_s^+ \rightarrow K^+\omega$	< 0.204 (90% CL)
$D_s^+ \rightarrow K^+\eta\omega$	< 0.769 (90% CL)

rection factor for each mode is listed in the last column of Table 5.2.

5.7 Results

In summary, we report the first observation of $D_s^+ \rightarrow \pi^+\pi^0\omega$ decay and first upper limits for $D_s^+ \rightarrow \pi^+\eta\omega$, $D_s^+ \rightarrow K^+\pi^0\omega$, $D_s^+ \rightarrow K^+\omega$, and $D_s^+ \rightarrow K^+\eta\omega$ decays. Our measurement of $D_s^+ \rightarrow \pi^+\omega$ decay is consistent with PDG [11]. The results are summarized in Table 5.3. The first error is statistical error and the second error is systematic error. For the upper limits, we conservatively increase the quoted upper limits by 1.28 times the systematic errors from Table 5.2.

Chapter 6

Decays of Charmed Mesons to Pairs of Pseudoscalars

There are many possible decays of charmed D mesons to a pair of mesons from the lowest-lying pseudoscalar meson nonet. The decay can be to any pair of K^+ , K^- , π^+ , π^- , η , η' , π^0 , K^0 , or \bar{K}^0 . Measurements of the branching fractions of the complete set of decays test flavor topology and SU(3) predictions [41]. The detectable neutral kaons are K_S^0 and K_L^0 , not K^0 and \bar{K}^0 , so the observable decays are XK_S^0 and XK_L^0 . In this thesis, we consider only K_S^0 , not K_L^0 . We report a bunch of branching fractions of Cabibbo-favored, singly-Cabibbo-suppressed, and doubly-Cabibbo-suppressed decays. We normalize against the Cabibbo-favored D modes, $D^0 \rightarrow K^-\pi^+$, $D^+ \rightarrow K^-\pi^+\pi^+$, and $D_s^+ \rightarrow K^+K_S^0$.

6.1 $D(D_s^+, D^+, D^0) \rightarrow PP$ Decays Review

The major objective of this analysis is to give a full set of measurements of D meson decay to two pseudoscalar mesons, using the full CLEO-c data sample. At CLEO, most of those modes have been measured, but not with the full data sample. The full list of $D \rightarrow PP$ decays, and the branching fractions given in CLEO-c previous published results of D^0 , D^+ and D_s^+ decays to two pseudoscalar mesons are listed in Table 6.1, Table 6.2, and Table 6.3 [42, 43, 44, 45, 46, 47, 48, 49, 50].

Table 6.1: CLEO-c previous published results of $D^0 \rightarrow PP$ decays, and $D^0 \rightarrow PP$ modes not measured.

Mode	\mathcal{B}	Dataset	Measurment
$D^0 \rightarrow K^+ K^-$	$(4.08 \pm 0.08 \pm 0.09) \times 10^{-3}$	281pb^{-1}	Phys. Rev. D 77 , 091106 (2008)
$D^0 \rightarrow K_S^0 K_S^0$	$(1.46 \pm 0.32 \pm 0.09) \times 10^{-4}$	281pb^{-1}	Phys. Rev. D 77 , 091106 (2008)
$D^0 \rightarrow K_S^0 K_L^0$	—	—	—
$D^0 \rightarrow K_L^0 K_L^0$	—	—	—
$D^0 \rightarrow \pi^+ \pi^-$	$(1.39 \pm 0.04 \pm 0.04 \pm 0.03 \pm 0.01) \times 10^{-3}$	281pb^{-1}	Phys. Rev. Lett. 96 , 081802 (2006)
$D^0 \rightarrow \pi^0 \pi^0$	$(0.79 \pm 0.05 \pm 0.06 \pm 0.01 \pm 0.01) \times 10^{-3}$	281pb^{-1}	Phys. Rev. Lett. 96 , 081802 (2006)
$D^0 \rightarrow K^- \pi^+$	$(3.891 \pm 0.035 \pm 0.059 \pm 0.035) \times 10^{-2}$	281pb^{-1}	Phys. Rev. D 76 , 112001 (2007)
$D^0 \rightarrow K^+ \pi^-$	—	—	—
$D^0 \rightarrow K_S^0 \pi^0$	$(1.240 \pm 0.017 \pm 0.031 \pm 0.047) \times 10^{-2}$	281pb^{-1}	Phys. Rev. Lett. 100 , 091801 (2008)
$D^0 \rightarrow K_L^0 \pi^0$	$(0.998 \pm 0.049 \pm 0.030 \pm 0.038) \times 10^{-2}$	281pb^{-1}	Phys. Rev. Lett. 100 , 091801 (2008)
$D^0 \rightarrow K_S^0 \eta$	$(4.42 \pm 0.15 \pm 0.28) \times 10^{-3}$	281pb^{-1}	Phys. Rev. Lett. 100 , 221801 (2008)
$D^0 \rightarrow K_L^0 \eta$	—	—	—
$D^0 \rightarrow \pi^0 \eta$	$(0.62 \pm 0.14 \pm 0.05 \pm 0.01 \pm 0.01) \times 10^{-3}$	281pb^{-1}	Phys. Rev. Lett. 96 , 081802 (2006)
$D^0 \rightarrow K_S^0 \eta'$	—	—	—
$D^0 \rightarrow K_L^0 \eta'$	—	—	—
$D^0 \rightarrow \pi^0 \eta'$	$(8.1 \pm 1.5 \pm 0.6) \times 10^{-4}$	281pb^{-1}	Phys. Rev. D 77 , 092003 (2008)
$D^0 \rightarrow \eta \eta$	$(16.7 \pm 1.4 \pm 1.3) \times 10^{-4}$	281pb^{-1}	Phys. Rev. D 77 , 092003 (2008)
$D^0 \rightarrow \eta \eta'$	$(12.6 \pm 2.5 \pm 1.1) \times 10^{-4}$	281pb^{-1}	Phys. Rev. D 77 , 092003 (2008)

Table 6.2: CLEO-c previous published results of $D^+ \rightarrow PP$ decays, and $D^+ \rightarrow PP$ modes not measured.

Mode	\mathcal{B}	Dataset	Measurment
$D^+ \rightarrow K_S^0 K^+$	$(3.14 \pm 0.09 \pm 0.08) \times 10^{-3}$	281pb^{-1}	Phys. Rev. D 77 , 091106 (2008)
$D^+ \rightarrow K_L^0 K^+$	—	—	—
$D^+ \rightarrow \pi^+ \pi^0$	$(1.25 \pm 0.06 \pm 0.07 \pm 0.04) \times 10^{-3}$	281pb^{-1}	Phys. Rev. Lett. 96 , 081802 (2006)
$D^+ \rightarrow K_S^0 \pi^+$	$(1.526 \pm 0.022 \pm 0.037 \pm 0.009) \times 10^{-2}$	281pb^{-1}	Phys. Rev. D 76 , 112001 (2007)
$D^+ \rightarrow K_L^0 \pi^+$	$(1.460 \pm 0.040 \pm 0.035 \pm 0.005) \times 10^{-2}$	281pb^{-1}	Phys. Rev. Lett. 100 , 091801 (2008)
$D^+ \rightarrow K^+ \pi^0$	$(2.28 \pm 0.36 \pm 0.15 \pm 0.08) \times 10^{-4}$	281pb^{-1}	Phys. Rev. D 74 , 071102(R) (2006)
$D^+ \rightarrow K^+ \eta$	—	—	—
$D^+ \rightarrow \pi^+ \eta$	$(3.61 \pm 0.25 \pm 0.23 \pm 0.12) \times 10^{-3}$	281pb^{-1}	Phys. Rev. Lett. 96 , 081802 (2006)
$D^+ \rightarrow K^+ \eta'$	—	—	—
$D^+ \rightarrow \pi^+ \eta'$	$(4.42 \pm 0.25 \pm 0.29) \times 10^{-3}$	281pb^{-1}	Phys. Rev. D 77 , 092003 (2008)

Table 6.3: CLEO-c previous published results of $D_s^+ \rightarrow PP$ decays, and $D_s^+ \rightarrow PP$ modes not measured.

Mode	\mathcal{B}	Dataset	Measurment
$D_s^+ \rightarrow K_S^0 K^+$	$(1.49 \pm 0.07 \pm 0.05) \times 10^{-2}$	298pb^{-1}	Phys. Rev. Lett. 100 , 161804 (2008)
$D_s^+ \rightarrow K_L^0 K^+$	—	—	—
$D_s^+ \rightarrow \pi^+ \pi^0 / K_S^0 K^+$	$< 4.1 \times 10^{-2} (90\% \text{C.L.})$	298pb^{-1}	Phys. Rev. Lett. 99 , 191805 (2007)
$D_s^+ \rightarrow K_S^0 \pi^+ / K_S^0 K^+$	$(8.2 \pm 0.9 \pm 0.2) \times 10^{-2}$	298pb^{-1}	Phys. Rev. Lett. 99 , 191805 (2007)
$D_s^+ \rightarrow K_L^0 \pi^+$	—	—	—
$D_s^+ \rightarrow K^+ \pi^0 / K_S^0 K^+$	$(5.5 \pm 1.3 \pm 0.7) \times 10^{-2}$	298pb^{-1}	Phys. Rev. Lett. 99 , 191805 (2007)
$D_s^+ \rightarrow K^+ \eta / \pi^+ \eta$	$(8.9 \pm 1.5 \pm 0.4) \times 10^{-2}$	298pb^{-1}	Phys. Rev. Lett. 99 , 191805 (2007)
$D_s^+ \rightarrow \pi^+ \eta$	$(1.58 \pm 0.11 \pm 0.18) \times 10^{-2}$	298pb^{-1}	Phys. Rev. Lett. 100 , 161804 (2008)
$D_s^+ \rightarrow K^+ \eta' / \pi^+ \eta'$	$(4.2 \pm 1.3 \pm 0.3) \times 10^{-2}$	298pb^{-1}	Phys. Rev. Lett. 99 , 191805 (2007)
$D_s^+ \rightarrow \pi^+ \eta'$	$(3.77 \pm 0.25 \pm 0.30) \times 10^{-2}$	298pb^{-1}	Phys. Rev. Lett. 100 , 161804 (2008)

6.2 Data Samples

6.2.1 $D^0\bar{D}^0$ and D^+D^- Data Sample

For D^0 and D^+ , we use an 818 pb^{-1} sample of e^+e^- colliding beam events, collected at a center-of-mass energy of 3770 MeV. The events were produced with the CESR-c storage ring and detected with the CLEO-c detector. The data sample contains about 2.4×10^6 D^+D^- events (our target sample), three million $D^0\bar{D}^0$ events (our target sample), fifteen million $e^+e^- \rightarrow u\bar{u}$, $d\bar{d}$, or $s\bar{s}$ continuum events, three million $e^+e^- \rightarrow \tau^+\tau^-$ events, and three million $e^+e^- \rightarrow \gamma\psi'$ radiative return events (sources of background), as well as Bhabha events, μ -pair events, and $\gamma\gamma$ events (useful for luminosity determination and resolution studies).

6.2.2 $D_s^{*+}D_s^-$ Data Sample

For D_s^+ , we use 586 pb^{-1} of data produced in e^+e^- collisions at CESR near the center-of-mass energy $\sqrt{s} = 4170 \text{ MeV}$, the same as we used in the D_s^+ inclusive study analysis.

6.2.3 Monte Carlo Sample

Efficiencies are obtained from signal MC samples. We generated 40k events for each mode. For the single-tag efficiency estimation of D^0 or D^+ modes (charge-conjugate modes are implicit throughout this note), we start with $D^0\bar{D}^0$ or D^+D^- . For D_s mode single-tag efficiency estimation, we start with $D_s^{*+}D_s^-$. We set that one D (For D_s , either primary or secondary) decays to the specific tag mode and the other decays generically. For charged modes, we separately generate ‘-’ and ‘+’ charged signal.

Corresponding $20 \times D\bar{D}$ generic Monte Carlo sample (for D^0 or D^+ modes) and $20 \times \text{mcDD-mix}$ sample (generic mixture of $D\bar{D}$ MC) with ISR (for D_s modes) are used to study the possible background features.

6.3 Single Tag Method at $\psi(3770)$

The $\psi(3770)$ resonance is below the kinematic threshold for $D\bar{D}\pi$ production, and so the events of interest, $e^+e^- \rightarrow \psi(3770) \rightarrow D\bar{D}$, have D mesons with energy equal to the beam energy. Having picked the particles being considered to make up a D meson, following Mark III [51] we define the two variables:

$$\Delta E \equiv \sum_i E_i - E_{\text{beam}}, \quad (6.1)$$

and

$$M_{\text{bc}} \equiv \sqrt{E_{\text{beam}}^2 - |\sum_i \vec{P}_i|^2}, \quad (6.2)$$

where E_i , \vec{P}_i are the energy and momentum of each D decay product. For a correct combination of particles, ΔE will be consistent with zero, and the beam-constrained mass M_{bc} will be consistent with the D mass. The detailed ΔE and M_{bc} distributions are shown in Fig. 6.1, 6.2, 6.3, 6.4, and 6.5.

Table 6.4: The definitions of ΔE signal region and the low and high side ΔE sideband regions for D^0 modes.

Mode	Signal (MeV)	Low (MeV)	High (MeV)
$D^0 \rightarrow K^+ K^-$	-20.0 — 20.0	-50.0 — -75.0	50.0 — 75.0
$D^0 \rightarrow K_S^0 K_S^0$	-20.0 — 20.0	-50.0 — -100.0	50.0 — 100.0
$D^0 \rightarrow \pi^+ \pi^-$	-30.0 — 30.0	-50.0 — -75.0	50.0 — 75.0
$D^0 \rightarrow \pi^0 \pi^0$	-50.0 — 40.0	-60.0 — -100.0	50.0 — 100.0
$D^0 \rightarrow K^- \pi^+$	-29.4 — 29.4	-50.0 — -75.0	50.0 — 75.0
$D^0 \rightarrow K_S^0 \pi^0$	-55.0 — 45.0	-65.0 — -100.0	55.0 — 100.0
$D^0 \rightarrow K_S^0 \eta$	-55.0 — 35.0	-65.0 — -100.0	50.0 — 100.0
$D^0 \rightarrow \pi^0 \eta$	-45.0 — 34.0	-55.0 — -100.0	50.0 — 100.0
$D^0 \rightarrow K_S^0 \eta'$	-20.0 — 18.0	-50.0 — -100.0	50.0 — 100.0
$D^0 \rightarrow \pi^0 \eta'$	-38.0 — 32.0	-50.0 — -100.0	50.0 — 100.0
$D^0 \rightarrow \eta \eta$	-33.0 — 30.0	-50.0 — -100.0	50.0 — 100.0
$D^0 \rightarrow \eta \eta'$	-27.0 — 23.0	-50.0 — -100.0	50.0 — 100.0

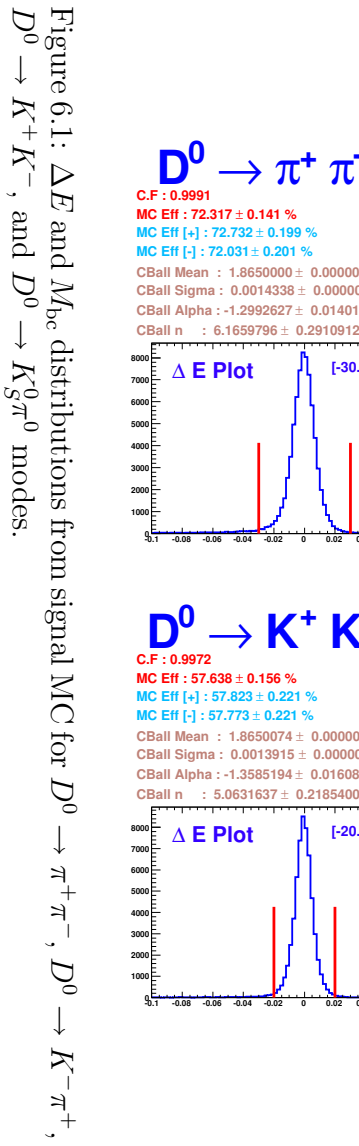


Figure 6.1: ΔE and M_{bc} distributions from signal MC for $D^0 \rightarrow \pi^+ \pi^-$, $D^0 \rightarrow K^- \pi^+$, $D^0 \rightarrow K^+ K^-$, and $D^0 \rightarrow K_S^0 \pi^0$ modes.

Figure 6.2: ΔE and M_{bc} distributions from signal MC for $D^0 \rightarrow K_S^0 \eta$, $D^0 \rightarrow \pi^0 \pi^0$, and $D^0 \rightarrow K_S^0 K_S^0$ modes.

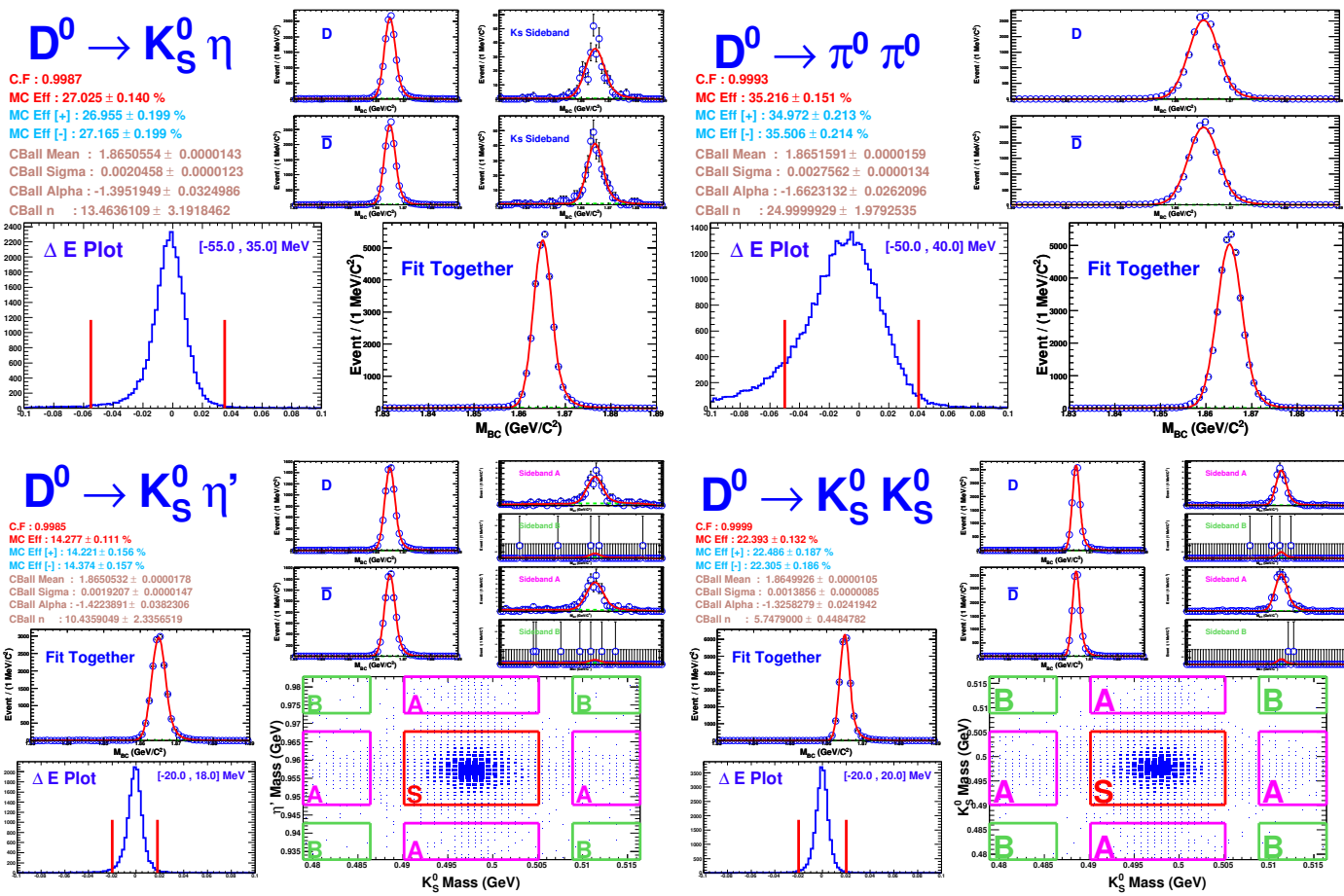
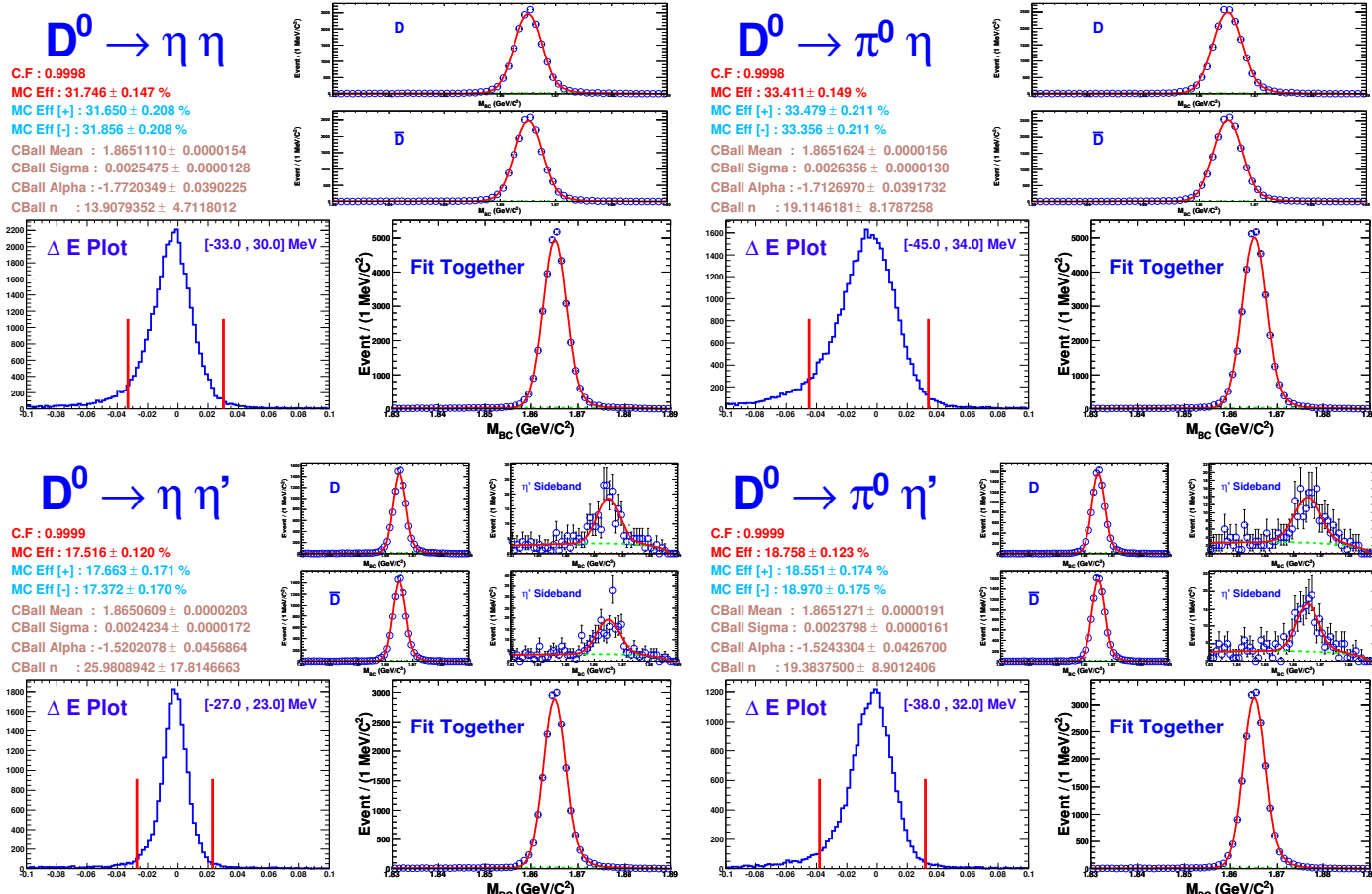


Figure 6.3: ΔE and M_{bc} distributions from signal MC for $D^0 \rightarrow \eta\eta$, $D^0 \rightarrow \pi^0\eta'$, and $D^0 \rightarrow \pi^0\eta$ modes.



6.3 Single Tag Method at $\psi(3770)$

Figure 6.4: ΔE and M_{bc} distributions from signal MC for $D^+ \rightarrow K^+\pi^0$, $D^+ \rightarrow K_S^0\pi^+$, $D^+ \rightarrow K_S^0K^+$, and $D^+ \rightarrow \pi^+\pi^0$ modes.

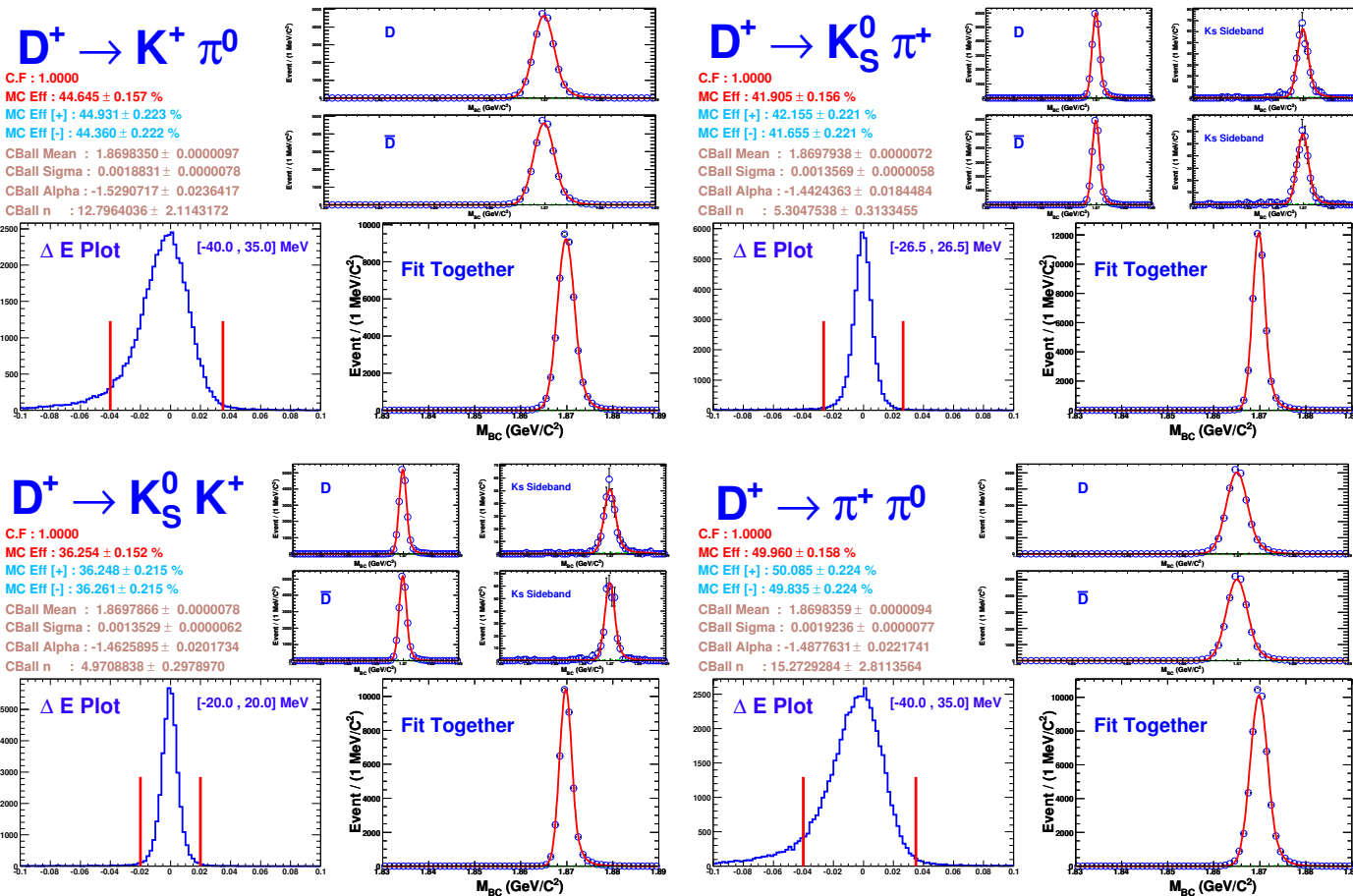


Figure 6.5: ΔE and M_{bc} distributions from signal MC for $D^+ \rightarrow K^+ \eta'$, $D^+ \rightarrow \pi^+ \eta'$, and $D^+ \rightarrow K^+ \eta$ modes.

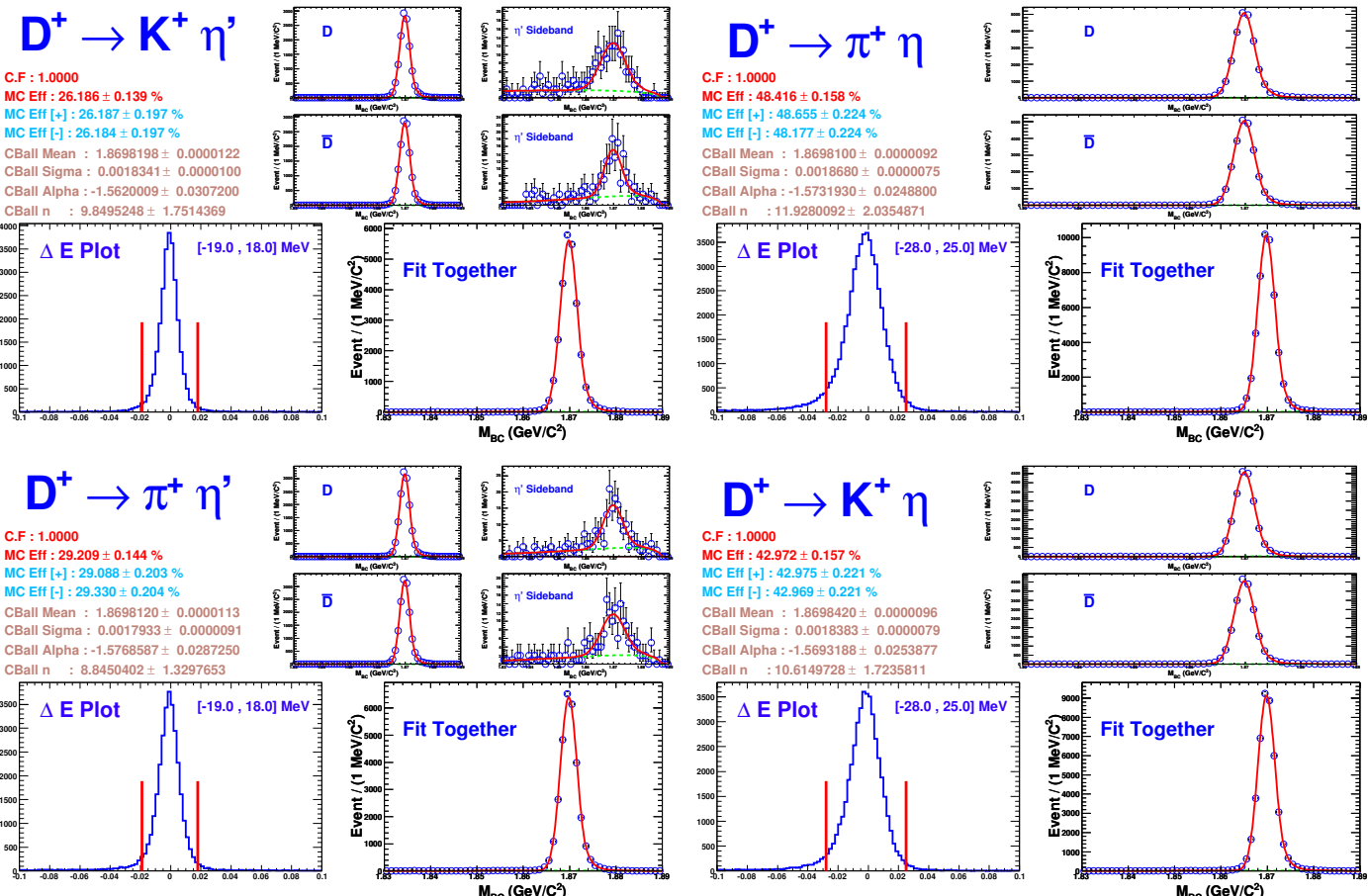


Table 6.5: The definitions of ΔE signal region and the low and high side ΔE sideband regions for D^+ modes.

Mode	Signal (MeV)	Low (MeV)	High (MeV)
$D^+ \rightarrow K^- \pi^+ \pi^+$	-21.8 — 21.8	-50.0 — -100.0	50.0 — 100.0
$D^+ \rightarrow K_S^0 K^+$	-20.0 — 20.0	-50.0 — -100.0	50.0 — 100.0
$D^+ \rightarrow \pi^+ \pi^0$	-40.0 — 35.0	-50.0 — -100.0	50.0 — 100.0
$D^+ \rightarrow K_S^0 \pi^+$	-26.5 — 26.5	-50.0 — -100.0	50.0 — 100.0
$D^+ \rightarrow K^+ \pi^0$	-40.0 — 35.0	-50.0 — -100.0	50.0 — 100.0
$D^+ \rightarrow K^+ \eta$	-28.0 — 25.0	-50.0 — -100.0	50.0 — 100.0
$D^+ \rightarrow \pi^+ \eta$	-28.0 — 25.0	-50.0 — -100.0	50.0 — 100.0
$D^+ \rightarrow K^+ \eta'$	-19.0 — 18.0	-50.0 — -100.0	50.0 — 100.0
$D^+ \rightarrow \pi^+ \eta'$	-19.0 — 18.0	-50.0 — -100.0	50.0 — 100.0

6.3.1 ΔE Distributions

The distributions in ΔE from signal Monte Carlo for the various modes are shown in Fig. 6.1, 6.2, 6.3, 6.4, and 6.5. If there are multiple candidates per mode per charm per event, we select the best D meson candidate with the smallest absolute value of ΔE . Candidates are required to have a value of ΔE which is within approximately 3 standard deviations of the mean. For final states consisting entirely of tracks, the ΔE resolution is small. A π^0 in the final state degrades this resolution. Modes with a π^0 always have a lower energy tail, hence an asymmetric ΔE window is used. The default ΔE requirements on the signal are indicated by the pairs of arrows in Fig. 6.1, 6.2, 6.3, 6.4, and 6.5. Here we also define the ΔE sideband regions for various decay modes to study the background shape in beam-constrained mass. Table 6.4 and 6.5 list the signal and sideband window values of ΔE .

6.3.2 Fit Function for M_{bc} Distribution

The M_{bc} distributions are fit using an ARGUS [52] shape for the background and a Crystal Ball [37] line shape for the signal. The ARGUS function is defined by the following equation

$$f(M_{bc}) = A \cdot M_{bc} [1 - (\frac{M_{bc}}{E_{Beam}})^2]^{P=\frac{1}{2}} \exp[C(1 - (\frac{M_{bc}}{E_{Beam}})^2)] \quad (6.3)$$

Here A is the overall normalization parameter, and C is the parameter that govern the shape.

The Crystal Ball line shape uses a Gaussian resolution for the core signal and a power law to describe the high-side tail in the M_{bc} distribution which results from initial state radiation. The Crystal Ball function is parameterized as Eq. 6.4 similar to that used for extracting photon signals from electromagnetic calorimeters because of the tail towards high M_{bc} caused by initial state radiation. For M_{bc} distribution, the tail should always be high side. Then the α is negative. The functional form is defined as

$$f(M_{\text{bc}}|M_D, \sigma_{M_{\text{bc}}}, \alpha, N) = \begin{cases} A \cdot \exp\left[-\frac{1}{2}\left(\frac{M_{\text{bc}}-M_D}{\sigma_{M_{\text{bc}}}}\right)^2\right] & \text{for } M_{\text{bc}} < M_D - \alpha \cdot \sigma_{M_{\text{bc}}} \\ A \cdot \frac{\left(\frac{N}{\alpha}\right)^N e^{-\frac{1}{2}\alpha^2}}{\left(\frac{M_{\text{bc}}-M_D}{\sigma_{M_{\text{bc}}}} + \frac{N}{\alpha} - \alpha\right)^N} & \text{for } M_{\text{bc}} > M_D - \alpha \cdot \sigma_{M_{\text{bc}}} \\ \text{Here } A^{-1} \equiv \sigma_{M_{\text{bc}}} \cdot \left[\frac{N}{\alpha} \cdot \frac{1}{N-1} e^{-\frac{1}{2}\alpha^2} + \sqrt{\frac{\pi}{2}} \left(1 + \text{erf}\left(\frac{\alpha}{\sqrt{2}}\right)\right)\right] & \end{cases} \quad (6.4)$$

When we fit the M_{bc} distributions for Monte Carlo, the shape parameters of the ARGUS function and the parameters, peak location, σ , α , and N of the Crystal Ball function are all allowed to float. We also allow both ARGUS background and Crystal Ball signal normalization parameters to float.

6.3.3 Monte Carlo Efficiencies

Monte Carlo reconstruction efficiency for each decay mode was obtained by computing the fraction of fitted D candidate number with respect to the number of generated events. Table 6.6 and 6.7 list the Monte Carlo reconstruction efficiencies for all D^0 and D^+ modes.

6.4 Single Tag Method at $E_{\text{cm}} = 4170 \text{ MeV}$

Unlike $D\bar{D}$ threshold energy runs, conventional ΔE and M_{bc} variables are no longer good variables for D_s from $D_s^{*+}D_s^-$ decays, as the D_s can either be a primary or secondary (from D_s^* decays) with different momentum. We use the reconstructed invariant mass of the D_s candidate, $M(D_s)$, and the mass recoiling against the D_s

Table 6.6: D^0 modes Monte Carlo efficiencies.

Mode	$D^0(\%)$	$\bar{D}^0(\%)$	Ave (%)
$D^0 \rightarrow K^+ K^-$	57.82 ± 0.22	57.77 ± 0.22	57.64 ± 0.16
$D^0 \rightarrow K_S^0 K_S^0$	22.49 ± 0.19	22.30 ± 0.19	22.39 ± 0.13
$D^0 \rightarrow \pi^+ \pi^-$	72.73 ± 0.20	72.03 ± 0.20	72.32 ± 0.14
$D^0 \rightarrow \pi^0 \pi^0$	34.97 ± 0.21	35.51 ± 0.21	35.22 ± 0.15
$D^0 \rightarrow K^- \pi^+$	64.61 ± 0.21	65.63 ± 0.21	65.11 ± 0.15
$D^0 \rightarrow K_S^0 \pi^0$	29.56 ± 0.20	29.69 ± 0.20	29.32 ± 0.14
$D^0 \rightarrow K_S^0 \eta$	26.96 ± 0.20	27.16 ± 0.20	27.03 ± 0.14
$D^0 \rightarrow \pi^0 \eta$	33.48 ± 0.21	33.36 ± 0.21	33.41 ± 0.15
$D^0 \rightarrow K_S^0 \eta'$	14.22 ± 0.16	14.37 ± 0.16	14.28 ± 0.11
$D^0 \rightarrow \pi^0 \eta'$	18.55 ± 0.17	18.97 ± 0.18	18.76 ± 0.12
$D^0 \rightarrow \eta \eta$	31.65 ± 0.21	31.86 ± 0.21	31.75 ± 0.15
$D^0 \rightarrow \eta \eta'$	17.66 ± 0.17	17.37 ± 0.17	17.52 ± 0.12

Table 6.7: D^+ modes Monte Carlo efficiencies.

Mode	$D^+(\%)$	$D^-(\%)$	Ave (%)
$D^+ \rightarrow K^- \pi^+ \pi^+$	54.66 ± 0.22	55.19 ± 0.22	54.92 ± 0.16
$D^+ \rightarrow K_S^0 K^+$	36.25 ± 0.22	36.26 ± 0.22	36.25 ± 0.15
$D^+ \rightarrow \pi^+ \pi^0$	50.08 ± 0.22	49.83 ± 0.22	49.96 ± 0.16
$D^+ \rightarrow K_S^0 \pi^+$	42.16 ± 0.22	41.65 ± 0.22	41.91 ± 0.16
$D^+ \rightarrow K^+ \pi^0$	44.93 ± 0.22	44.36 ± 0.22	44.65 ± 0.16
$D^+ \rightarrow K^+ \eta$	42.98 ± 0.22	42.97 ± 0.22	42.97 ± 0.16
$D^+ \rightarrow \pi^+ \eta$	48.65 ± 0.22	48.18 ± 0.22	48.42 ± 0.16
$D^+ \rightarrow K^+ \eta'$	26.19 ± 0.20	26.18 ± 0.20	26.19 ± 0.14
$D^+ \rightarrow \pi^+ \eta'$	29.09 ± 0.20	29.33 ± 0.20	29.21 ± 0.14

candidate,

$$M_{\text{recoil}}(D_s) = \sqrt{E_{\text{recoil}}^2 - \vec{p}_{\text{recoil}}^2} \quad (6.5)$$

$$= \sqrt{(\sqrt{s} - E_{D_s})^2 - (\vec{p}_{\text{Lab}} - \vec{p}_{D_s})^2} \quad (6.6)$$

$$= \sqrt{(\sqrt{s} - \sqrt{m_{D_s}^2 + \vec{p}_{D_s}^2})^2 - (\vec{p}_{\text{Lab}} - \vec{p}_{D_s})^2}, \quad (6.7)$$

as our primary kinematic variables to select a D_s candidate. Here \vec{p}_{D_s} is the momentum of the D_s candidate, $E_{D_s} = \sqrt{m_{D_s}^2 + \vec{p}_{D_s}^2}$, and m_{D_s} is the known D_s mass [11]. We make no requirements on the decay of the other D_s in the event. Typical mass distributions are shown in Fig. 6.6 and 6.7.

6.4.1 First Recoil Mass Variable $M_{\text{recoil}}(D_s)$

There are two components in the recoil mass distribution, a peak around the D_s^* mass if the candidate is due to the primary D_s and a rectangular shaped distribution if the candidate is due to the secondary D_s from D_s^* decays. The edges of $M_{\text{recoil}}(D_s)$ from the secondary D_s are kinematically determined (as a function of \sqrt{s} and known masses), and at $\sqrt{s} = 4170$ MeV, $\Delta M_{\text{recoil}}(D_s) \equiv M_{\text{recoil}}(D_s) - m_{D_s^*}$ is in the range $[-54, 57]$ MeV. Initial state radiation causes a tail on the high side, above 57 MeV. We select D_s candidates within the $-55 \text{ MeV} \leq \Delta M_{\text{recoil}}(D_s) < +55 \text{ MeV}$ range.

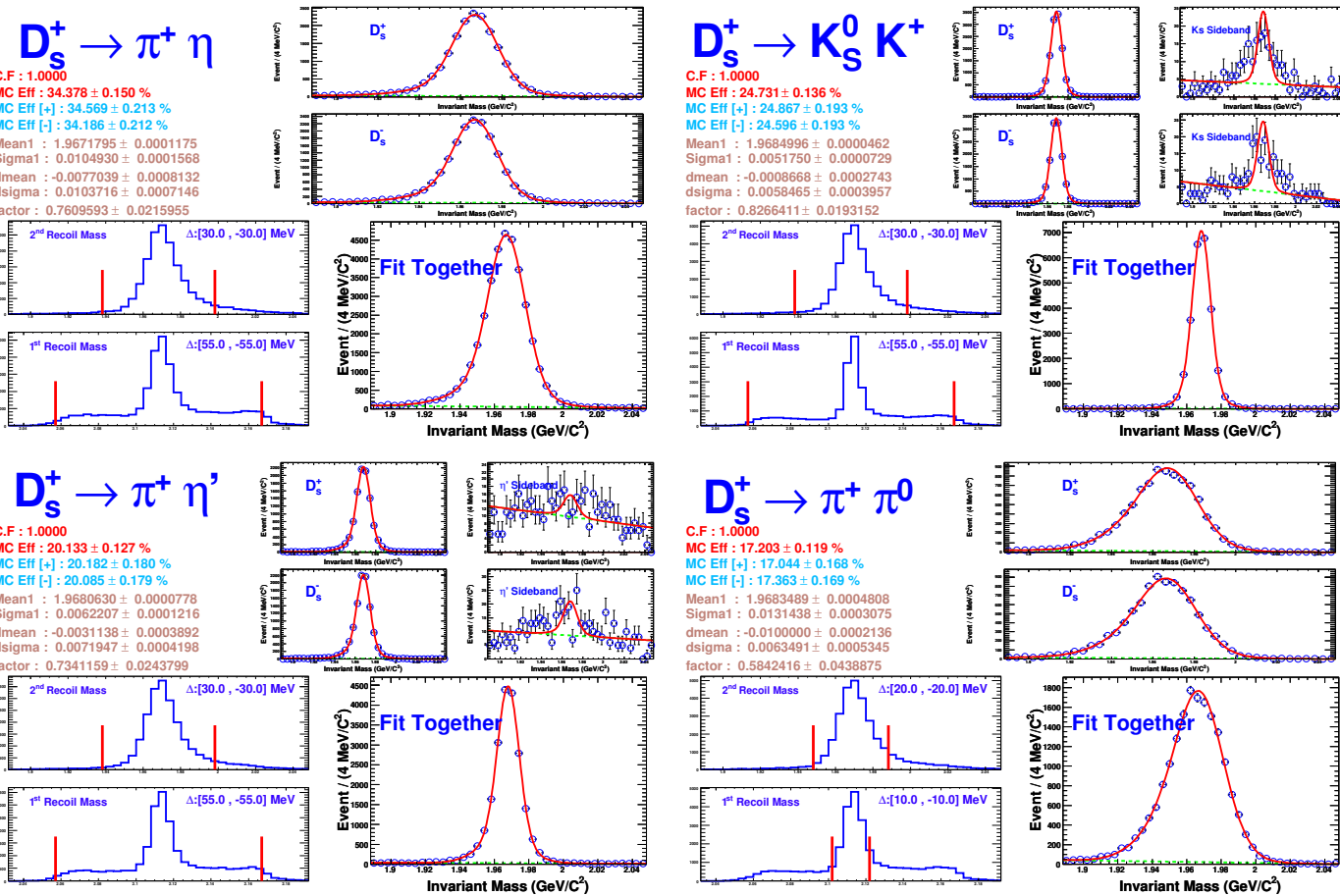
6.4.2 Second Recoil Mass Variable $M_{\text{recoil}}(D_s + \gamma)$

We also require a photon consistent with coming from $D_s^{*+} \rightarrow D_s^+ \gamma$ decay, by looking at the mass recoiling against the D_s candidate plus γ system,

$$M_{\text{recoil}}(D_s + \gamma) \equiv \sqrt{(\sqrt{s} - E_{D_s} - E_\gamma)^2 - (\vec{p}_{\text{Lab}} - \vec{p}_{D_s} - \vec{p}_\gamma)^2}. \quad (6.8)$$

For correct combinations, this recoil mass peaks at m_{D_s} , regardless of whether the candidate is due to a primary or a secondary D_s . We base on the value of $M_{\text{recoil}}(D_s + \gamma)$ to select best D_s candidate and require $|M_{\text{recoil}}(D_s + \gamma) - m_{D_s}| < 30$ MeV. This requirement improves the signal to noise ratio, important for the suppressed modes. Monte Carlo studies indicate that tightening the requirements on $M_{\text{recoil}}(D_s)$ to

Figure 6.6: $M(D_s)$, $M_{\text{recoil}}(D_s)$, and $M_{\text{recoil}}(D_s + \gamma)$ distributions from signal MC for $D_s^+ \rightarrow \pi^+ \eta$, $D_s^+ \rightarrow K_S^0 K^+$, $D_s^+ \rightarrow \pi^+ \eta'$, and $D_s^+ \rightarrow \pi^+ \pi^0$ modes.



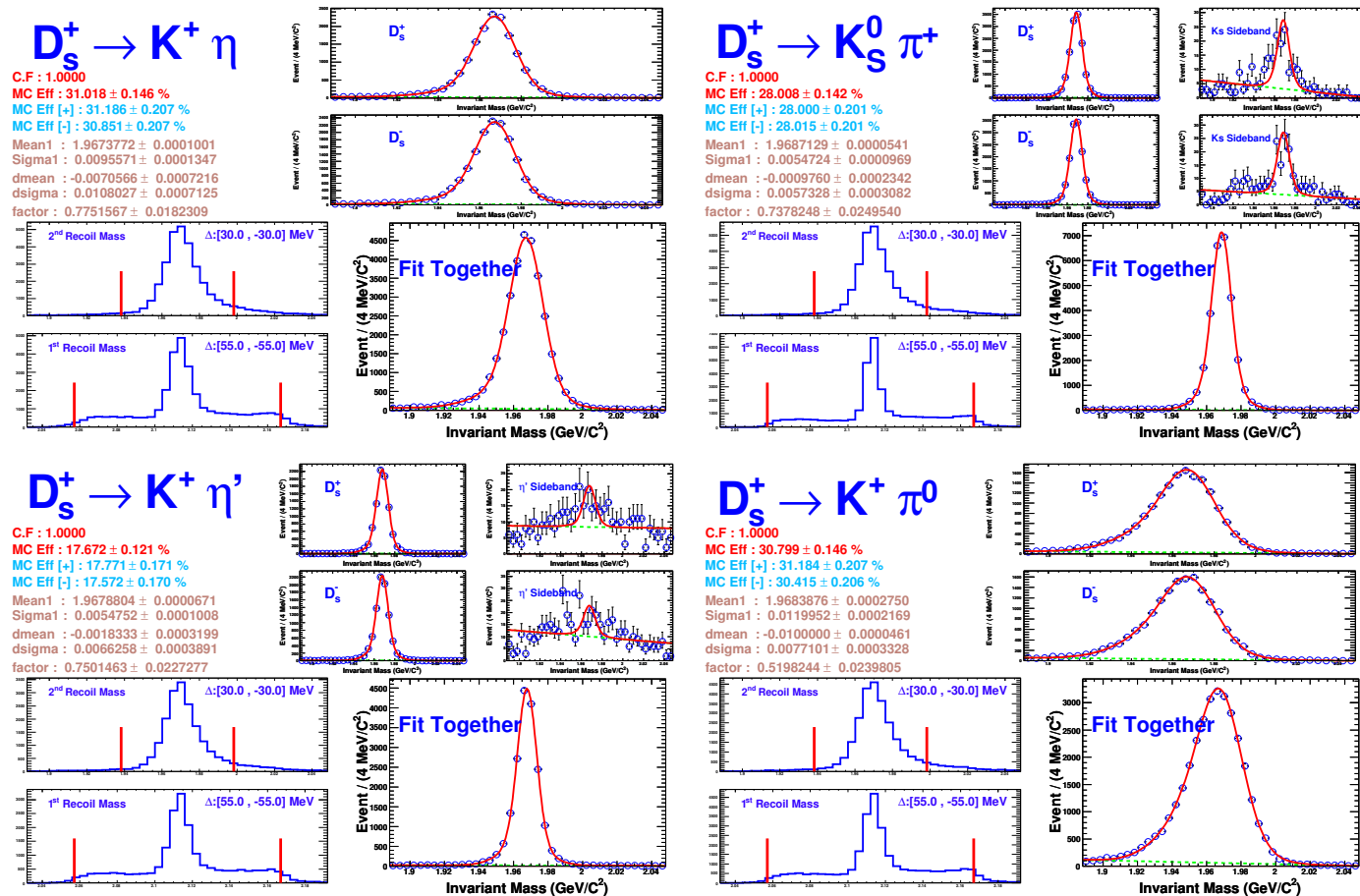


Figure 6.7: $M(D_s)$, $M_{\text{recoil}}(D_s)$, and $M_{\text{recoil}}(D_s + \gamma)$ distributions from signal MC for $D_s^+ \rightarrow K^+ \eta$, $D_s^+ \rightarrow K_s^0 \pi^+$, $D_s^+ \rightarrow K^+ \eta'$, and $D_s^+ \rightarrow K^+ \pi^0$ modes.

± 10 MeV and $M_{\text{recoil}}(D_s + \gamma)$ to ± 20 MeV should improve the upper limit for $D_s^+ \rightarrow \pi^+ \pi^0$ decay.

6.4.3 Slow Track Veto and K_S^0 Flight Significance Requirement

The D_s invariant mass distributions of the backgrounds to $D_s^+ \rightarrow K^+ K_S^0$ and $D_s^+ \rightarrow \pi^+ K_S^0$ are not smooth, but have bumps, caused by $D^{*+} D^{*-}$ events followed by $D^{*\pm} \rightarrow \pi^\pm D^0$ decays. The low-momentum π^\pm from $D^{*\pm}$ decay ($p < 80$ MeV/c), in combination with a particle from D^0 decay, can create a fake K_S^0 . To reduce the bump structure, which complicates fitting the background, we reject those $D_s^+ \rightarrow K^+ K_S^0$ and $D_s^+ \rightarrow \pi^+ K_S^0$ candidates that contain a π^+ or π^- with momentum below 100 MeV/c. To maintain cancellation of systematic errors, we also reject events with a K^\pm with momentum below 100 MeV/c. Further, we require that the K_S^0 has traveled a measurable distance from the interaction point before decaying, *i.e.*, that the distance along the flight path, from interaction point to K_S^0 decay vertex, be greater than zero with a 3σ significance. After the low-momentum track veto and K_S^0 flight significance requirement are applied, no bump structures remain.

6.4.4 Fit Function for $M(D_s)$ Distribution

We fit the invariant mass of D_s candidate to a signal (double Gaussian) plus background (second degree polynomial) function to get the yield of D_s candidate:

$$f(x) = A_1 \left(G_1(x; \mu_1, \sigma_1) + \frac{A_2}{A_1} \cdot G_2(x; \mu_2, \sigma_2) \right) + (p_0 + p_1 \cdot x + p_2 \cdot x^2), \quad (6.9)$$

where $G(x; \mu, \sigma) = \frac{1}{\sqrt{2\pi}\sigma} e^{-\frac{(x-\mu)^2}{2\sigma^2}}$.

6.4.5 Monte Carlo Efficiencies

Efficiencies obtained from signal MC samples with ISR are summarized in Table 6.8. The efficiencies of D_s^+ and D_s^- are listed in the second and third columns, the average values are listed in the last column.

Table 6.8: D_s^+ modes Monte Carlo efficiencies.

Mode	$D_s^+ (\%)$	$D_s^- (\%)$	Ave (%)
$D_s^+ \rightarrow K_S^0 K^+$	24.87 ± 0.19	24.60 ± 0.19	24.73 ± 0.14
$D_s^+ \rightarrow \pi^+ \pi^0$	17.04 ± 0.17	17.36 ± 0.17	17.20 ± 0.12
$D_s^+ \rightarrow K_S^0 \pi^+$	28.00 ± 0.20	28.02 ± 0.20	28.01 ± 0.14
$D_s^+ \rightarrow K^+ \pi^0$	31.18 ± 0.21	30.41 ± 0.21	30.80 ± 0.15
$D_s^+ \rightarrow K^+ \eta$	31.19 ± 0.21	30.85 ± 0.21	31.02 ± 0.15
$D_s^+ \rightarrow \pi^+ \eta$	34.57 ± 0.21	34.19 ± 0.21	34.38 ± 0.15
$D_s^+ \rightarrow K^+ \eta'$	17.77 ± 0.17	17.57 ± 0.17	17.67 ± 0.12
$D_s^+ \rightarrow \pi^+ \eta'$	20.18 ± 0.18	20.08 ± 0.18	20.13 ± 0.13

6.5 Tag Selection Requirements

Our standard final-state particle selection requirements are described in detail elsewhere [44]. Charged tracks produced in the D decay are required to satisfy criteria based on the track fit quality, have momenta above 50 MeV/ c , and angles with respect to the beam line, θ , satisfying $|\cos \theta| < 0.93$. They must also be consistent with coming from the interaction point in three dimensions. Pion and kaon candidates are required to have dE/dx measurements within three standard deviations (3σ) of the expected value. For tracks with momenta greater than 700 MeV/ c , RICH information, if available, is combined with dE/dx . The efficiencies (95% or higher) and misidentification rates (a few per cent) are determined with charged pions and kaons from hadronic D decays.

The K_S^0 candidates are selected from pairs of oppositely-charged and vertex-constrained tracks having invariant mass within 7.5 MeV, or roughly 3σ , of the known K_S^0 mass. We identify π^0 candidates via $\pi^0 \rightarrow \gamma\gamma$, detecting the photons in the CsI calorimeter. To avoid having both photons in a region of poorer energy resolution, we require that at least one of the photons be in the “good barrel” region, $|\cos \theta_\gamma| < 0.8$. We require that the calorimeter clusters have a measured energy above 30 MeV, have a lateral distribution consistent with that from photons, and not be matched to any charged track. The invariant mass of the photon pair is required to be within 3σ ($\sigma \sim 6$ MeV) of the known π^0 mass. A π^0 mass constraint is imposed when π^0 candidates are used in further reconstruction. We reconstruct η candidates in the decay of $\eta \rightarrow \gamma\gamma$, candidates are formed using a similar procedure

as for π^0 except that $\sigma \sim 12$ MeV. We reconstruct η' candidates in the decay mode $\eta' \rightarrow \pi^+ \pi^- \eta$. We require $|m_{\pi^+ \pi^- \eta} - m_{\eta'}| < 10$ MeV.

6.6 Non-Resonant D Decay Background

In principle, non-resonant D decays could enter into our signal modes with the same final particles. For example, non-resonant $D^+ \rightarrow \pi^+(\pi^+ \pi^-)$ could appear in the $D^+ \rightarrow \pi^+ K_S^0, K_S^0 \rightarrow \pi^+ \pi^-$ mode. To understand the background from non-resonant D decays, we look at M_{bc} , in D^0 and D^+ modes, and $M(D_s)$, in D_s modes, distributions in the sideband region of the intermediate resonance (η' or K_S^0) invariant mass. For $D^0 \rightarrow K_S^0 K_S^0$ (or $D^0 \rightarrow K_S^0 \eta'$) mode, the scatter plot of K_S^0 candidate invariant mass against the other K_S^0 (or η') candidate invariant mass is used to define a signal region and two kinds of sideband regions to remove the non-resonant decay background.

6.7 Yields in Data

6.7.1 Absolute and Relative Branching Fractions

The absolute branching fractions of our interested modes are given by

$$\mathcal{B}_{\text{sig}} = \mathcal{B}_{\text{ref}} \times \frac{N_{\text{sig}}}{N_{\text{ref}}} \times \frac{\epsilon_{\text{ref}}}{\epsilon_{\text{sig}}},$$

and the ratios of suppressed mode over favored mode are given by

$$\mathcal{R} = \frac{\mathcal{B}_{\text{Suppressed}}}{\mathcal{B}_{\text{Favored}}} = \frac{N_{\text{Suppressed}}}{N_{\text{Favored}}} \times \frac{\epsilon_{\text{Favored}}}{\epsilon_{\text{Suppressed}}},$$

N is the yield number of D candidates in interested modes and reference modes. ϵ is the reconstruction efficiency. In this analysis, we normalize against the Cabibbo-favored D modes, $D^0 \rightarrow K^- \pi^+$, $D^+ \rightarrow K^- \pi^+ \pi^+$, and $D_s^+ \rightarrow K^+ K_S^0$.

6.7.2 Data Yields

The fit results are shown from Fig. 6.8 to Fig. 6.36. The corresponding fit yields are summarized in Table 6.9 for D^0 modes, Table 6.10 for D^+ modes, and Table 6.11 for D_s^+ modes.

Table 6.9: D^0 mode Monte Carlo efficiency and data yield.

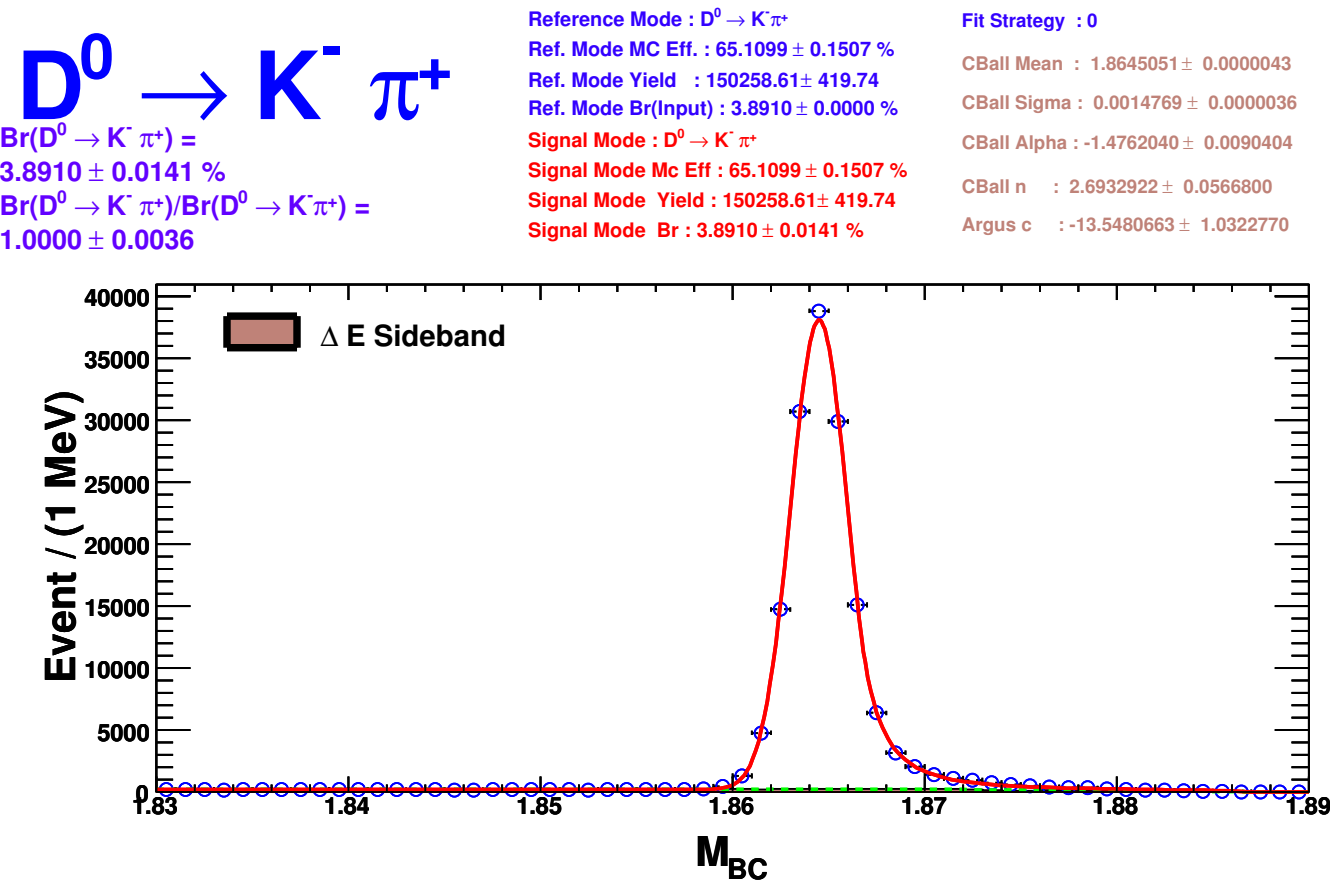
Mode	MC ϵ (%)	Yield
$D^0 \rightarrow K^+ K^-$	57.64 ± 0.16	13782.3 ± 135.8
$D^0 \rightarrow K_S^0 K_S^0$	22.39 ± 0.13	214.8 ± 22.7
$D^0 \rightarrow \pi^+ \pi^-$	72.32 ± 0.14	6210.0 ± 93.3
$D^0 \rightarrow \pi^0 \pi^0$	35.22 ± 0.15	1566.7 ± 53.5
$D^0 \rightarrow K^- \pi^+$	65.11 ± 0.15	150258.6 ± 419.7
$D^0 \rightarrow K_S^0 \pi^0$	29.32 ± 0.14	20045.4 ± 164.5
$D^0 \rightarrow K_S^0 \eta$	27.03 ± 0.14	2863.8 ± 65.4
$D^0 \rightarrow \pi^0 \eta$	33.41 ± 0.15	481.0 ± 40.2
$D^0 \rightarrow K_S^0 \eta'$	14.28 ± 0.11	1320.6 ± 42.3
$D^0 \rightarrow \pi^0 \eta'$	18.76 ± 0.12	158.8 ± 18.9
$D^0 \rightarrow \eta \eta$	31.75 ± 0.15	430.4 ± 28.7
$D^0 \rightarrow \eta \eta'$	17.52 ± 0.12	66.0 ± 15.1

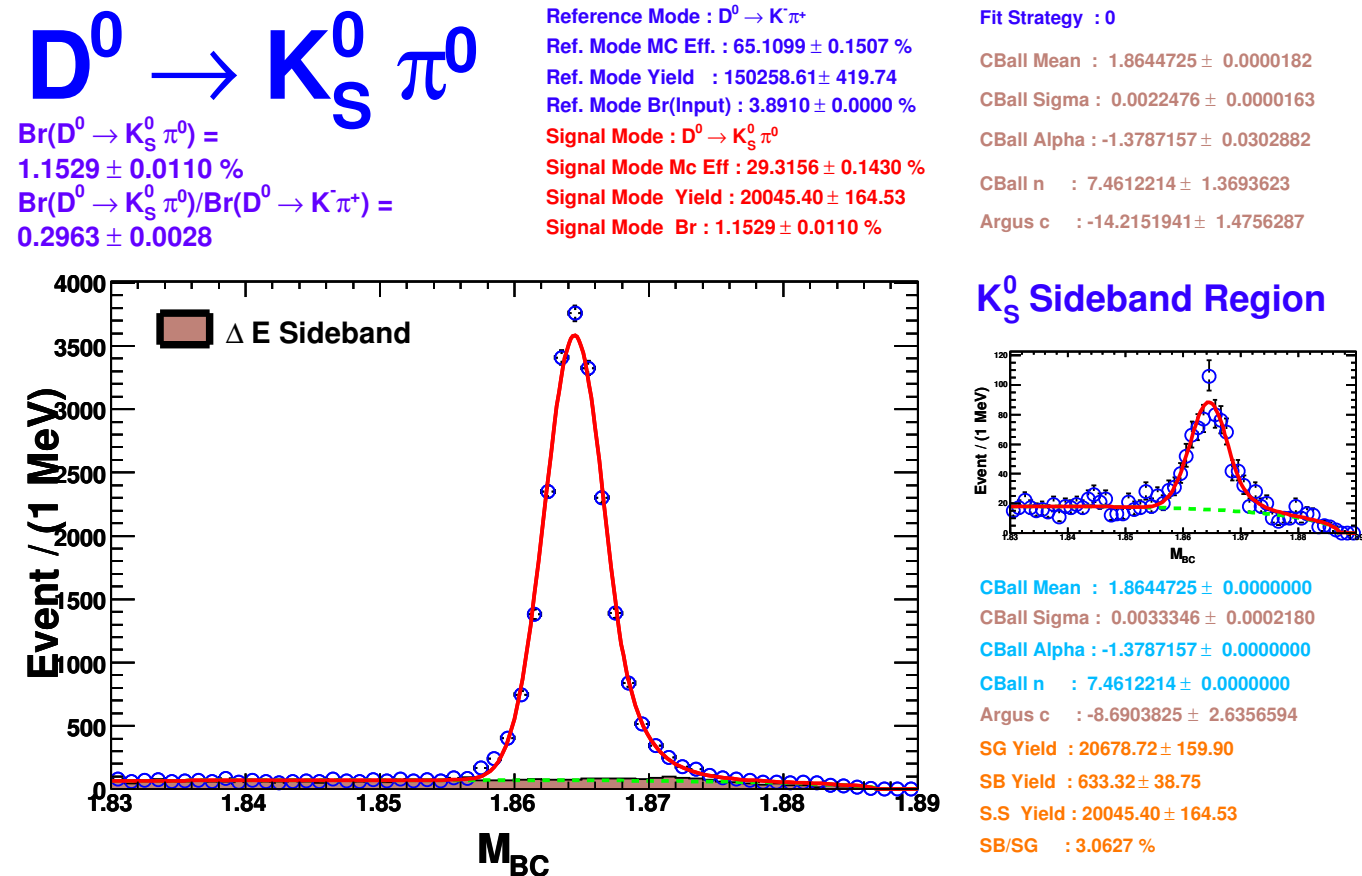
Table 6.10: D^+ mode Monte Carlo efficiency and data yield.

Mode	MC ϵ (%)	Yield
$D^+ \rightarrow K^- \pi^+ \pi^+$	54.92 ± 0.16	231058.2 ± 515.3
$D^+ \rightarrow K_S^0 K^+$	36.25 ± 0.15	5161.2 ± 85.6
$D^+ \rightarrow \pi^+ \pi^0$	49.96 ± 0.16	2649.0 ± 76.2
$D^+ \rightarrow K_S^0 \pi^+$	41.91 ± 0.16	30094.7 ± 191.3
$D^+ \rightarrow K^+ \pi^0$	44.65 ± 0.16	342.9 ± 36.7
$D^+ \rightarrow K^+ \eta$	42.97 ± 0.16	60.5 ± 24.1
$D^+ \rightarrow \pi^+ \eta$	48.42 ± 0.16	2940.5 ± 67.6
$D^+ \rightarrow K^+ \eta'$	26.19 ± 0.14	22.8 ± 18.4
$D^+ \rightarrow \pi^+ \eta'$	29.21 ± 0.14	1036.8 ± 34.7

Table 6.11: D_s^+ mode Monte Carlo efficiency and data yield.

Mode	MC ϵ (%)	Yield
$D_s^+ \rightarrow K_S^0 K^+$	24.73 ± 0.14	4075.5 ± 71.2
$D_s^+ \rightarrow \pi^+ \pi^0$	17.20 ± 0.12	19.4 ± 28.3
$D_s^+ \rightarrow K_S^0 \pi^+$	28.01 ± 0.14	393.2 ± 33.1
$D_s^+ \rightarrow K^+ \pi^0$	30.80 ± 0.15	202.2 ± 70.4
$D_s^+ \rightarrow K^+ \eta$	31.02 ± 0.15	222.4 ± 41.0
$D_s^+ \rightarrow \pi^+ \eta$	34.38 ± 0.15	2586.7 ± 89.4
$D_s^+ \rightarrow K^+ \eta'$	17.67 ± 0.12	55.7 ± 17.1
$D_s^+ \rightarrow \pi^+ \eta'$	20.13 ± 0.13	1436.3 ± 46.7

Figure 6.8: $D^0 \rightarrow K^- \pi^+$ decay study.

Figure 6.9: $D^0 \rightarrow K_S^0 \pi^0$ decay study.

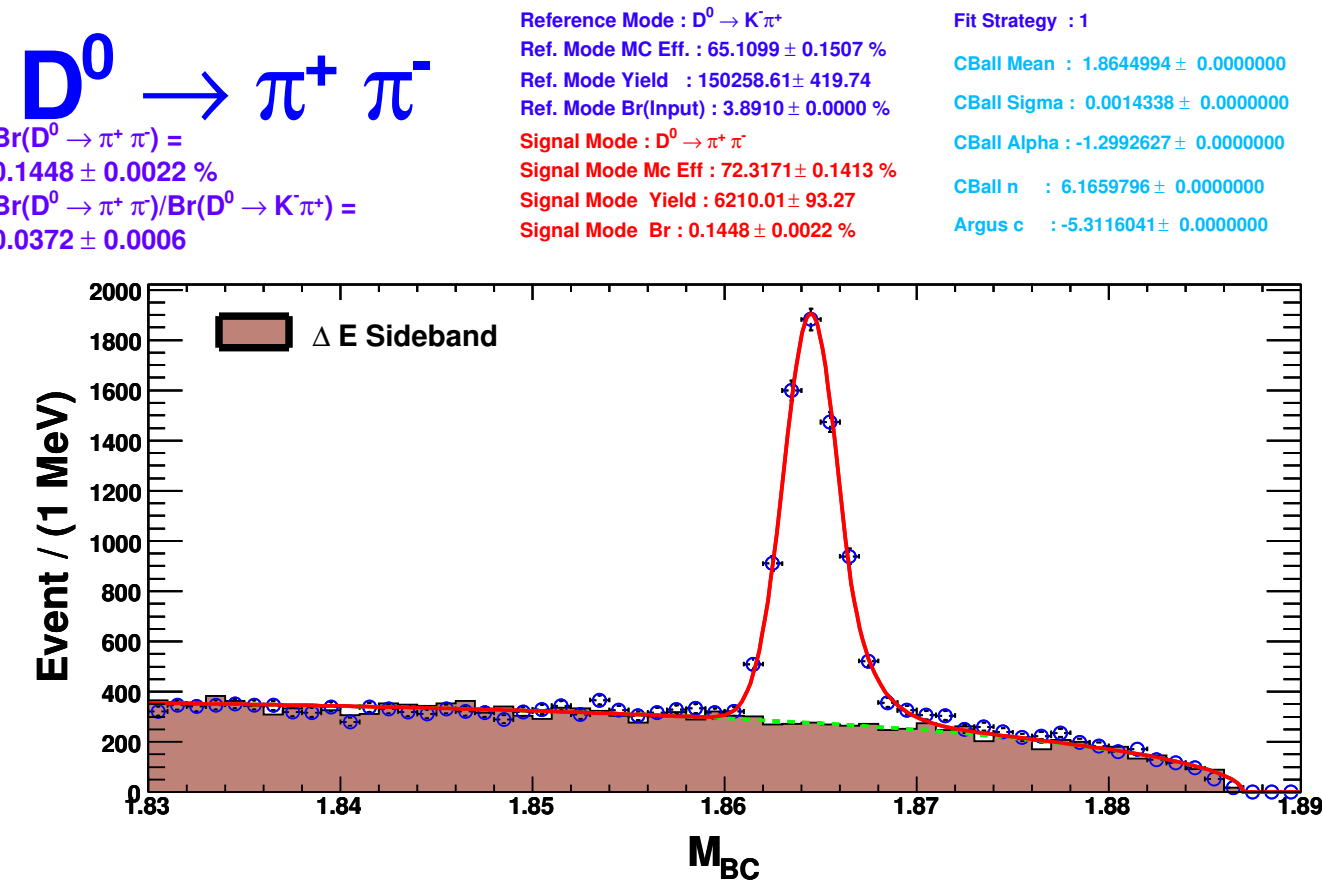


Figure 6.10: $D^0 \rightarrow \pi^+ \pi^-$ decay study.

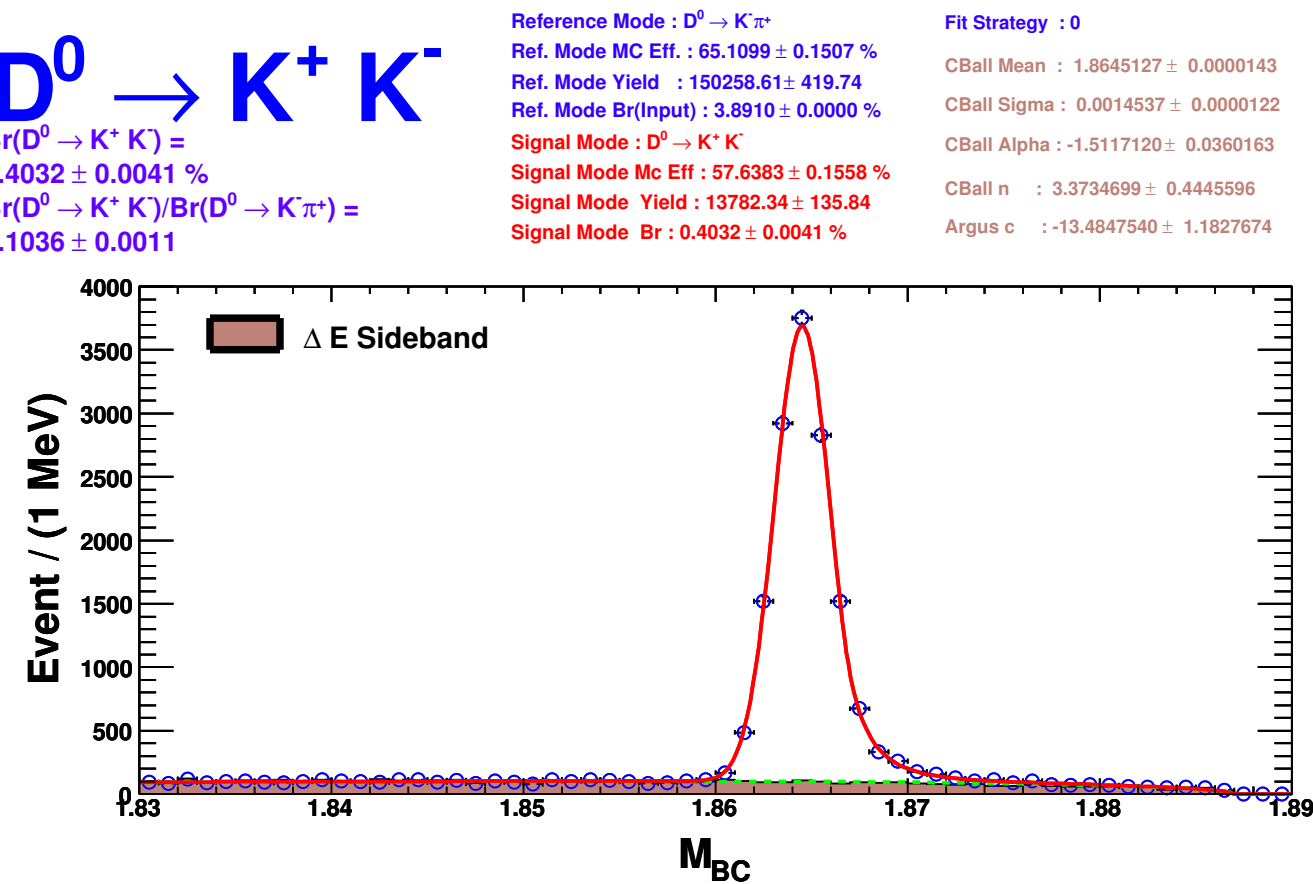
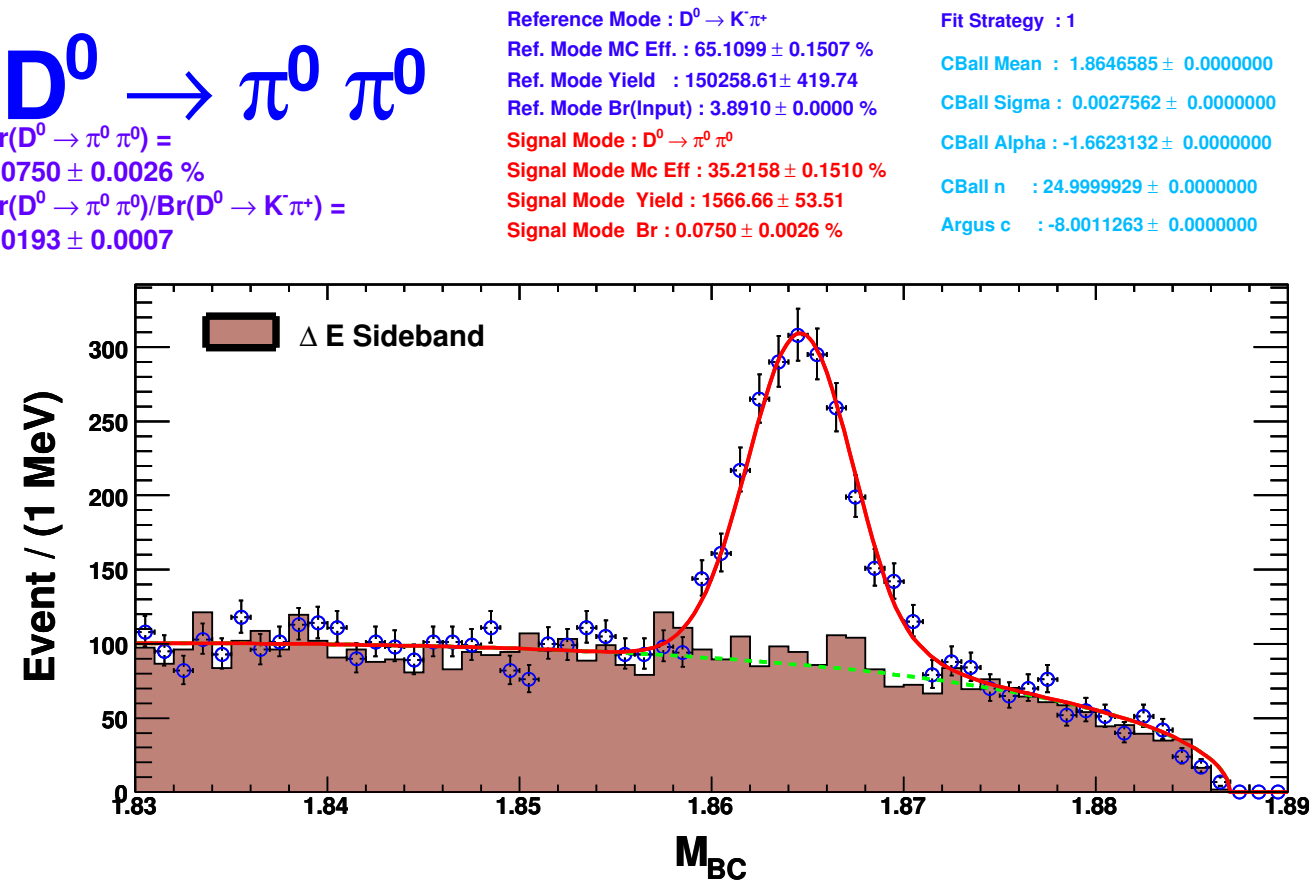


Figure 6.11: $D^0 \rightarrow K^+ K^-$ decay study.

Figure 6.12: $D^0 \rightarrow \pi^0 \pi^0$ decay study.

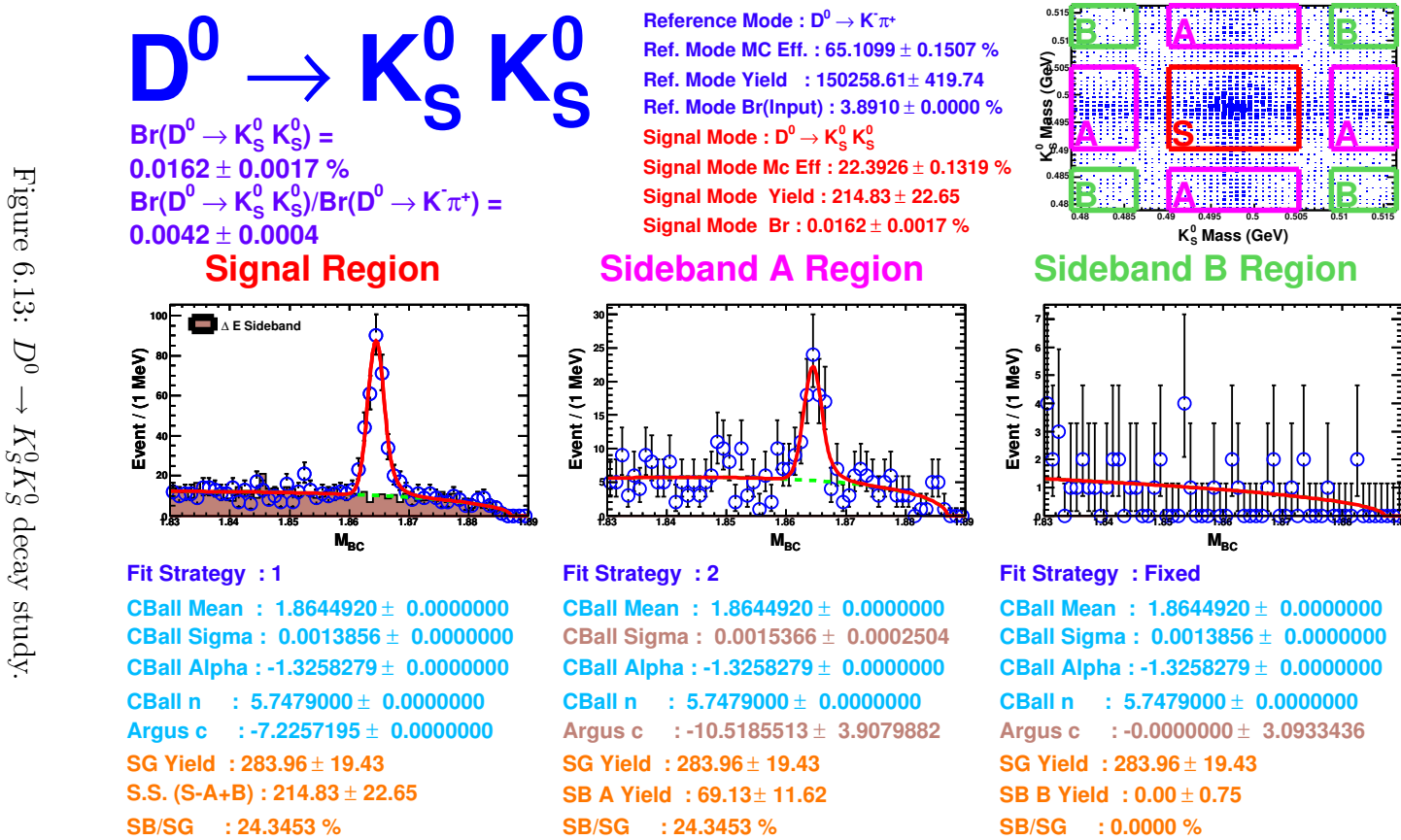
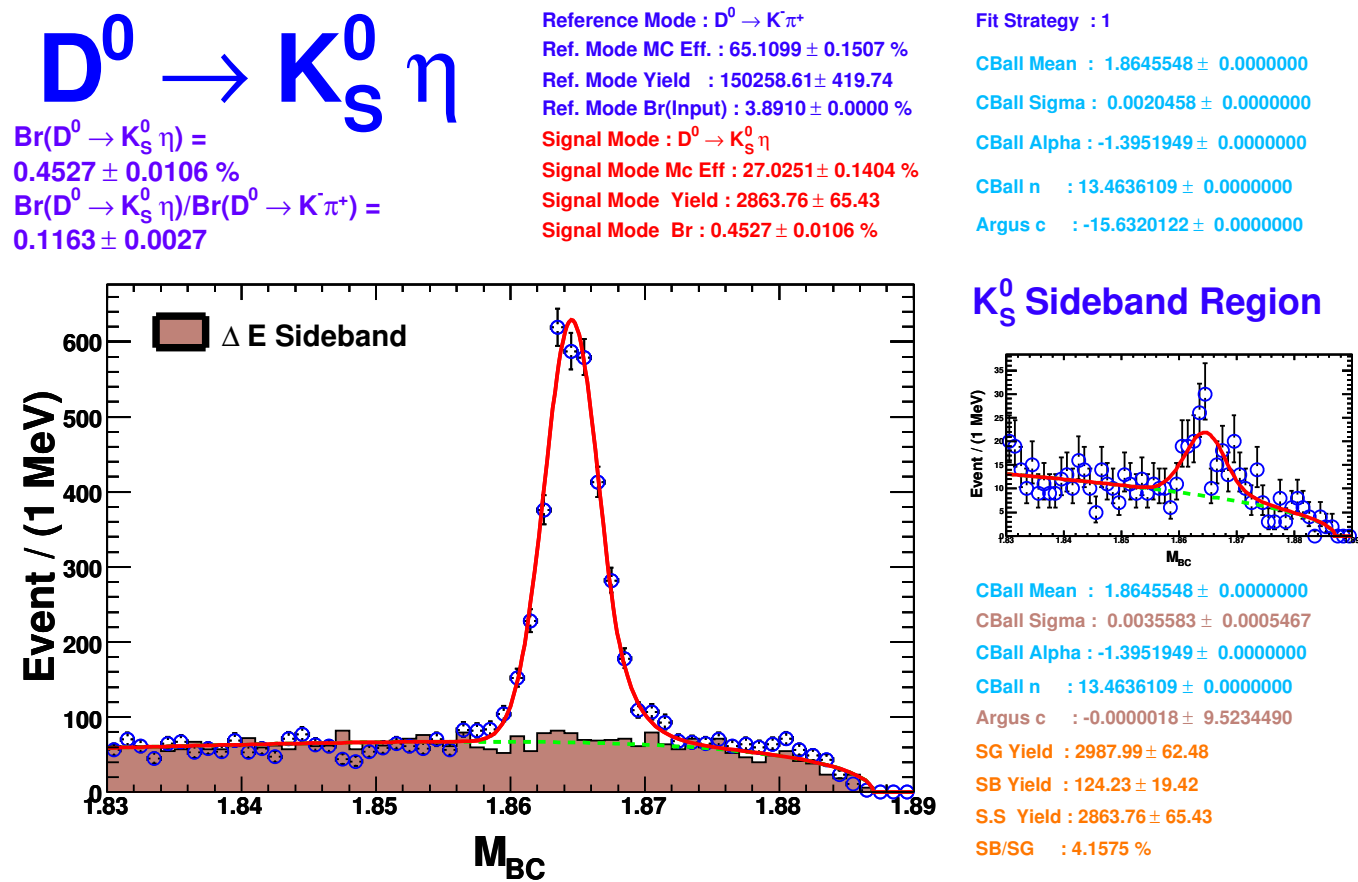
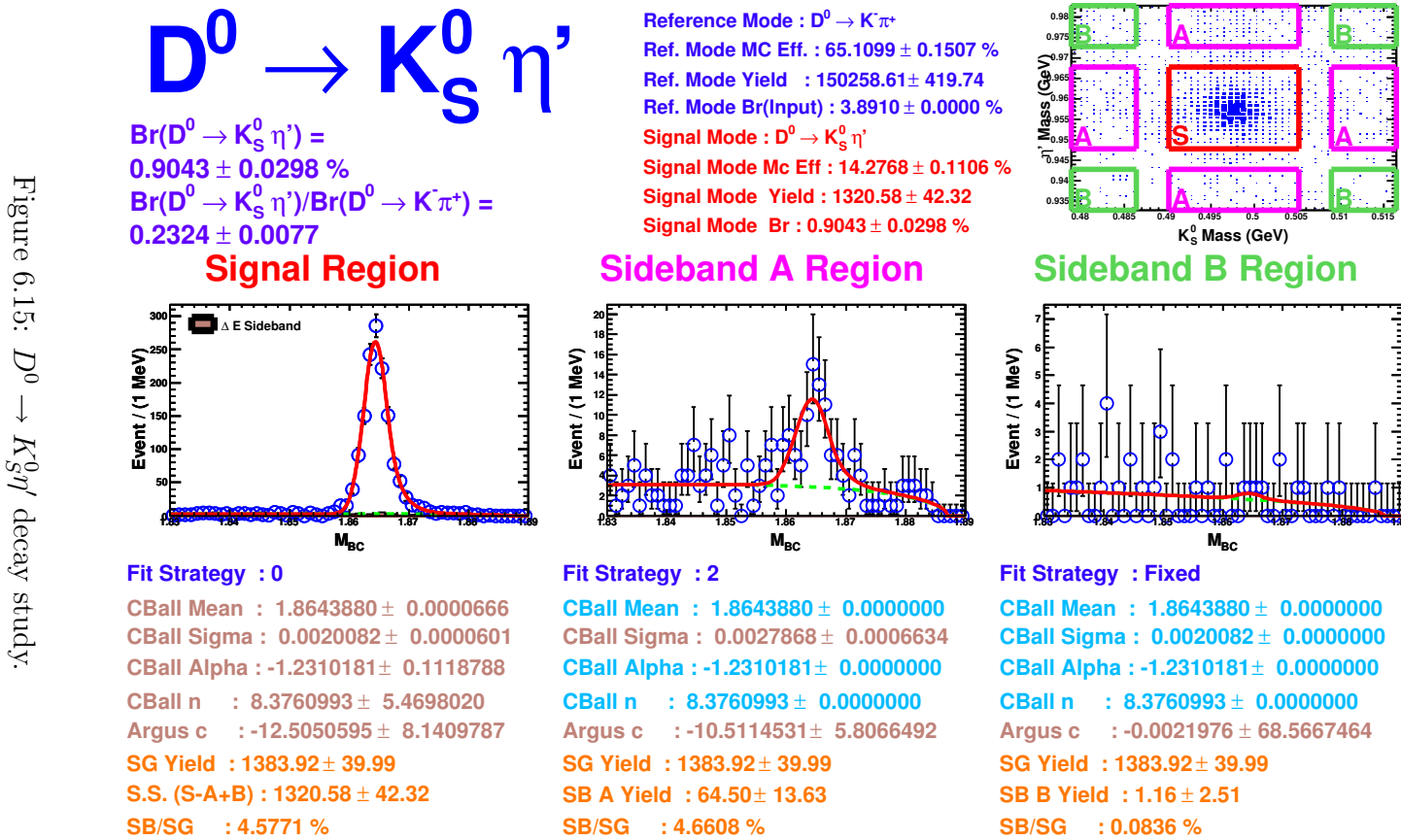
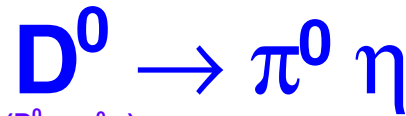


Figure 6.13: $D^0 \rightarrow K_S^0 K_S^0$ decay study.

Figure 6.14: $D^0 \rightarrow K_S^0 \eta$ decay study.

Figure 6.15: $D^0 \rightarrow K_S^0 \eta'$ decay study.



$$\begin{aligned} Br(D^0 \rightarrow \pi^0 \eta) &= 0.0615 \pm 0.0051 \% \\ Br(D^0 \rightarrow \pi^0 \eta)/Br(D^0 \rightarrow K\pi^+) &= 0.0158 \pm 0.0013 \end{aligned}$$

Reference Mode : $D^0 \rightarrow K\pi^+$
 Ref. Mode MC Eff. : $65.1099 \pm 0.1507 \%$
 Ref. Mode Yield : 150258.61 ± 419.74
 Ref. Mode Br(Input) : $3.8910 \pm 0.0000 \%$
 Signal Mode : $D^0 \rightarrow \pi^0 \eta$
 Signal Mode Mc Eff : $33.4106 \pm 0.1492 \%$
 Signal Mode Yield : 480.96 ± 40.15
 Signal Mode Br : $0.0615 \pm 0.0051 \%$

Fit Strategy : 1
 CBall Mean : 1.8646619 ± 0.0000000
 CBall Sigma : 0.0026356 ± 0.0000000
 CBall Alpha : -1.7126970 ± 0.0000000
 CBall n : 19.1146181 ± 0.0000000
 Argus c : -5.6762769 ± 0.0000000

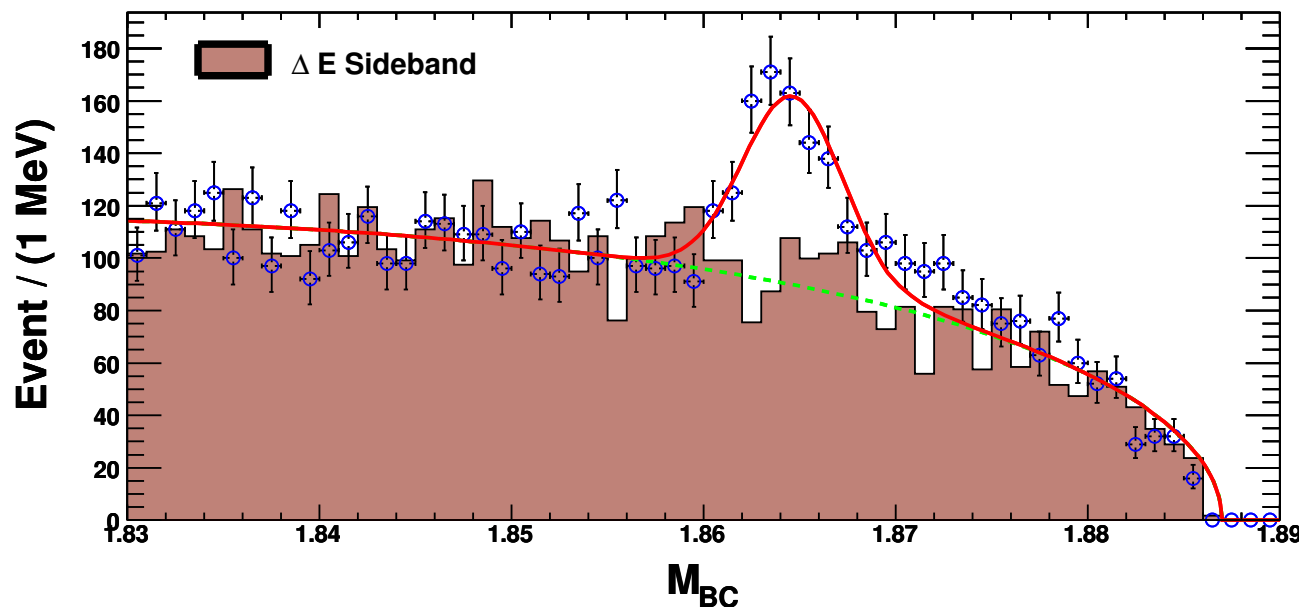
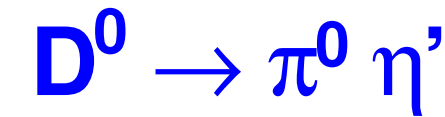


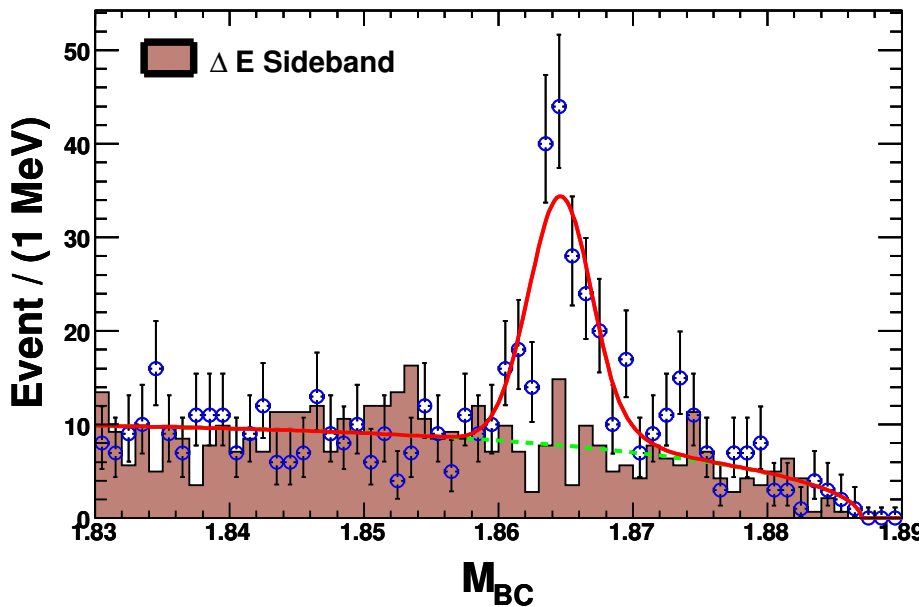
Figure 6.16: $D^0 \rightarrow \pi^0 \eta$ decay study.



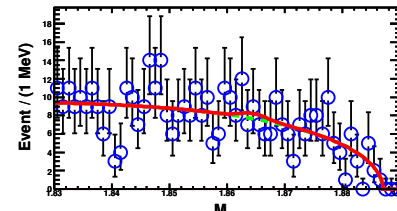
$$\begin{aligned} Br(D^0 \rightarrow \pi^0 \eta') &= 0.0828 \pm 0.0099 \% \\ Br(D^0 \rightarrow \pi^0 \eta')/Br(D^0 \rightarrow K\pi^+) &= 0.0213 \pm 0.0025 \end{aligned}$$

Reference Mode : $D^0 \rightarrow K\pi^+$
 Ref. Mode MC Eff. : $65.1099 \pm 0.1507 \%$
 Ref. Mode Yield : 150258.61 ± 419.74
 Ref. Mode Br(Input) : $3.8910 \pm 0.0000 \%$
 Signal Mode : $D^0 \rightarrow \pi^0 \eta'$
 Signal Mode Mc Eff : $18.7581 \pm 0.1235 \%$
 Signal Mode Yield : 158.83 ± 18.93
 Signal Mode Br : $0.0828 \pm 0.0099 \%$

Fit Strategy : 1
 CBall Mean : 1.8646265 ± 0.0000000
 CBall Sigma : 0.0023798 ± 0.0000000
 CBall Alpha : -1.5243304 ± 0.0000000
 CBall n : 19.3837500 ± 0.0000000
 Argus c : -5.7142515 ± 0.0000000

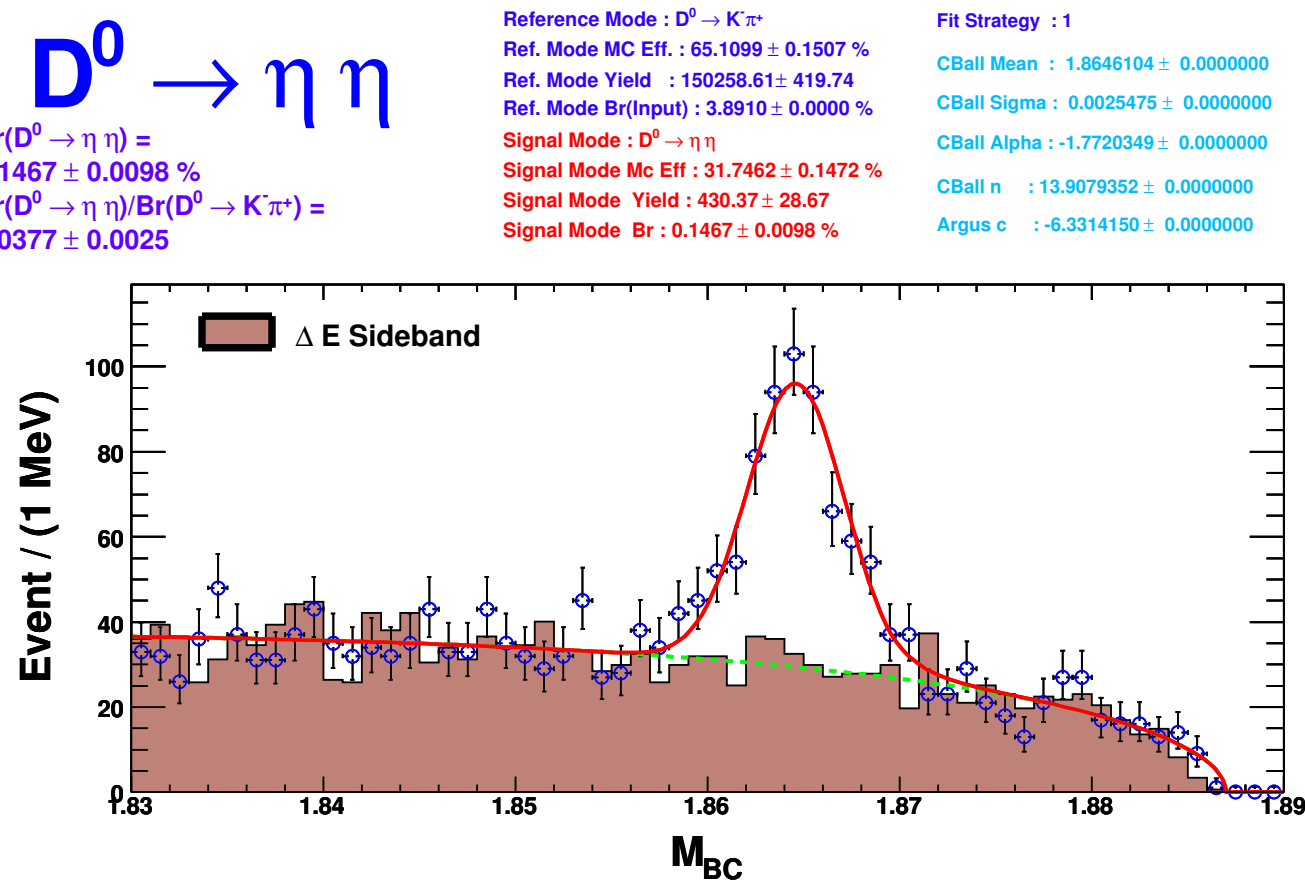


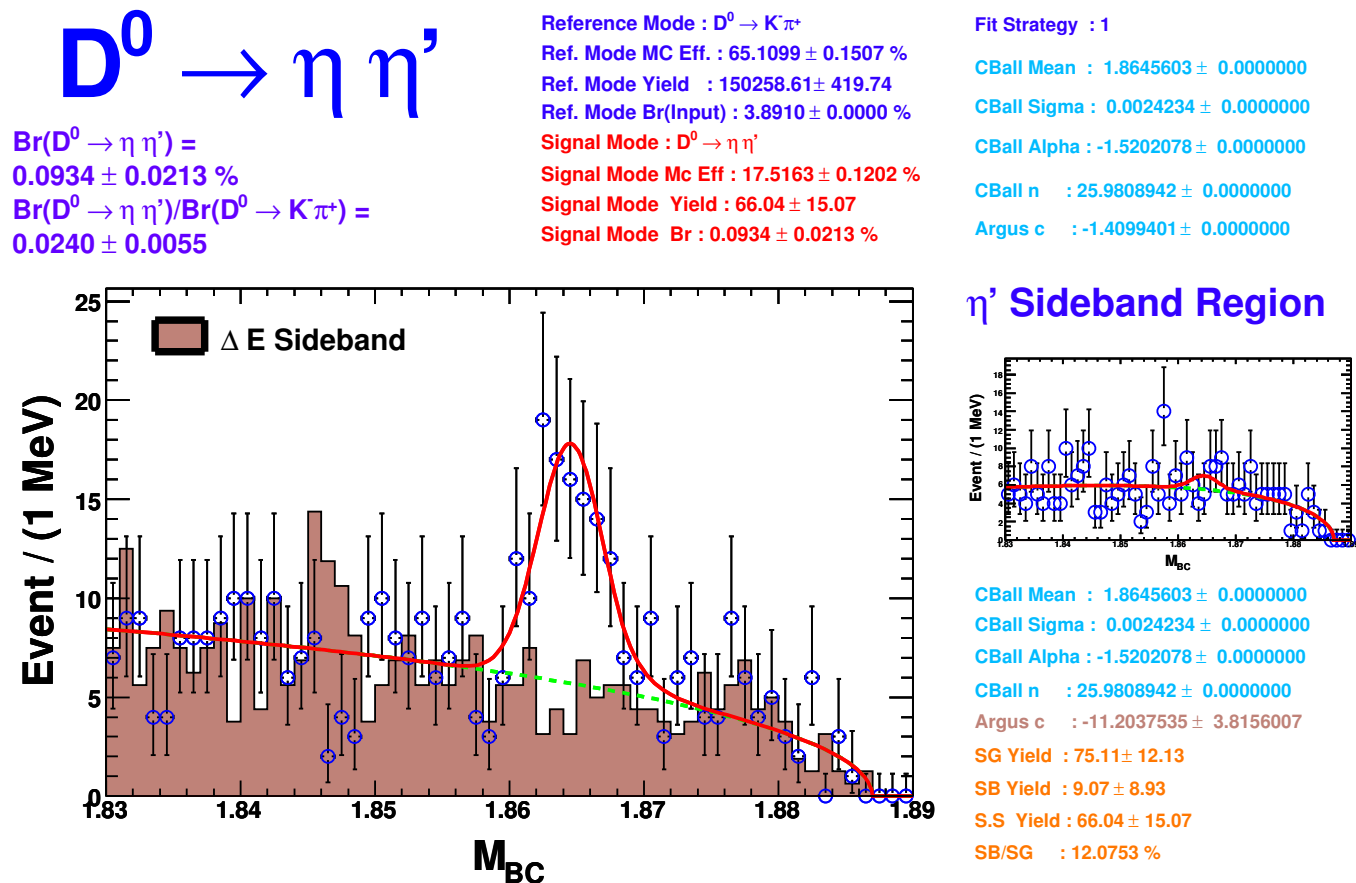
η' Sideband Region

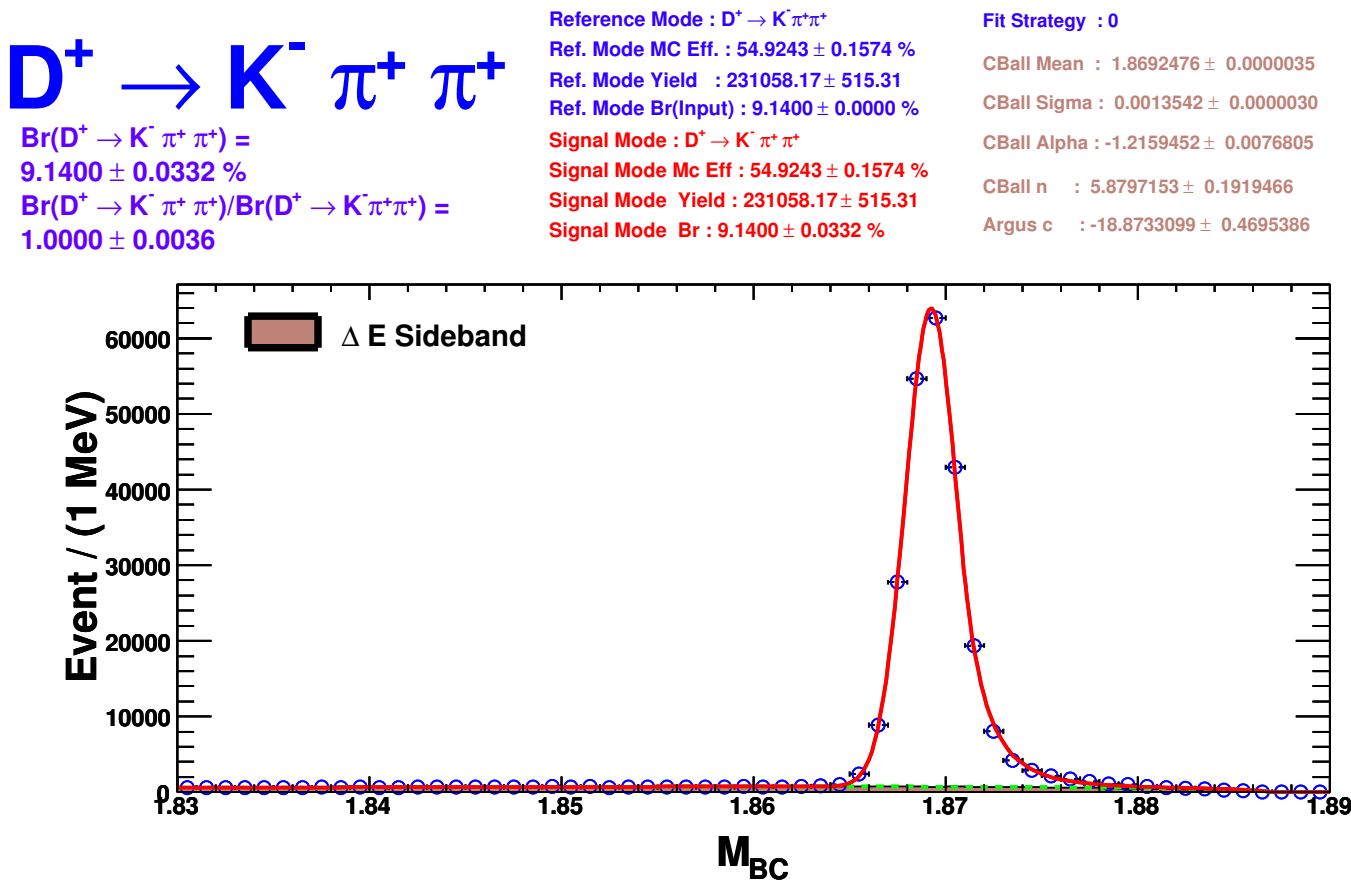


CBall Mean : 1.8646265 ± 0.0000000
 CBall Sigma : 0.0023798 ± 0.0000000
 CBall Alpha : -1.5243304 ± 0.0000000
 CBall n : 19.3837500 ± 0.0000000
 Argus c : -6.6265742 ± 3.1912506
 SG Yield : 162.28 ± 16.30
 SB Yield : 3.44 ± 9.62
 S.S. Yield : 158.83 ± 18.93
 SB/SG : 2.1214%

Figure 6.17: $D^0 \rightarrow \pi^0 \eta'$ decay study.

Figure 6.18: $D^0 \rightarrow \eta \eta$ decay study.

Figure 6.19: $D^0 \rightarrow \eta \eta'$ decay study.

Figure 6.20: $D^+ \rightarrow K^- \pi^+ \pi^+$ decay study.

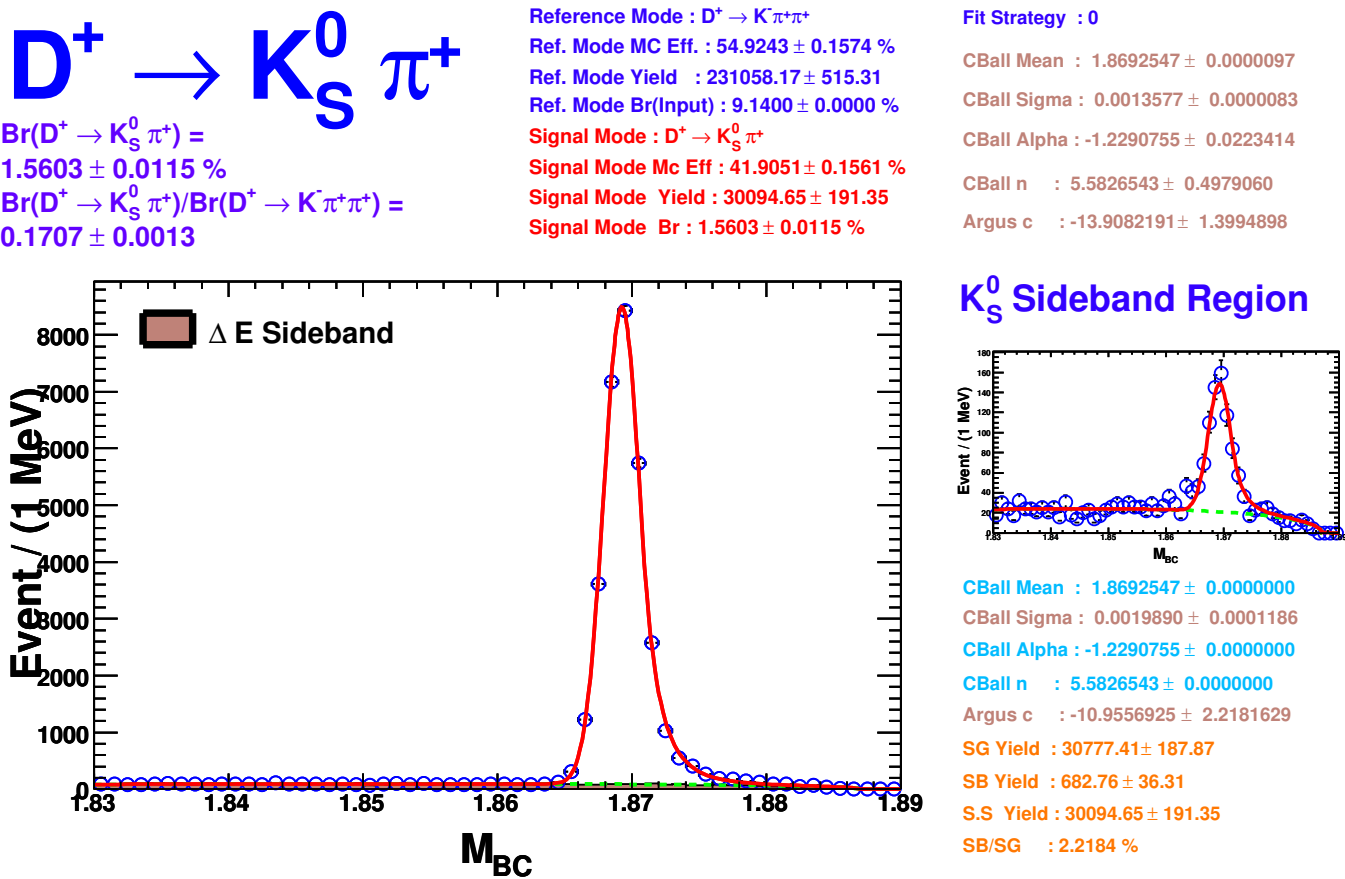
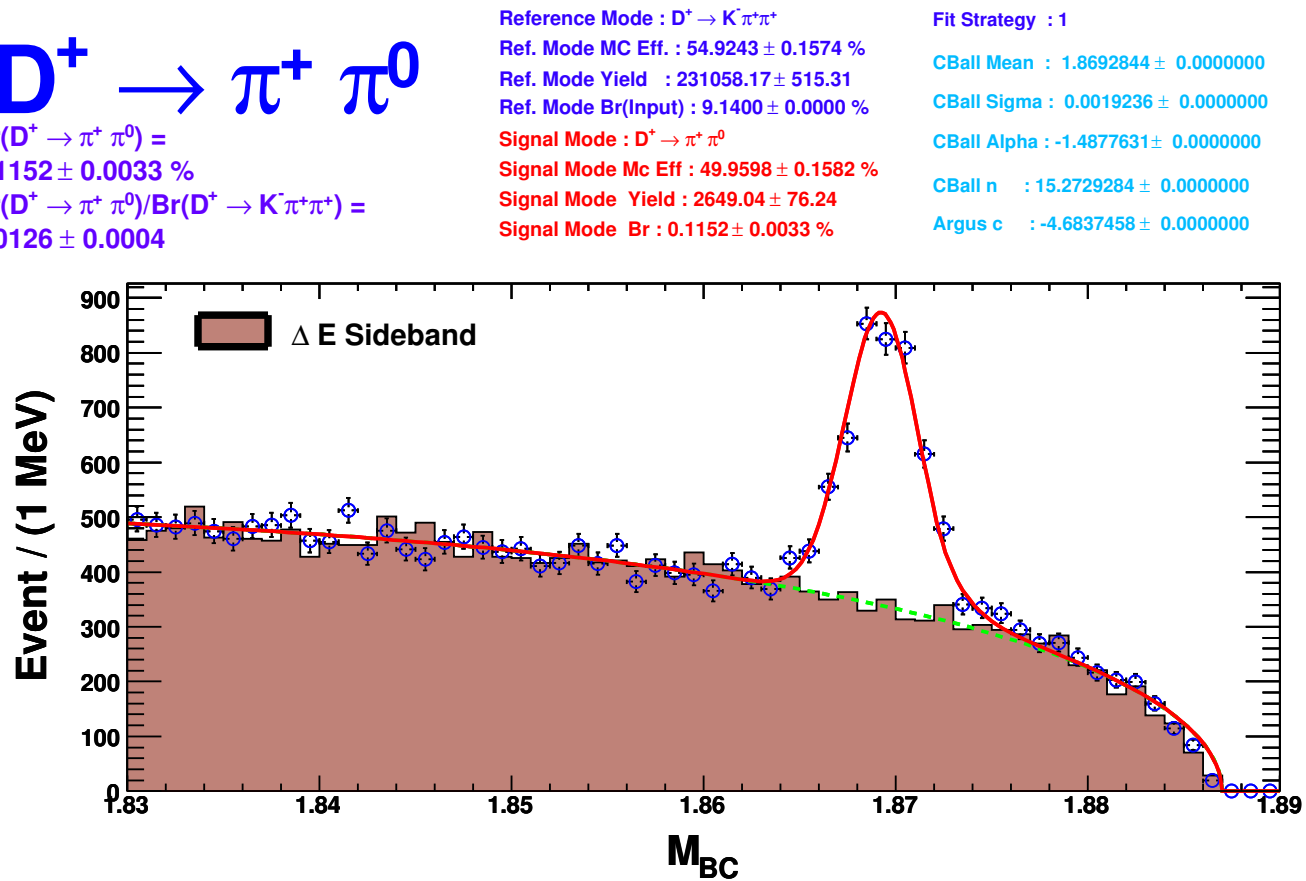
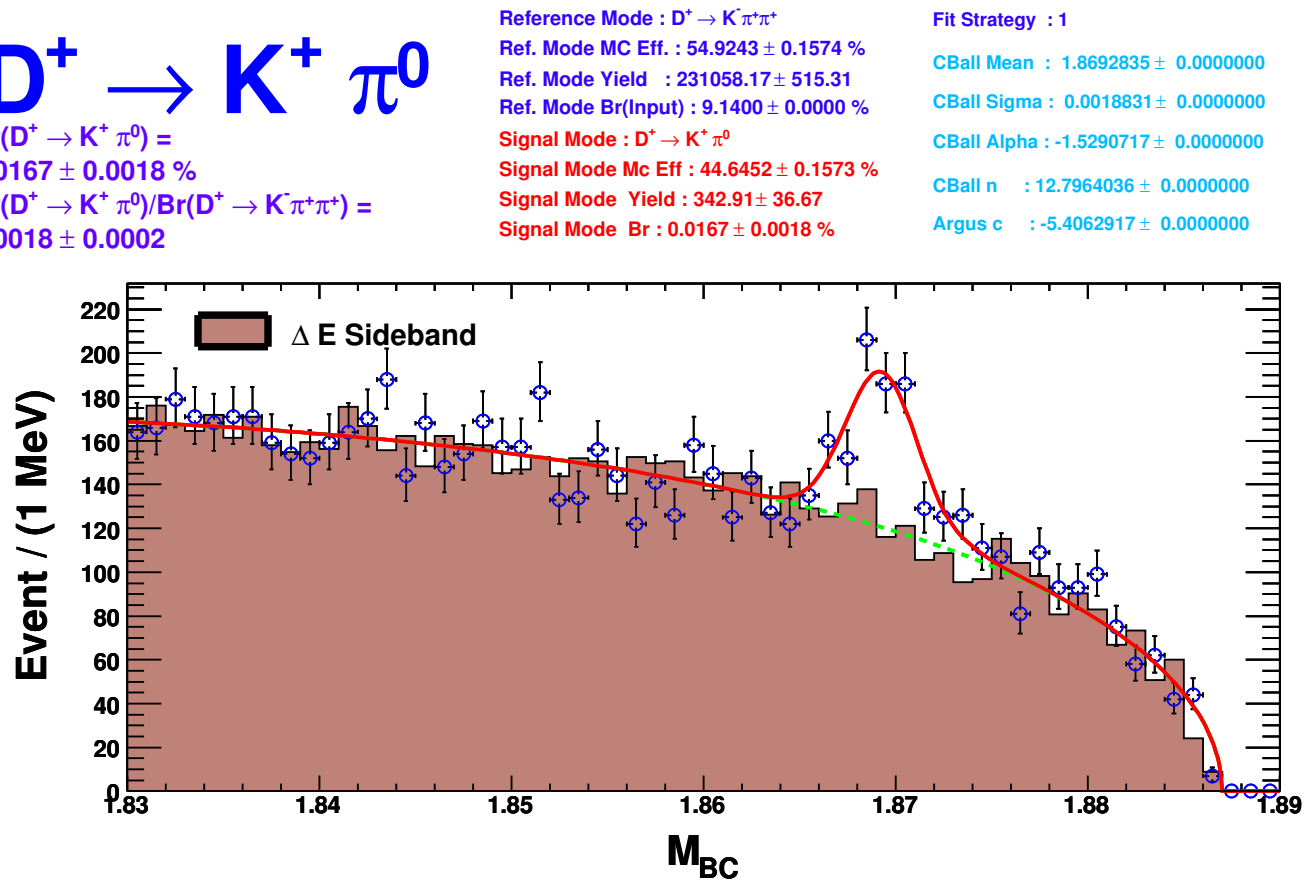


Figure 6.21: $D^+ \rightarrow K_S^0 \pi^+$ decay study.

Figure 6.22: $D^+ \rightarrow \pi^+ \pi^0$ decay study.

Figure 6.23: $D^+ \rightarrow K^+\pi^0$ decay study.

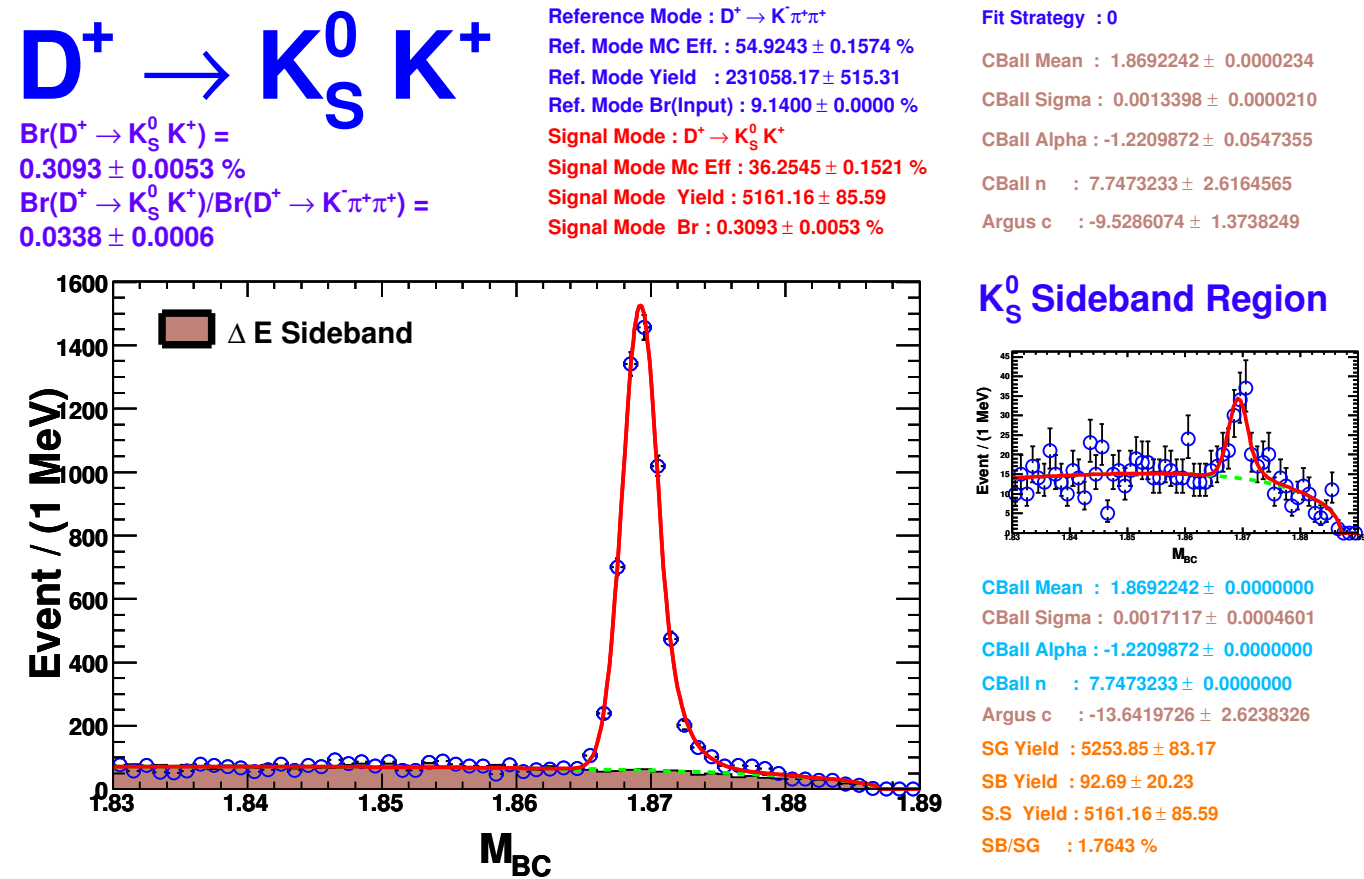
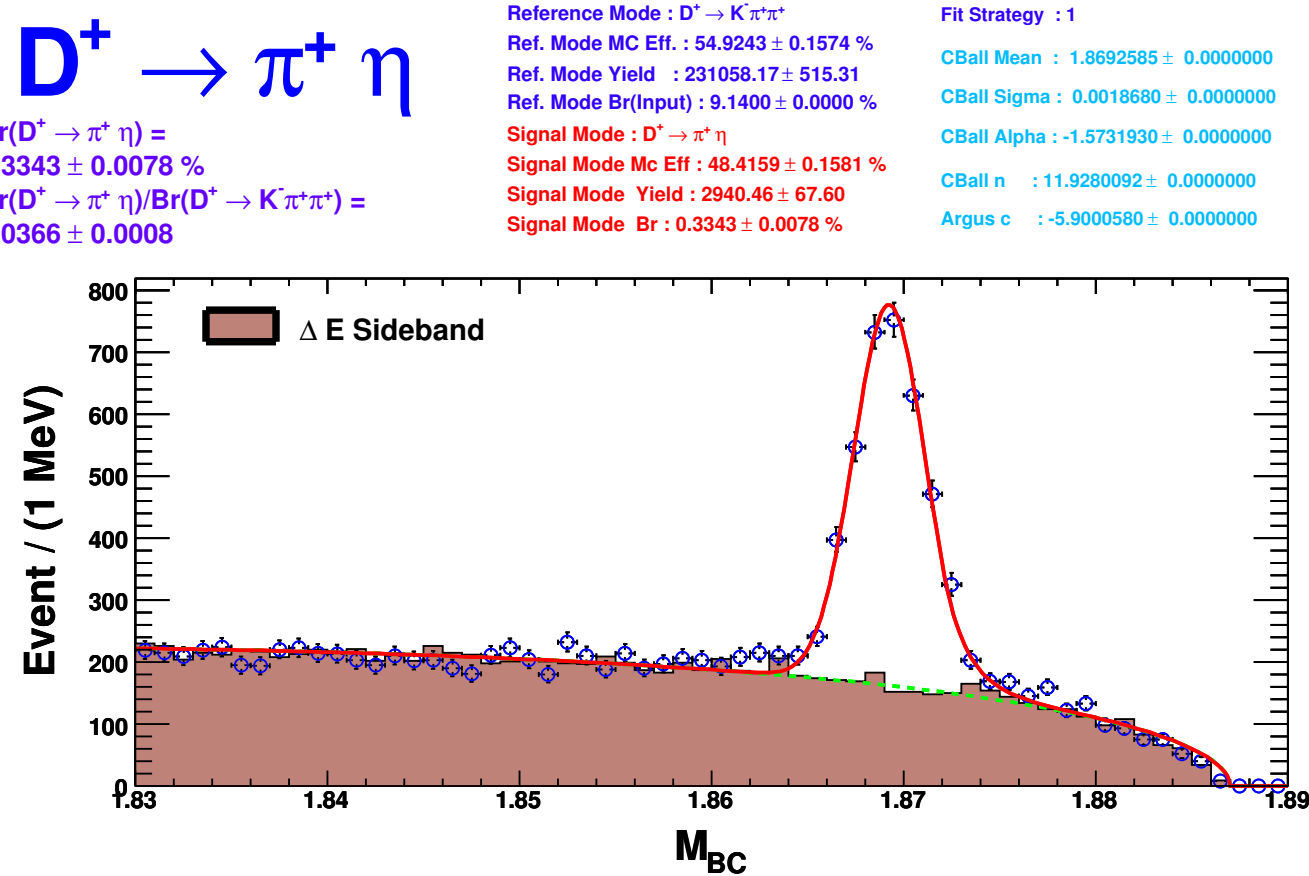
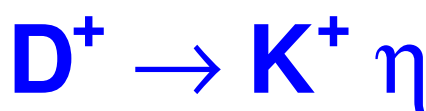


Figure 6.24: $D^+ \rightarrow K_S^0 K^+$ decay study.

Figure 6.25: $D^+ \rightarrow \pi^+ \eta$ decay study.



$$\begin{aligned} Br(D^+ \rightarrow K^+ \eta) &= 0.0077 \pm 0.0031 \% \\ Br(D^+ \rightarrow K^+ \eta)/Br(D^+ \rightarrow K\pi^+\pi^+) &= 0.0008 \pm 0.0003 \end{aligned}$$

Reference Mode : $D^+ \rightarrow K\pi^+\pi^+$
 Ref. Mode MC Eff. : $54.9243 \pm 0.1574 \%$
 Ref. Mode Yield : 231058.17 ± 515.31
 Ref. Mode Br(Input) : $9.1400 \pm 0.0000 \%$
 Signal Mode : $D^+ \rightarrow K^+ \eta$
 Signal Mode Mc Eff : $42.9722 \pm 0.1566 \%$
 Signal Mode Yield : 60.49 ± 24.09
 Signal Mode Br : $0.0077 \pm 0.0031 \%$

Fit Strategy : 1
 CBall Mean : 1.8692905 ± 0.0000000
 CBall Sigma : 0.0018383 ± 0.0000000
 CBall Alpha : -1.5693188 ± 0.0000000
 CBall n : 10.6149728 ± 0.0000000
 Argus c : -7.4985161 ± 0.0000000

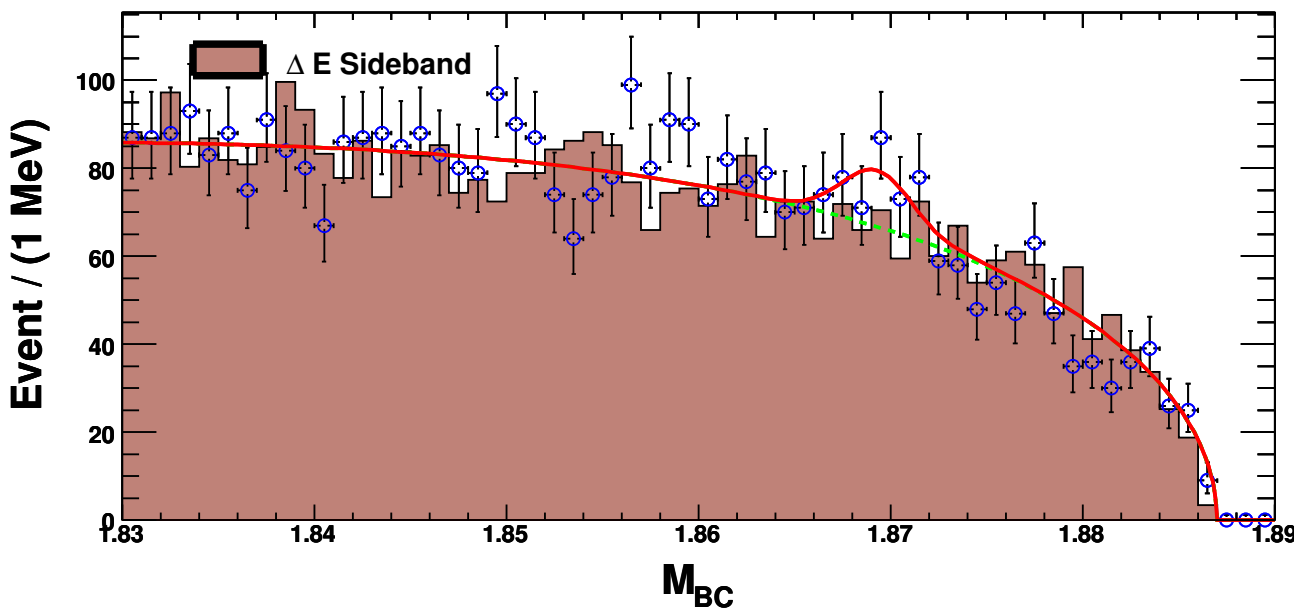
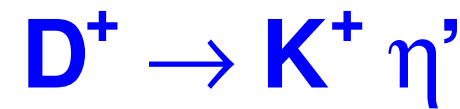


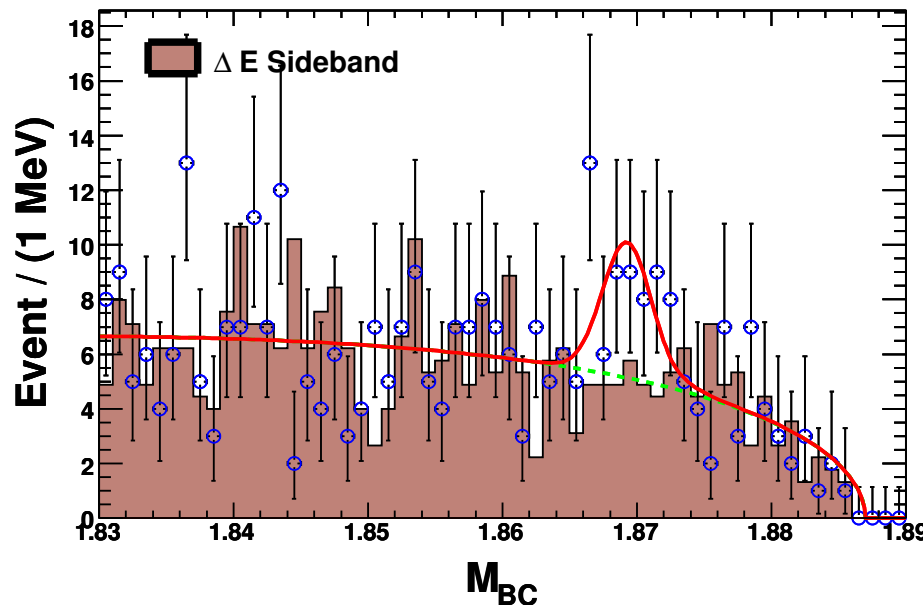
Figure 6.26: $D^+ \rightarrow K^+ \eta$ decay study.



$$\begin{aligned} Br(D^+ \rightarrow K^+ \eta') &= 0.0110 \pm 0.0089 \% \\ Br(D^+ \rightarrow K^+ \eta')/Br(D^+ \rightarrow K^+\pi^+\pi^+) &= 0.0012 \pm 0.0010 \end{aligned}$$

Reference Mode : $D^+ \rightarrow K^+\pi^+\pi^+$
 Ref. Mode MC Eff. : $54.9243 \pm 0.1574 \%$
 Ref. Mode Yield : 231058.17 ± 515.31
 Ref. Mode Br(Input) : $9.1400 \pm 0.0000 \%$
 Signal Mode : $D^+ \rightarrow K^+ \eta'$
 Signal Mode Mc Eff : $26.1857 \pm 0.1391 \%$
 Signal Mode Yield : 22.81 ± 18.40
 Signal Mode Br : $0.0110 \pm 0.0089 \%$

Fit Strategy : 1
 CBall Mean : 1.8692683 ± 0.0000000
 CBall Sigma : 0.0018341 ± 0.0000000
 CBall Alpha : -1.5620009 ± 0.0000000
 CBall n : 9.8495248 ± 0.0000000
 Argus c : -7.3085399 ± 0.0000000



η' Sideband Region

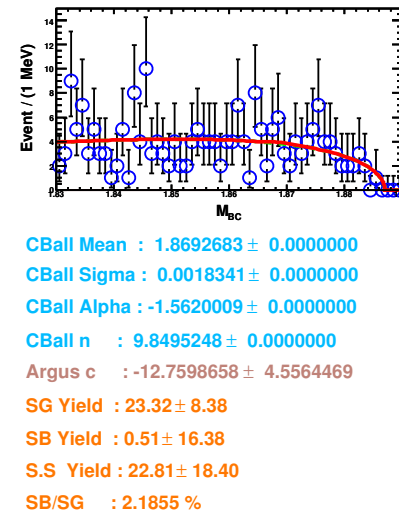


Figure 6.27: $D^+ \rightarrow K^+ \eta'$ decay study.

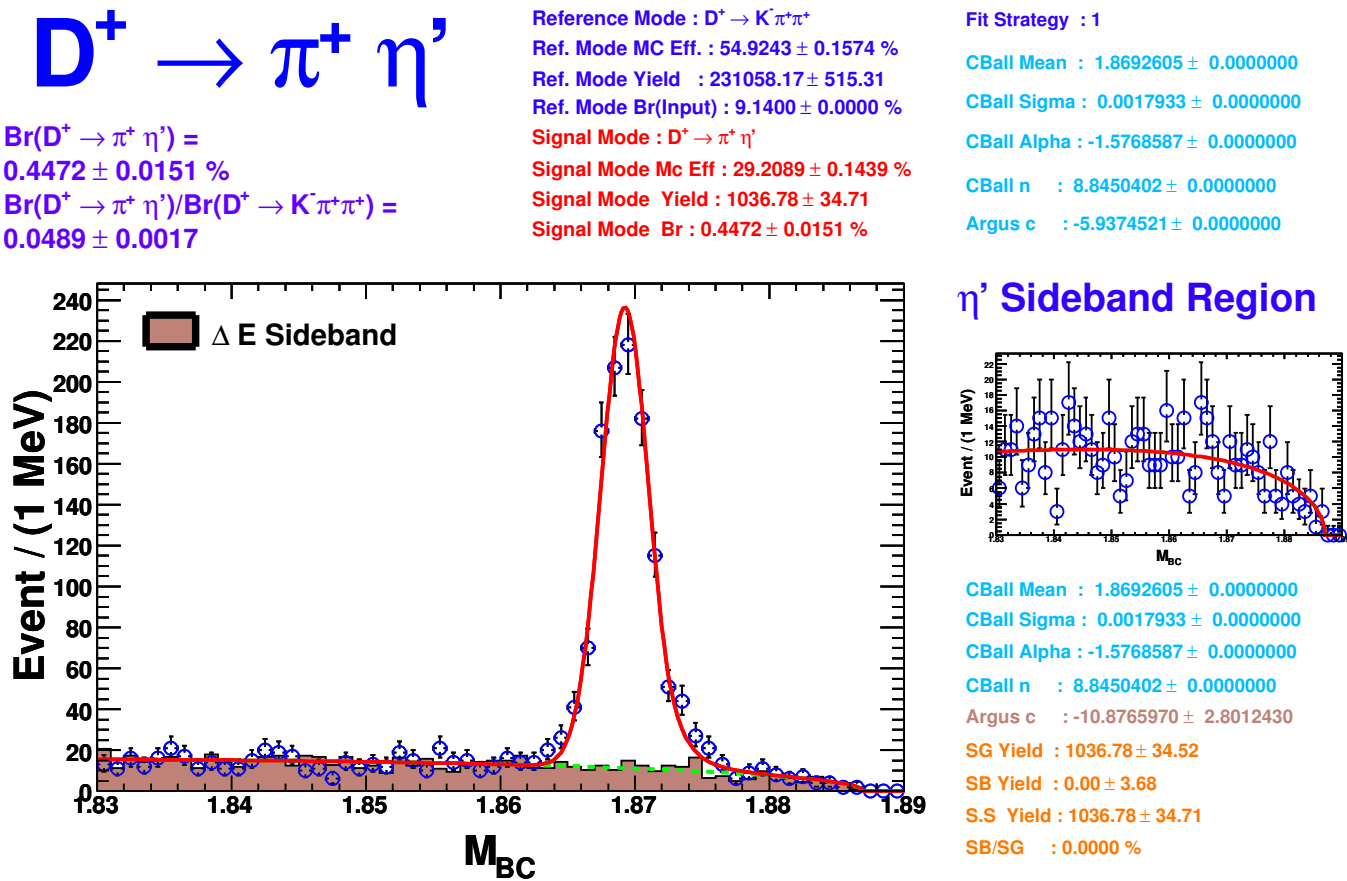


Figure 6.28: $D^+ \rightarrow \pi^+ \eta'$ decay study.

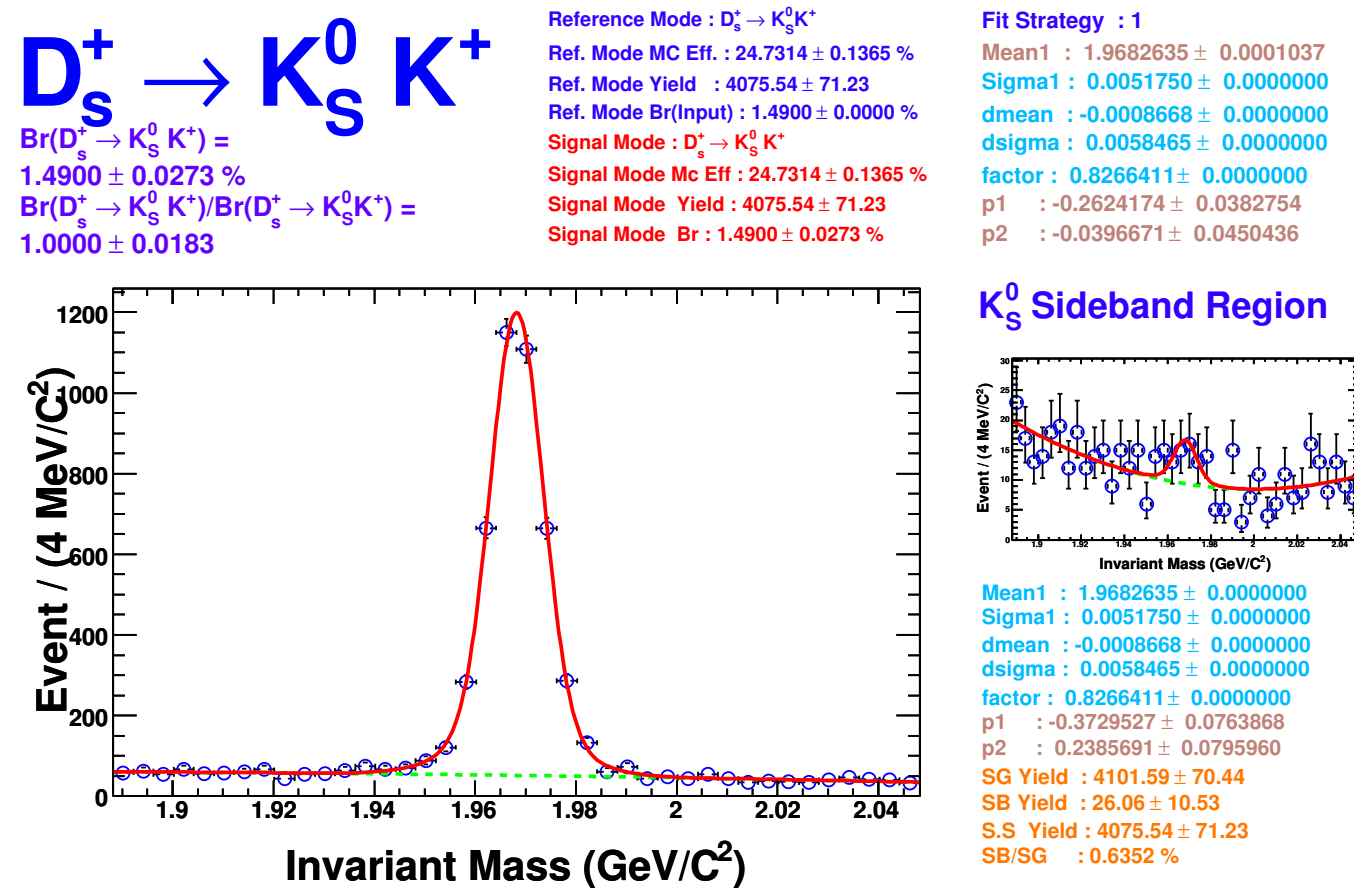


Figure 6.29: $D_s^+ \rightarrow K_s^0 K^+$ decay study.

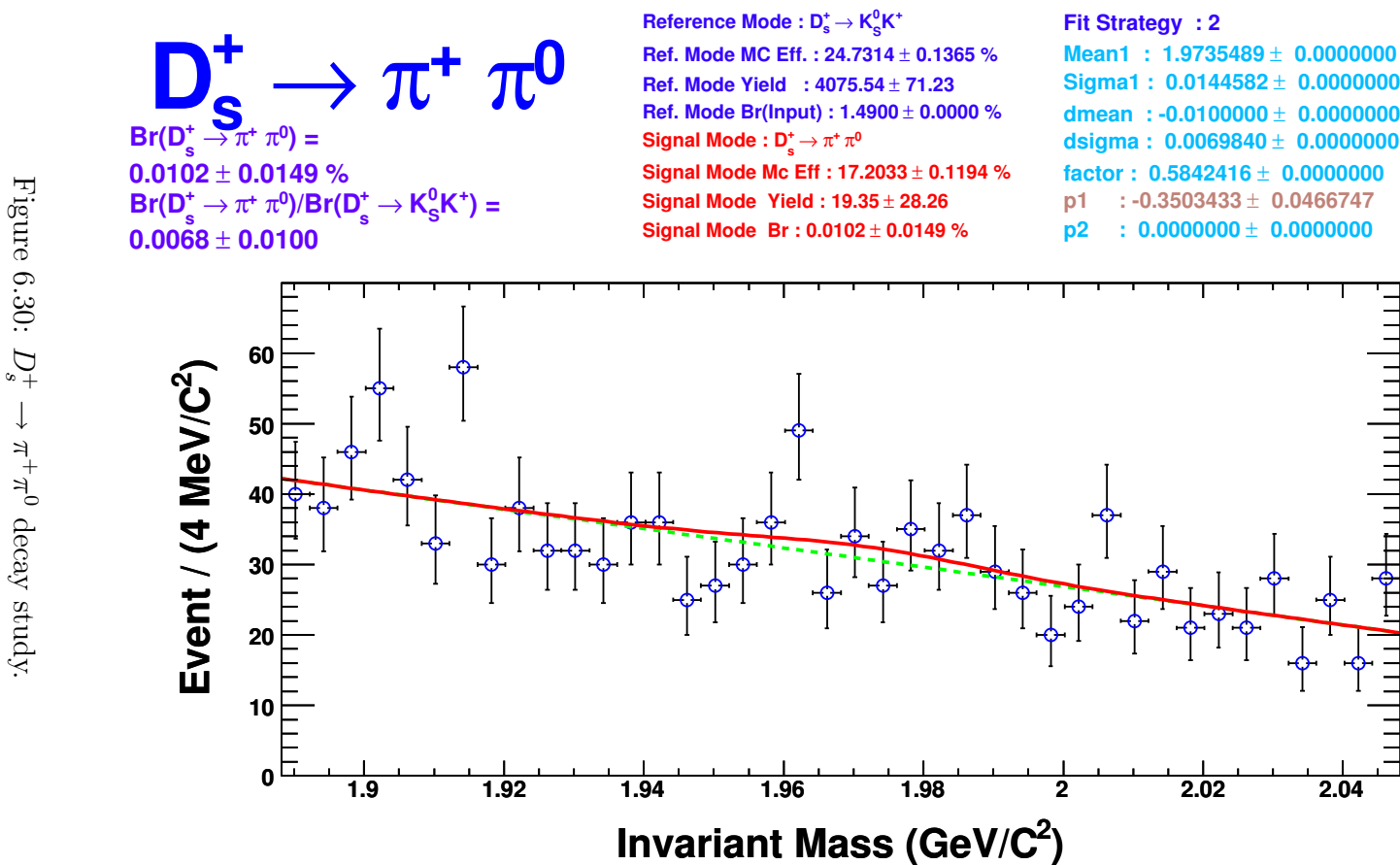
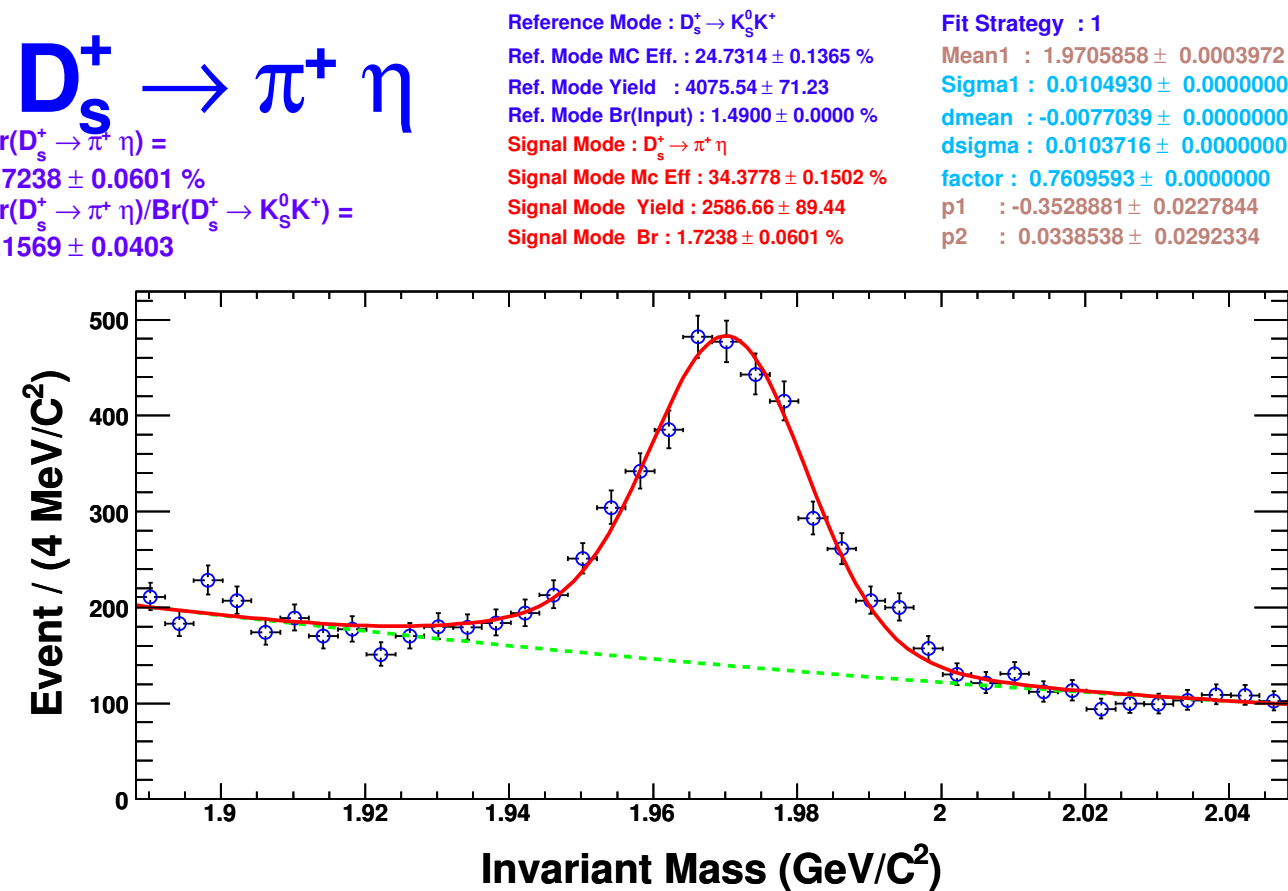
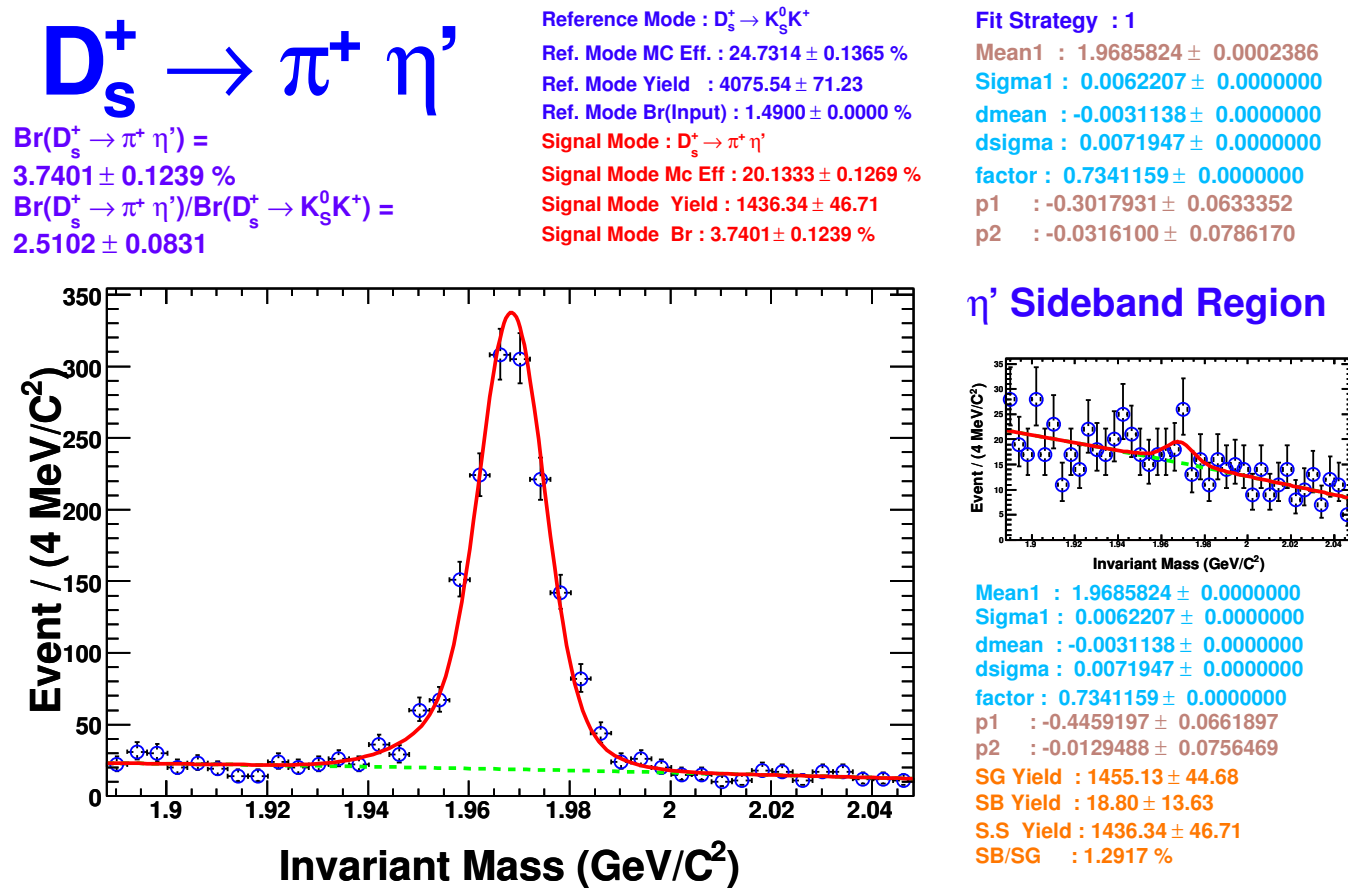
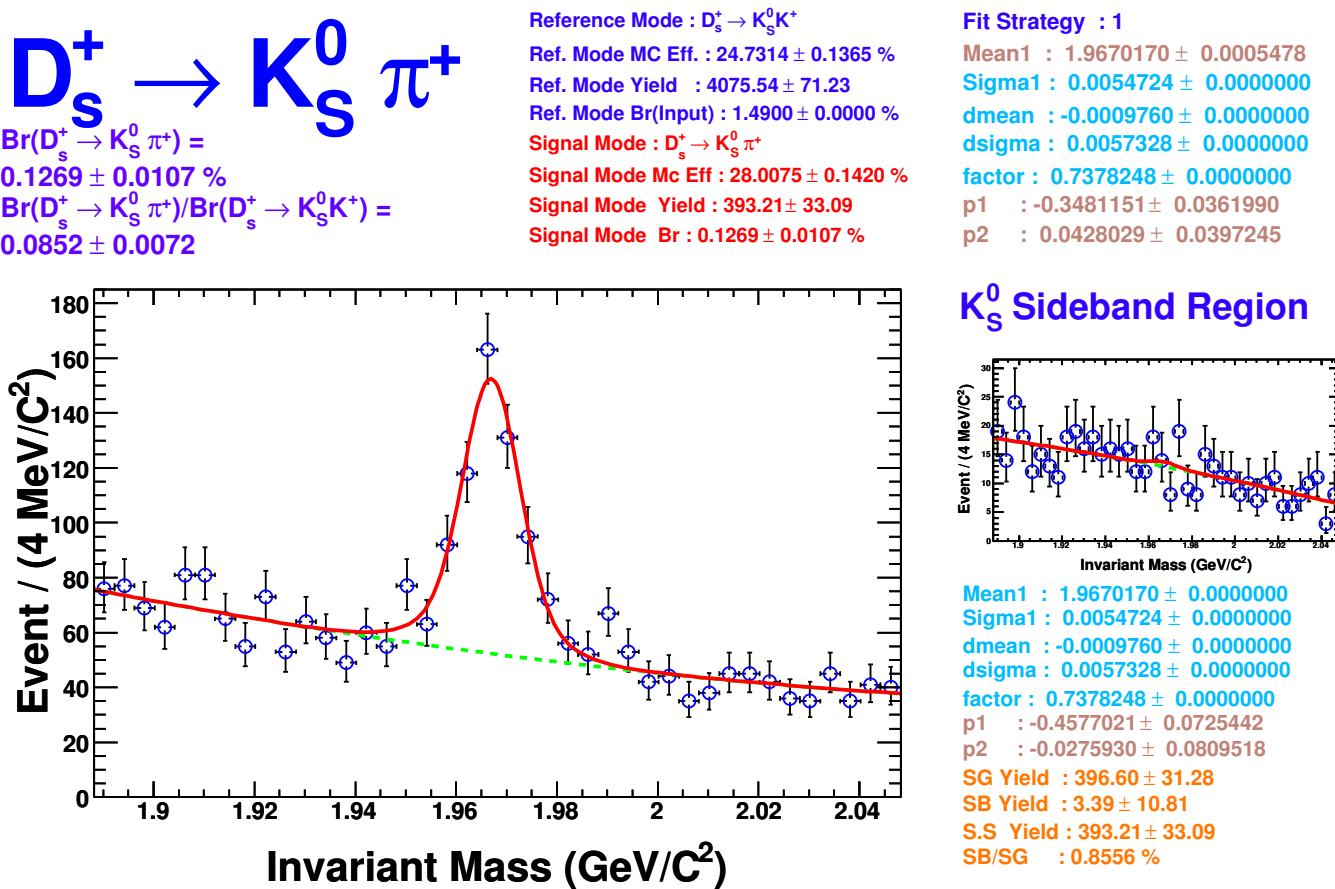
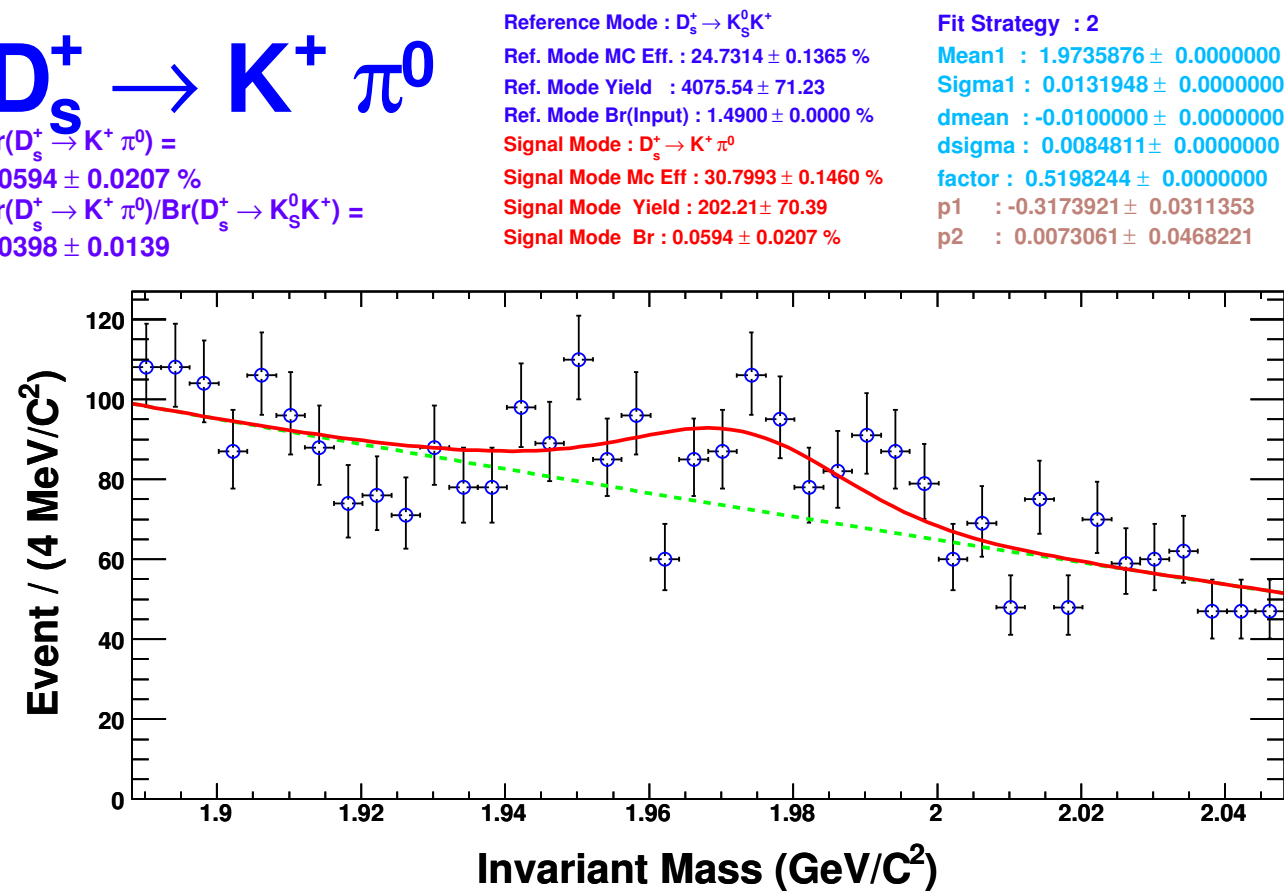


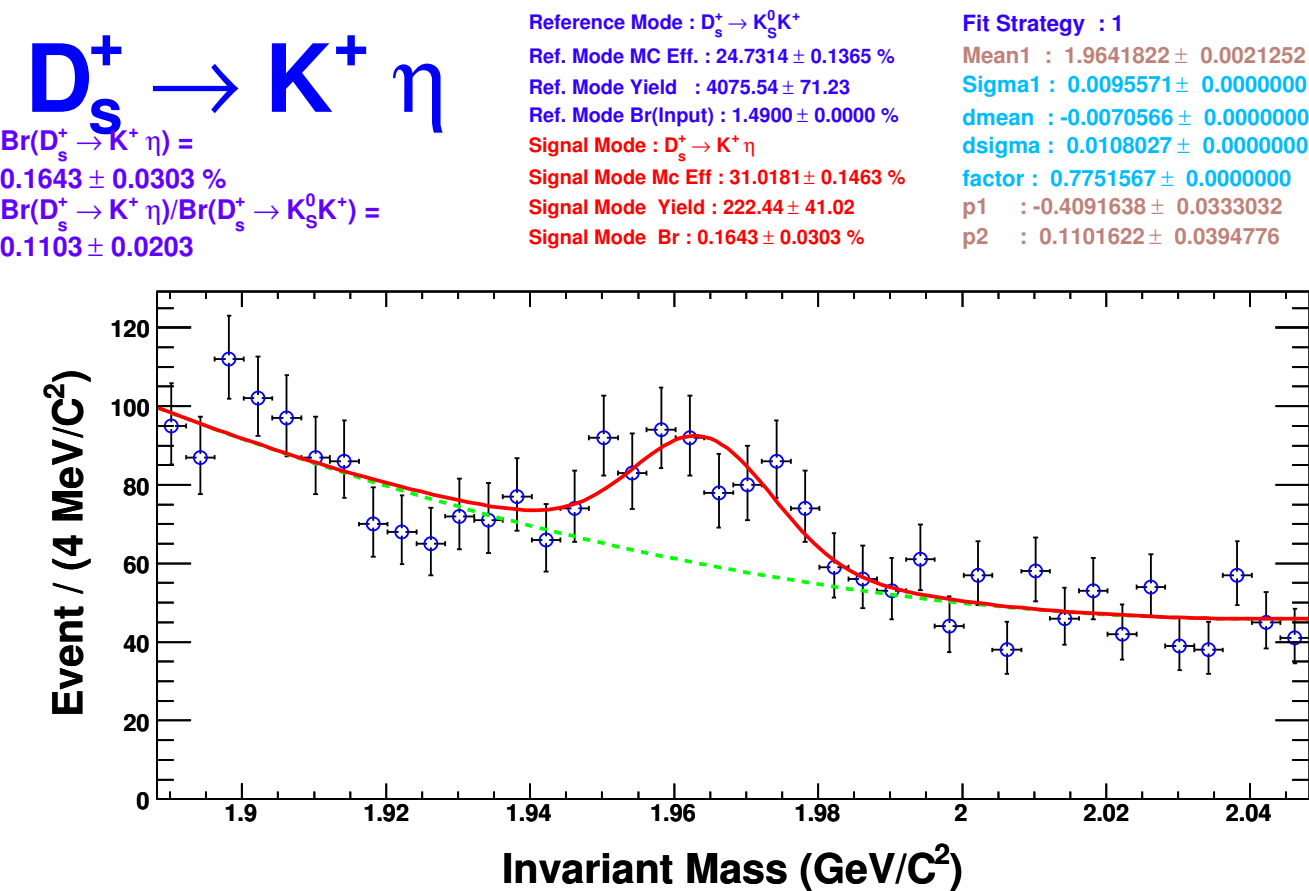
Figure 6.30: $D_s^+ \rightarrow \pi^+ \pi^0$ decay study.

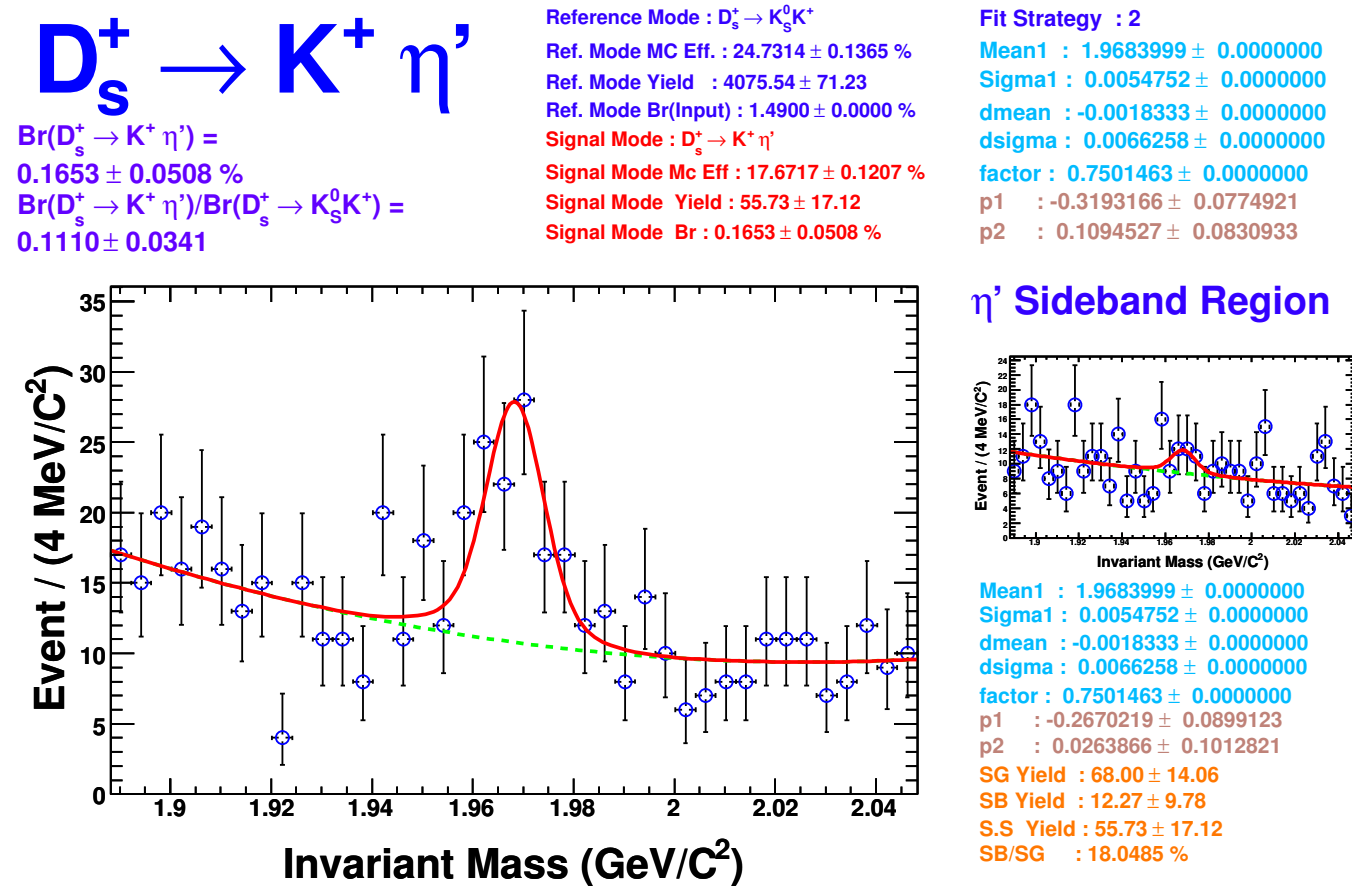
Figure 6.31: $D_s^+ \rightarrow \pi^+ \eta$ decay study.

Figure 6.32: $D_s^+ \rightarrow \pi^+ \eta'$ decay study.

Figure 6.33: $D_s^+ \rightarrow K_s^0 \pi^+$ decay study.

Figure 6.34: $D_s^+ \rightarrow K^+ \pi^0$ decay study.

Figure 6.35: $D_s^+ \rightarrow K^+ \eta$ decay study.


 Figure 6.36: $D_s^+ \rightarrow K^+ \eta'$ decay study.

6.8 Systematics

We have considered several sources of systematic uncertainties.

1. Tracking systematics
2. Additional Kaon track
3. π PID
4. K PID
5. π^0, K_S^0, η reconstruction
6. ΔE requirements
7. Background shape
8. Crystal Ball σ
9. Crystal Ball α
10. Crystal Ball n
11. ISR
12. FSR
13. Reference mode \mathcal{B}
14. Reference mode yield

6.8.1 Recoil Mass Requirements for D_s^+ Modes

We have applied $M_{\text{recoil}}(D_s)$ and $M_{\text{recoil}}(D_s + \gamma)$ requirements for both signal D_s^+ mode and reference D_s^+ mode ($D_s^+ \rightarrow K_S^0 K^+$). Then the systematics due to these two recoil mass requirements should cancel in the final D_s^+ absolute branching fractions.

Table 6.12: Uncertainties and Correction Factors

Source	Uncertainty (%)	Corr. Fact. (%)	Scheme
Tracking finding	0.3	—	per track
K^\pm track	0.6	—	per K^\pm
K_S^0 finding	1.9	—	per K_S^0
π^0 finding	1.0	-6.0	per π^0
η finding	4.0	-6.5	per η
π^\pm PID	0.3	-0.5	per π^\pm PID Cut
K^\pm PID	0.3	-1.0	per K^\pm PID Cut

6.8.2 MC Efficiencies, Tracking, and PID

Finite MC statistics in determining reconstruction efficiencies introduces uncertainties at the level of less than 1%. The uncertainty associated with the efficiency for finding a track is 0.3%; an additional 0.6% systematic uncertainty for each kaon track is added. Uncertainties in the charged pion and kaon identification efficiencies are 0.3% per pion and 0.3% per kaon [44].

6.8.3 π^0 , η , and K_S^0 Systematics

The relative systematic uncertainties for π^0 , η , and K_S^0 efficiencies are 1.0%, 4.0%, and 1.8%, respectively. The systematic uncertainty from the K_S^0 flight significance requirement is 0.5% [50]. We assign 1.9% as the systematic uncertainty for K_S^0 by combining uncertainties in K_S^0 finding and flight significance requirement. The values of uncertainties and correction factors that are used for this analysis are listed in Table 6.12.

6.8.4 ΔE Requirement for D^0 and D^+ Modes

Imperfect agreement in the ΔE resolution results in a systematic difference in efficiency due to the ΔE requirement. We estimate the associated uncertainty by increasing the ΔE window by an additional amount, and repeating the analysis. We take the relative difference as the uncertainty.

6.8.5 Background Shape

For high statistics D^0 and D^+ modes, we allow the ARGUS background shape parameter to float during the fit. For low statistics D^0 and D^+ modes, the shape parameter of ARGUS background function is determined from the ΔE sideband M_{bc} distribution and the systematic uncertainty is obtained by shifting the ARGUS background shape parameter up and down by one standard deviation. For all D_s^+ modes, the background shape parameters of second degree polynomial are allowed to float during the fit.

6.8.6 Crystal Ball Signal Shape for D^0 and D^+ Modes

During the fit for high statistics D^0 and D^+ modes, the signal shape parameters of Crystal Ball function are allowed to float. For low statistics D^0 and D^+ modes, the signal shape parameters are taken from MC simulation, and have uncertainties related to possible flaws in simulation. The uncertainties are studied by allowing Crystal Ball signal shape parameters to float one by one and repeating the fit.

6.8.7 Double Gaussian Signal Shape for D_s^+ Modes

For the signal of the D_s^+ mode, we use the sum of two Gaussians for the line shape. The signal shape parameters are determined by fits to $M(D_s)$ distributions obtained from Monte Carlo simulation, with the proviso that the peak location of the primary Gaussian is allowed to shift in the fits to the Cabibbo-favored modes, and all other peak locations are shifted by the same amount. For $D_s^+ \rightarrow K^+ \pi^0$ and $D_s^+ \rightarrow \pi^+ \pi^0$, where no appropriate Cabibbo-favored D_s decay exists, we have used the D^0 energy distribution of $D^0 \rightarrow K_S^0 \pi^0$, which indicates a peak shift of 5 MeV and a peak broadening of 10%. The systematic uncertainties due to signal fits are studied by using Cabibbo-favored modes, and apply the same fitting systematic uncertainty on their corresponding suppressed modes.

6.8.8 Input Branching Fraction

The uncertainties in the input branching fractions of normalization modes are 1.98% for $D^0 \rightarrow K^- \pi^+$, 2.16% for $D^+ \rightarrow K^- \pi^+ \pi^+$, and 5.77% for $D_s^+ \rightarrow K_S^0 K^+$.

6.8.9 Systematic Summary

The systematic uncertainties from each source and total systematic for all D^0 , D^+ and D_s modes are summarized in Table 6.13, 6.14, and 6.15.

6.9 Results Summary

The relative and absolute branching fractions of all $D \rightarrow PP$ modes are summarized in Table 6.16 (D^0 modes), Table 6.17 (D^+ modes), and Table 6.18 (D_s^+ modes). Previous published CLEO-c results are listed as a comparison.

I leave the theoretical interpretation of this set of 28 measured branching fractions to others.

Table 6.13: D^0 mode systematics summary.

Mode	1	2	3	4	5	6	7	8	9	10	11	12	13	14	Sum
$D^0 \rightarrow K^+ K^-$	0.00	0.60	0.30	0.30	0.00	0.05	0.00	0.00	0.00	0.00	0.50	0.50	1.98	0.36	2.26
$D^0 \rightarrow K_S^0 K_S^0$	0.60	0.60	0.30	0.30	3.80	0.06	0.79	3.04	1.20	0.10	0.50	0.50	1.98	0.36	5.58
$D^0 \rightarrow \pi^+ \pi^-$	0.00	0.60	0.30	0.30	0.00	0.07	0.25	1.44	1.30	0.91	0.50	0.50	1.98	0.36	3.12
$D^0 \rightarrow \pi^0 \pi^0$	0.60	0.60	0.30	0.30	2.00	1.38	0.77	0.55	2.03	0.09	0.50	0.50	1.98	0.36	4.05
$D^0 \rightarrow K^- \pi^+$	0.00	0.00	0.00	0.00	0.00	0.00	0.00	0.00	0.00	0.00	0.50	0.50	1.98	0.36	2.13
$D^0 \rightarrow K_S^0 \pi^0$	0.00	0.60	0.30	0.30	2.15	0.04	0.00	0.00	0.00	0.00	0.50	0.50	1.98	0.36	3.11
$D^0 \rightarrow K_S^0 \eta$	0.00	0.60	0.30	0.30	4.43	0.03	0.34	0.97	2.62	0.98	0.50	0.50	1.98	0.36	5.80
$D^0 \rightarrow \pi^0 \eta$	0.60	0.60	0.30	0.30	4.12	0.38	2.10	1.55	3.04	0.50	0.50	0.50	1.98	0.36	6.23
$D^0 \rightarrow K_S^0 \eta'$	0.60	0.60	0.30	0.30	4.43	0.48	0.00	0.00	0.00	0.00	0.50	0.50	1.98	0.36	5.03
$D^0 \rightarrow \pi^0 \eta'$	0.00	0.60	0.30	0.30	4.12	0.74	1.81	2.32	3.43	0.79	0.50	0.50	1.98	0.36	6.61
$D^0 \rightarrow \eta \eta$	0.60	0.60	0.30	0.30	8.00	0.17	1.23	1.00	0.76	0.12	0.50	0.50	1.98	0.36	8.52
$D^0 \rightarrow \eta \eta'$	0.00	0.60	0.30	0.30	8.00	0.59	3.50	0.10	2.43	0.33	0.50	0.50	1.98	0.36	9.36

Table 6.14: D^+ mode systematics summary.

Mode	1	2	3	4	5	6	7	8	9	10	11	12	13	14	Sum
$D^+ \rightarrow K^- \pi^+ \pi^+$	0.00	0.00	0.00	0.00	0.00	0.00	0.00	0.00	0.00	0.00	0.50	0.50	2.16	0.36	2.30
$D^+ \rightarrow K_S^0 K^+$	0.00	0.00	0.60	0.00	1.90	0.11	0.00	0.00	0.00	0.00	0.50	0.50	2.16	0.36	3.04
$D^+ \rightarrow \pi^+ \pi^0$	0.60	0.60	0.30	0.30	1.00	1.17	0.72	1.83	1.73	0.70	0.50	0.50	2.16	0.36	3.99
$D^+ \rightarrow K_S^0 \pi^+$	0.00	0.60	0.30	0.30	1.90	0.06	0.00	0.00	0.00	0.00	0.50	0.50	2.16	0.36	3.07
$D^+ \rightarrow K^+ \pi^0$	0.60	0.00	0.60	0.00	1.00	0.94	0.72	1.83	1.73	0.70	0.50	0.50	2.16	0.36	3.90
$D^+ \rightarrow K^+ \eta$	0.60	0.00	0.60	0.00	4.00	1.00	0.41	2.01	1.66	0.46	0.50	0.50	2.16	0.36	5.49
$D^+ \rightarrow \pi^+ \eta$	0.60	0.60	0.30	0.30	4.00	0.09	0.41	2.01	1.66	0.46	0.50	0.50	2.16	0.36	5.42
$D^+ \rightarrow K^+ \eta'$	0.00	0.00	0.00	0.00	4.00	0.89	0.41	1.58	1.39	0.91	0.50	0.50	2.16	0.36	5.24
$D^+ \rightarrow \pi^+ \eta'$	0.00	0.60	0.30	0.30	4.00	1.30	0.41	1.58	1.39	0.91	0.50	0.50	2.16	0.36	5.38

Table 6.15: D_s^+ mode systematics summary.

Mode	1	2	3	4	5	6	7	8	9	10	11	12	13	14	Sum
$D_s^+ \rightarrow K_S^0 K^+$	0.00	0.00	0.00	0.00	0.00	0.00	0.00	0.77	0.00	0.00	0.50	0.50	5.77	1.83	6.15
$D_s^+ \rightarrow \pi^+ \pi^0$	0.60	0.60	0.30	0.30	2.15	0.00	0.00	2.44	0.00	0.00	0.50	0.50	5.77	1.83	6.97
$D_s^+ \rightarrow K_S^0 \pi^+$	0.00	0.60	0.30	0.30	0.00	0.00	0.00	0.00	0.00	0.00	0.50	0.50	5.77	1.83	6.14
$D_s^+ \rightarrow K^+ \pi^0$	0.60	0.00	0.00	0.00	2.15	0.00	0.00	4.55	0.00	0.00	0.50	0.50	5.77	1.83	7.93
$D_s^+ \rightarrow K^+ \eta$	0.60	0.00	0.00	0.00	4.43	0.00	0.00	1.05	0.00	0.00	0.50	0.50	5.77	1.83	7.63
$D_s^+ \rightarrow \pi^+ \eta$	0.60	0.60	0.30	0.30	4.43	0.00	0.00	1.05	0.00	0.00	0.50	0.50	5.77	1.83	7.67
$D_s^+ \rightarrow K^+ \eta'$	0.00	0.00	0.60	0.00	4.43	0.00	0.00	1.60	0.00	0.00	0.50	0.50	5.77	1.83	7.73
$D_s^+ \rightarrow \pi^+ \eta'$	0.00	0.60	0.90	0.30	4.43	0.00	0.00	1.60	0.00	0.00	0.50	0.50	5.77	1.83	7.79
$\frac{D_s^+ \rightarrow \pi^+ \pi^0}{D_s^+ \rightarrow K_S^0 K^+}$	0.60	0.60	0.30	0.30	2.15	0.00	0.00	2.44	0.00	0.00	0.50	0.50	0.00	1.83	3.92
$\frac{D_s^+ \rightarrow K^+ \pi^0}{D_s^+ \rightarrow K_S^0 K^+}$	0.60	0.00	0.00	0.00	2.15	0.00	0.00	4.55	0.00	0.00	0.50	0.50	0.00	1.83	5.44
$\frac{D_s^+ \rightarrow K_S^0 \pi^+}{D_s^+ \rightarrow K^0 K^+}$	0.00	0.60	0.30	0.30	0.00	0.00	0.00	0.00	0.00	0.00	0.50	0.50	0.00	1.83	2.10
$\frac{D_s^+ \rightarrow K^+ \eta}{D_s^+ \rightarrow K^0 K^+}$	0.00	0.60	0.30	0.30	0.00	0.00	0.00	0.00	0.00	0.00	0.50	0.50	0.00	3.49	3.63
$\frac{D_s^+ \rightarrow \pi^+ \eta}{D_s^+ \rightarrow K^+ \eta'}$	0.00	0.60	0.30	0.30	0.00	0.00	0.00	0.00	0.00	0.00	0.50	0.50	0.00	3.31	3.47
$\frac{D_s^+ \rightarrow \pi^+ \eta'}{D_s^+ \rightarrow \pi^+ \eta'}$	0.00	0.60	0.30	0.30	0.00	0.00	0.00	0.00	0.00	0.00	0.50	0.50	0.00	3.31	3.47

Table 6.16: Relative and absolute branching fractions of $D^0 \rightarrow PP$ modes.

Mode	$\mathcal{B}_{\text{mode}}/\mathcal{B}_{\text{ref}} (\%)$	$\mathcal{B}_{\text{mode}} (\%)$	$\mathcal{B}(281\text{pb}^{-1})(\%)$
$D^0 \rightarrow K^+K^-$	$10.4138 \pm 0.1064 \pm 0.1063$	$0.4052 \pm 0.0041 \pm 0.0041 \pm 0.0082$	$0.4080 \pm 0.0080 \pm 0.0090$
$D^0 \rightarrow K_S^0K_S^0$	$0.4095 \pm 0.0432 \pm 0.0213$	$0.0159 \pm 0.0017 \pm 0.0008 \pm 0.0003$	$0.0146 \pm 0.0032 \pm 0.0009$
$D^0 \rightarrow \pi^+\pi^-$	$3.7023 \pm 0.0561 \pm 0.0883$	$0.1441 \pm 0.0022 \pm 0.0034 \pm 0.0029$	$0.1390 \pm 0.0040 \pm 0.0050$
$D^0 \rightarrow \pi^0\pi^0$	$2.1491 \pm 0.0740 \pm 0.0754$	$0.0836 \pm 0.0029 \pm 0.0029 \pm 0.0017$	$0.0790 \pm 0.0050 \pm 0.0060$
$D^0 \rightarrow K^-\pi^+$	1.0000	3.8910 used	$3.8910 \pm 0.0350 \pm 0.0690$
$D^0 \rightarrow K_S^0\pi^0$	$31.0495 \pm 0.2964 \pm 0.7382$	$1.2081 \pm 0.0115 \pm 0.0287 \pm 0.0243$	$1.2400 \pm 0.0170 \pm 0.0560$
$D^0 \rightarrow K_S^0\eta$	$12.2575 \pm 0.2872 \pm 0.6662$	$0.4769 \pm 0.0112 \pm 0.0259 \pm 0.0096$	$0.4420 \pm 0.0150 \pm 0.0280$
$D^0 \rightarrow \pi^0\eta$	$1.7714 \pm 0.1481 \pm 0.1045$	$0.0689 \pm 0.0058 \pm 0.0041 \pm 0.0014$	$0.0620 \pm 0.0140 \pm 0.0050$
$D^0 \rightarrow K_S^0\eta'$	$24.7307 \pm 0.8154 \pm 1.1398$	$0.9623 \pm 0.0317 \pm 0.0443 \pm 0.0194$	—
$D^0 \rightarrow \pi^0\eta'$	$2.4084 \pm 0.2874 \pm 0.1517$	$0.0937 \pm 0.0112 \pm 0.0059 \pm 0.0019$	$0.0810 \pm 0.0150 \pm 0.0060$
$D^0 \rightarrow \eta\eta$	$4.2495 \pm 0.2838 \pm 0.3518$	$0.1653 \pm 0.0110 \pm 0.0137 \pm 0.0033$	$0.1670 \pm 0.0140 \pm 0.0130$
$D^0 \rightarrow \eta\eta'$	$2.7318 \pm 0.6235 \pm 0.2498$	$0.1063 \pm 0.0243 \pm 0.0097 \pm 0.0021$	$0.1260 \pm 0.0250 \pm 0.0110$

Table 6.17: Relative and absolute branching fractions of $D^+ \rightarrow PP$ modes.

Mode	$\mathcal{B}_{\text{mode}}/\mathcal{B}_{\text{ref}} (\%)$	$\mathcal{B}_{\text{mode}} (\%)$	$\mathcal{B}(281\text{pb}^{-1})(\%)$
$D^+ \rightarrow K^-\pi^+\pi^+$	1.0000	9.1400 used	$9.1400 \pm 0.1000 \pm 0.1700$
$D^+ \rightarrow K_S^0 K^+$	$3.3502 \pm 0.0573 \pm 0.0709$	$0.3062 \pm 0.0052 \pm 0.0065 \pm 0.0067$	$0.3140 \pm 0.0090 \pm 0.0080$
$D^+ \rightarrow \pi^+\pi^0$	$1.3208 \pm 0.0382 \pm 0.0441$	$0.1207 \pm 0.0035 \pm 0.0040 \pm 0.0026$	$0.1250 \pm 0.0060 \pm 0.0080$
$D^+ \rightarrow K_S^0 \pi^+$	$16.8160 \pm 0.1239 \pm 0.3628$	$1.5370 \pm 0.0113 \pm 0.0332 \pm 0.0336$	$1.5260 \pm 0.0220 \pm 0.0380$
$D^+ \rightarrow K^+\pi^0$	$0.1923 \pm 0.0206 \pm 0.0062$	$0.0176 \pm 0.0019 \pm 0.0006 \pm 0.0004$	$0.0228 \pm 0.0036 \pm 0.0017$
$D^+ \rightarrow K^+\eta$	< 0.1442 (90% C.L.)	< 0.0132 (90% C.L.)	—
$D^+ \rightarrow \pi^+\eta$	$3.8538 \pm 0.0895 \pm 0.1911$	$0.3522 \pm 0.0082 \pm 0.0175 \pm 0.0077$	$0.3610 \pm 0.0250 \pm 0.0260$
$D^+ \rightarrow K^+\eta'$	< 0.2032 (90% C.L.)	< 0.0187 (90% C.L.)	—
$D^+ \rightarrow \pi^+\eta'$	$5.2061 \pm 0.1762 \pm 0.2558$	$0.4758 \pm 0.0161 \pm 0.0234 \pm 0.0104$	$0.4420 \pm 0.0250 \pm 0.0290$

Table 6.18: Relative and absolute branching fractions of $D_s^+ \rightarrow PP$ modes.

Mode	$\mathcal{B}_{\text{mode}}/\mathcal{B}_{\text{ref}} (\%)$	$\mathcal{B}_{\text{mode}} (\%)$	$\mathcal{B}(298\text{pb}^{-1})(\%)$
$D_s^+ \rightarrow K_S^0 K^+$	1.0000	1.4900 used	$1.4900 \pm 0.0700 \pm 0.0500$
$D_s^+ \rightarrow \pi^+ \pi^0$	< 2.3492 (90% C.L.)	< 0.0376 (90% C.L.)	—
$D_s^+ \rightarrow K_S^0 \pi^+$	$8.4766 \pm 0.7147 \pm 0.1778$	$0.1263 \pm 0.0106 \pm 0.0026 \pm 0.0073$	—
$D_s^+ \rightarrow K^+ \pi^0$	$4.2383 \pm 1.4756 \pm 0.2304$	$0.0632 \pm 0.0220 \pm 0.0034 \pm 0.0036$	—
$D_s^+ \rightarrow K^+ \eta$	$11.7933 \pm 2.1753 \pm 0.5888$	$0.1757 \pm 0.0324 \pm 0.0088 \pm 0.0101$	—
$D_s^+ \rightarrow \pi^+ \eta$	$123.1123 \pm 4.2907 \pm 6.2133$	$1.8344 \pm 0.0639 \pm 0.0926 \pm 0.1059$	$1.5800 \pm 0.1100 \pm 0.1800$
$D_s^+ \rightarrow K^+ \eta'$	$11.9866 \pm 3.6840 \pm 0.6158$	$0.1786 \pm 0.0549 \pm 0.0092 \pm 0.0103$	—
$D_s^+ \rightarrow \pi^+ \eta'$	$269.8080 \pm 8.9375 \pm 14.0957$	$4.0201 \pm 0.1332 \pm 0.2100 \pm 0.2320$	$3.7700 \pm 0.2500 \pm 0.3000$
$\frac{D_s^+ \rightarrow \pi^+ \pi^0}{D_s^+ \rightarrow K_S^0 K^+}$	< 2.3492 (90% C.L.)	—	< 4.1000 (90% C.L.)
$\frac{D_s^+ \rightarrow K^+ \pi^0}{D_s^+ \rightarrow K_S^0 K^+}$	$4.2383 \pm 1.4756 \pm 0.2304$	—	$5.5000 \pm 1.3000 \pm 0.7000$
$\frac{D_s^+ \rightarrow K_S^0 \pi^+}{D_s^+ \rightarrow K^+ \pi^0}$	$8.4766 \pm 0.7147 \pm 0.1778$	—	$8.2000 \pm 0.9000 \pm 0.2000$
$\frac{D_s^+ \rightarrow K^0 K^+}{D_s^+ \rightarrow K^+ \pi^0}$	$9.5793 \pm 1.7669 \pm 0.3479$	—	$8.9000 \pm 1.5000 \pm 0.4000$
$\frac{D_s^+ \rightarrow \pi^+ \eta}{D_s^+ \rightarrow \pi^+ \eta'}$	$4.4426 \pm 1.3654 \pm 0.1540$	—	$4.2000 \pm 1.3000 \pm 0.3000$

Bibliography

- [1] S. Weinberg, Phys. Rev. Lett. **19**, 1264 (1967); A. Salam, p. 367 of *Elementary Particle Theory*, ed. N. Svartholm (Almqvist and Wiksell, Stockholm, 1969); S. L. Glashow, J. Iliopoulos, and L. Maiani, Phys. Rev. D, **2**, 1285 (1970).
- [2] F. J. Hasert *et al.* Phys. Lett. **46B** 121 (1973)
- [3] Fig. 1.1 is from Wiki web page: <http://en.wikipedia.org>, as is Table 1.1.
- [4] B. Bhattacharya and J. L. Rosner, Phys. Rev. D **79**, 034016 (2009).
- [5] M. Gronau and J. L. Rosner, arXiv:0903.2287 [hep-ph].
- [6] I. I. Y. Bigi, Z. Phys. C **5** 313 (1979); Z. Phys. C **9**, 197 (1981); Nucl. Phys. **B177**, 395 (1981); I. I. Y. Bigi and M. Fukugita, Phys. Lett. **97B**, 121 (1980); I. I. Bigi and N. G. Uraltsev, Phys. Lett. B **280**, 271 (1992); Nucl. Phys. **B423**, 33 (1994); M. Neubert and C. T. Sachrajda, Nucl. Phys. **B483**, 339 (1997); M. B. Voloshin, Phys. Lett. B **515**, 74 (2001); A. K. Leibovich, Z. Ligeti, and M. B. Wise, Phys. Lett. B **539**, 242 (2002); H.-Y. Cheng, Eur. Phys. J. C **26**, 551 (2003); S. Fajfer, A. Prapotnik, P. Singer, and J. Zupan, Phys. Rev. D **68**, 094012 (2003); P. Gambino, J. Ossola, and N. Uraltsev, JHEP **0509**, 010 (2005); P. Gambino, P. Giordano, G. Ossola and N. Uraltsev, JHEP **0710**, 058 (2007). Further references may be found in S. Bianco, F. L. Fabbri, D. Benson and I. Bigi, Riv. Nuovo Cim. **26N7**, 1 (2003).
- [7] J. L. Rosner *et al.* (CLEO Collaboration), Phys. Rev. Lett. **96**, 121801 (2006).
- [8] B. Aubert *et al.* [BABAR Collaboration], arXiv:0708.1753 [hep-ex].
- [9] P. Gambino, P. Giordano, G. Ossola and N. Uraltsev, Ref. [6].

- [10] M. Gronau and J. L. Rosner, arXiv:0902.1363 [hep-ph], to be published in Phys. Rev. D.
- [11] C. Amsler *et al.* [Particle Data Group], Phys. Lett. B **667**, 1 (2008).
- [12] S. Okubo, Phys. Lett. **5**, 165 (1963); G. Zweig, CERN Report No. 8419/TH-412 (1964); J. Iizuka, Prog. Theor. Phys. Suppl. **37**, 21 (1966).
- [13] E. Fermi, Phys. Rev. **92**, 452 (1953); **93**, 1434(E) (1954); K. M. Watson, Phys. Rev. **85**, 852 (1952); I. Smushkevich, Dokl. Akad. Nauk SSSR **103**, 235 (1955); A. Pais, Ann. Phys. (N.Y.) **9**, 548 (1960); **22**, 274 (1963); M. Peshkin, Phys. Rev. **121**, 636 (1961).
- [14] M. Peshkin and J. L. Rosner, Nucl. Phys. B **122**, 144 (1977).
- [15] C. Quigg and J. L. Rosner, Phys. Rev. D **17**, 239 (1977).
- [16] M. Gronau, Y. Grossman, and J. L. Rosner, Phys. Lett. B **508**, 37 (2001).
- [17] D. Atwood, I. Dunietz, and A. Soni, Phys. Rev. Lett. **78**, 3257 (1997); Phys. Rev. D **63**, 036005 (2001).
- [18] B. Bhattacharya and J. L. Rosner, Phys. Rev. D **77**, 114020 (2008) [arXiv:0803.2385 [hep-ph]].
- [19] L. L. Chau, Phys. Rep. **95**, 1 (1983).
- [20] L. L. Chau and H.-Y. Cheng, Phys. Rev. Lett. **56**, 2655 (1986).
- [21] “CLEO-c and CESR-c: A New Frontier of Weak and Strong Interactions”.
- [22] Alexander Scott, Ph. D thesis, *Measurement of Quantum Correlation Parameters at the $\psi(3770)$ resonance*, University of Minnesota (2007).
- [23] Credit - LEPP Publications Office.
- [24] R. A. Briere *et al.* (CESR-c and CLEO-c Taskforces, CLEO-c Collaboration), Cornell University, LEPP Report No. CLNS 01/1742 (2001) (unpublished).
- [25] Y. Kubota *et al.* (CLEO Collaboration), Nucl. Instrum. Meth. A **320**, 66 (1992).

- [26] D. Peterson *et al.*, Nucl. Instrum. Methods Phys. Res., Sec. A **478**, 142 (2002).
- [27] M. Artuso *et al.*, Nucl. Instrum. Methods Phys. Res., Sec. A **502**, 91 (2003).
- [28] D. Cronin-Hennessy *et al.* (CLEO Collaboration), arXiv:0801.3418.
- [29] “Developments in $D_{(s)}$ -Tagging”, P. Onyisi and W. Sun, CBX 06-11.
- [30] “A Study of $D_s^+ \rightarrow \tau^+ \nu_\tau \rightarrow e^+ \nu_e \bar{\nu}_\tau \nu_\tau$ Decays”, C. S. Park and E. Thorndike, CBX 07-32.
- [31] K. M. Ecklund *et al.* (CLEO Collaboration), Phys. Rev. Lett. **100**, 161801 (2008).
- [32] “CLEO-c D Tagging: 2005 Version (aka Version 1 DTags)” R. Briere, G-P. Chen, P. Zweber, CBX07-30.
- [33] “A Study of $D \rightarrow e^+ X$ Decays”, C. S. Park and E. Thorndike, CBX 05-73.
- [34] T. E. Coan *et al.* (CLEO Collaboration), Phys. Rev. Lett. **95**, 181802 (2005).
- [35] EID web page:
<http://www.lns.cornell.edu/restricted/CLEO/CLEO3/soft/hints/EID.html>.
- [36] G. S. Huang *et al.* (CLEO Collaboration), Phys. Rev. D **74**, 112005 (2006).
- [37] T. Skwarnicki, Ph.D thesis, Institute for Nuclear Physics, Krakow, Poland, 1986.
- [38] S. Dobbs *et al.* (CLEO Collaboration), Phys. Rev. D **76**, 112001 (2007).
- [39] P. U. E. Onyisi *et al.* (CLEO Collaboration), Phys. Rev. D **79**, 052002 (2009).
- [40] J. P. Alexander *et al.* (CLEO Collaboration), Phys. Rev. D **79**, 052001 (2009).
- [41] C. W. Chiang, Z. Luo, and J. L. Rosner, Phys. Rev. D **67**, 014001 (2003).
- [42] G. Bonvicini *et al.* (CLEO Collaboration), Phys. Rev. D **77**, 091106 (2008)
- [43] P. Rubin *et al.* (CLEO Collaboration), Phys. Rev. Lett. **96**, 081802 (2006)
- [44] S. Dobbs *et al.* (CLEO Collaboration), Phys. Rev. D **76**, 112001 (2007)

- [45] Q. He *et al.* (CLEO Collaboration), Phys. Rev. Lett. **100**, 091801 (2008)
- [46] J. L. Rosner *et al.* (CLEO Collaboration), Phys. Rev. Lett. **100**, 221801 (2008)
- [47] M. Artuso *et al.* (CLEO Collaboration), Phys. Rev. D **77**, 092003 (2008)
- [48] M. Artuso *et al.* (CLEO Collaboration), S. A. Dytman **74**, 071102(R) (2006)
- [49] J. P. Alexander *et al.* (CLEO Collaboration), Phys. Rev. Lett. **100**, 161804 (2008)
- [50] G. S. Adams *et al.* (CLEO Collaboration), Phys. Rev. Lett. **99**, 191805 (2007)
- [51] J. Adler *et al.* (Mark III Collaboration), Phys. Rev. Lett. **62**, 1821 (1989).
- [52] H. Albrecht *et al.* (ARGUS Collaboration), Phys. Lett. B **229**, 304 (1989).